Well Integrity Assessment of CFU31-F2 and CFU-31F3

For

Statistical Analysis of CO_2 Exposed Wells to Predict Long Term Leakage through the Development of an Integrated Neural-Genetic Algorithm

May 23, 2017

Prepared by: Andrew Duguid Ph.D., P.E.
Battelle
505 King Avenue
Columbus, Ohio 43201

Submitted to:

Boyun Guo
University of Louisiana at Lafayette

BATTELLE

Table of Contents

List of Tables

List of Figures

Page

1 Introduction

Carbon capture utilization storage (CCUS) is a potential technology to store anthropogenic emissions for CO_2. Utilization often refers to CO_2-enhanced oil recovery (CO_2-EOR). An important factor in the success of CO_2 storage in saline formations or CO_2-EOR reservoirs is ensuring that the storage occurs safely and is long-term. Assessment of well integrity has become more important for CCS and CO_2-EOR as it has become apparent that wells represent the most likely migration pathway for CO_2 to leave a CCS storage unit or a CO_2-EOR reservoir. Although wells represent a migration pathway they are also the best vehicle for employing technology monitoring CO_2 injection and storage. This contradiction of being a potential migration path and key monitoring technology leads to a need to understand how monitoring wells may be similar or different in comparison to other types of wells with respect to migration risk. The maturation and completion US Department of Energy sponsored research projects presents an opportunity to assess the integrity of monitoring wells that have been exposed to injected CO_2. This paper discusses an integrity assessment of two monitoring wells in an operating CO_2-EOR flood in Mississippi, USA.

Well integrity has been studied by several groups to understand well leakage risk or if individual wells may contain or become leakage pathways at CO_2 storage or CO_2-EOR projects. Studies have included logging and sampling of CO_2 exposed wells at SACROC [1], Weyburn [2], and Cranfield [3] Fields and the well studied by the CCP2 project [4]. Each of these studies recognized that well cements interact with CO_2 from the production and injection reservoir and none of the cements measured had carbonated to the point where both calcium silicate hydrate (C-S-H) and portlandite ($Ca(OH)_2$) had been completely reacted. The SACROC cement was collected at the surface and was the result of a sidetrack cut in the well. The well was constructed in 1950 and first exposed to CO_2 in 1975. The Weyburn, Cranfield, and CCP2 studies were similar to this study in that they had logging, testing, and sampling. Each study used well integrity logs and collected cased-hole sidewall cores. These wells were 54 (Weyburn), 68 (Cranfield) and 30 (CCP2) years old at the time of their respective studies. Additional studies of the pre-exposure condition of legacy wells were conducted by Duguid et al. [5] Duguid et al. used a combination of cased-hole well integrity logging and cased-hole pressure testing and sidewall core collection determine flow properties. Duguid et al. [5] found that the casing-cement and cement-formation interfaces in the well represent the most likely pathways for vertical fluid movement. They also found that the cements used to construct the wells had not been leached (removal of calcium) by exposure to native formation fluids.

The Southeast Regional Carbon Sequestration Partnership (SECARB) has been studying storage associated with CO_2-EOR at Cranfield Field, near Natchez, Mississippi, USA. To gain an understanding of the injection project impact on the reservoir and overlying strata, the partnership used multiple monitoring technologies to locate and quantify CO_2 using two constructed-for-purpose monitoring wells on the eastern flank of the field [6]. The wells were used to deploy permanent and temporary monitoring technologies, inside and outside the casing, in and above the reservoir [7, 8, 9]. The objective of this study was to apply methods similar to those of Crow et al. [4] and Duguid et al. [5] to study the integrity of CO_2 monitoring wells at Cranfield Field.

2 Background

The degradation of cement through exposure to CO_2 and carbonic acid has been studied by researchers including Kutchko et al.[10], Duguid et al.[11, 12, 13] and Barlet-Gouédard et al. [14] Earlier researchers Andac and Glasser [15], Revertegat, Richet, and Gégout [16], Onan [17] and Bruckdorfer [18]. Kutchko et al. [10], Duguid et al. [11, 12, 13] and Barlet-Gouédard et al. [14] all found that the cement phases reacted following the equations below:

CO_2 dissociation:

$$CO_2 + H_2O \leftrightarrow H_2CO_3 \leftrightarrow H^+ + HCO_3^- \leftrightarrow 2H^+ + CO_3^{2-} \quad \text{[Equation 1]}$$

Cement dissolution:

$$Ca(OH)_2(s) + 2H^+ + CO_3^{2-} \rightarrow CaCO_3(s) + 2H_2O \quad \text{[Equation 2]}$$

$$C_{3.4}\text{-}S_2\text{-}H_8(s) + 2H^+ + CO_3^{2-} \rightarrow CaCO_3(s) + SiO_xOH_x(s) \quad \text{[Equation 3]}$$

$$Ca(OH)_2(s) + H^+ + HCO_3^- \rightarrow CaCO_3(s) + 2H_2O \quad \text{[Equation 4]}$$

$$C_{3.4}\text{-}S_2\text{-}H_8(s) + H^+ + HCO_3^- \rightarrow CaCO_3(s) + SiO_xOH_x(s) \quad \text{[Equation 5]}$$

Calcium carbonate dissolution:

$$CO_2 + H_2O + CaCO_3(s) \leftrightarrow Ca^{2+} + 2HCO_3^- \quad \text{[Equation 6]}$$

$$2H^+ + CaCO_3(s) \leftrightarrow CO_2 + Ca^{2+} + H_2O \quad \text{[Equation 7]}$$

Equations 1 through 5 describe how calcium is leached from cement and forms calcium carbonate. Several researchers [1, 4, 10, 11] have shown that, as cement is exposed to carbonic acid, the $Ca(OH)_2$ in the cement reacts before $C_{3.4}\text{-}S_2\text{-}H_8$. The research also shows that $Ca(OH)_2$ acts to buffer the carbonic acid by creating and precipitating $CaCO_3$ and precipitation in the pores affects the transport properties of the cement by blocking pores and allowing less flow. Duguid et al. [11] found that $CaCO_3$ fills the pores and slows transport of the carbonic acid into the cement and the reaction products out of the cement. Kutchko et al.[10] found that the precipitation of $CaCO_3$ in their samples leads to a strengthening of the cement in the precipitation zone. However, the reaction product, calcium carbonate ($CaCO_3$) is also subject to degradation due to exposure to carbonic acid (Equations 6 and 7). If the exposure is long enough or the carbonic acid is refreshed often, the calcium carbonate will eventually be removed leaving the cement matrix with less strength [10, 14, 18], higher porosity [1, 4, 16] and higher permeability[1, 11] than the unreacted cement.

The CFU31F-2 and CFU31F-3 wells were constructed as monitoring wells as part of the SECARB Phase III Injection Project at Cranfield Field. Cranfield field sits east of Natchez, MS in Adams and Franklin Counties (Figure 1). The field was discovered in 1943. The field was produced between 1943 and 1966 [9]. CO_2-EOR in the field began in 2008. Injection and production are in the D and E sands of the Tuscaloosa formation.

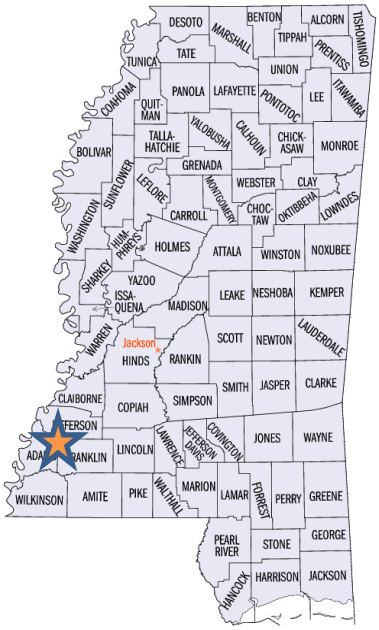

Figure 1 Map showing the approximate location of Cranfield Field in Mississippi.

The wells are similarly constructed and purpose-built for monitoring. The wells are spaced approximately 92 ft apart at the surface. They are on the margin of Cranfield Field down dip from an injection well (CFU31F-1). CFU31F-1, CFU31F-2, and CFU31F-3 are arranged along a line with CFU31F-2 being approximately 200 ft away from CFU31F-1 and CFU31F-3 being approximately 295 ft away from CFU31F-1at the surface. Figure 2 shows the location of CFU31F-2 and CFU31F-3.

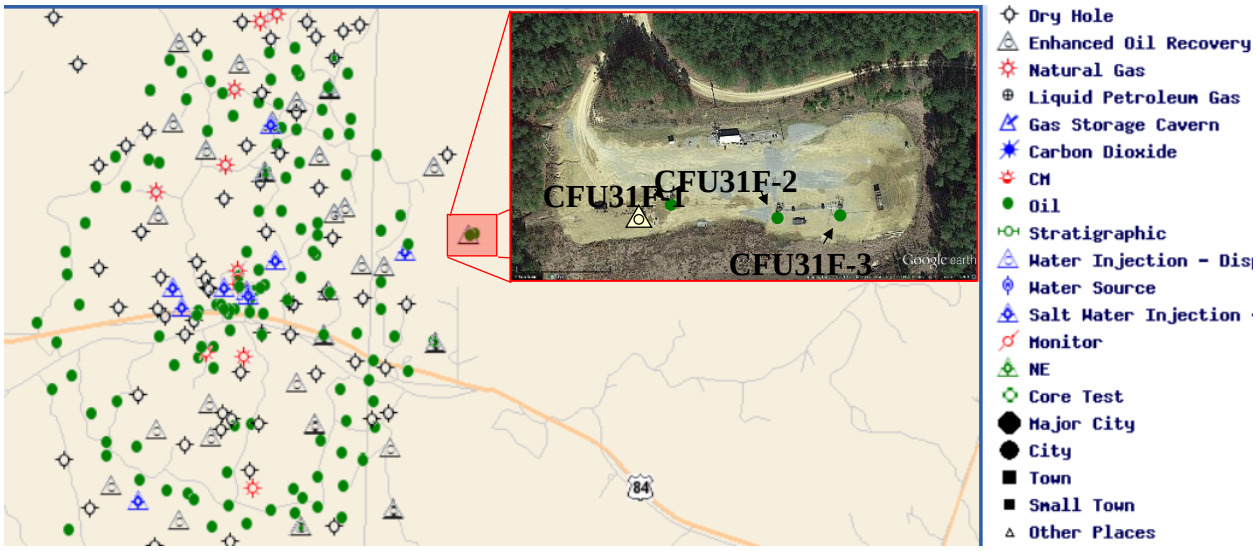

Figure 2 Map of Cranfield Field wells in the Mississippi Oil and Gas Board database [10] with an aerial image showing CFU31F-1, CFU31F-2, and CFU31F-3 wells.

CFU31F-2 was spudded 22 July, 2009 and reached total depth (TD) 18 August, 2009 [20]. CFU31F-3 was spudded 25 June, 2009 and reached TD 12 July, 2009 [21]. Each of the monitoring wells were constructed with multiple monitoring technologies mounted to the long-string casing. The specific construction details of each

well are provided in Table 1 through Table 7 and Figure 3. The surface and intermediate sections of each well were conventionally designed. The long-string section of each well included both conventional N80 grade steel casing and Bluebox 2500 fiberglass casing (Figure 4). Pressure and temperature sensors were mounted to the outside of the steel casing, electrical resistivity tomography electrodes were mounted in the fiberglass section, above, in, and below the reservoir. Casing mounted fiber optic systems extended from the surface through the reservoir on both wells. The long-string casing on both wells were cemented using a 35:65:6 Class H lead Slurry (35% flyash, 65% class H cement with 6% bentonite) and a Class H and Silica Flour tail slurry. The typical composition of Class H cement [23], Class C fly ash [24], and silica flour [25] are presented in Table 1 to Table 4.

Table 1 Long-string cement information

Well	Slurry	Cement	Mass (sacks)	Yield (ft3/sack)	Volume (bbls)	Density (ppg)
CFU31-F2	Lead	35:65:6	565	1.48	148.5	12.8
CFU31-F2	Tail	Class H + Silica Flour	440	1.91	149.69	16.2
CFU31-F3	Lead	35:65:6	770	1.48	202.38	12.8
CFU31-F3	Tail	Class H + Silica Flour	465	1.91	158.19	16.2

Table 2 Typical Composition of Class H Cement [23].

Cement chemistry nomenclature	C3S	B-C2S	C3A	C4AF
Chemical composition	3CaO-SIO2	2CaO-SIO2	3CaO-Al2O	4CaO-Al2O3-Fe2O3
wt%	50	30	4	12

Table 3 Composition of Class C Fly Ash [24].

Component	**Weight percent in Class C Fly Ash**
SiO_2	40
Al_20_3	17
Fe_2O_3	6
CaO (Lime)	24
MgO	5
SO_3	3

Table 4 Composition of silica flour [25].

Compounds	WT% in Silica Flour
SiO_2	95.70
Al2O3	2.00
Fe2O3	0.20
SO3	1.80

Using these values the Ca/Si, Ca/Fe, and Ca/Al ratios can be estimated (Table 5 and Table 6).

Table 5 Estimated approximate values for lead slurry ratios.

	Ca/Si	Ca/Al	Ca/Fe
Mass/Mass	2.55	4.63	5.35
Mole/Mole	1.79	3.12	7.45

Table 6 Estimated approximate values for tail slurry ratios.

	Ca/Si	Ca/Al	Ca/Fe
Mass/Mass	1.24	9.18	9.76
Mole/Mole	0.87	6.18	13.60

Injection commenced December 1, 2009 and continued into June 2015 [13]. Using the ERT arrays breakthrough was seen in CFU31F-2 on December 12, 2009 (12 days after injection) and seen in CFU31F-3 on December 16, 2009; 16 days after injection. [9] The wells were logged with openhole tools prior to casing and cementing to collect gamma-ray, array resistivity, bulk density, photoelectric effect, and caliper data. Pulsed neutron logging tools were used to collect the neutron porosity data and were also used to establish fluid saturations near the wellbore [7]. The pulsed neutron results agree with the ERT results of Carrigan [9] and show CO_2 in the reservoir down-dip from the injector surrounding CFU31F-2 and CFU31F-3 after injection commenced.

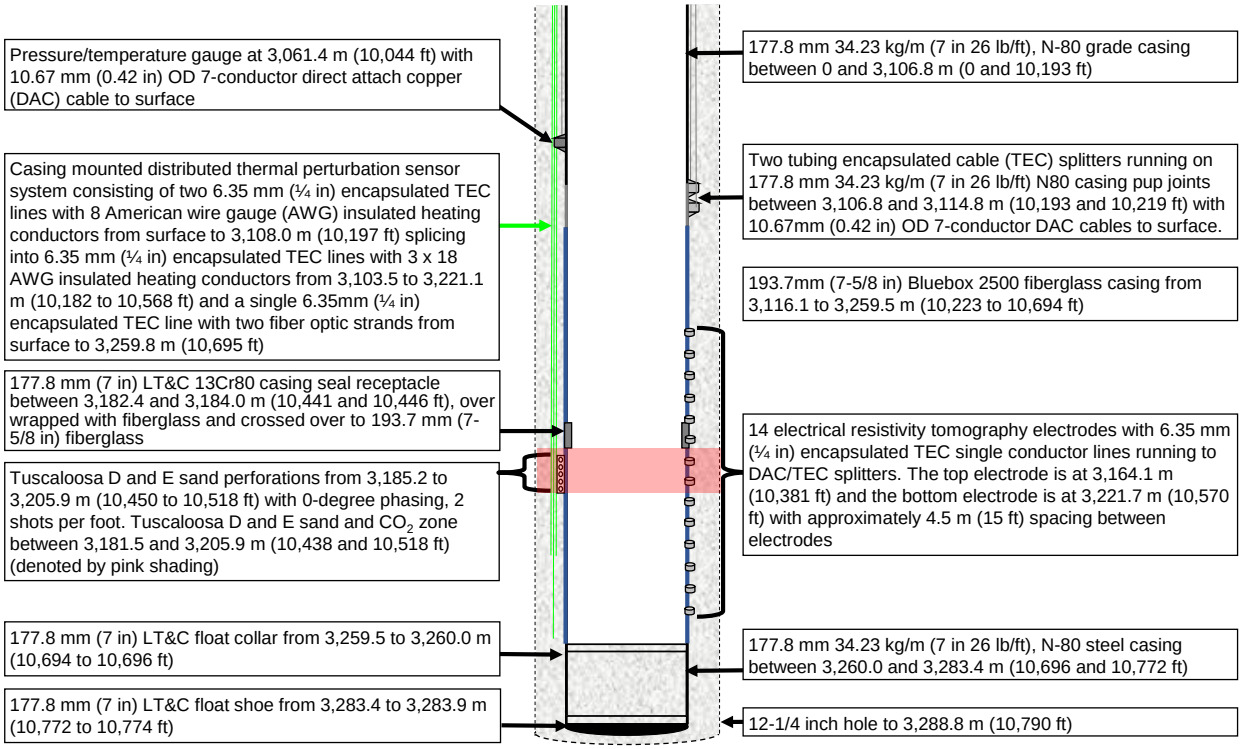

Figure 3 Construction schematic for CFU31-F2.

Table 7 Well construction details of the long-string portions of CFU31F-2 and CFU31F-3.

Well Component	Size	CFU31F-2		CFU31F-3	
		Top	Bottom	Top	Bottom
		(ft)	(ft)	(ft)	(ft)
Hole	12-1/4 in	0.0	10790.0	0.0	10789
Casing	7 in 26 lb/ft, N-80 grade casing	0.0	10219.0	0.0	10221.67
Casing	7-5/8 in Bluebox 2500 fiberglass casing	10219.0	10693.9	10221.67	10693.21
Float Collar	7 in LT&C float collar	10693.9	10695.6	10693.21	10694.9
Casing	7 in 26 lb/ft, N-80 steel casing	10695.6	10772.2	10694.9	10770.13
Float Shoe	7 in LT&C float shoe	10772.2	10774.0	10770.13	10771.9
Casing Seal Receptacle	7 in LT&C 13Cr80 casing seal receptacle over wrapped with fiberglass and crossed over to 7-5/8 in fiberglass	10441.0	10446.0	10440.2	10445.4
Perforations	Tuscaloosa D and E sand perforations, 0-degree phasing, 2 shots per foot.	10450.0	10518.0	10450	10520
Reservoir	Tuscaloosa D and E sand	10438.0	10518.0	10440	10520
Monitoring Equipment					
Monitoring Equipment		Pressure/temperature gauge at 10044 ft with 0.42 in OD 7-conductor direct attach copper (DAC) cable to surface		Pressure/temperature gauge at 10447 ft with 0.42 in OD 7-conductor direct attach copper (DAC) cable to surface	
Monitoring Equipment		Casing mounted distributed thermal perturbation sensor system consisting of two ¼ in encapsulated TEC lines with 8 American wire gauge (AWG) insulated heating conductors from surface to 10197 ft splicing into ¼ in encapsulated TEC lines with 3 x 18 AWG insulated heating conductors from 10182 to 10568 ft and a single ¼ in encapsulated TEC line with two fiber optic strands from surface to 10695 ft		Casing mounted distributed temperature sensor system consisting of two 0.433 in round ¼ in encapsulated TEC lines with 8 American wire gauge (AWG) insulated heating conductors from surface to 10207 ft splicing into 0.433 in round ¼ in encapsulated TEC lines with 3 x 18 AWG insulated heating conductors from 10207 to 10569 ft and a single ¼ in round 1/8 in encapsulated TEC line with two fiber optic strands from surface to 10694 ft	
Monitoring Equipment		Two tubing encapsulated cable (TEC) splitters running on pup joints between 10193 and 10219 ft with 0.42 in OD 7-conductor DAC cables to surface.		One DAC/TEC splitter on a pup joint between 10208.4 - 10221.7 ft with 0.42 in OD 7-conductor DAC cables to surface.	
Monitoring Equipment		14 electrical resistivity tomography electrodes with ¼ in encapsulated TEC single conductor lines running to DAC/TEC splitters. The top electrode is at 10381 ft and the bottom electrode is at 10570 ft with approximately 15 ft spacing between electrodes		7 electrical resistivity tomography electrodes with 0.433 in square encapsulated ¼ in TEC single conductor lines running to DAC/TEC splitters. The top electrode is at 10394 ft and the bottom electrode is at 10569 ft with approximately 29 ft spacing between electrodes	

Figure 4 Bluebox 2500 casing used to construct both monitoring wells.

3 Methods

The methods used in this study included logging, field and laboratory testing and analysis. Logging was performed by Schlumberger Carbon Services using standard Schlumberger logging tools (Section 3.1). Pressure test analysis (Section 3.2) was performed by Schlumberger -Doll Research using their patented technique to estimate cement permeability using the Cased Hole Formation Dynamics Tester (CHDT). Laboratory analyses were performed on cores collected using Schlumberger's Mechanical Sidewall Coring Tool (MSCT) using Laser Ablation Inductively Coupled Plasma Mass Spectroscopy (LA-ICP-MS), X-ray diffraction (XRD), Environmental Scanning Electron Microscopy (ESEM), Energy Dispersive X-ray Spectroscopy (EDS), micro computed tomography (micro-CT), and visual assessment (Section 3.3).

3.1 Logs and Log Comparisons

Methods employed in this study were similar to those used in Crow et al. [4] and Duguid et al. [5] and included using ultrasonic imaging tools, cement bond logging tools, and sidewall coring tools. Two ultrasonic mapping tools were used to collect data in each well. Schlumberger's Ultrasonic Imaging Tool (USIT) was used to collect casing, acoustic impedance, and solid liquid gas maps in September 2009 and Schlumberger's Isolation Scanner was used to collect casing, acoustic impedance, flexural attenuation, and solid liquid gas maps in April 2015. Two sonic logging tools were also used to collect data in each well. Schlumberger's Digital Sonic Logging Tool (DSLT) was used to collect cement bond log (CBL) and variable density log (VDL) data in September 2009 and Schlumberger's Slim Cement Mapping Tool (SCMT) was used to collect CBL, VDL and image log data in April 2015. Sidewall cores were collected through the casing steel casing in CFU31F-2 at 7900, 9530, and 9800 ft using Schlumberger's Mechanical Sidewall Coring Tool. The operating principles of the cement bond and ultrasonic imaging tools are described in detail in *Well Cementing* [23].

The integrity of CFU31F-2 and CFU31F-3 was studied, in part, by comparing cement bond logs and ultrasonic image maps collected when the well was constructed (2009) to the logs run prior to plugging and abandonment (2015). The sidewall cores samples were visually analyzed for signs of reaction. Table 8 and Table 9 show the type of tool, name of the tool and depth interval logged for each well.

Table 8 Logging and sampling information for CFU31F-2.

Date	Tool	Logged Interval	Data Collected
14 September, 2009	DSLT	5240 to 10662 ft	CBL and VDL
15 September, 2009	USIT	7500 to 10642 ft	casing thickness, acoustic impedance, solid-liquid-gas, and micro debonding images
22 April, 2015	SCMT	7850 to 9850 ft	CBL, VDL, and amplitude map
22 April, 2015	Isolation Scanner	7850 to 9850 ft	casing thickness, acoustic impedance, solid-liquid-gas, micro debonding, and flexural attenuation images
21 April, 2015	MSCT	7900, 9530, and 9800 ft	Sidewall cores

Table 9 Logging and sampling information for CFU31F-3.

Date	Tool	Logged Interval	Data Collected
14 September, 2009	DSLT	7500 to 10618 ft	CBL and VDL
16 September, 2009	USIT	7500 to 10648 ft	casing thickness, acoustic impedance, solid-liquid-gas, and micro debonding images
09 April, 2015	USIT	9600 to 10600 ft	casing thickness, acoustic impedance, solid-liquid-gas, and micro debonding images
10 April, 2015	Isolation Scanner	9600 to 10600 ft	casing thickness, acoustic impedance, solid-liquid-gas, micro debonding, and flexural attenuation images
09 April, 2015	MSCT	10042, 10268, 10380, 10450, 10470, and 10477 ft	Sidewall cores

3.2 Test Analysis

The methodology for data analysis is based on US patents by Ramakrishnan et al. [26, 27] that disclose quantitative methods to evaluate the permeability of the cement behind the casing based on pressure transients recorded in a single probe well test. In the context of this project, the permeability estimation is done via the relationship established between the observed pressure and the flow rate through a pressure probe set on or within the cemented annulus, and the decompression characteristics of the fluid in the CHDT tool. A separate flow rate measurement is unnecessary. The pressure relaxation in the test is fit using Equation 8 to back out τ which is then used to estimate cement permeability using Equation 9. The cement permeability is assumed to be the same in all directions.

$$P_p(t) = P_f + (P_p(t_0) - P_f)\exp\left(-\frac{t-t_0}{\tau}\right) \qquad \text{Equation 8}$$

Where:

P_f = formation pressure

P_p = pressure recorded at the probe

t_0 = Time at the start of the recovery

τ = Relaxation time constant

t= time

$$k_c = \frac{\mu c V}{4 r_p \tau}\left(1 - \frac{2\ln 2}{\pi}\frac{r_p}{l_c} - F\left(\frac{r_p}{l_c};\frac{l_p}{l_c}\right)\right) \quad \text{Equation 9}$$

Where:

k_c = Cement permeability

l_c = Thickness of the cement sheath

l_p = Depth of penetration of the drill bit into the cement

r_p = measurement probe radius

μ = Fluid viscosity

c = fluid compressibility

V = Tool chamber volume

F = a correction term for given values of r_p/l_c and l_p/l_c

Given the uncertainty in the quantities appearing in Equation 10, we first provide a rough estimate for the possible range of their values and simplify Equation 10 to obtain a magnitude estimate for the expected value of τ

$$k_c = \Omega/\tau \quad \text{Equation 10}$$

The expected ranges for values of the tool and fluid parameters used in the analysis are given in Table 10. The range for fluid viscosity is largely defined by the temperature dependence, whereas compressibility will be most sensitive to the presence of gas bubbles and will be estimated *in situ* from the pressure drops and volume changes during the packer seal tests performed before the CHDT measurements.

Table 10 Expected ranges for tool and fluid parameters.

Variable	Minimum Value	Maximum Value
μ (Pa s)	0.0003	0.0011
c (Pa^{-1})	$4.3x10^{-10}$	$5x10^{-9}$
V (m^3)	$3x10^{-4}$	$3.5x10^{-4}$
r_p (m)	0.0035	0.0035
l_c (m)	0.01	0.05
F	0	0.8
Ω (mD s)	0.1	160

As follows from Equation 10 and Table 10, with a relaxation time constant, τ, of 100 s we expect the cement permeability to be between 1 µD and 1.6 mD, whereas if the values of τ is 1000 s, the estimated cement permeability is likely to be between 0.1 µD and 160 µD.

Assumptions:

Based on the well specifications provided in DLIS files, the job was performed in 8.5 in well with 7 in casing. In the absence of the caliper data, the casing is assumed to be centralized. Therefore, the thickness of cement annulus is 0.75 in.

Based on the casing weight specification (7 in OD, 26 lbm/ft), the casing thickness is 0.362 in (with ID 6.276 in). In situ casing thickness can differ from the specification due to corrosion and may be inferred from CHDT test data (hydraulic motor torque, pressure response corresponding to the drill-bit penetration). Hydraulic motor torque data was not available in the test files provided, therefore, in situ casing thickness is to be confirmed based on pressure response data only.

The fluid in the tool flowlines is assumed to be water with in situ compressibility and viscosity to be computed based on NIST REFPROP software package [28] for values of pressure and temperature during the test.

3.3 Core Analyses

Laboratory analyses were performed on the sidewall cores after they were collected. The analyses consisted of Micro-CT, LA-ICP-MS, ESEM with EDS, and XRD. Prior to these lab techniques the external surface of the cores was examined and described. After sectioning the sectioned surface of the cores were described. All cores were analyzed but not every core received every analysis, Table 11 provides a key to the analyses applied to individual cores. The following sections describe techniques employed on this project.

Table 11 Analyses applied to individual samples.

Well	Sample Depth (ft)	Micro-CT	LA-ICP-MS	ESEM	XRD
CFU31-F2	7900	X	X	X	X
CFU31-F2	9530	X	X		X
CFU31-F2	9800	X	X	X	X
CFU31-F3	10268	X	X	X	X
CFU31-F3	10380	X	X	X	X
CFU31-F3	10450	X	X		X
CFU31-F3	10470	X	X		X
CFU31-F3	10477	X	X	X	X

3.3.1 Micro-CT

Micro-CT was performed at Ohio University. Cores from both wells were analyzed using this technique. The Micro CT analyzer used was a TriFoil Imaging eXplore CT 120 Small Animal X-Ray CT Scanner with a Custom generator producing 5 kW peak power. The analyzer had a feature detectability of 4 microns. The energy was between 40–120 kV with a maximum current of 50 mA.

3.3.2 LA-ICP-MS

LA-ICP-MS was performed at the Ohio State University on a Perkin Elmer Nexion 350D ICP-MS and a Photo Machines Exite He1Ex 193nm Laser with a 50 x 50 μm spot size. A NIST 612 standard was used before and after the scans on each sample to account for machine drift. Lines were collected at 20μm/s. LA-ICP-MS was conducted on portions of the sectioned samples with no additional surface preparation.

3.3.3 ESEM

ESEM with EDS was conducted at Ohio State University Center for Electron Microscopy and Analysis using an FEI QUANTA 200 SEM in ESEM Mode. The analysis was conducted on portions of the sectioned samples that were polished to 1 micron prior to analysis. Excitation energy ranged from 10 to 20 KV.

3.3.4 XRD

XRD was conducted at Ohio State University Center for Electron Microscopy and Analysis using a Rigaku MiniFlex 600 analyzer. The samples were run using a 40Kv voltage and a 15mA current. The radiation source was an interlock CU tube. Scans were run from 5 to 80 degrees at 1 degree per minute. The samples were ground using a ceramic mortar and pestle to a half micron and loaded into amorphous glass sample holders.

4 Results

4.1 CFU31-F2

4.1.1 CFU31-F2 Initial Log Assessment

Each well was logged using the USIT and DSLT after construction in 2009. The USIT logs shows cement from the top of the log to the bottom of the log. The CBL data do not start to show a good bond until 9200 ft. Table 12 summarizes the interpretation of the 2009 USIT and CBL logs.

Table 12 General log interpretation for the 2009 well integrity logs run in CFU31F-2

Depth (ft)	Well Architecture	USIT	DSLT
7490-7800	7-in 26lb/ft Casing. Control lines.	Low acoustic impedance in raw acoustic impedance, generally less than 3 Mrayl (Raw Acoustic Imped. Track). Generally, Microdebonded cement and liquid in cement map.	CBL and VDL show little bond.
7800-8140	7-in 26lb/ft Casing. Control lines.	Low values of acoustic impedance, generally less than 4 Mrayl, in raw acoustic impedance track. Solid cement, microdebonded cement and liquid in the cement map.	CBL between 20 and 60 mV. No formation returns in VDL.
8140-8600	7-in 26lb/ft Casing. Control lines.	Middle to low values of acoustic impedance, 5 Mrayl or less, in the raw acoustic impedance track. Monitoring control line(s) visible in the raw acoustic impedance image. Generally, microdebonded cement with some solid cements and liquids.	CBL between 20 and 60 mV. No formation returns in VDL.
8600-9100	7-in 26lb/ft Casing. Control lines.	Middle to low values of acoustic impedance, 5 Mrayl or less, in the raw acoustic impedance track. Monitoring control line(s) visible in the raw acoustic impedance image. Generally, even amounts of solid and microdebonded cement in the cement map with some liquid.	CBL between 5 and 20 mv, generally near 10 mV. VDL shows weak formation returns.
9100-9470	7-in 26lb/ft Casing. Control lines.	High values of acoustic impedance, 7.5 to 8 Mrayl, in the raw acoustic impedance track. Solid cement in the cement map track. Control line(s) visible in both the raw acoustic impedance track and cement map (vertical microdebonded feature).	CBL Between 20 and 40 mV between 9100 and 9110 ft. CBL between 10 and 20 mV between 9110 and 9200 ft. CBL generally less than 4 mV between 9200 and 9470 ft with some zones reaching 10 mV. VDL shows good formation returns throughout.
9470-9550	7-in 26lb/ft Casing. Control lines.	Medium to low raw acoustic impedance (5 Mrayl or less) with some spotty areas with high values (7 Mrayl +) in the raw acoustic impedance track. The cement map shows	CBL between 10 and 20 mV between 9470 and 9500 ft. CBL between 5 and 20 mV between 9500 and 9550 ft. VDL

Depth (ft)	Well Architecture	USIT	DSLT
		about half microdebonded material, slightly less than half solid cement, some fluid.	shows good formation returns throughout.
9550-9620	7-in 26lb/ft Casing. Control lines.	Medium acoustic impedance in the acoustic impedance track. The cement map more than half solid cement with the balance microdebonded cement with a very small amount of fluid. The control lines are visible in both tracks.	CBL between 5 and 10 mV between 9550 and 9578 ft. CBL between 5 and 10 between 9578 and 9620 ft. Good formation returns on VDL throughout.
9620-9670	7-in 26lb/ft Casing. Control lines.	High values of acoustic impedance, 7.5 to 8 Mrayl, in the raw acoustic impedance track. Solid cement in the cement map track. Control line(s) visible in both the raw acoustic impedance track and cement map (vertical microdebonded feature).	CBL between 10 and 20 mV between 9620 and 9650 ft. CBL between 2 and 4 mV between 9650 and 9670 ft.
9670-9900	7-in 26lb/ft Casing. Control lines.	Medium acoustic impedance in the acoustic impedance track. The cement map more than half solid cement with the balance microdebonded cement with a very small amount of fluid. The control lines are visible in both tracks.	CBL generally between 1 and 5 mV between 9670 and 9738 ft. CBL between 1 and 10 mV between 9738 and 9900 ft, with the higher values where the casing collars of jewelry is ringing. VDL shows good formation returns throughout.
9900-10180	7-in 26lb/ft Casing. Control lines. Pressure/temperature gauge at 10044 ft.	High values of acoustic impedance, 7.5 to 8 Mrayl, in the raw acoustic impedance track. Solid cement in the cement map track. Control line(s) visible in both the raw acoustic impedance track and cement map (vertical microdebonded feature).	CBL generally between 5 and 10 mV between 9900 and 10000 ft. CBL generally less than 2 mV between 10000 and 10100 ft, CBL generally between 5 and 10 mV between 10100 and 10140 ft). CBL between 15 and 60 mV between 10140 and 10168 ft. CBL between 5 and 10 mV between 10168 and 10180 ft. Good formation returns on VDL throughout.
10180-10224	7-in 26lb/ft Casing. Control lines. Two DAC/TEC splitters at 10192 ft and 10206 ft	High and low values of acoustic impedance in raw acoustic impedance track. Solid cement, with a possible fluid channel and microdebonding at the edge of the channel. Lines and splitters visible.	CBL between 5 and 10 mV between 10180 and 10190 ft. CBL between 10 and 25 mV. Good formation returns on VDL throughout.
10224-10642	Fiberglass casing with 14 ERT electrodes	Medium acoustic impedance in raw acoustic impedance track. Almost completely solid cement. No control lines are visible.	No CBL in fiberglass. Good formation returns throughout fiberglass section in VDL

The monitoring technology attached to the outside of the casing is visible in the raw and processed acoustic impedance tracks in the 2009 ultrasonic image logs. In the Raw Acoustic Impedance track the monitoring hardware is visible as linear vertical and horizontal patterns of low acoustic impedance which translate to linear and horizontal microdebonded or fluid-filled features in the processed track (Cement Map with Impedance Classification). Figure 5 shows an example section of the 2009 USIT log where monitoring hardware can be identified. In the figure the line coming into the splitters in the well is clearly visible as a vertical linear feature

between 10170 and 10190 ft in the raw and processed acoustic impedance tracks. The splitters are visible at 10193 and 10206 ft. The lines coming out of the splitters are responsible for the wide low impedance, liquid feature between 10193 ft and the bottom of the figure. Figure 6 shows a photograph a splitter with a single line running into it and seven lines running out of it [9].

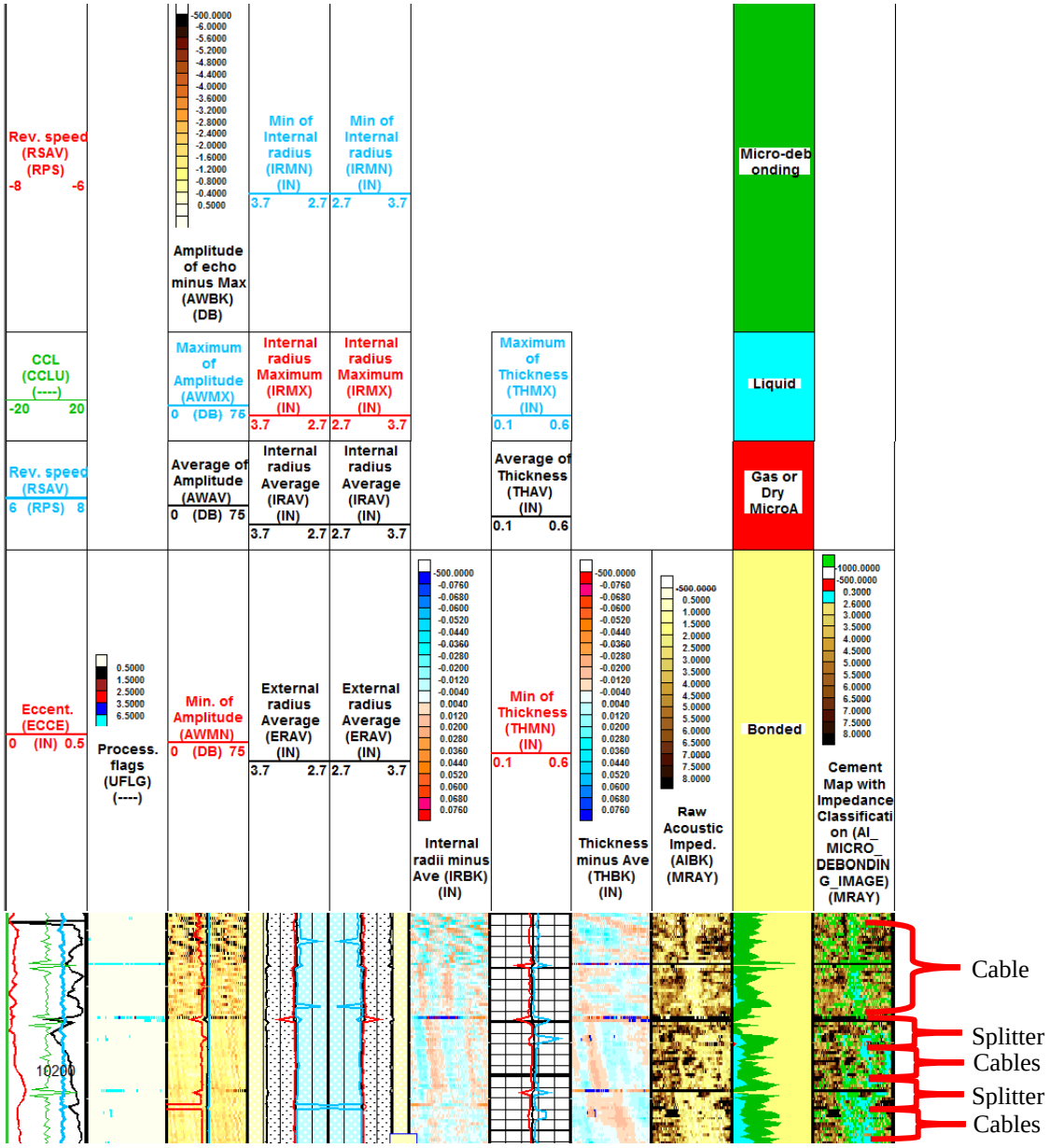

Figure 5 USIT data collected in CFU31F-2 in 2009 showing the location of monitoring technology attached to the outside of the long-string casing.

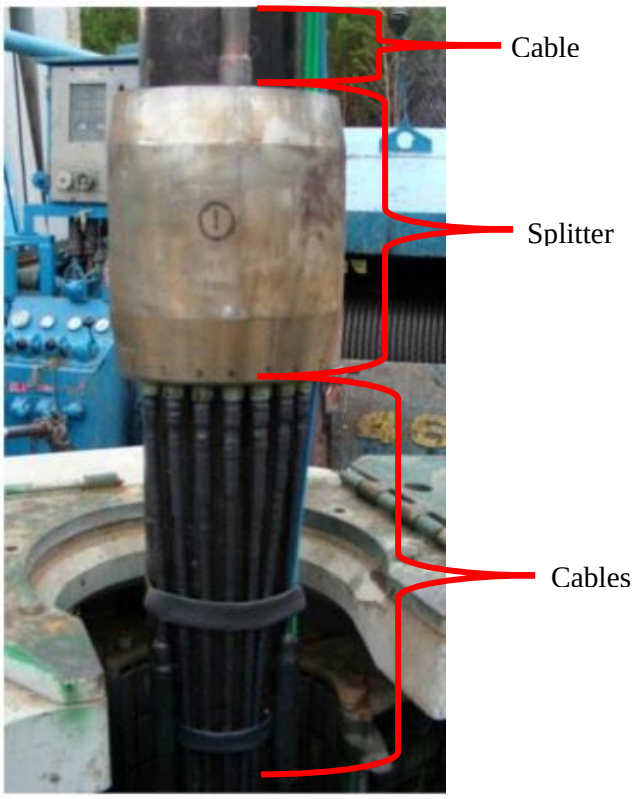

Figure 6 Photograph of a Splitter and lines installed on a pup joint used in the monitoring wells adapted from Carrigan et al. [9].

The lines from the splitter run down to the ERT electrodes in the fiberglass section can be seen as a lower impedance feature in the raw and processed acoustic impedance tracks collected in the fiberglass section (Figure 7).

Updated versions of both tools were used to relog the well in 2015. The Isolation Scanner was used to collect new cement maps between 7850 and 9850 ft. The SCMT was used to collect cement bond information between 7850 and 9850 ft. Data could not be collected below 9850 ft because the well was plugged below that depth due to damage in the fiberglass section resulting from well operations leading up to plugging and abandonment. In general, both logs run in 2015 (Isolation Scanner and SCMT) show a deterioration of cement quality or cement bond over the cemented interval. To compare the logs we have selected the cored intervals at 7900, 9530, and 9800 ft and an uncored section around 9200 ft.

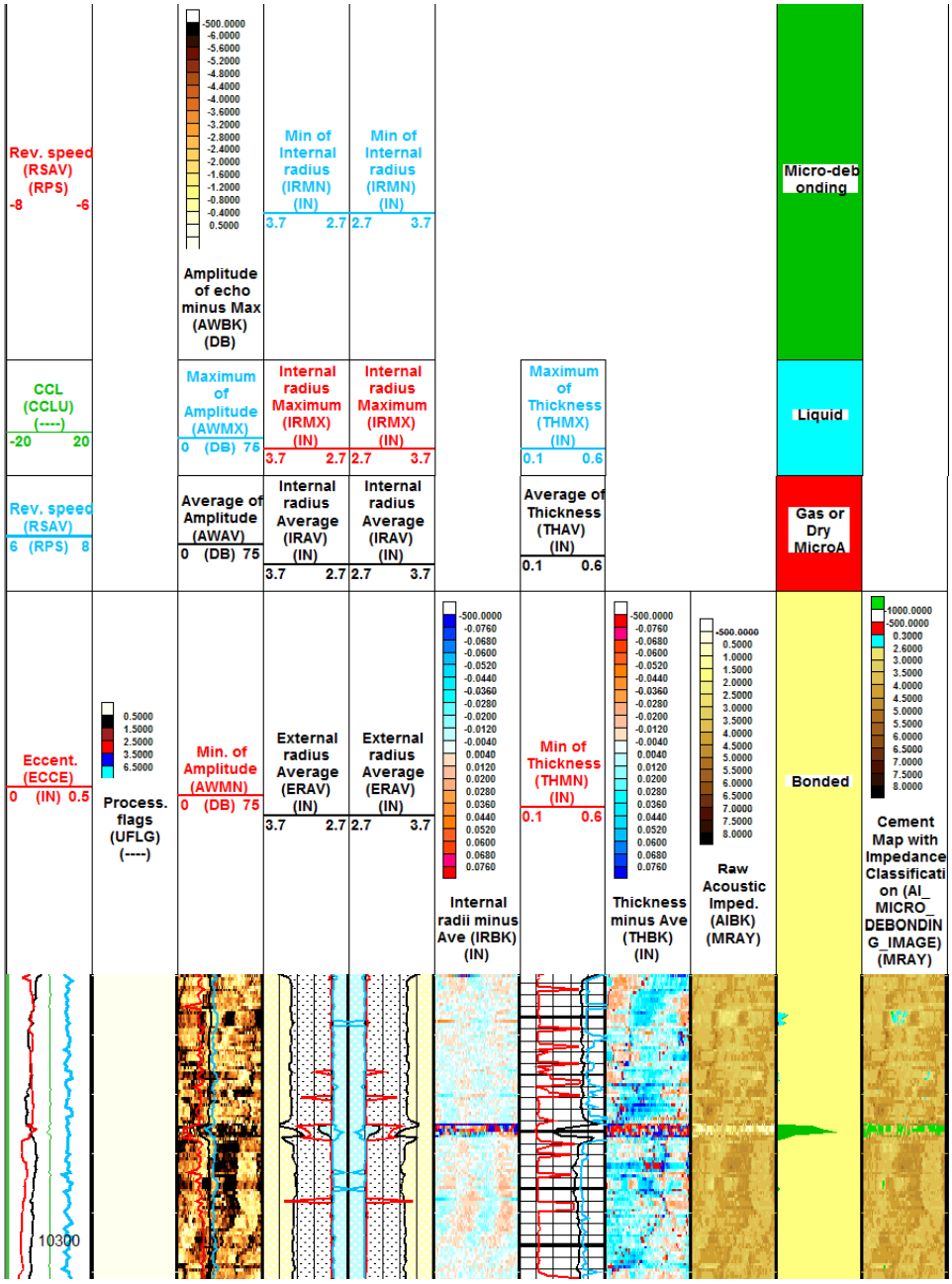

Figure 7 USIT data collected in the fiberglass section of CFU31F-2 showing low acoustic impedance features as a result of lines running from the splitters to the ERT electrodes in the well.

4.1.2 CFU31-F2 Core Points

4.1.2.1 CFU31-F2 7900 ft sidewall core sample

The upper core in CFU31F-2 was collected at 7900 ft. The core was solid cement with a crack running through it from the casing side of the annulus toward the formation side. The crack is approximately 1/2-mm-wide and 35-mm-long. There is an approximately ½- to 1-mm-wide discolored zone surrounding the crack and crystals precipitated in the cement in the crack (Figure 8).

Figure 8 Sidewall core collected at 7900 ft showing crack starting at the casing end (left) and extending toward the formation end (right). Note, the sidewall core is approximately 23 mm in diameter and each square in the background is 5.08 mm on a side. It is discolored on the formation side due to exposure to hydrocarbon in the sidewall coring tool.

A comparison of the CBL logs collected at this depth shows a generally poor bond (approximately 48 mV) in the 2009 log and a better, but still poor, bond (approximately 36 mV) in the 2015 log (Figure 9). The cement ultrasonic image logs show little change of cement quality. The raw acoustic impedance tracks are similar in the 2015 track versus the 2009 track (Figure 10). Averages of the acoustic impedance data for solid, liquid, gas, and un-attributable phases (E in Figure 11) show that the solid material behind the casing increased, the microdebonded material decreased, the liquid increased and the un-attributable signals increased. This can be seen in the right-most track in Figure 11 where tracks that move to the right of zero show an increase from 2009 to 2015 and tracks that move to the left show a decrease. Overall at this depth the solid material (the sum of microdebonded and solid cement) decreased from 0.86 to 0.72 between 2009 and 2015.

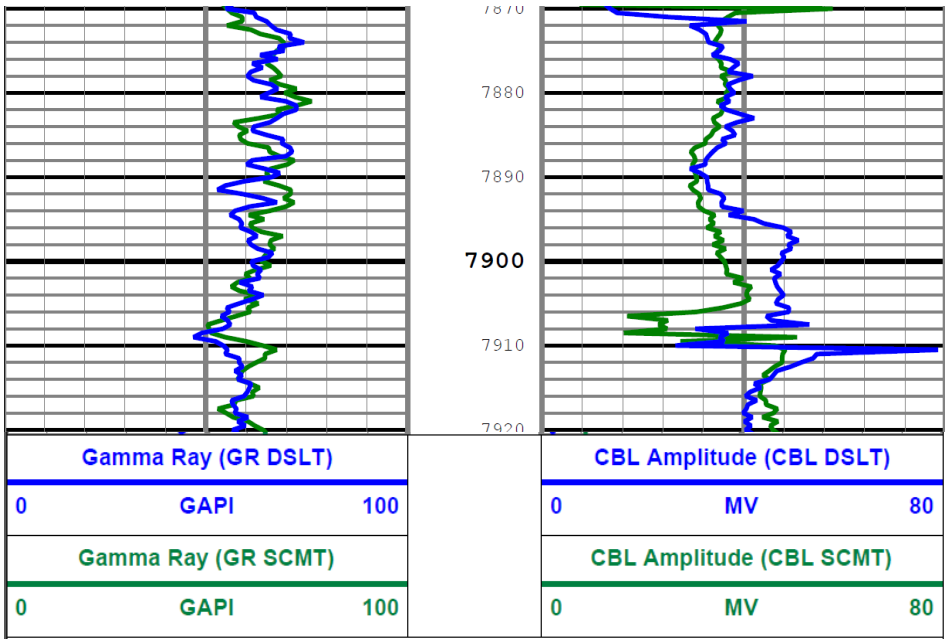

Figure 9 Comparison of CBL data at 7900 ft collected in CFU31F-2.

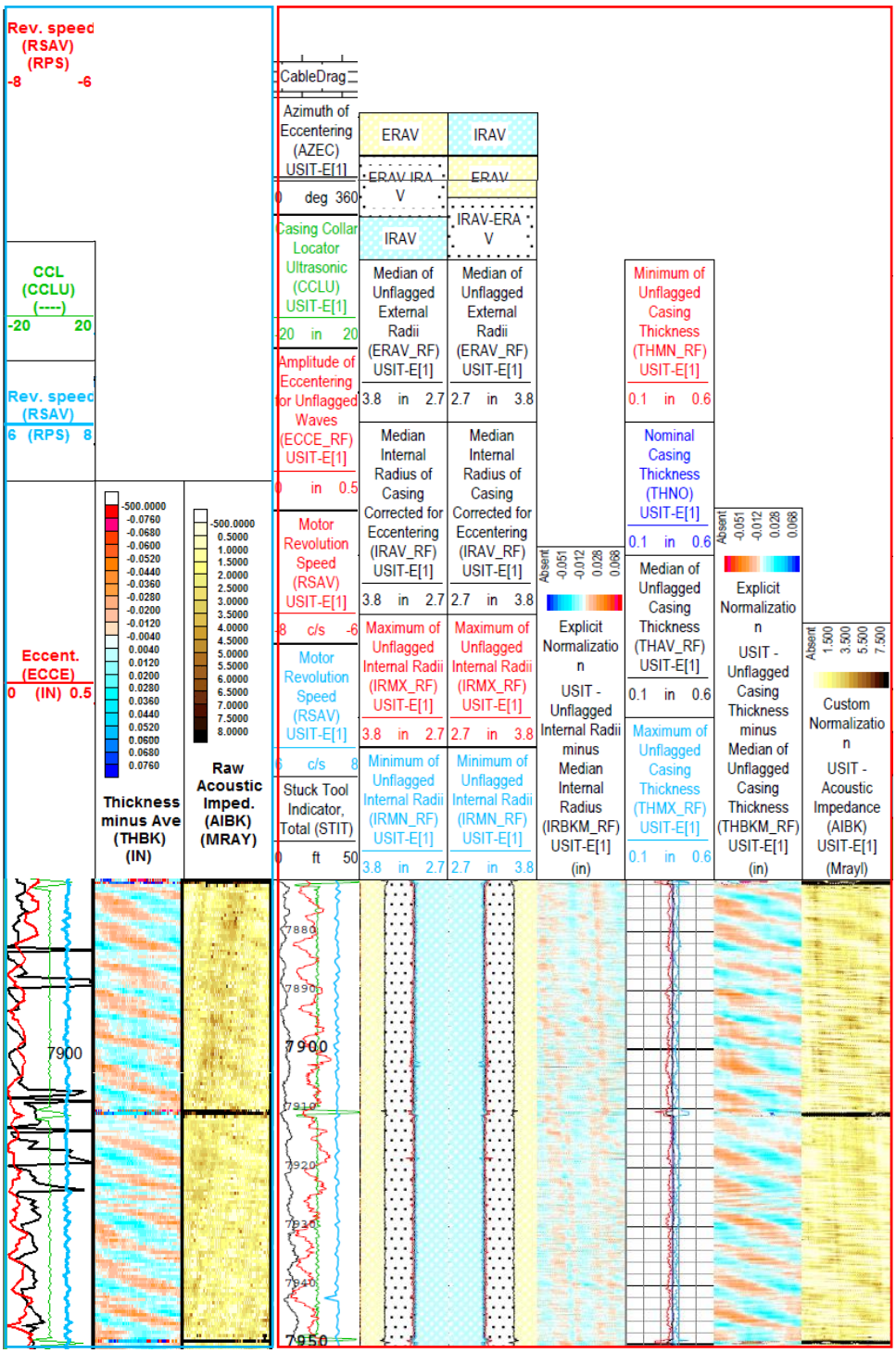

Figure 10 Comparison of ultrasonic maps collected at 7900 ft in CFU31F-2. Note the 2009 data are shown on the left and are outlined in blue and the 2015 data are shown on the right and are outlined in red.

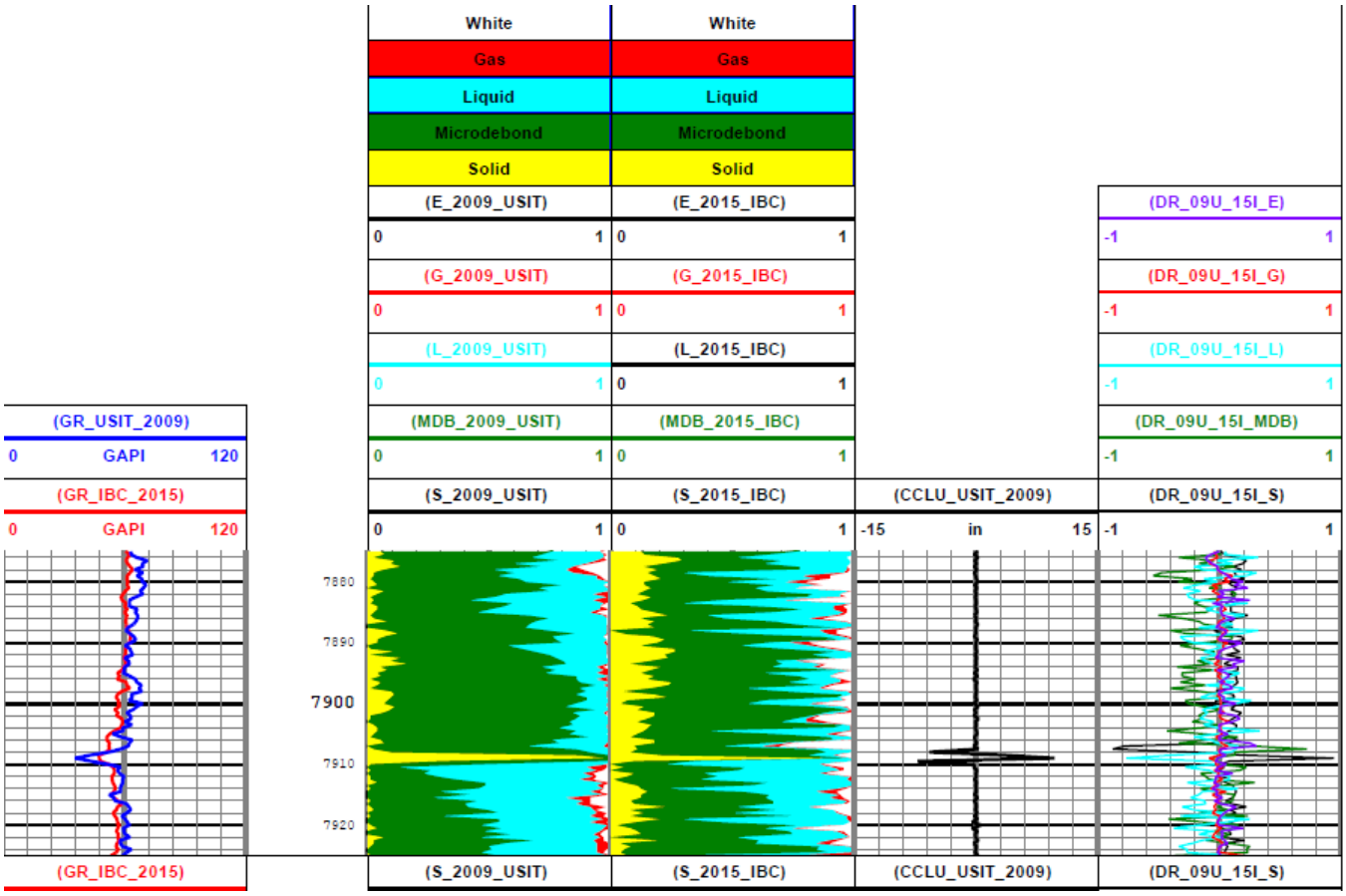

Figure 11 Comparison of ultrasonic data collected at 7900 ft in CFU31F-2. Note the 2009 data are denoted with USIT and the 2015 data are denoted with IBC.

Micro-CT images of the cement core (Figure 12) clearly identify the crack running through the core with an alteration zone surrounding the crack. This is most evident in Figure 12 as the light-colored feature running from middle-left to upper center in the circular cross-sectional view.

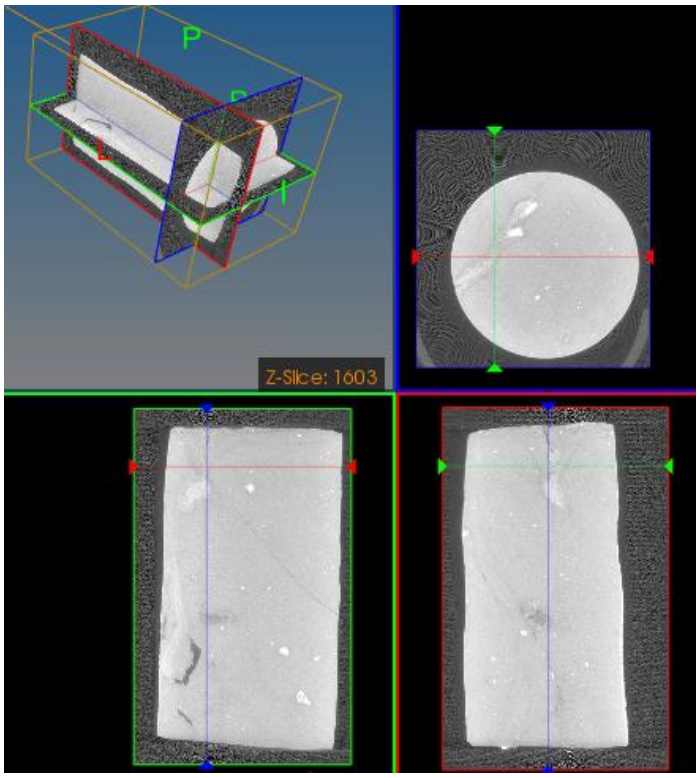

Figure 12 Micro-CT image of the cement sample collected in CFU31-F2 at 7900 ft.

The sample was sectioned for further analysis using the micro-CT scan to aid sectioning the crack and surrounding reaction zone (Figure 13). Visual analysis of the sectioned core showed that there is a 1 to 2 mm visible reaction zone surrounding the crack. Visual analysis also shows that the crack is filled along some portions of the core and open in others.

Figure 13 CFU31-F2 7900 ft sample cut for further analyses.

A portion of the sample (Figure 14) was polished and used for ESEM imaging and EDS analysis.

Figure 14 Section of sidewall core collected in CFU31-F2 and 7900 ft used to conduct ESEM and EDS measurement

Figure 15 shows an ESEM image of the sample collected in CFU31-F2 at 7900 ft spanning the crack in the sample. Note, the crack runs from the upper left to lower right of the image and the EDS analyses are roughly perpendicular to the crack.

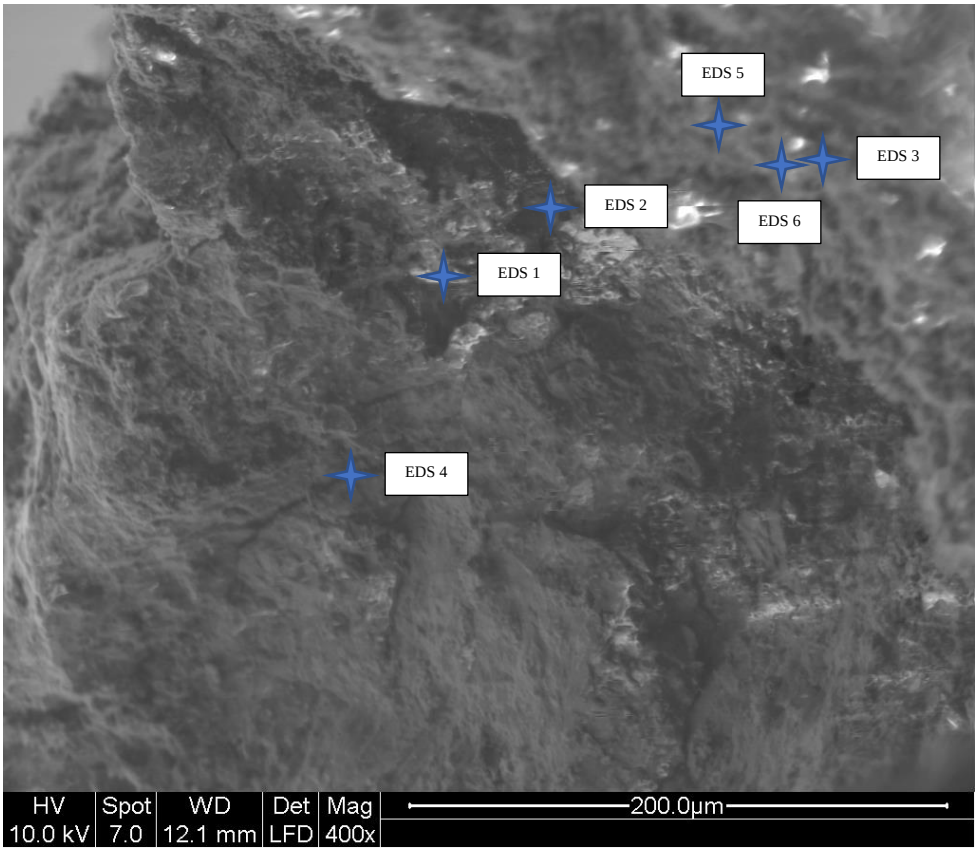

Figure 15 ESEM image showing the EDS analysis points spanning the crack in the sample collected at 7900ft.

Each of the EDS analyses showed C, O, Fe, Na, Mg, Al, Si, and Ca (Table 13).

Table 13 EDS points on the ESEM sample from CFU31-F2 at 7900ft

Element	EDS1	EDS2	EDS3	EDS4	EDS5	EDS6
C	15.04	5.74	15.91	9.42	2.59	1.11
O	61.78	47.74	54.1	62.58	66.12	66.67
Fe	0.48	0.15	0.24	0.10	2.06	0.45
Na	1.03	0.08	0.42	0.80	0.75	1.27
Mg	0.99	0.14	2.19	0.75	0.93	0.96
Al	0.53	0.10	0.56	0.68	2.19	1.60
Si	4.00	2.30	6.69	8.44	9.97	13.35
Cl	0.35	0.27	0.64	-	0.96	0.55
S	-	-	0.36	-	0.66	0.57
Ca	15.8	43.48	18.89	17.22	13.77	13.45

The same portion of the sidewall core was used conducting LA-ICP-MS. Figure 16 shows the location of a micro-CT line that was collected across the crack in the sample. The results (Figure 17) shows the center of the crack at about 3,300 microns. Moving out in either direction from the crack the Ca/Si ratio generally increases symmetrically. However, at the edge of the visibly altered zone around 2,200 microns there is a spike in Ca/Si. There is no corresponding spike at 4,400 microns. A second line collected across the crack shows similar behavior (Figure 18 and Figure 19)

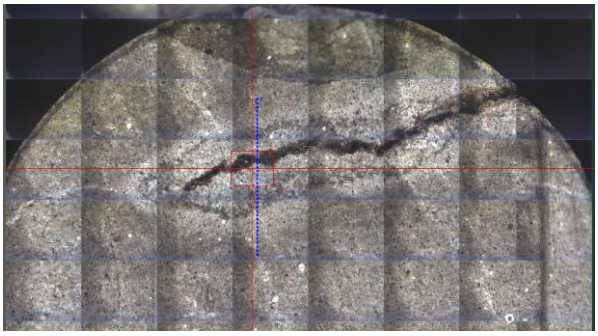

Figure 16 LA-ICP-MS Line 1 across crack in sample collected in CFU31-F2 at 7900 ft.

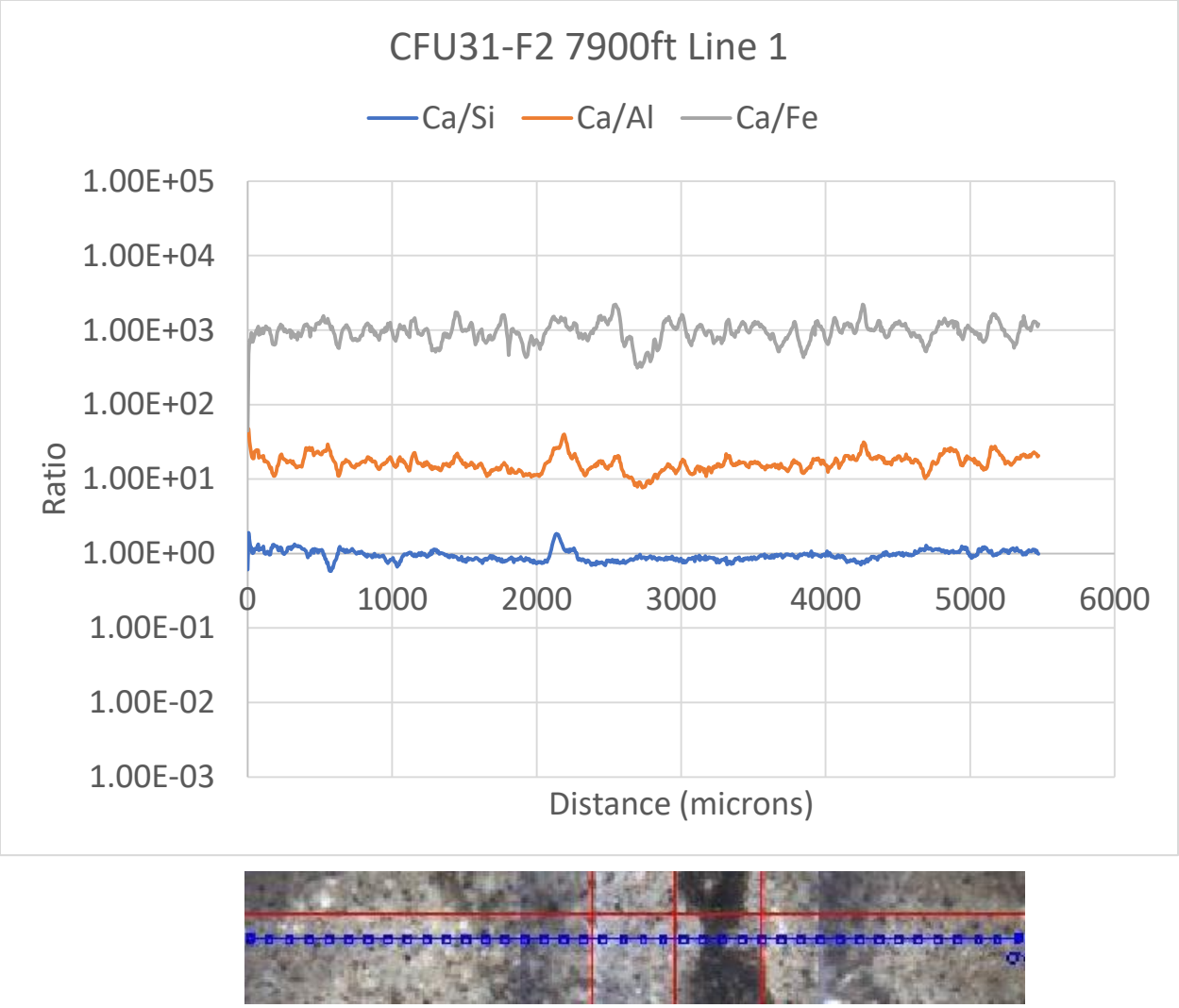

Figure 17 LA-ICP-MS Line 1 results across crack in sample collected in CFU31-F2 at 7900 ft showing Ca/Si, Ca/Al, and Ca/Fe mole ratios.

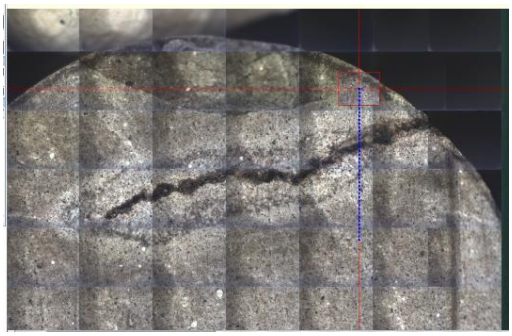

Figure 18 LA-ICP-MS Line 2 across crack in sample collected in CFU31-F2 at 7900 ft

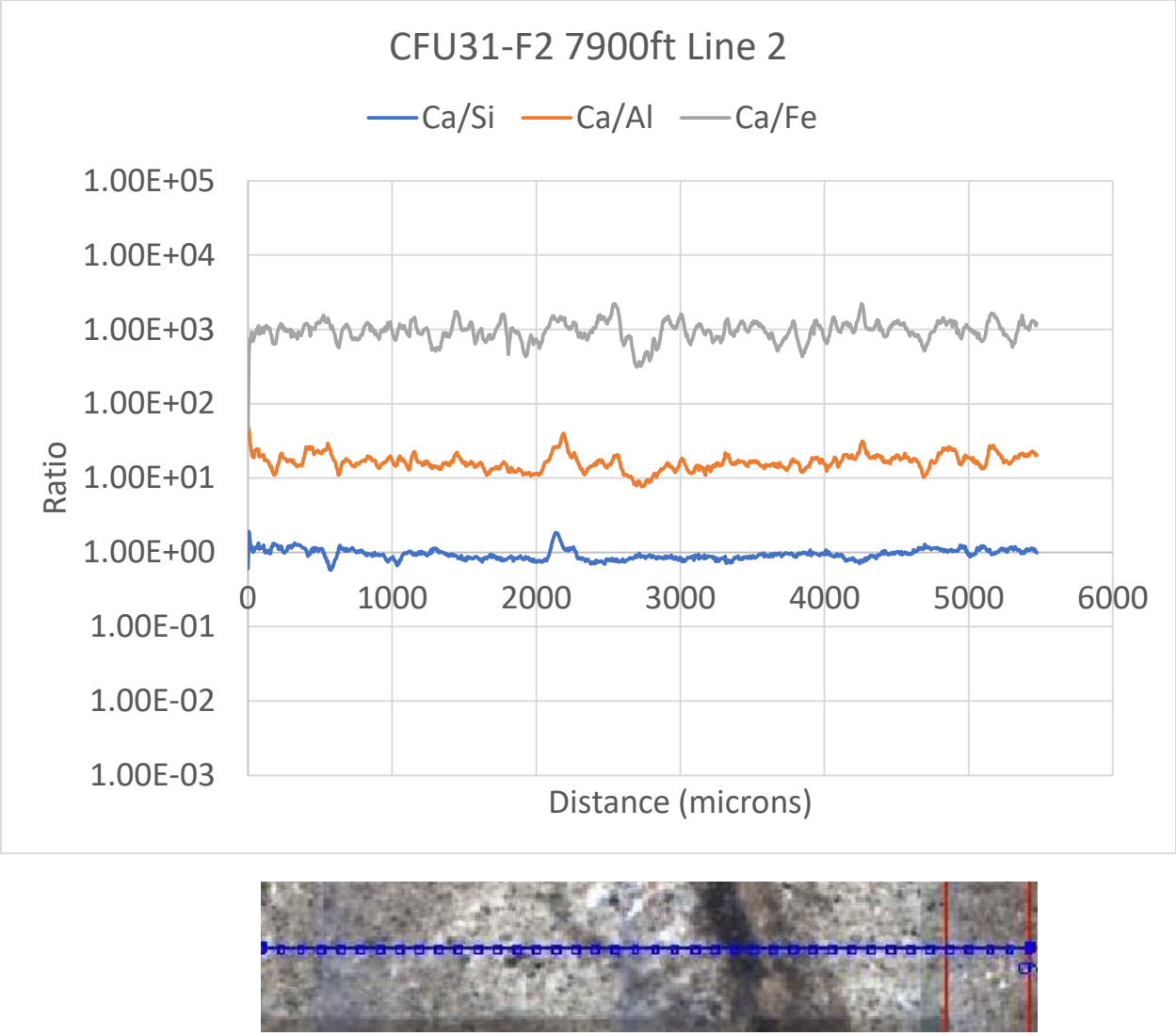

Figure 19 LA-ICP-MS Line 2 results across crack in sample collected in CFU31-F2 at 7900 ft showing Ca/Si, Ca/Al, and Ca/Fe mole ratios.

Additional LA-ICP-MS scans were performed to collect ratio data away from the reacted zones and provide elemental data of round features in the cement. Figure 20 through Figure 23 show the images of the scan line locations and their corresponding results. The scans generally show Ca/Si above one. The circular feature at 2,500 microns in Figure 23 shows little change in ratios. However, to the right of the feature all of ratios show variation for about 1,000 microns.

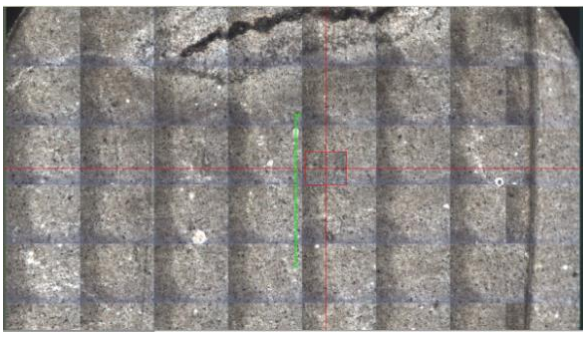

Figure 20 LA-ICP-MS Line 3 across crack in sample collected in CFU31-F2 at 7900 ft.

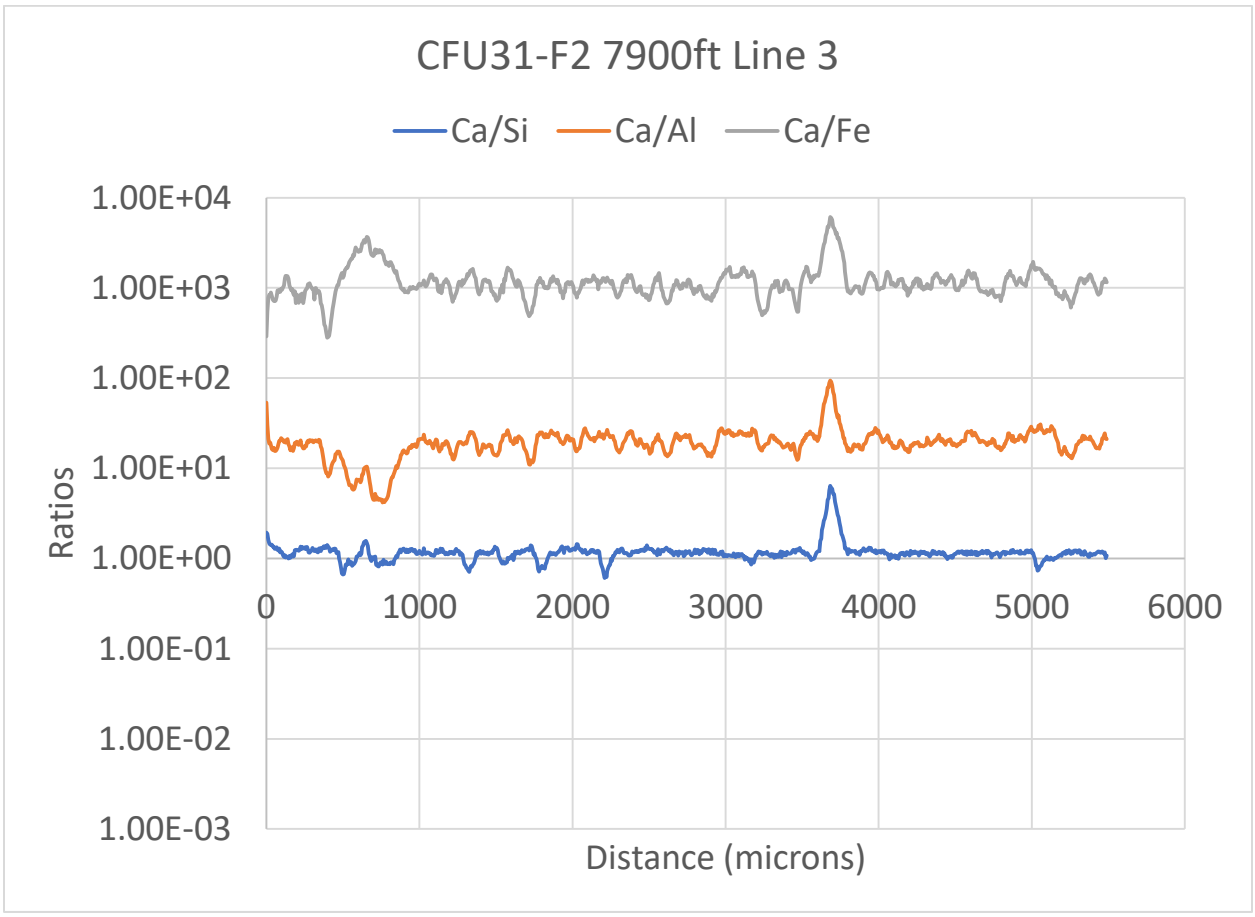

Figure 21 LA-ICP-MS Line 3 results across the sample collected in CFU31-F2 at 7900 ft showing Ca/Si, Ca/Al, and Ca/Fe mole ratios.

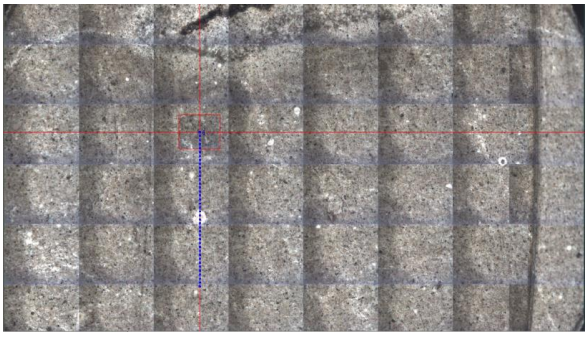

Figure 22 LA-ICP-MS Line 4 across the sample collected in CFU31-F2 at 7900 ft

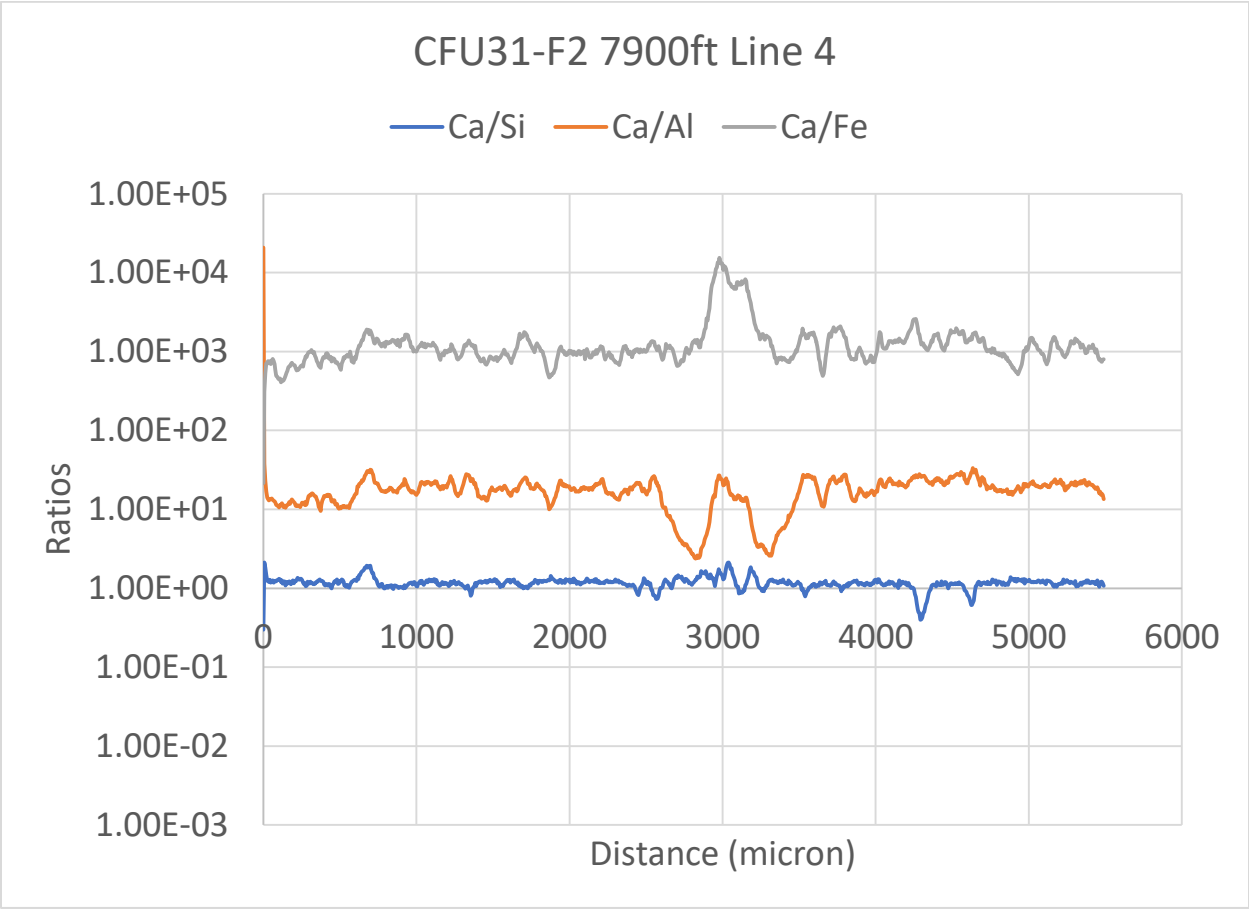

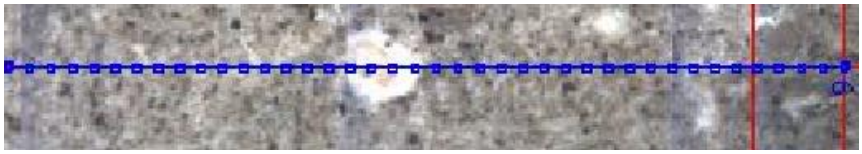

Figure 23 LA-ICP-MS Line 1 results across the sample collected in CFU31-F2 at 7900 ft showing Ca/Si, Ca/Al, and Ca/Fe mole ratios.

After LA-ICP-MS was conducted, portions of the sample were crushed to a half micron grain size and XRD analysis was performed. XRD on the sample collected at 7900 ft was divided into two zones. Zone 1 contained the crack and visible reaction zone. Zone 2 was outside of the crack and reaction zone. The results show the same crystalline phases identified in both zones (Table 14). Zone 1 was richer in Tilleyite, Tobormorite, and Calcite. Zone 2 was richer in quartz. Both zones were similar in calcium-silicate-hydrate, brownmillerite, and halite.

Table 14 XRD Results for the cement sample collected in CFU31-F2 at 7900 ft.

	Zone 1	Zone 2
Phase name	**Weight %**	**Weight %**
Quartz	20	42
Tilleyite	26	18
Tobermorite M	11	5.8
Calcium Silicate Hydrate	10	10
Brownmillerite, Fe-rich	10	7.2
Calcite	19	10
Halite	4.7	6

4.1.2.2 CFU31-F2 9530 ft sidewall core sample

The core collected at 9530 ft consisted of solid cement (Figure 24). A comparison of the CBL data collected at this depth was conducted. The 2009 data show a bond amplitude generally between 5 and 16 mV with higher values at the casing joint between 9514 and 9518 ft in the 2009, DSLT, log. The 2015 SCMT CBL data show a deterioration of the bond with signals between 16 and 48 mV (Figure 26). The cement ultrasonic image logs also show a deterioration of cement quality. The raw acoustic impedance tracks exhibit a lower acoustic impedance (lighter color) in the 2015 track versus the 2009 track (Figure 28). Averages of the acoustic impedance data for solid, liquid, gas, and un-attributable phases (E in Figure 27) show that the solid material behind the casing decreased, the microdebonded material increased, the liquid decreased and the un-attributable signals remained nearly unchanged. This can be seen in the right-most track in Figure 27 where tracks that move to the right of zero show an increase from 2009 to 2015 and tracks that move to the left show a decrease. At this depth, the ratio of overall solid material (the sum of microdebonded and solid cement) to all material behind the casing decreased from 0.86 to 0.61 between 2009 and 2015.

Figure 24 Sidewall core collected at 9530 ft. The casing end of the core is on the left and the formation end is on the right. Note, the sidewall core is approximately 23 mm in diameter. The jagged marks on the left half of the core are caused by reciprocation of the core bit during coring.

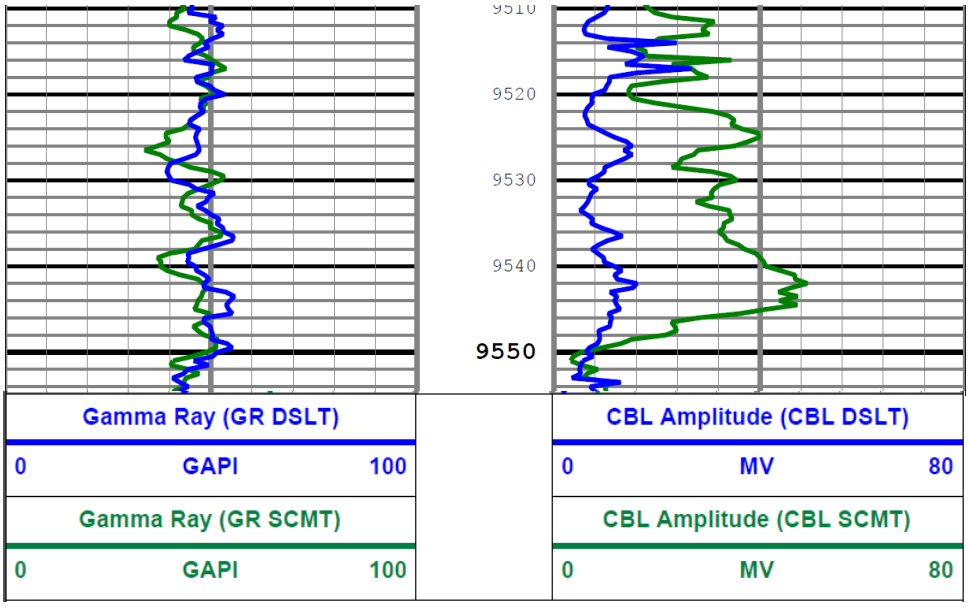

Figure 25 Comparison of CBL data at 9530 ft collected in CFU31F-2.

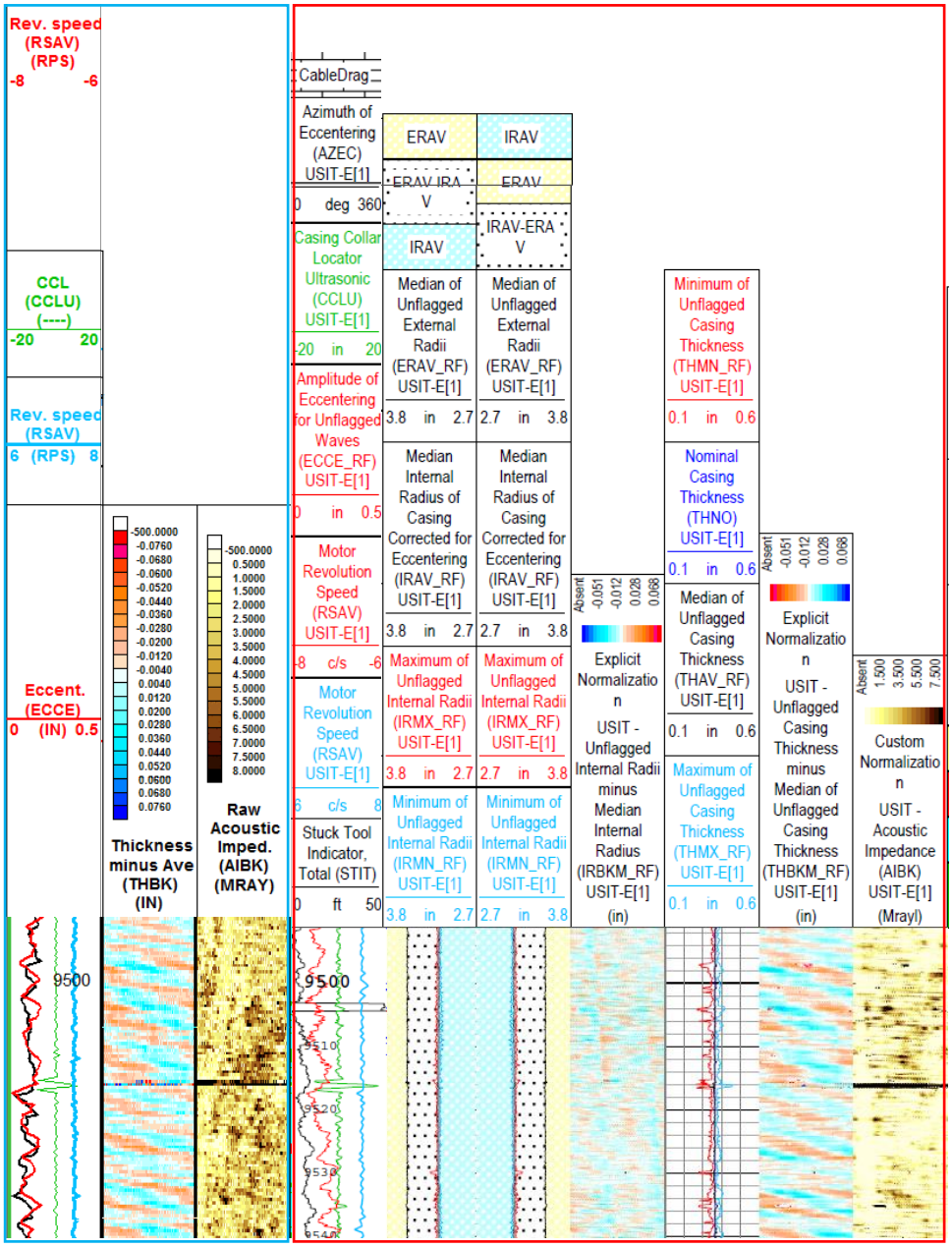

Figure 26 Comparison of ultrasonic maps collected at 9530 ft in CFU31F-2. Note the 2009 data are shown on the left and are outlined in blue and the 2015 data are shown on the right and are outlined in red.

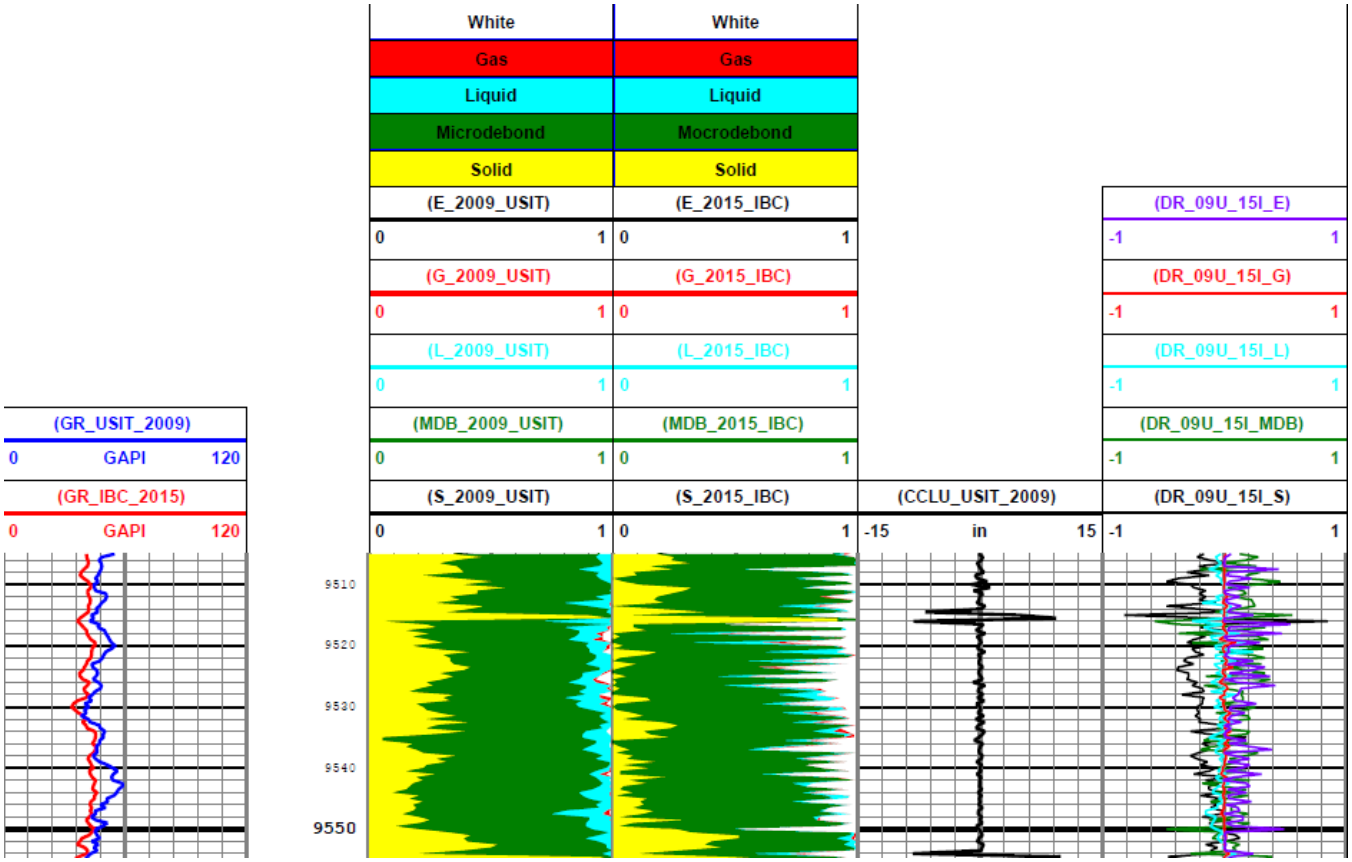

Figure 27 Comparison of ultrasonic data collected at 9530 ft in CFU31F-2. Note the 2009 data are denoted with USIT and the 2015 data are denoted with IBC.

Micro-CT images of the cement core (Figure 28) identify a potential reaction front running perpendicular to the long-axis of the sample and potential cracks running diagonal to the long-axis. Other irregular features are also evident in all views of the sample.

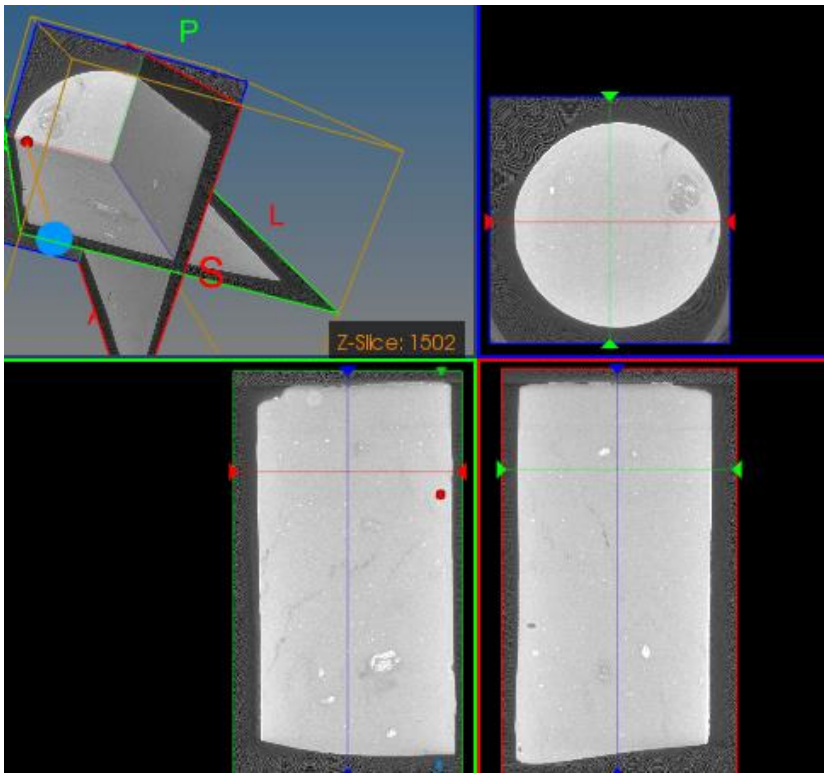

Figure 28 Micro-CT image of the cement sample collected in CFU31-F2 at 9530 ft.

The sample was sectioned for further analysis using the micro-CT scan to select the best plain for sectioning. Visual analysis of the sectioned core showed that there is an approximately 0.5-mm-wide tan reaction front followed by an approximately 5.5-mm-wide grey reaction on the casing side of the core perpendicular to the long axis of the core (parallel to the casing in the well). Adjacent to the grey reaction front there is an approximately 0.5-mm-wide white front. Visual analysis also shows a filled in crack or fracture running diagonally across the sectioned surface of the core. ESEM analysis was not conducted on this sample.

Figure 29 CFU31-F2 cement sample sectioned for further analysis

The sectioned sidewall core was used conducting LA-ICP-MS. LA-ICP-MS Figure 30 shows the location of a first six micro-CT lines collected across in the sample. The results of Line 1 (Figure 31) show three spikes in Ca/Si and Ca/Al over the first 500 microns. Ca/Fe shows a rise with a peak corresponding to the third peak for Ca/Si and Ca/Al. After 500 microns the Ca/Si slowly increases from around 1.1 to 1.3 at the end of the line around 4,540 microns. The second line (Figure 32) starts with a Ca/Si around 1.3 to about 720 microns where there is a dip to just under 1 corresponding to the beginning of the white zone. The white zone jumps to Ca/Si around 1.2 and slowly increases to about 1.3 at 1000 microns, where it ends and Ca/Si jumps to about 1.4 and slowly increases to about 1.5 by the end of the line. Lines 3 through 6 (Figure 33 through Figure 36) show some variation but are basically flat with Ca/Si around 1.5. Line 5 crosses the white filled crack in the sample and there is a slight decrease in the Ca/Si from around 1.5 to around 1.3 at that point (4,020 microns).

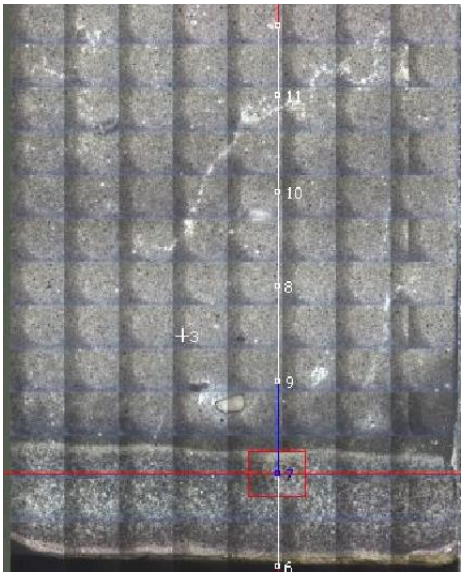

LA-ICP-MS Figure 30 LA-ICP-MS Lines 1 to 6 across the sample collected in CFU31-F2 at 9530 ft.

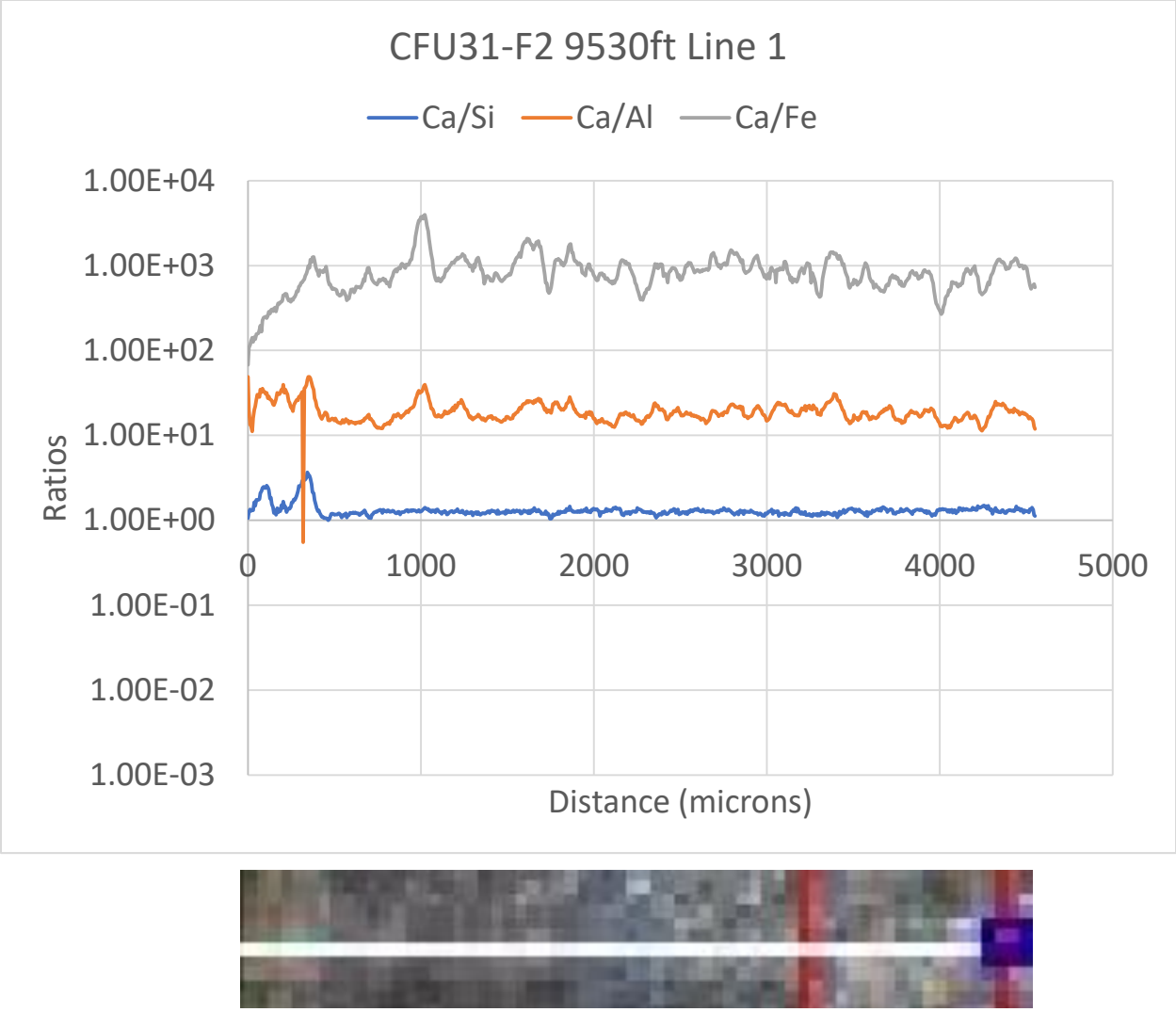

Figure 31 LA-ICP-MS Line 1 results across the sample collected in CFU31-F2 at 9530 ft showing Ca/Si, Ca/Al, and Ca/Fe mole ratios.

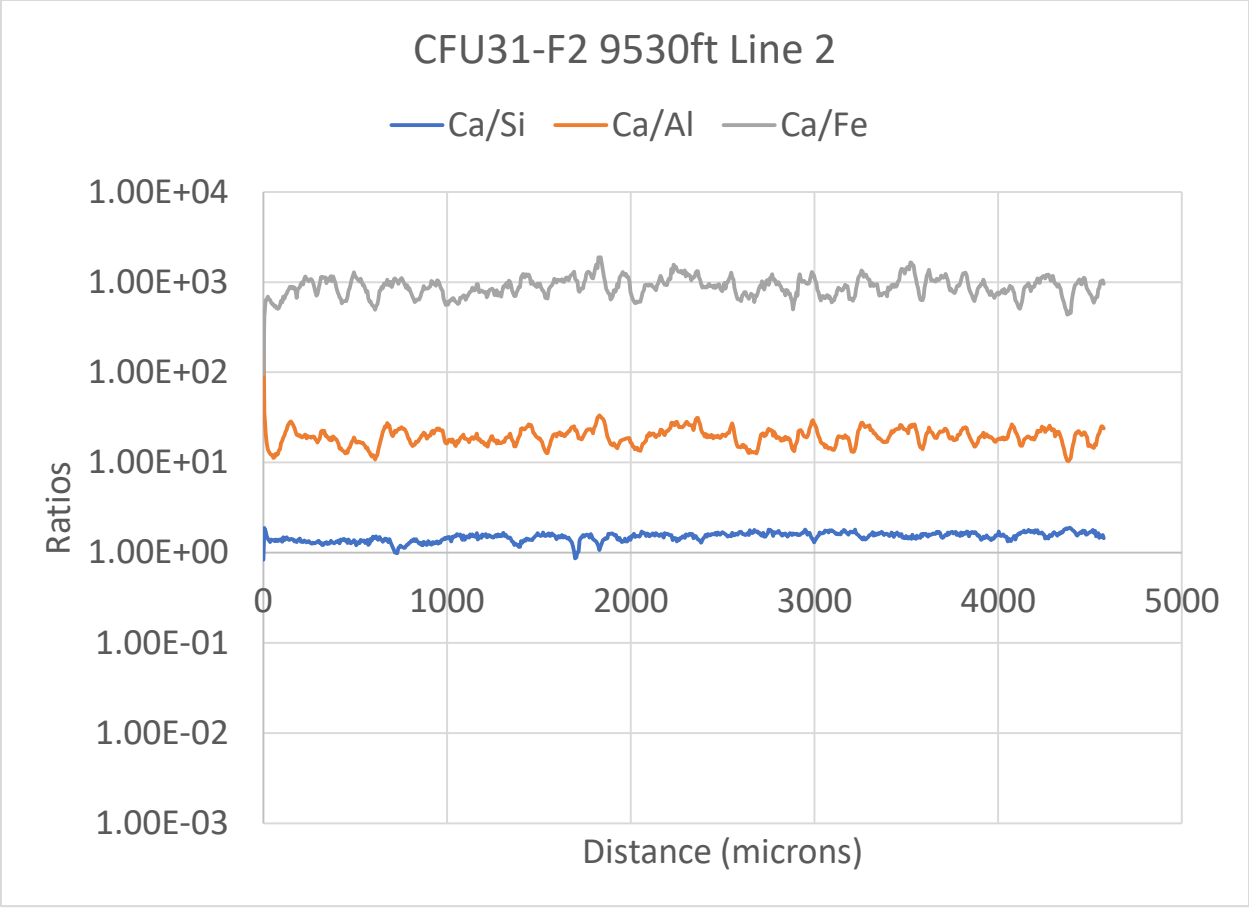

Figure 32 LA-ICP-MS Line 2 results across the sample collected in CFU31-F2 at 9530 ft showing Ca/Si, Ca/Al, and Ca/Fe mole ratios.

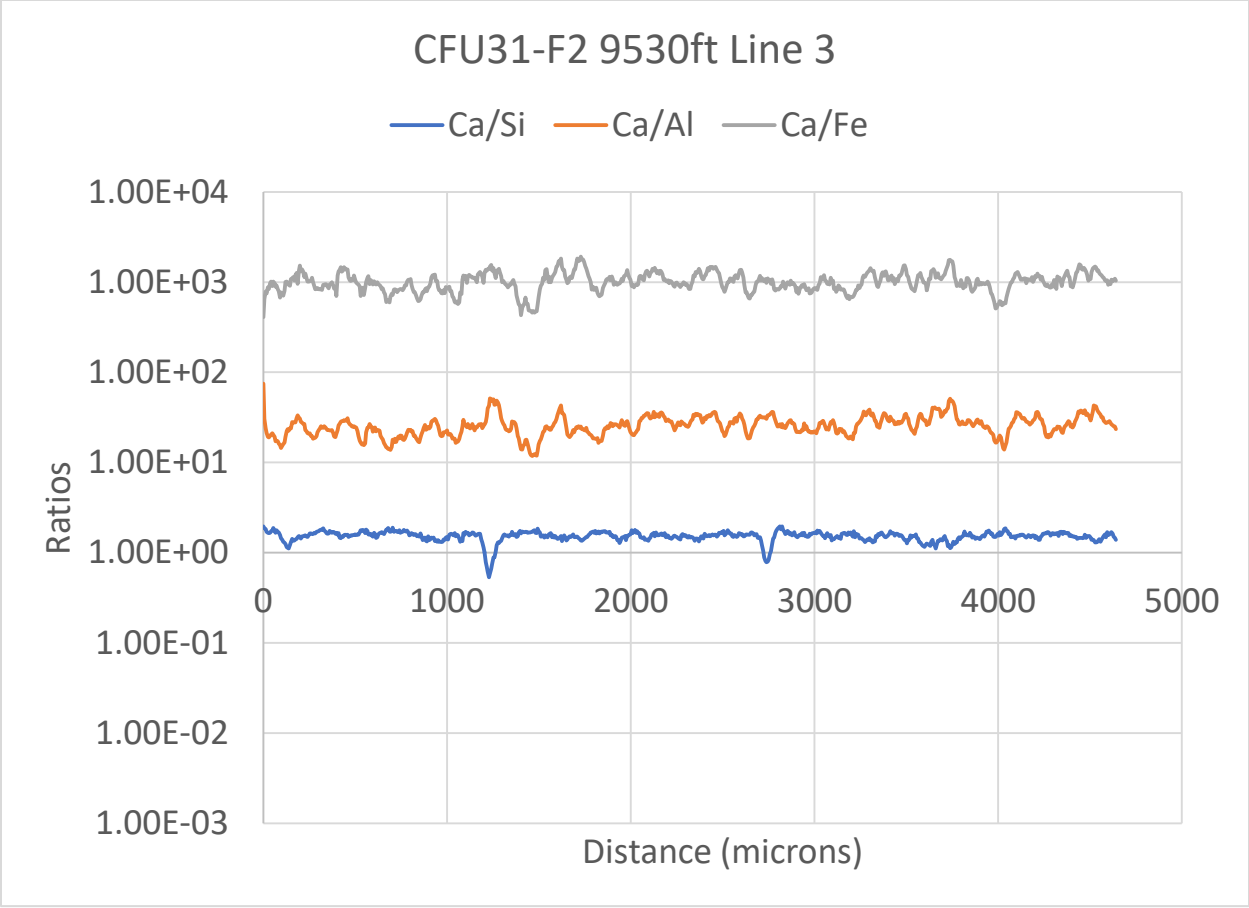

Figure 33 LA-ICP-MS Line 3 results across the sample collected in CFU31-F2 at 9530 ft showing Ca/Si, Ca/Al, and Ca/Fe mole ratios.

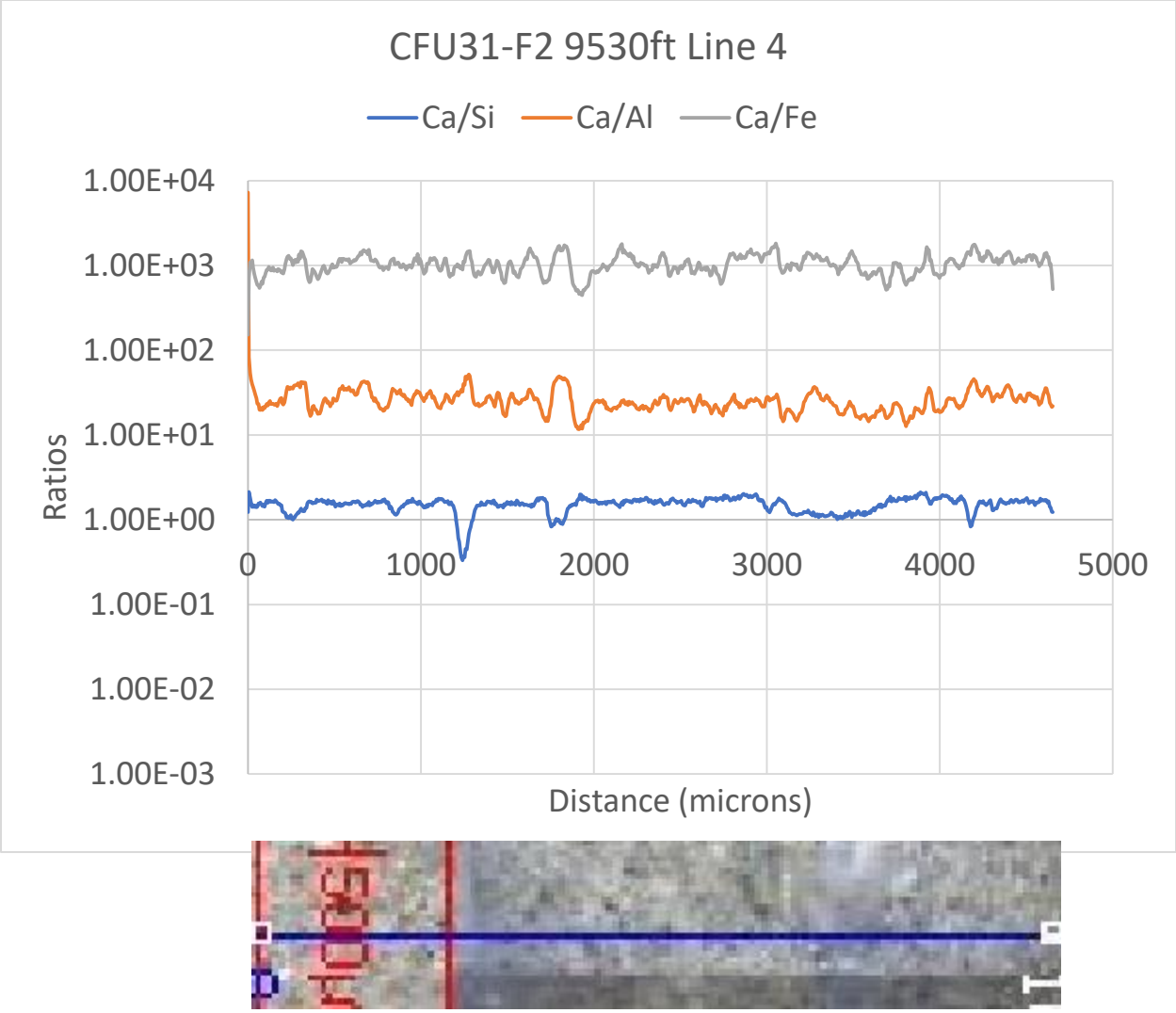

Figure 34 LA-ICP-MS Line 4 results across the sample collected in CFU31-F2 at 9530 ft showing Ca/Si, Ca/Al, and Ca/Fe mole ratios.

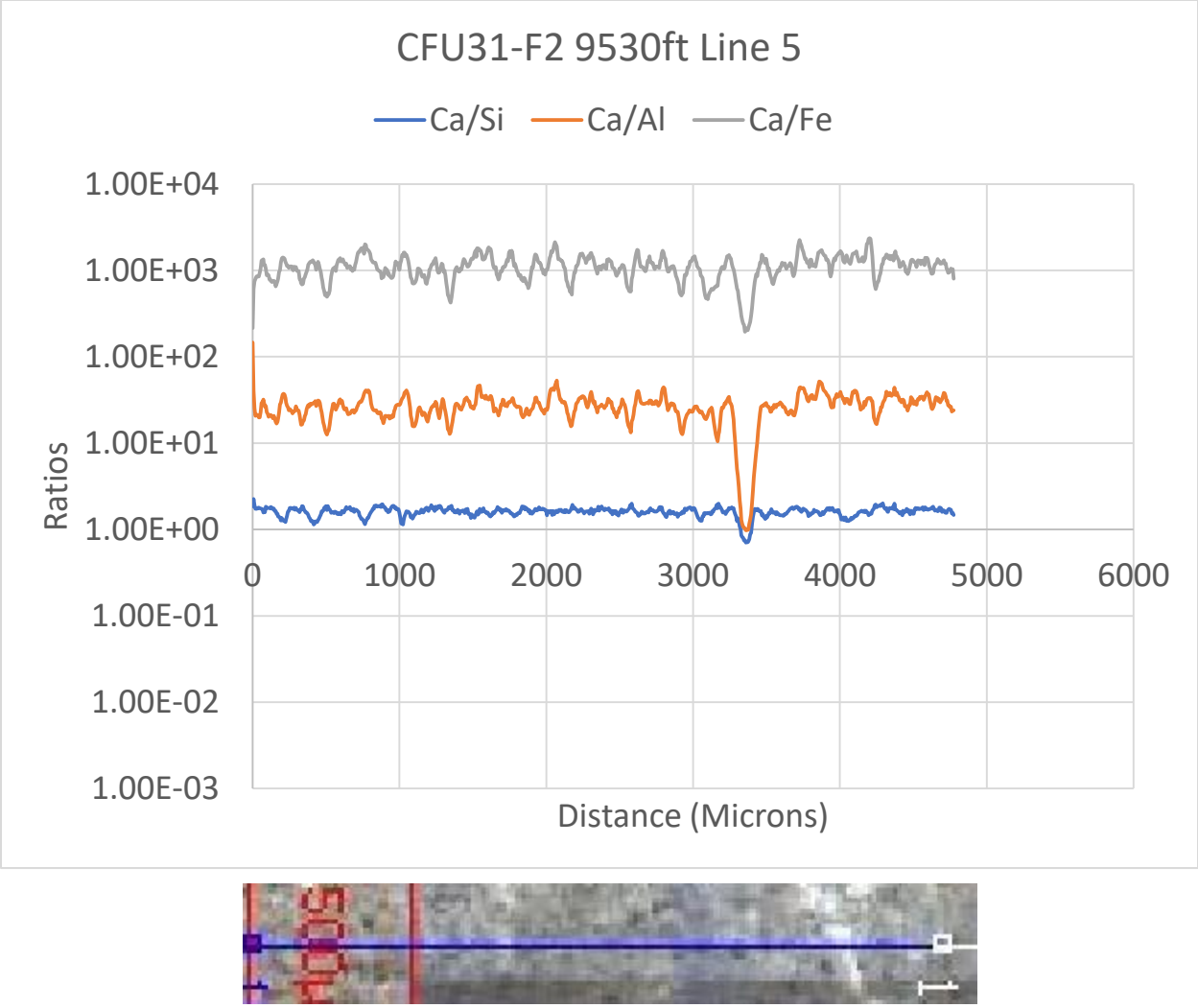

Figure 35 LA-ICP-MS Line 5 results across the sample collected in CFU31-F2 at 9530 ft showing Ca/Si, Ca/Al, and Ca/Fe mole ratios.

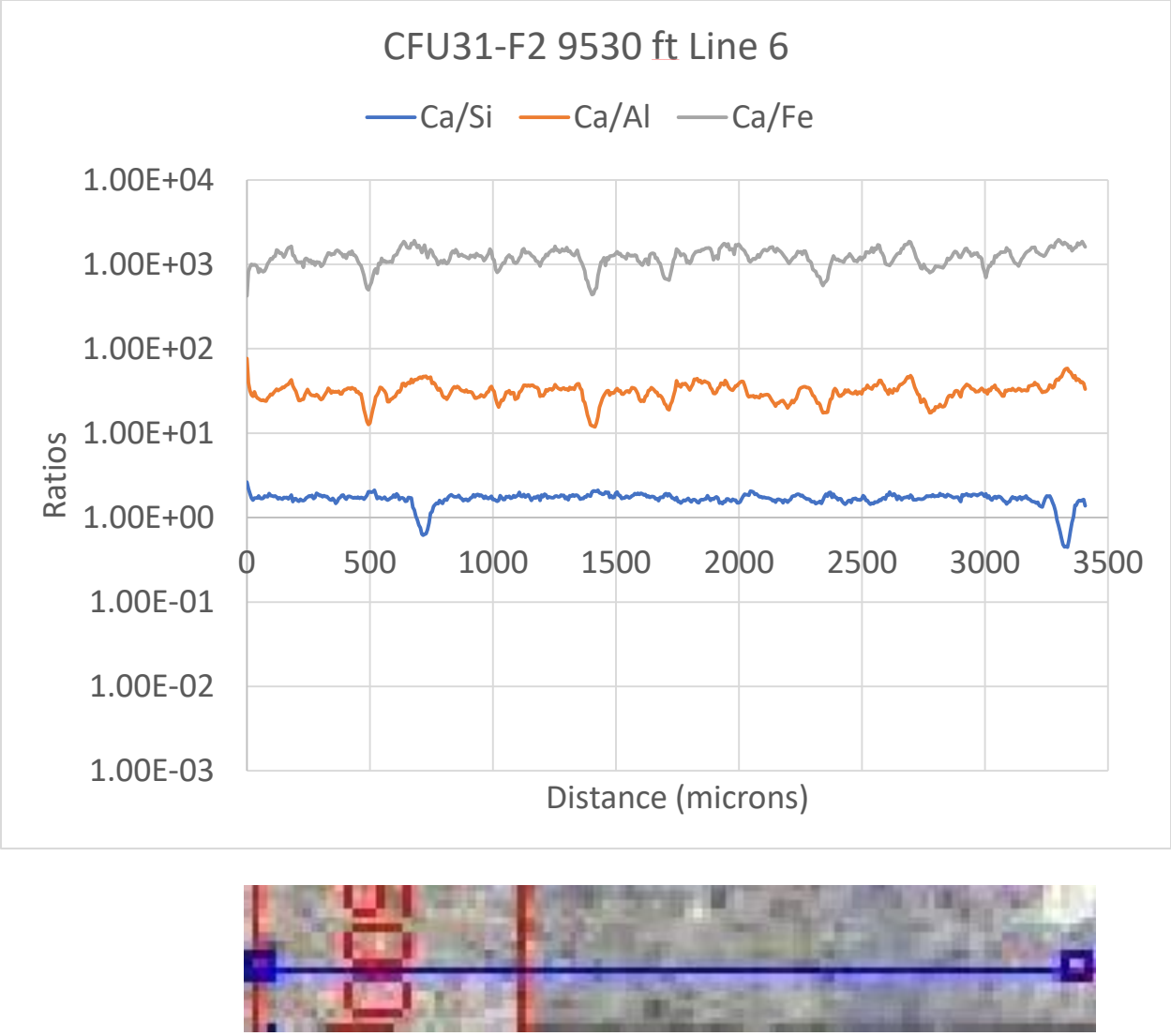

Figure 36 LA-ICP-MS Line 6 results across the sample collected in CFU31-F2 at 9530 ft showing Ca/Si, Ca/Al, and Ca/Fe mole ratios.

After LA-ICP-MS was conducted portions of the sample were crushed and XRD analysis was performed. XRD on the sample collected at 9530 ft was divided into three zones. Zone 1 comprised the tan reacted zone at the end of the sample, Zone 2 was made up of the grey zone, and Zone 3 was from the center of the sample. The all of the zones had similar crystalline phases. Carbonate phases differed with Zone 1 being richer in calcite than the inner zones and Zone 3 being richer in vaterite that outer zones. Brownmillerite was not present in zone 1 but was present in the other zones. The XRD results are presented in Table 15.

Table 15 XRD data collected from the cement sidewall core in CFU31-F2 at 9530ft.

	Zone 1	Zone 2	Zone 3
Phase name	**Weight %**	**Weight %**	**Weight %**
Quartz	21	24	40
Tobermorite 9A	18	16	15
Calcite	26	10.5	7.0
Vaterite	8.3	3.8	21
Brownmillerite (Mg, Si-exchanged)	-	11	6.3
Scawtite	14	13	-
Halite	3.5	3.6	5.0
Tilleyite	10	18	6.0

A pretest was performed using the CHDT tool 5 feet below the depth where the sidewall core was collected, the pretest was performed at 9535 ft. Figure 37 shows pressure signals recorded by the quartz gauge and the strain gauge, along with the drill-bit penetration and the evolution of the pretest volume during the job. Temperature recorded by the quartz gauge and the strain gauge are also shown. Due to electrical noise, recorded data had to be cleaned-up to remove spikes. For illustration, the original uncleaned data is shown for strain gauge temperature and pretest volume channels at time interval 2300–2700 s. First, two packer-seal pretests were performed (200–900 s and 1000–2000 s). In both pretests, observed pressure response was consistent with expansion of fluid due to a rise in temperature. At T = 248 ^{o}F (approximately 120 ^{o}C) and P = 3000 psi (approximately 20.7 MPa), thermal expansivity of water is β = 8x10-4 K^{-1}, and water compressibility c = 4.8x10-10 Pa^{-1}. Therefore, the expected temperature effect on isochoric pressure change is:

$$\Delta P = \beta / c = 1.6 \text{ MPa/K} \approx 129 \text{ psi/}^{o}\text{F}.$$

After the CHDT drill-bit penetrated through the casing (at 4550 s), the pressure at the probe showed clear recovery after initial pressure drop (see Figure 37 and Figure 38). Based on the drill-bit position at the point of the assumed casing exit, the estimated thickness of the cemented annulus at that depth is 0.36”, consistent with the casing specifications listed in the previous section.

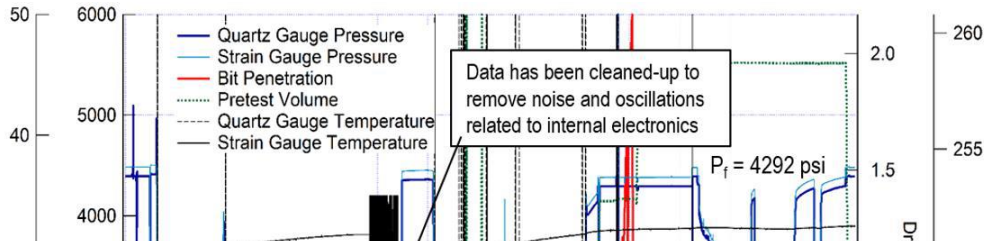

Figure 37 Pressure, drill-bit penetration, temperature, and pretest volume data from CHDT job at 9535 ft.

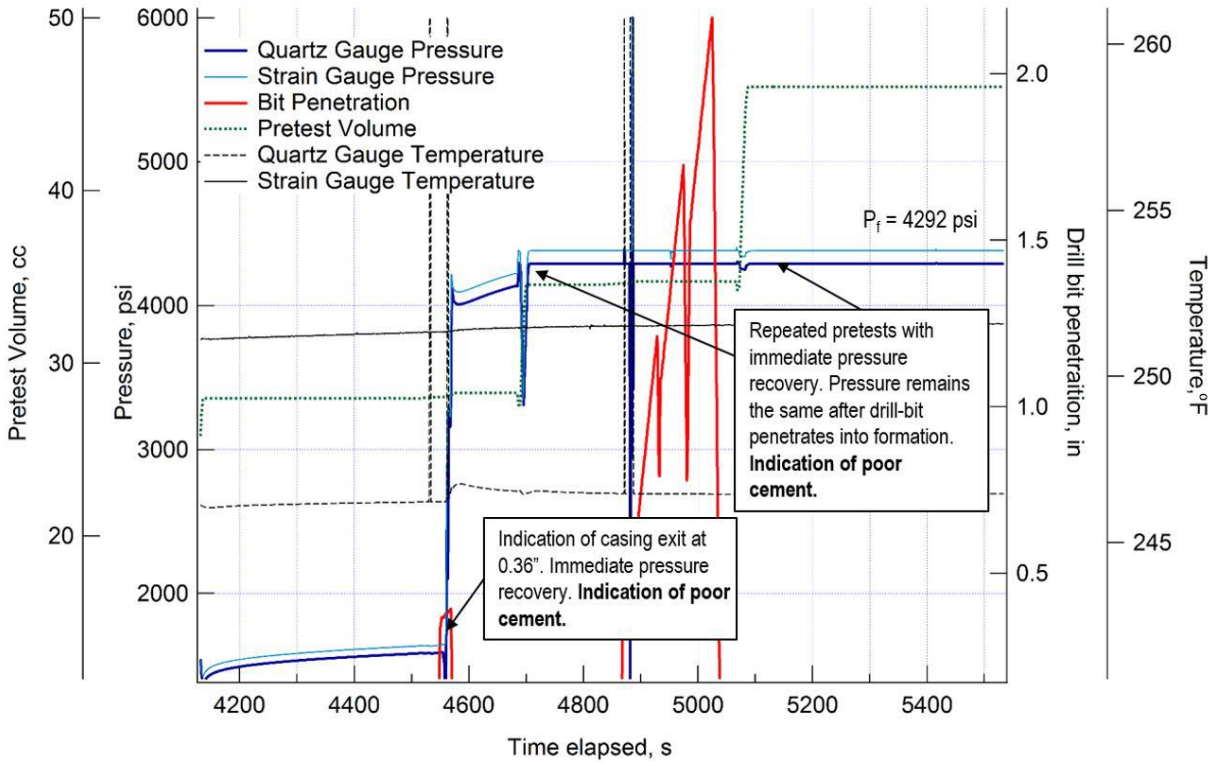

Figure 38 Analysis of data after drill-bit penetration through casing, cement, and into formation.

A rapid pressure recovery during the pretest after the casing exit to the value very close to the pressure recorded after subsequent drill-bit penetration through cement annulus into formation (4900-5050s), suggests that the cement annulus provides very poor hydraulic isolation at that depth.

4.1.2.3 CFU31-F2 9800 ft sidewall core sample

The core collected at 9800 ft consisted of solid cement (Figure 39). Based on external visual analysis, there is an approximately 8-mm-wide discolored front on the formation side of the core.

Figure 39 Sidewall core collected at 9800 ft showing a discolored zone on the formation side (right). Note, the sidewall core is approximately 23mm in diameter.

The 2009 CBL (DSLT) data collected at this depth show a bond amplitude between 3 and 13 mV with higher values at the casing joint at 9822 ft. The 2015 SCMT CBL data show an increase in amplitude at 9800 ft from around 8 mV in the 2009 data to around 21mV in the 2015 data, and an increase from 10 mV in the 2009 data to around 34 mV in the 2015 data at 9809 ft, and an increase from around 3 mV in the 2009 data to 16 mV in the 2015 data around 9817 ft (Figure 40). The cement acoustic impedance logs show a similar deterioration in signal (Figure 41); with cement in the annulus showing a lower acoustic impedance (lighter color) at the same depths, 9800, 9809, and 9817 ft, in the 2015 track versus the 2009 track. A cable is visible in both the 2009 and 2015 logs as a vertical low acoustic impedance feature in the raw acoustic impedance tracks. Averages of the acoustic impedance data for solid, liquid, gas, and un-attributable phases (E in Figure 27) show that the solid material behind the casing decreased, the microdebonded material increased, the liquid decreased and the un-attributable signals remained nearly unchanged. This can be seen in the right-most track in Figure 27 where tracks that move to the right of zero show an increase from 2009 to 2015 and tracks that move to the left show a decrease. At this depth the ratio of overall solid material (the sum of microdebonded and solid cement) to all material behind the casing decreased from 0.99 to 0.72 between 2009 and 2015.

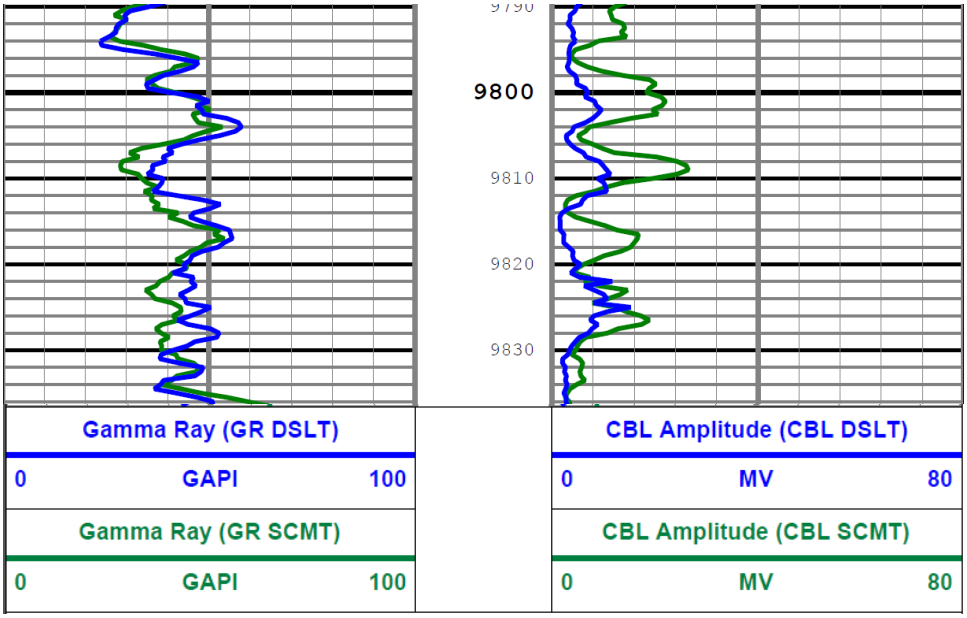

Figure 40 Comparison of CBL data at 9800 ft collected in CFU31F-2

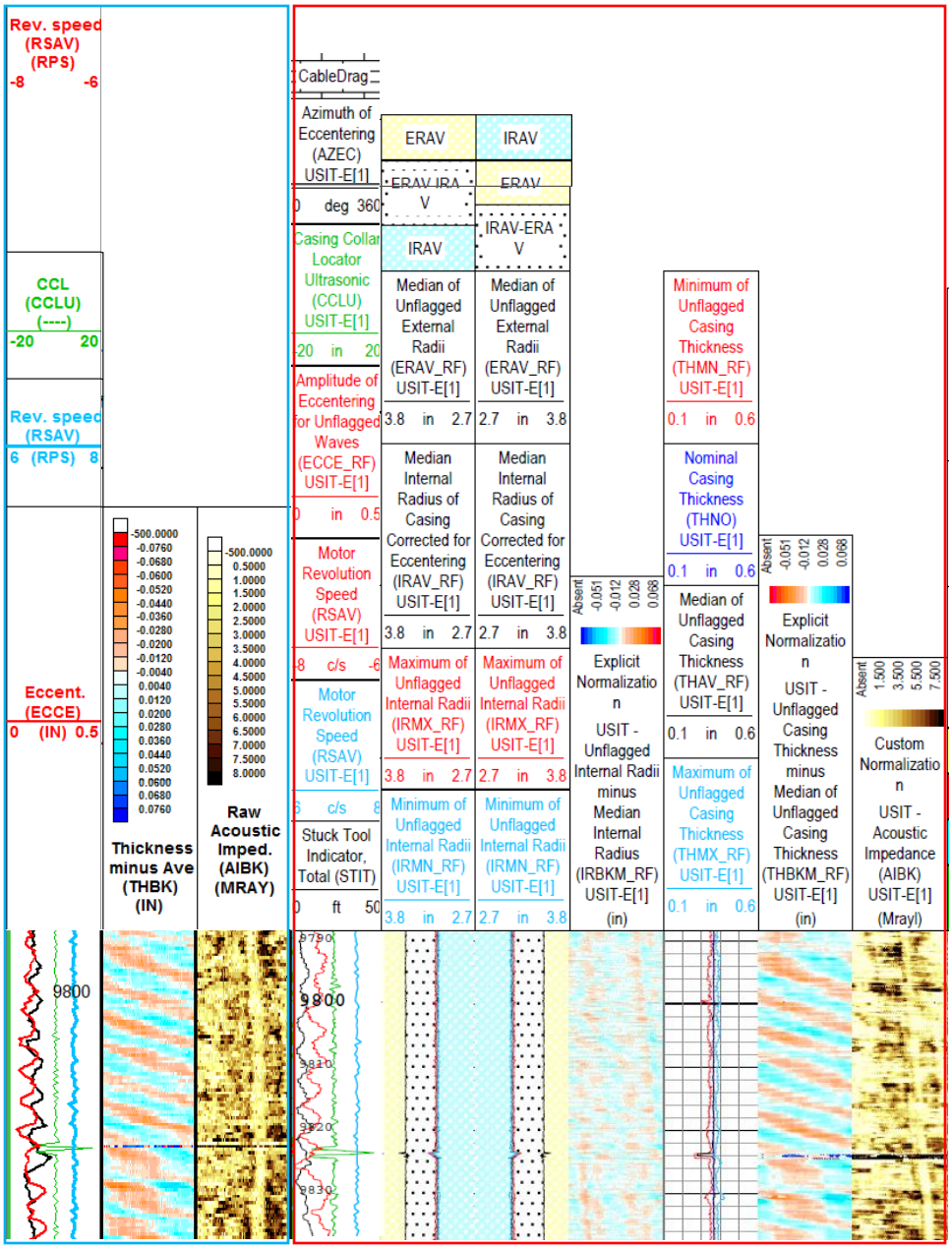

Figure 41 Comparison of ultrasonic maps collected at 9800 ft in CFU31F-2. A cable is visible in both acoustic impedance tracks (2009 and 2015) as a vertical low acoustic impedance feature. Note the 2009 data are shown on the left and are outlined in blue and the 2015 data are shown on the right and are outlined in red.

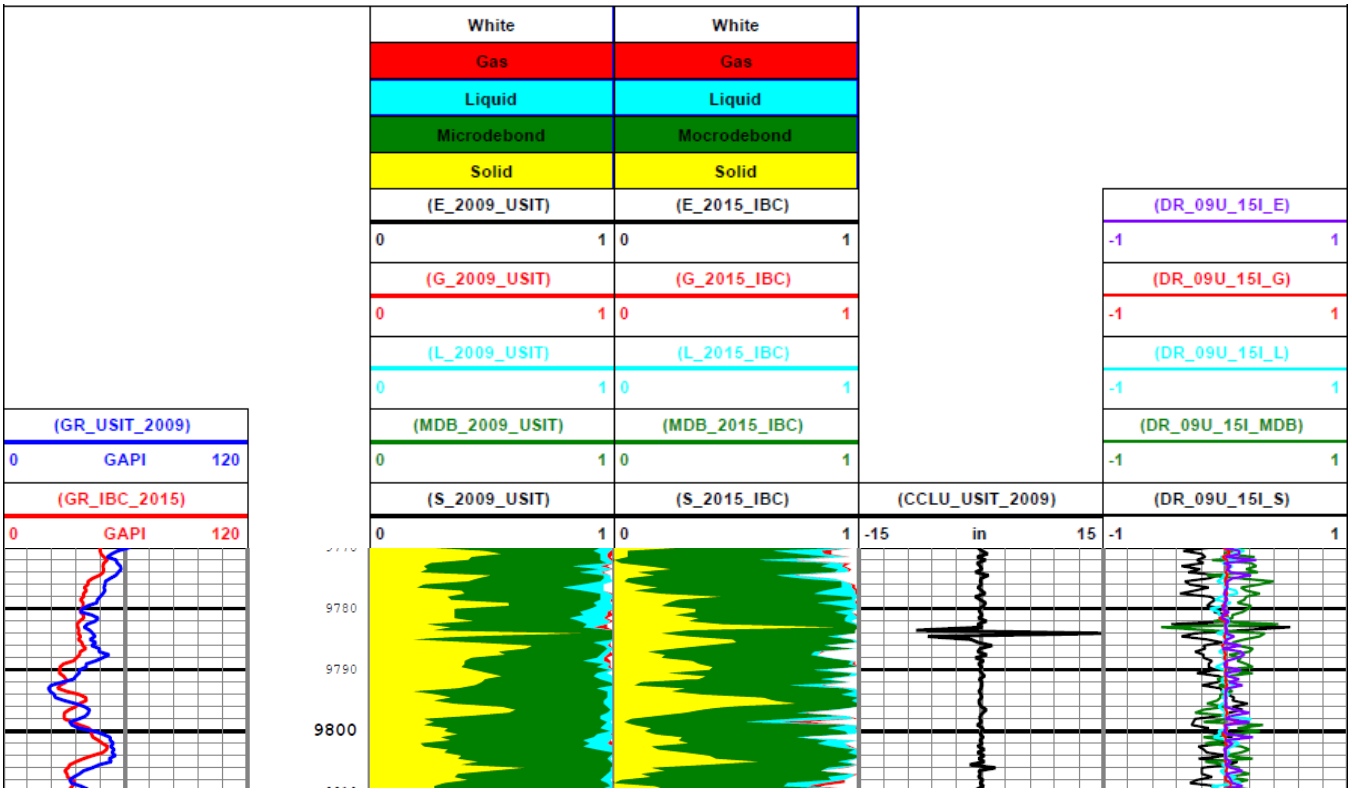

Figure 42 Comparison of ultrasonic data collected at 9800 ft in CFU31F-2. Note the 2009 data are denoted with USIT and the 2015 data are denoted with IBC.

Micro-CT images of the cement core (Figure 43) identify multiple potential reaction fronts running perpendicular to the long-axis of the sample on the formation-side of the sample (bottom of the sample in lower portion of Figure 43) and a reaction front on the casing-side of the sample (top of the sample in lower portion of Figure 43). The micro-CT scan was used to select area to cut the sample for further analyses.

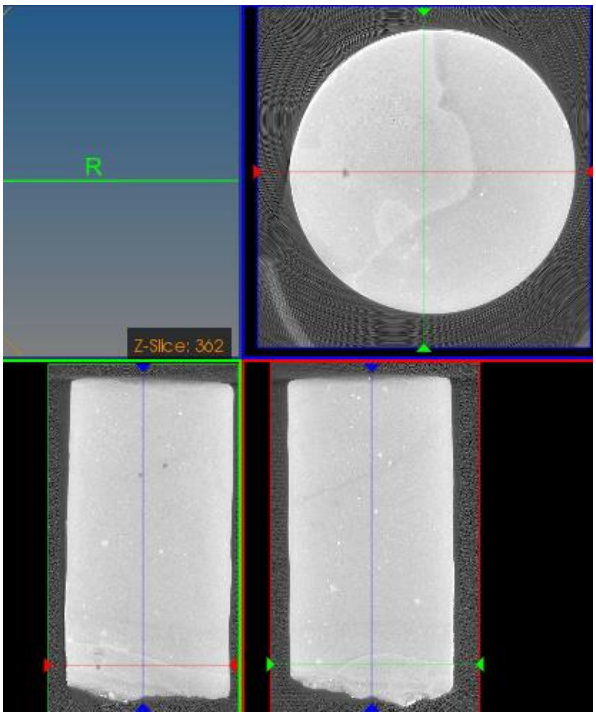

Figure 43 Micro-CT image of the cement sample collected in CFU31-F2 at 9800 ft.

Visual analysis of the sectioned sample confirms multiple reaction fronts moving into the sample from the formation side. There are at least five fronts moving in from the formation side; four are tan. The inner-most front is light grey in color. Visual analysis of the sectioned sample also confirms the existence of a tan reaction front on the casing end of the sample. Figure 44 shows the sectioned sample and provides approximate widths of the reaction fronts. Also visible is a fracture that runs diagonally through the sample. The fracture is partially filled with white material and changes direction in the tan reaction fronts on the formation side, indicating that the fracture formed after the reactions were proceeding into the sample. Changes in material properties caused the direction of the crack to change.

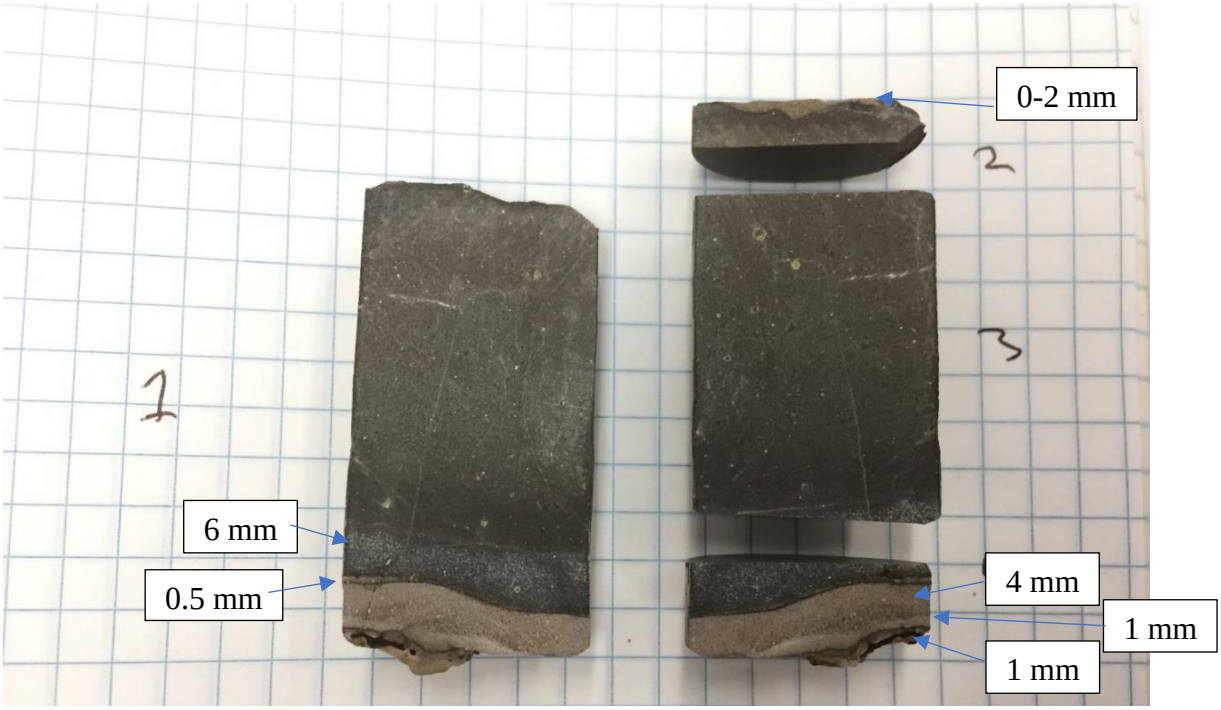

Figure 44 CFU31-F2 9800 ft cement sample sectioned for further analyses.

ESEM analyses were conducted on reacted zones on the formation-side of the sample (Figure 45) and the interior of the sample (Figure 49).

Figure 46 shows an ESEM image of the outermost reacted zone. The results EDS analyses the outer reacted zones (inside the outermost reacted zone) contain calcium in all points measured and carbon in two points measured (Figure 47 and Table 16). Moving into the sample, the widest tan reaction front, shows points with and without calcium with no carbon or points that are rich in carbon (Figure 48 and Table 17). Moving further into the sample away from the visually reacted zones and around the diagonal fracture there are no measurements containing carbon and all measurements contain calcium. Note, the calcium values are generally higher than those measured moving toward the formation-side of the sample (Figure 50 and Table 18).

Figure 45 Photograph showing the portion of the sample collected at 9800 ft used for ESEM analyses of the formation-side reaction fronts.

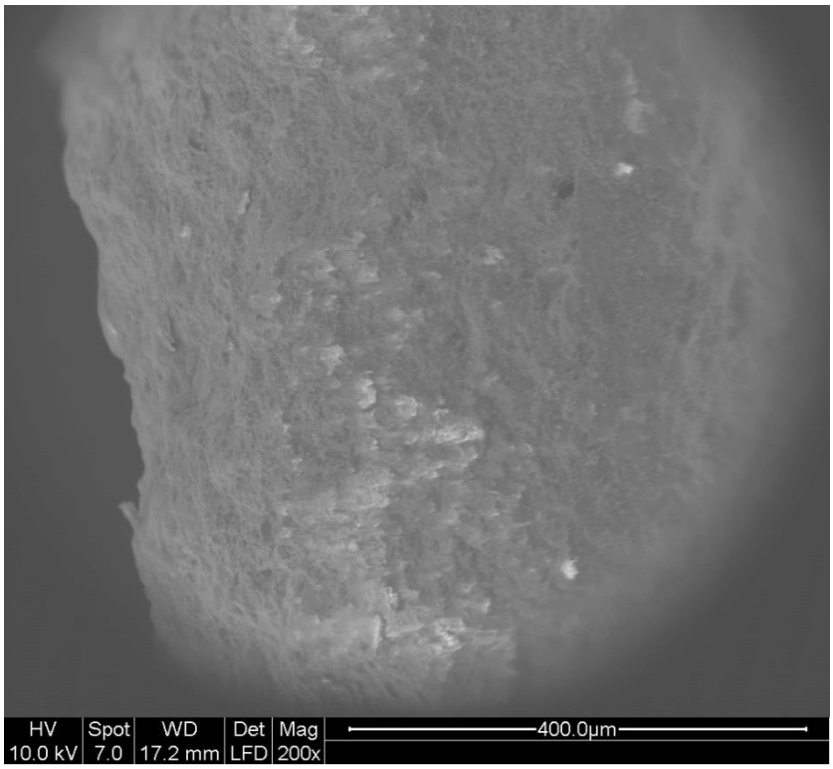

Figure 46 ESEM image of the outermost reacted zone on the formation-side of the sample collected at 9800 ft.

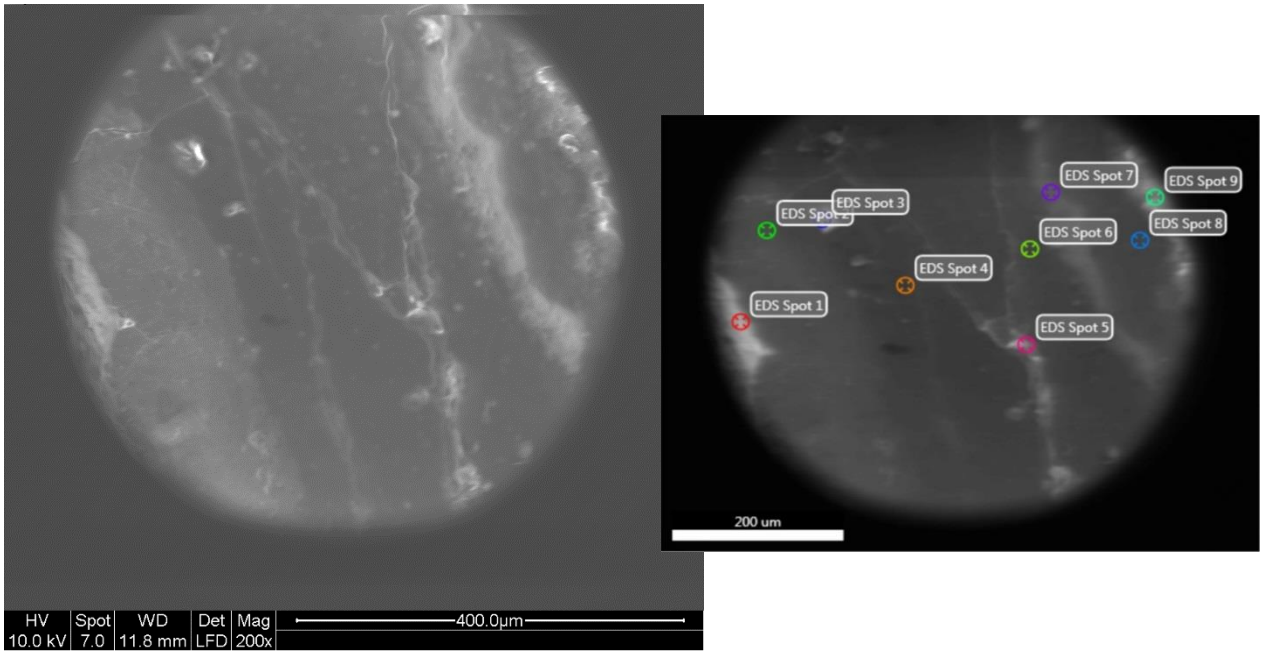

Figure 47 ESEM image of the reacted area moving in from the outermost reacted zone (very left of the image) of the sample collected at 9800 ft (Left) and corresponding EDS points (Right).

Table 16 EDS data corresponding to the points shown in Figure 47 .

	EDS1	EDS2	EDS3	EDS4	EDS5	EDS6	EDS7	EDS8	EDS9
Element	Atom %	Atom %	Atom %	Atom %	Atom %	Atom %	Atom %	Atom %	Atom %
C	-	-	-	-	12.85	-	-	-	11.34
O	56.32	67.47	59.97	67.75	58.66	68.26	71.73	68.75	64.21
Si	24.27	18.02	23.06	16.05	14.64	16.16	14.39	17.89	10.06
Na	2.75	2.07	2.70	2.73	-	2.18	-	2.37	1.90
Cl	-	-	-	-	1.00	-	-	-	-
Mg	-	-	-	-	1.39	-	-	-	-
Al	-	2.89	7.29	2.62	1.54	2.76	1.97	2.09	1.39
Ca	15.40	9.54	2.58	10.84	9.93	10.64	11.91	8.90	9.82
S	-	-	-	-	-	-	-	-	1.29
K	1.27	-	4.41	-	-	-	-	-	-

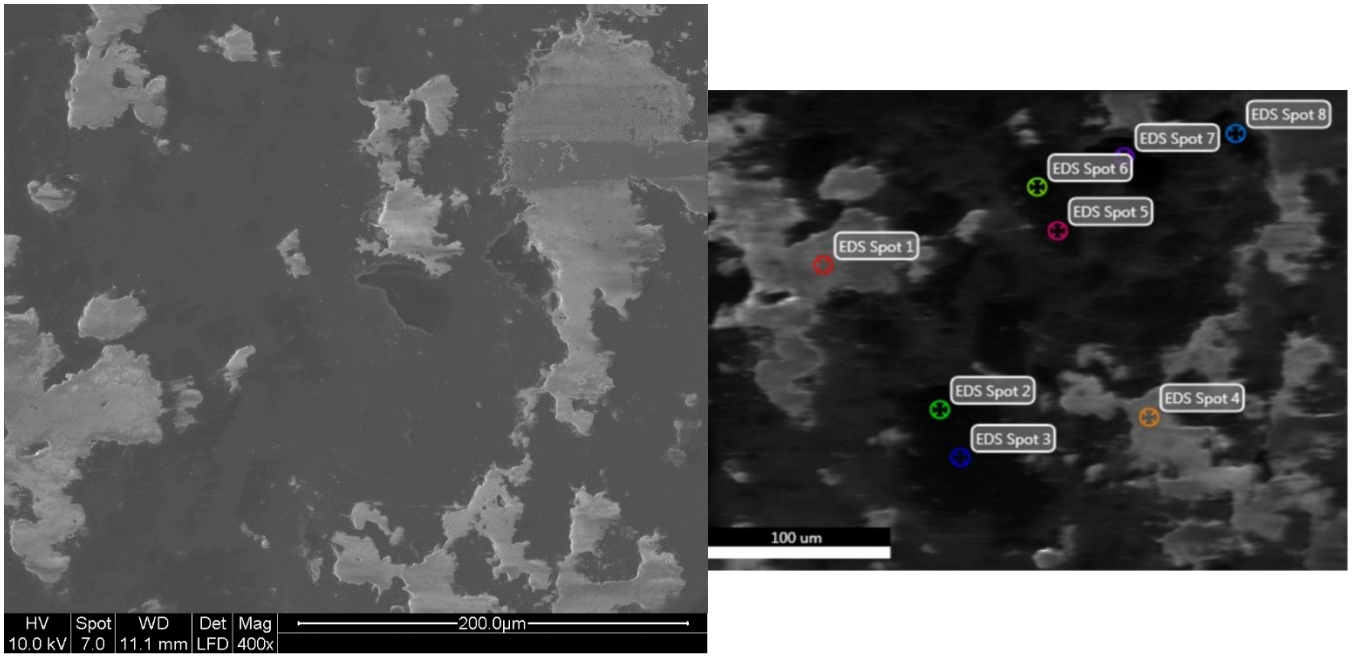

Figure 48 ESEM image collected of the innermost (approximately 4-mm-wide) tan reaction front) in the sample collected at 9800 ft (Left) and corresponding EDS points (Right).

Table 17 EDS data corresponding to the points shown in Figure 48

	EDS1	EDS2	EDS3	EDS4	EDS5	EDS6	EDS7	EDS8
Element	Atom %	Atom %	Atom %	Atom %	Atom %	Atom %	Atom %	Atom %
C	-	-	-	-	-	-	77.87	64.57
O	66.44	69.55	70.48	63.74	69.98	70.22	18.83	27.9
Si	22.49	30.45	29.52	17.76	30.02	29.78	0.51	2.63
Na	-	-	-	-	-	-	-	1.00
Cl	-	-	-	-	-	-	0.73	-
Mg	-	-	-	-	-	-	-	0.58
Al	1.69	-	-	1.23	-	-	-	0.51
Ca	9.38	-	-	17.26	-	-	1.38	2.48
S	-	-	-	-	-	-	0.69	-
Mo	-	-	-	-	-	-	-	0.32

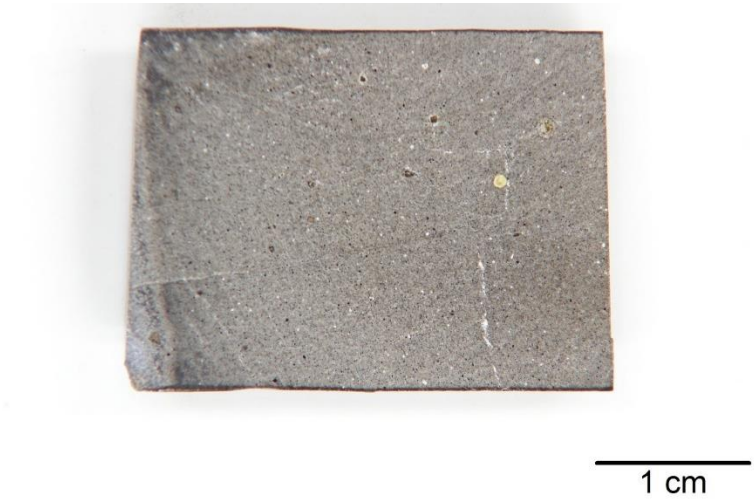

Figure 49 Photograph showing another portion of the sample collected at 9800 ft used for ESEM analyses.

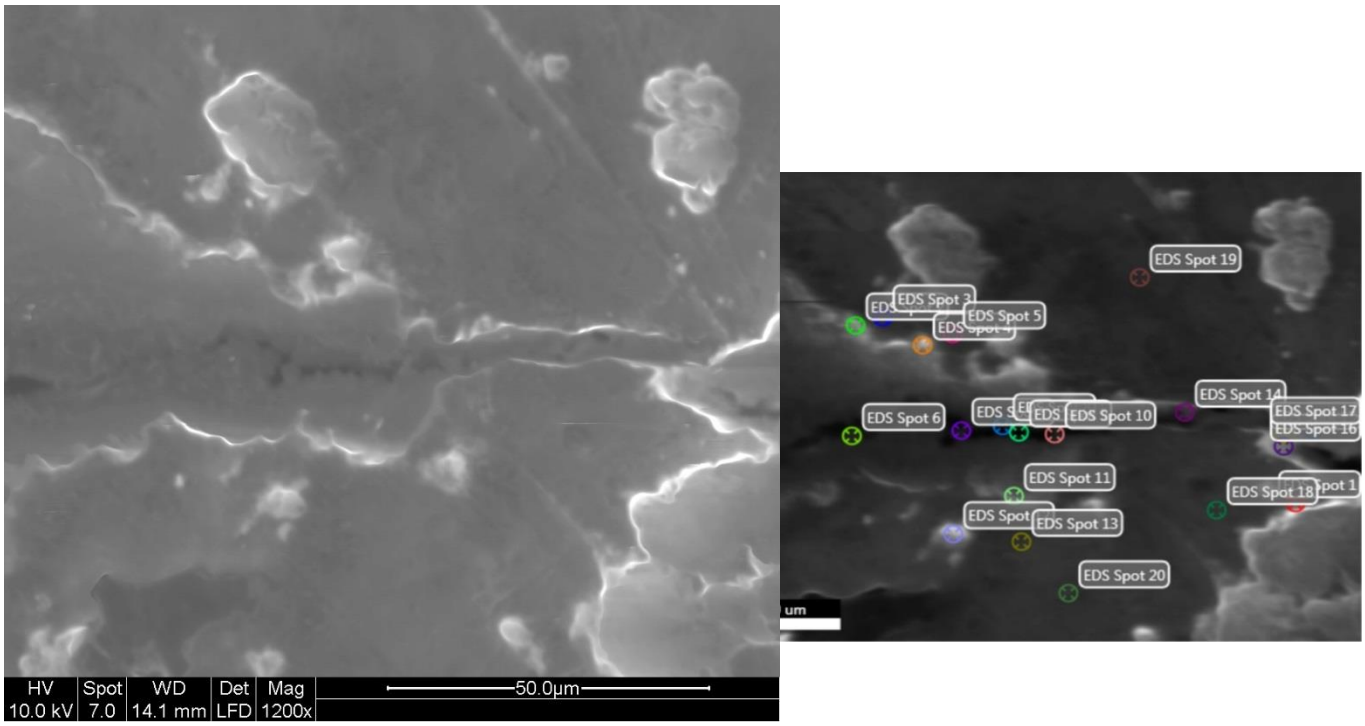

Figure 50 ESEM image collected in the visually in the central portion (not in a visually reacted zone) of the sample collected at 9800 ft (Left) and corresponding EDS points (Right).

Table 18 EDS data corresponding to the points shown in Figure 51.

	EDS1	EDS2	EDS3	EDS4	EDS5	EDS6	EDS7	EDS8	EDS9	EDS10	EDS11	EDS12	EDS13	EDS14	EDS15	EDS16	EDS17	EDS18	EDS
Element	Atom %	Atom %	Atom %	Atom %	Atom %	Atom %	Atom %	Atom %	Atom %	Atom %	Atom %	Atom %	Atom %	Atom %	Atom %	Atom %	Atom %	Atom %	Atom
C	-	-	-	-	-	-	-	-	-	-	-	-	-	-	-	-	-	-	-
O	63.92	54.22	68.7	53.68	62.63	63.96	54.00	43.07	46.48	53.27	66.82	60.39	67.12	28.45	42.59	38.60	66.20	62.95	70.0
Si	13.55	16.97	12.02	15.51	16.93	17.13	11.76	12.15	13.72	15.42	13.07	14.54	15.66	57.37	24.37	22.59	16.04	19.34	8.6
Na	-	-	-	-	-	-	-	-	-	-	-	-	-	-	-	-	-	-	-
Cl	1.90	2.97	1.07	3.43	2.63	1.04	-	1.67	-	1.78	2.16	1.84	0.86	0.86	1.87	2.58	1.10	1.92	1.1
Mg	1.03	0.88	-	0.40	-	0.94	-	-	-	0.33	-	2.89	-	-	-	-	-	-	-
Al	1.42	1.07	2.37	0.90	1.01	1.09	-	-	-	0.54	0.64	1.19	1.06	0.64	0.98	0.73	1.01	1.07	1.2
Ca	18.17	22.88	15.83	26.07	16.04	15.83	34.24	43.1	39.8	28.67	16.82	19.14	15.30	12.69	30.19	35.49	15.66	14.71	18.1
S	-	1.02	-	-	-	-	-	-	-	-	-	-	-	-	-	-	-	-	0.7
Mo	-	-	-	-	-	-	-	-	-	-	-	-	-	-	-	-	-	-	-
As	-	-	-	-	0.76	-	-	-	-	-	0.49	-	-	-	-	-	-	-	-

The sectioned sidewall core was used conducting LA-ICP-MS starting on the casing side and moving toward the formation side. The LA-ICP-MS scan line images and corresponding data are presented in Figure 51 through Figure 76. Line 1, moving into the sample across the reacted zone on the casing side shows an increase in ratios to about

100 microns for Ca/Si and Ca/Al and an increase in ratios for Ca/Fe to about 250 microns. After the initial increases the ratios remain fairly steady. Ca/Si remains around 1.5 to the end of the scan (Figure 52). Ca/Si slowly decreases over the next six lines (Figure 53 to Figure 62) where is reaches a value near 1 until crossing the fracture in the grey reacted zone (approximately 2000 microns into line 7, Figure 62) where Ca/Si jumps up to between 1.1 and 1.4. When the Line reaches the next front (approximately 4250 microns) Ca/Si increases again with two spikes around 1.6 and two spikes around 3.6. At the next transition to the light tan wide front, Ca/Si drops closer to 1 for the rest of the line. The Ca/Si increases moving into the grey zone with values as high as 2 and the decreases again by the end of the zone with values around 0.7 where the line transitions into the next reaction zone (approximately 3000 microns in Figure 64). In this zone Ca/Si increases to around 1.1 and then drops to around 0.4 around 3600 microns where the zone ends and the next zone begins. That zone is between 3600 and 4800 microns, it has several peaks and ranges between 0.5 and 1.2 Ca/Si. The next zone starts at 4800 microns and runs to around 5200 microns. The Ca/Si over this zone is smoother than the previous zone dropping from around 0.6 to 0.4 across the zone. In the last, outermost, reacted zone the Ca/Si rises to around 0.9 and then drops to around 0.2 at the end of the line, around 5550 microns. Figure 66 shows the behavior of the ratios across the grey zone without the crack. The Ca/Si behavior is smoother than across the crack. Figure 67 through Figure 76 show additional lines across the reaction fronts at on the formation side of the sample.

Figure 51 LA-ICP-MS Line 1 across the sample collected in CFU31-F2 at 9800 ft.

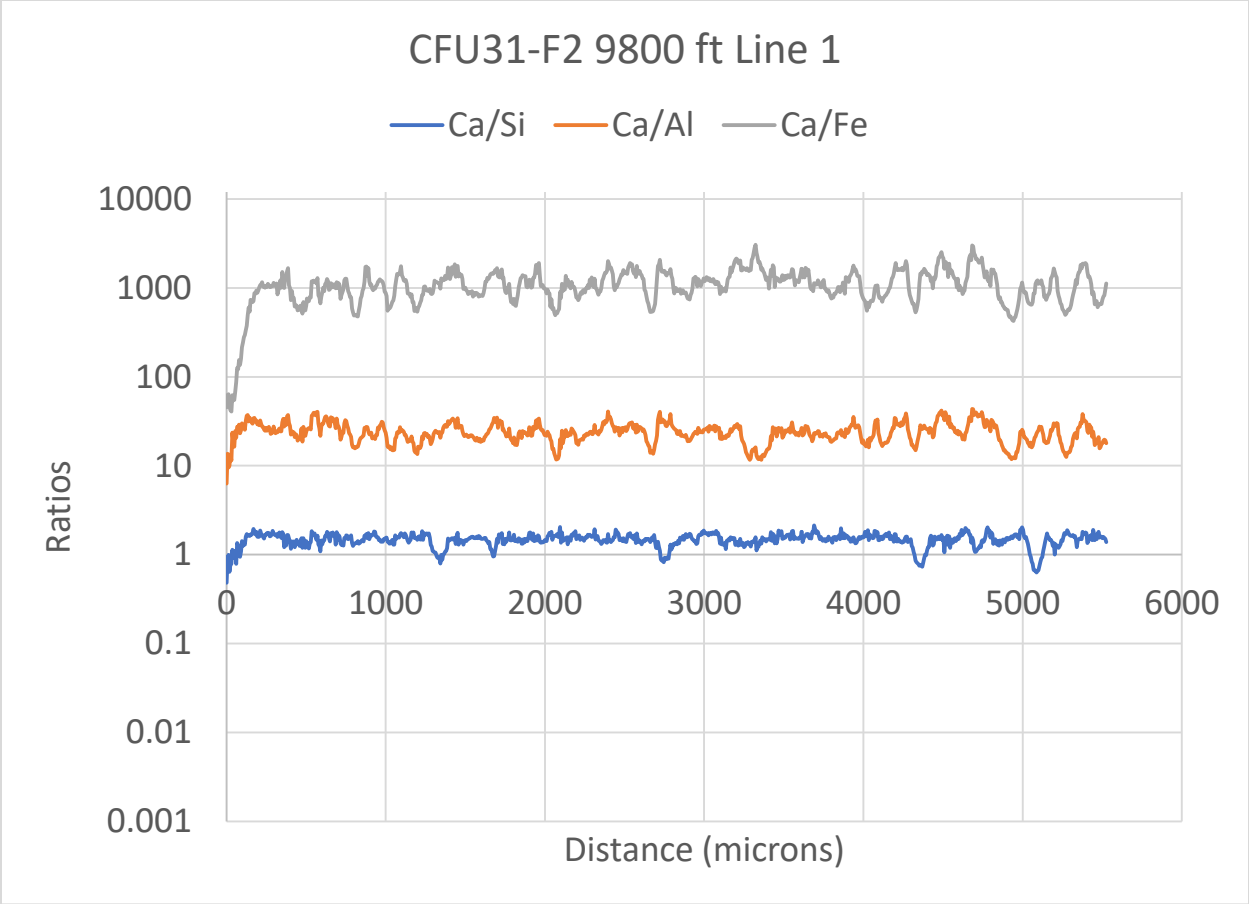

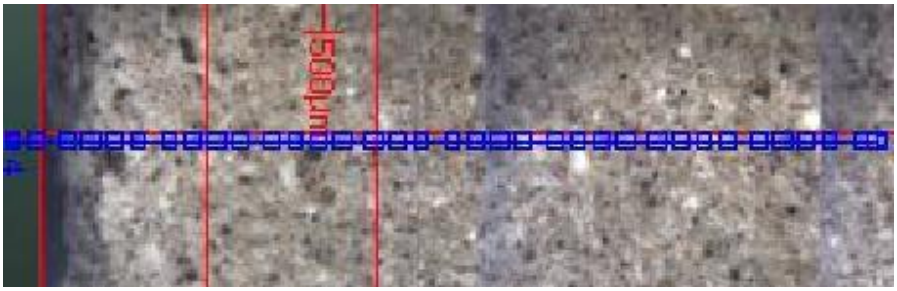

Figure 52 LA-ICP-MS Line 1 results across the sample collected in CFU31-F2 at 9800 ft.

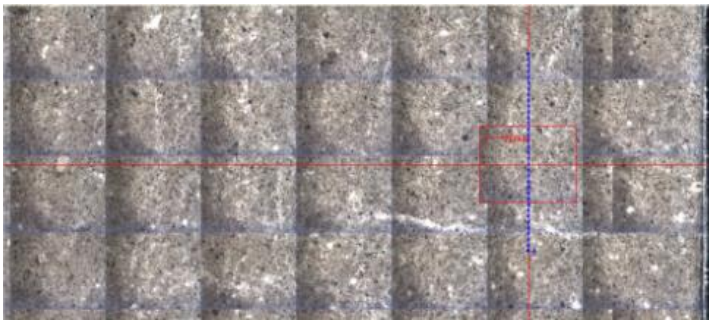

Figure 53 LA-ICP-MS Line 3 across the sample collected in CFU31-F2 at 9800 ft.

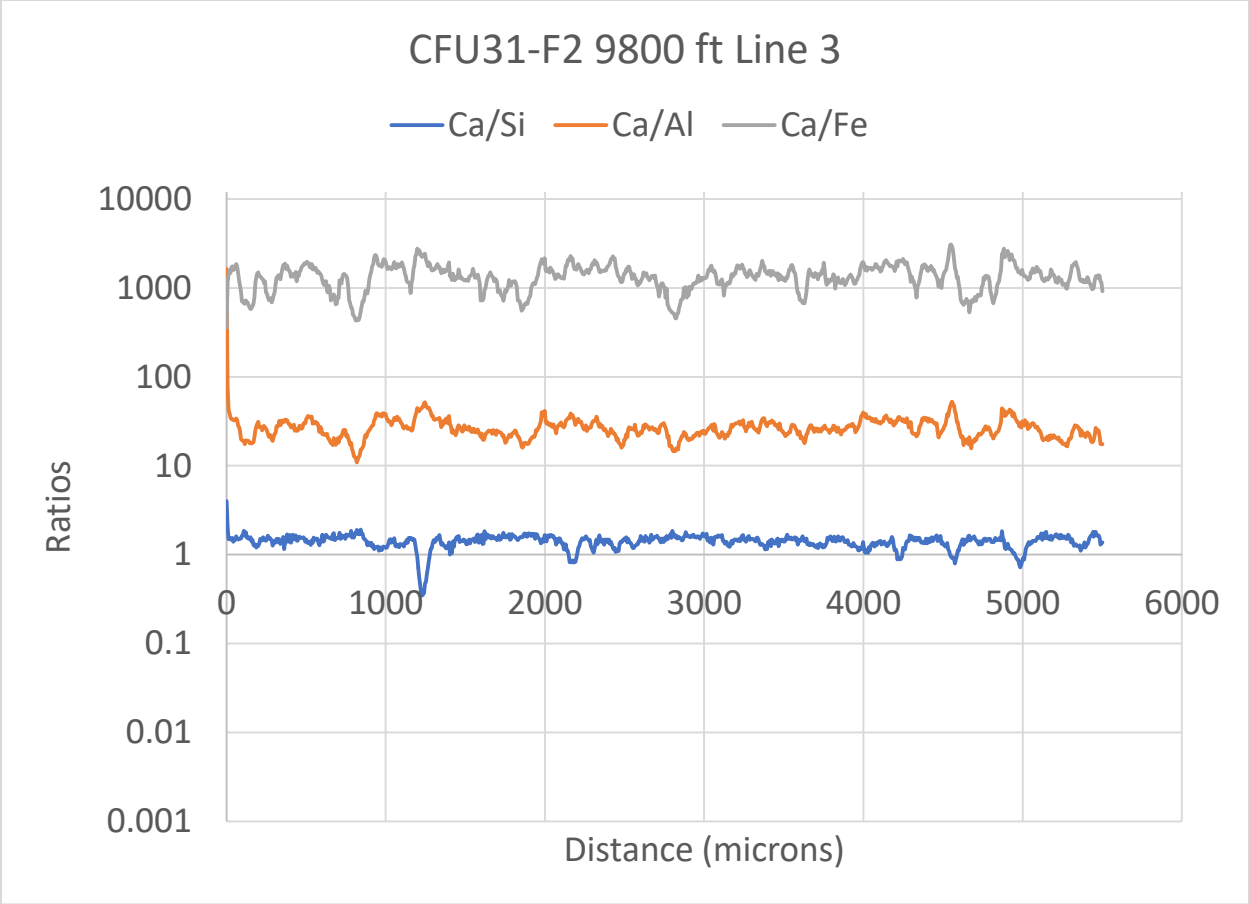

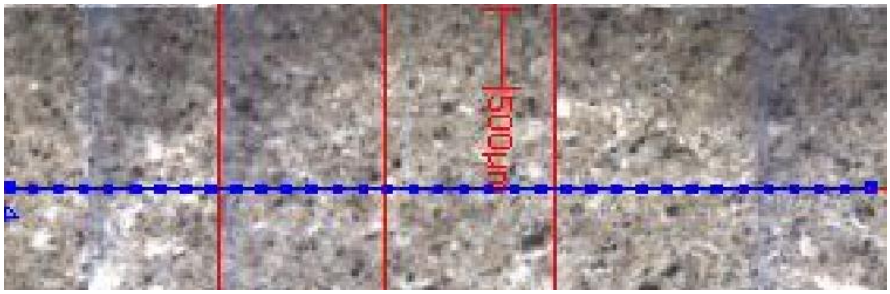

Figure 54 LA-ICP-MS Line 3 results across the sample collected in CFU31-F2 at 9800 ft.

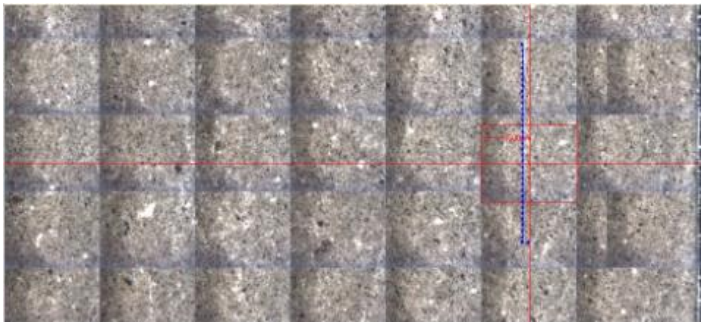

Figure 55 LA-ICP-MS Line 4 across the sample collected in CFU31-F2 at 9800 ft.

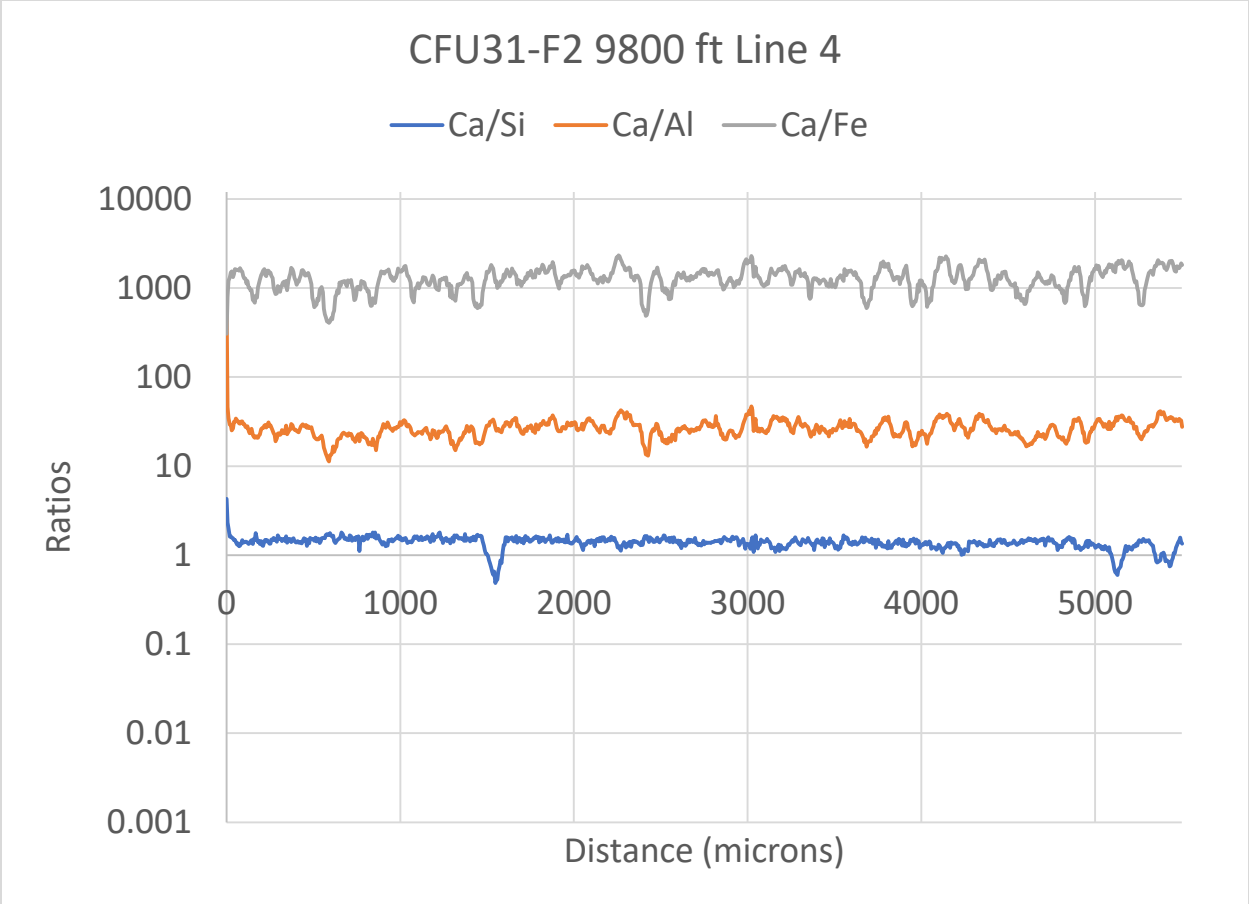

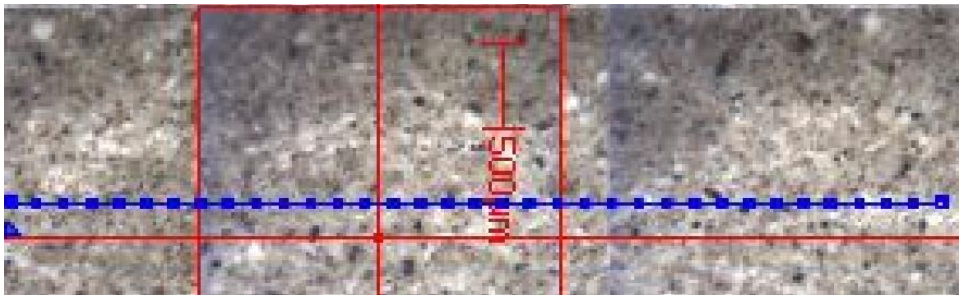

Figure 56 LA-ICP-MS Line 4 results across the sample collected in CFU31-F2 at 9800 ft.

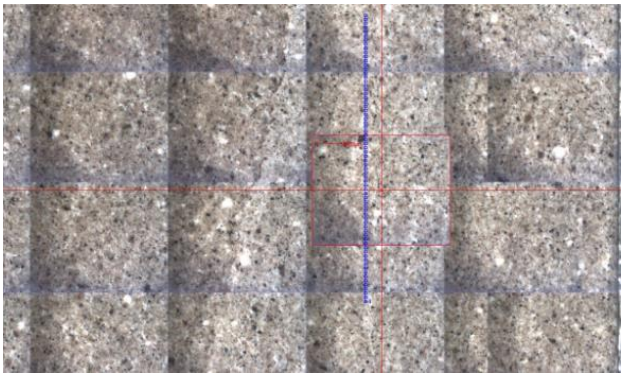

Figure 57 LA-ICP-MS Line 5 across the sample collected in CFU31-F2 at 9800 ft.

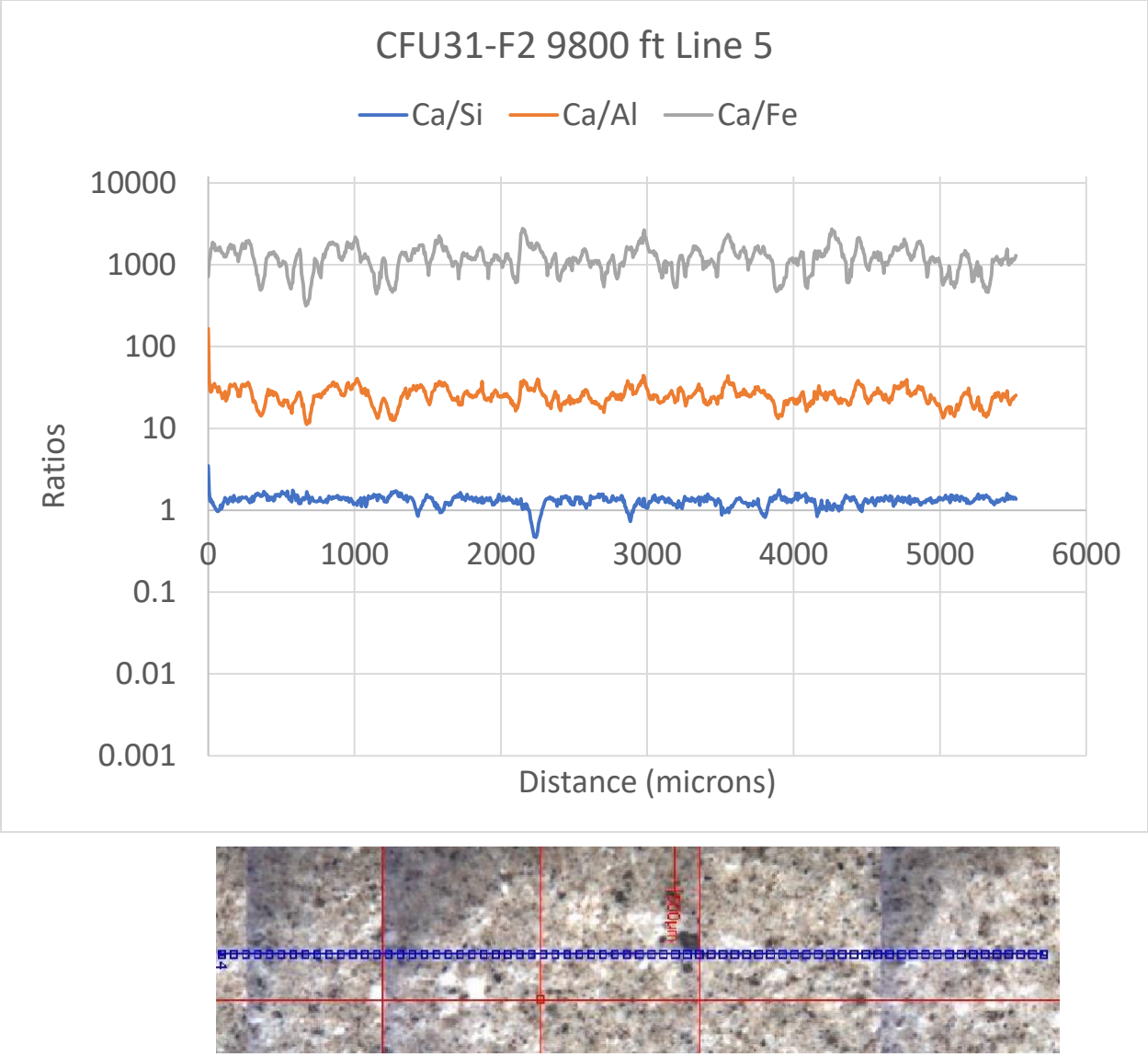

Figure 58 LA-ICP-MS Line 5 results across the sample collected in CFU31-F2 at 9800 ft showing Ca/Si, Ca/Al, and Ca/Fe mole ratios.

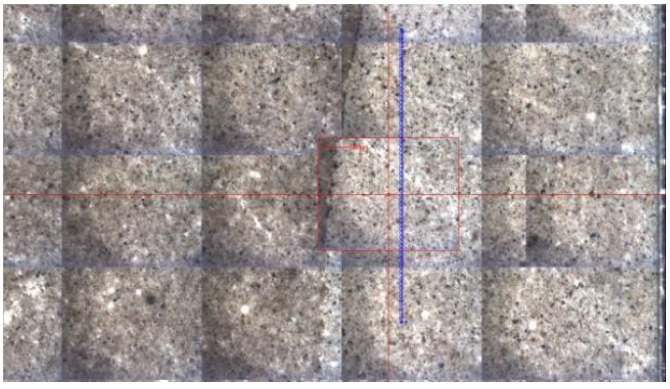

Figure 59 LA-ICP-MS Line 6 across the sample collected in CFU31-F2 at 9800 ft.

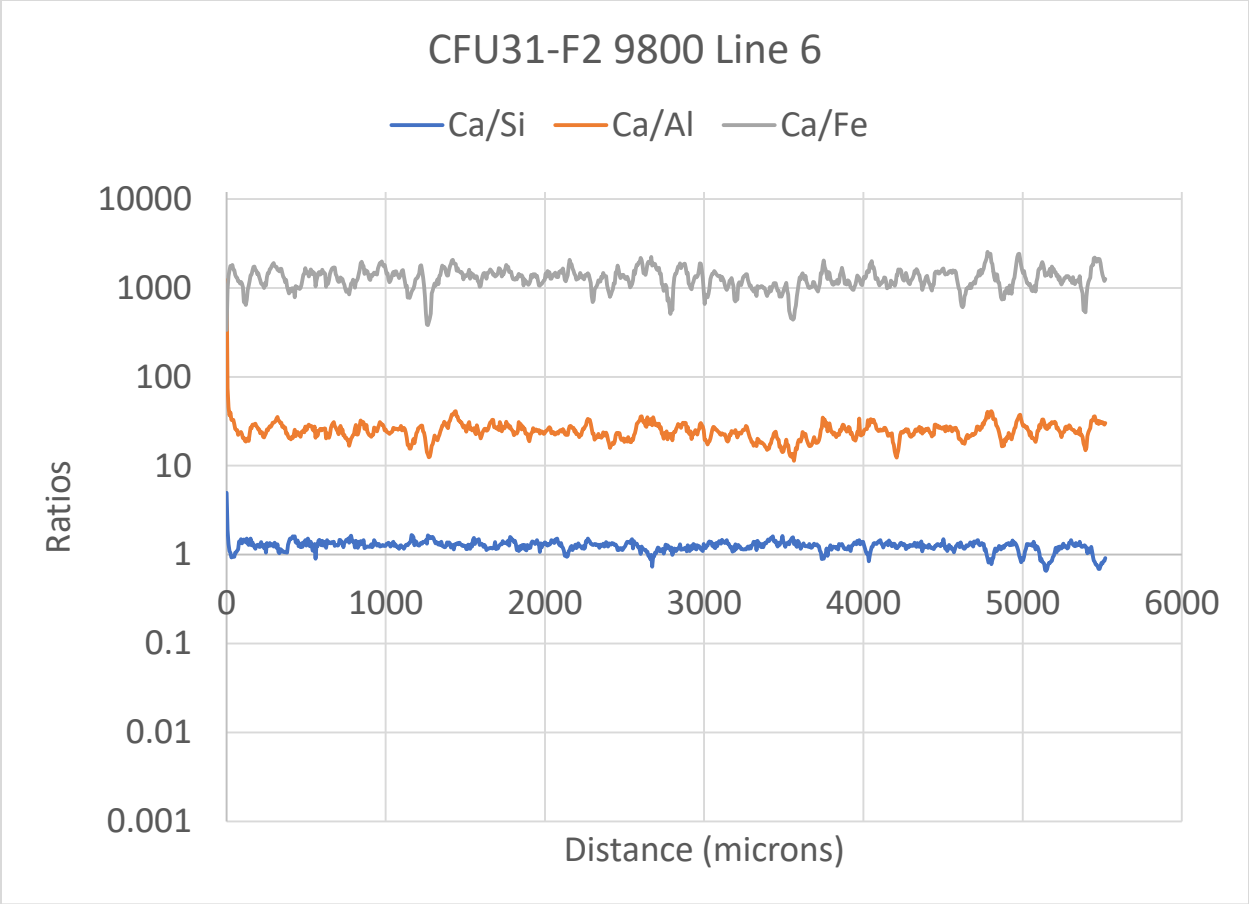

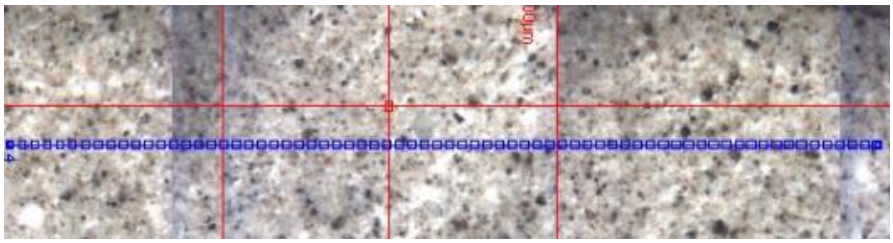

Figure 60 LA-ICP-MS Line 6 results across the sample collected in CFU31-F2 at 9800 ft.

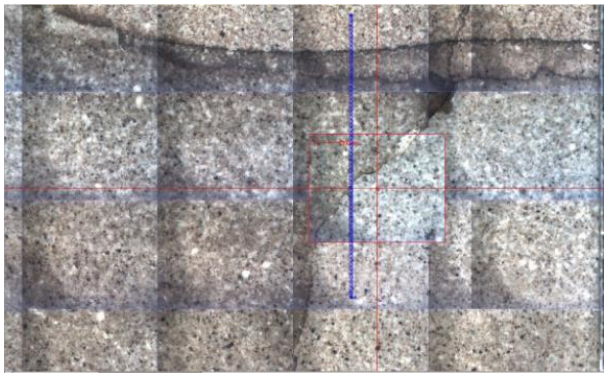

Figure 61 LA-ICP-MS Line 7 across the sample collected in CFU31-F2 at 9800 ft.

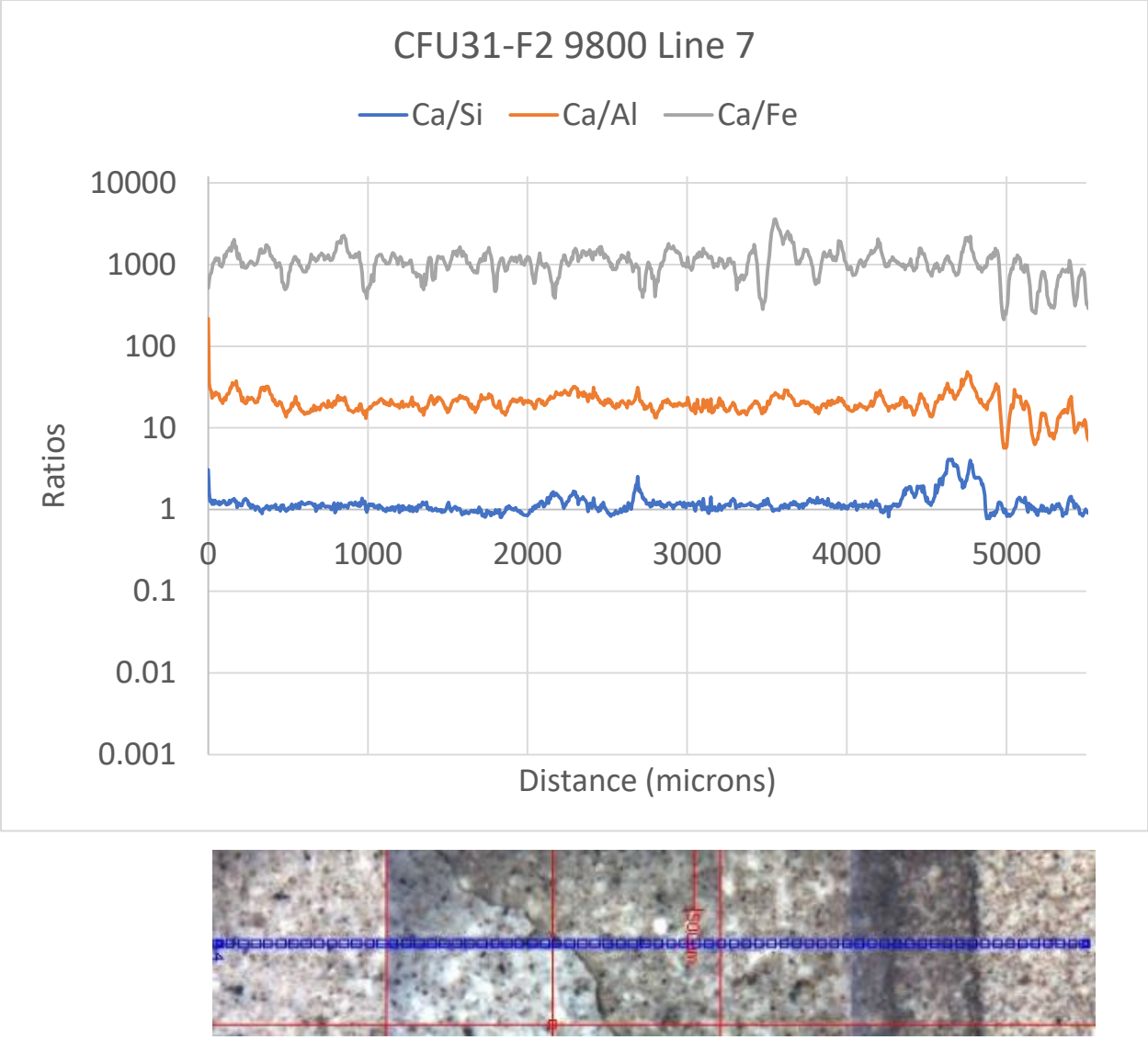

Figure 62 LA-ICP-MS Line 7 results across the sample collected in CFU31-F2 at 9800 ft showing Ca/Si, Ca/Al, and Ca/Fe mole ratios.

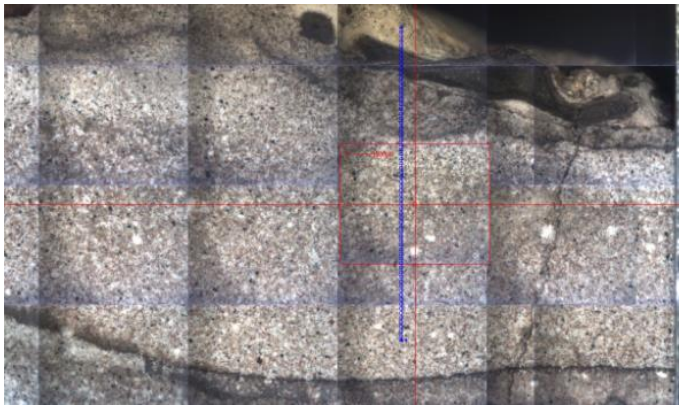

Figure 63 LA-ICP-MS Line 8 across the sample collected in CFU31-F2 at 9800 ft.

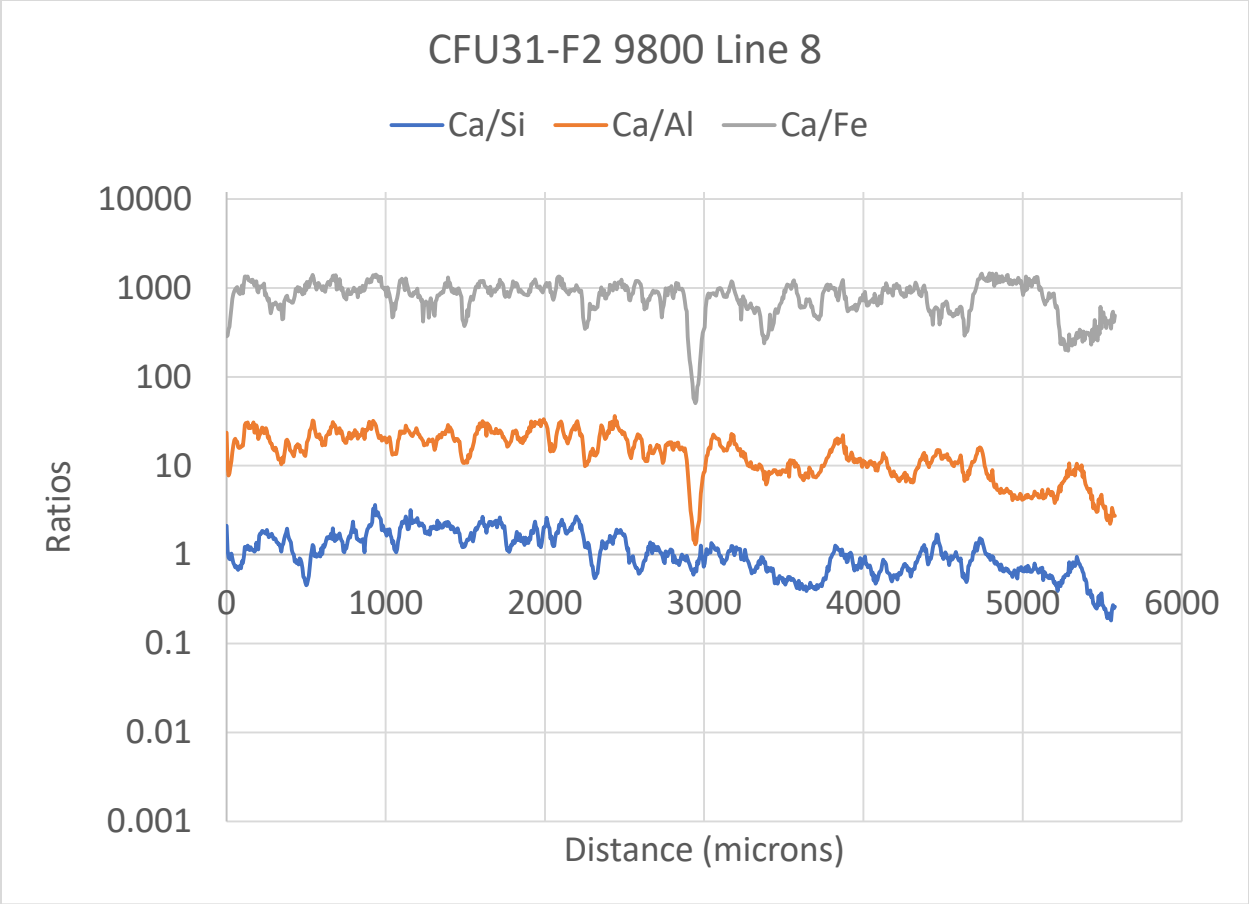

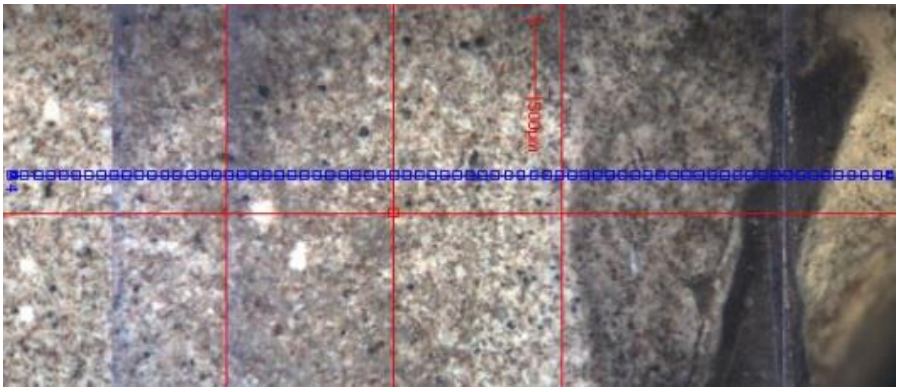

Figure 64 LA-ICP-MS Line 8 results across the sample collected in CFU31-F2 at 9800 ft showing Ca/Si, Ca/Al, and Ca/Fe mole ratios.

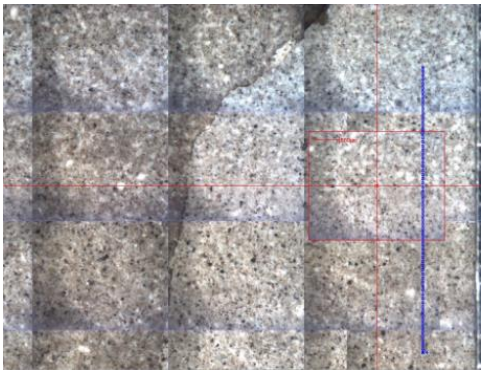

Figure 65 LA-ICP-MS Line 9 across the sample collected in CFU31-F2 at 9800 ft.

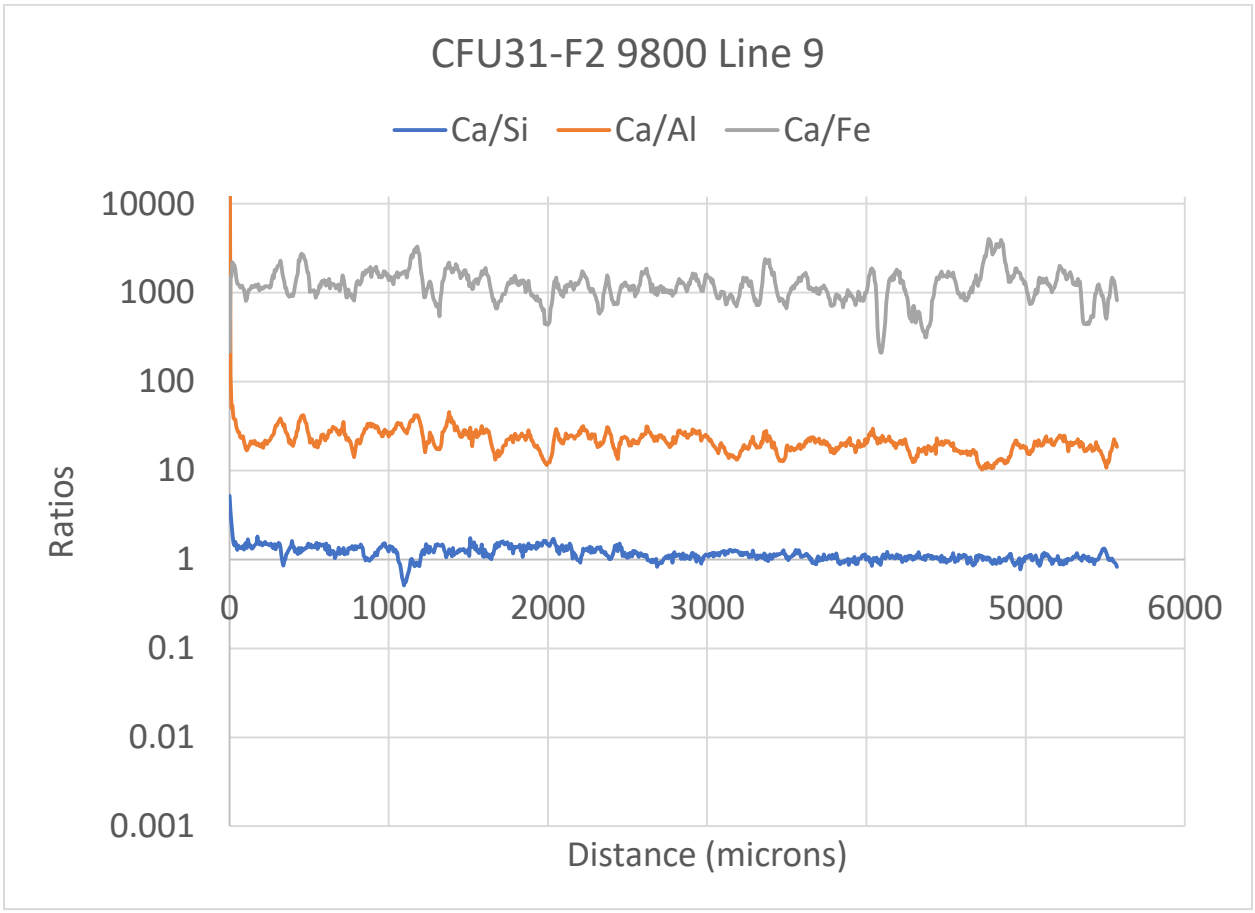

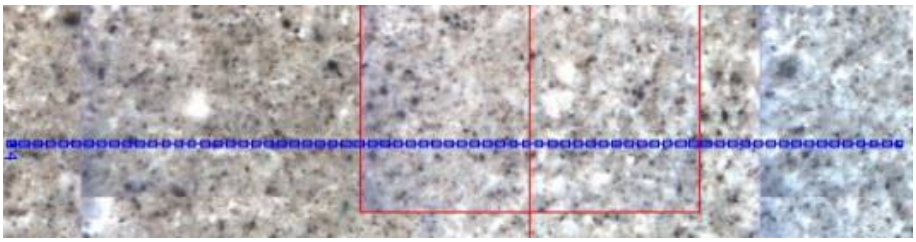

Figure 66 LA-ICP-MS Line 9 results across the sample collected in CFU31-F2 at 9800 ft showing Ca/Si, Ca/Al, and Ca/Fe mole ratios.

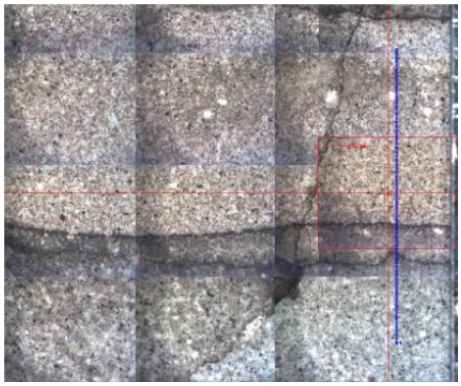

Figure 67 LA-ICP-MS Line 10 across the sample collected in CFU31-F2 at 9800 ft.

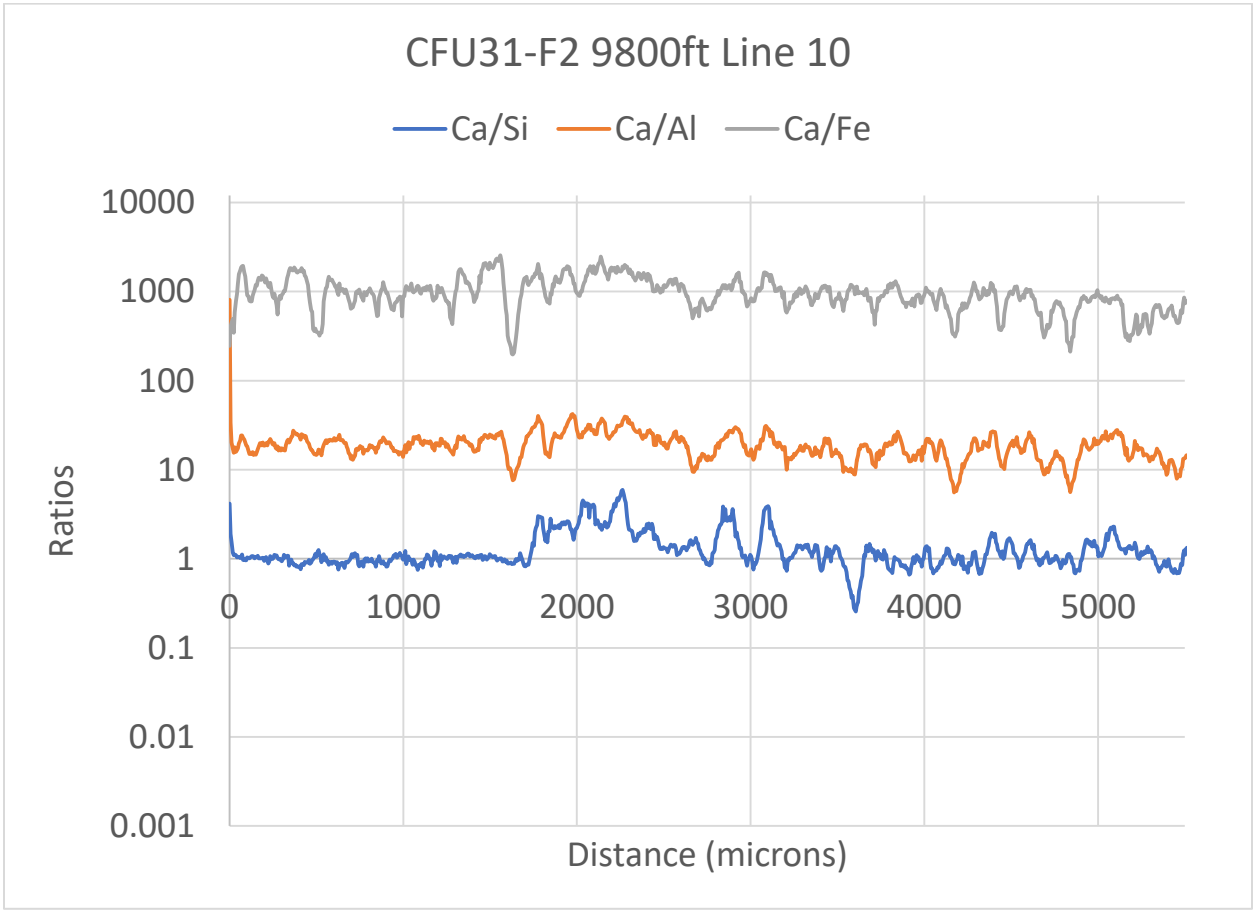

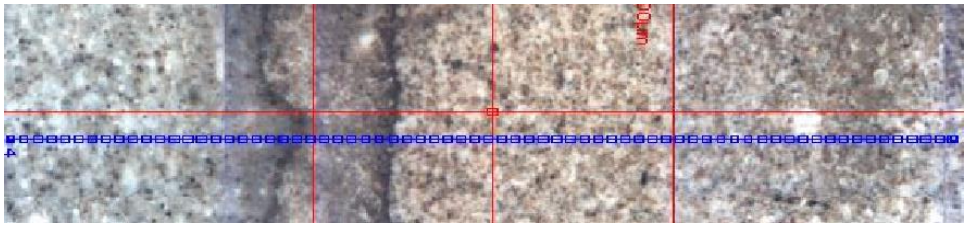

Figure 68 LA-ICP-MS Line 10 results across the sample collected in CFU31-F2 at 9800 ft showing Ca/Si, Ca/Al, and Ca/Fe mole ratios.

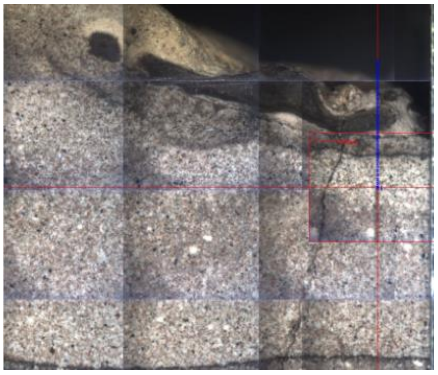

Figure 69 LA-ICP-MS Line 11 across the sample collected in CFU31-F2 at 9800 ft.

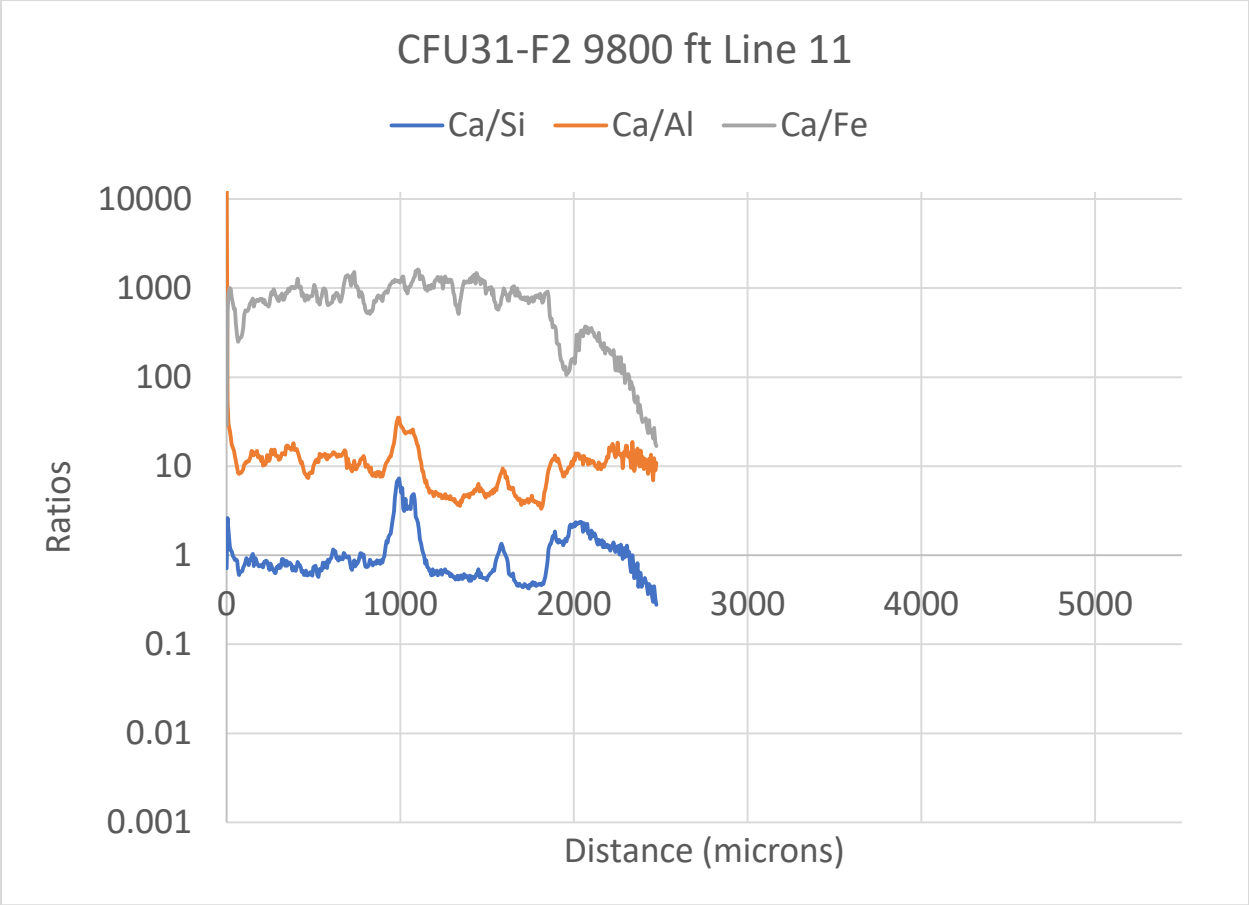

Figure 70 LA-ICP-MS Line 11 results across the sample collected in CFU31-F2 at 9800 ft showing Ca/Si, Ca/Al, and Ca/Fe mole ratios.

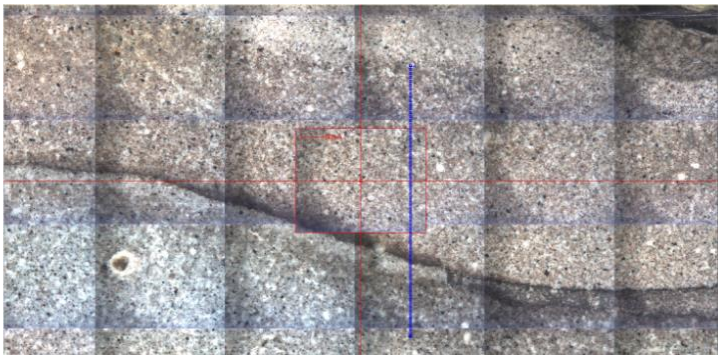

Figure 71 LA-ICP-MS Line 12 across the sample collected in CFU31-F2 at 9800 ft.

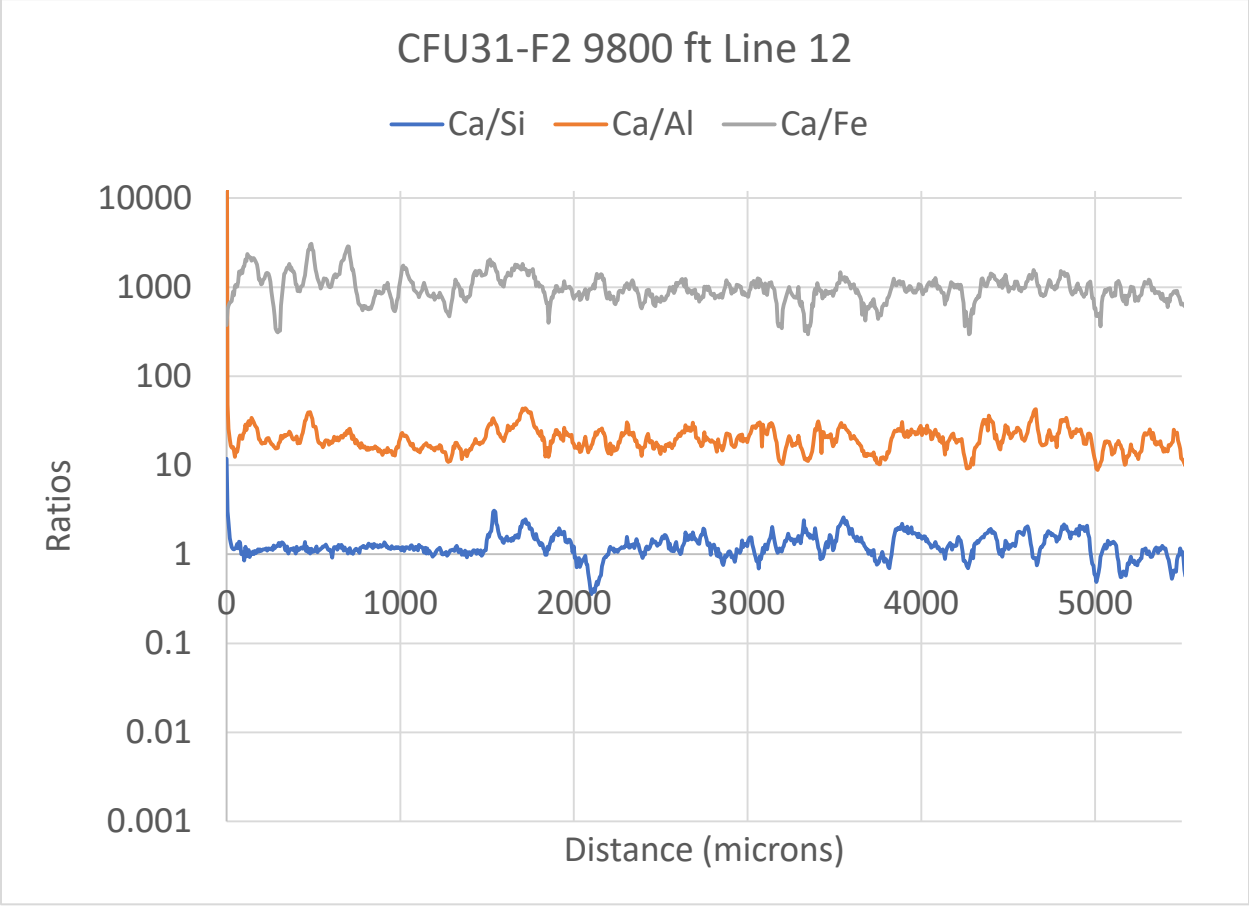

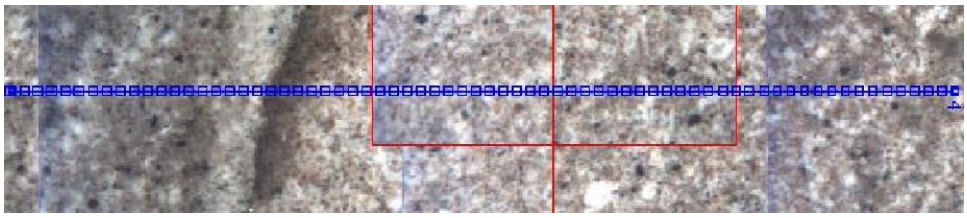

Figure 72 LA-ICP-MS Line 12 results across the sample collected in CFU31-F2 at 9800 ft showing Ca/Si, Ca/Al, and Ca/Fe mole ratios.

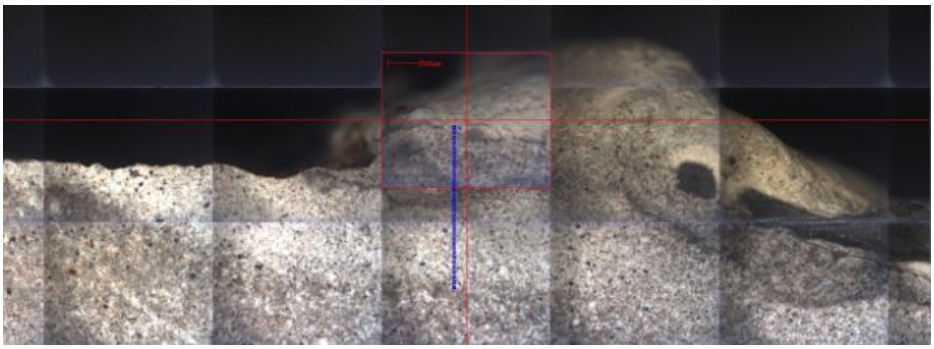

Figure 73 LA-ICP-MS Line 13 across the sample collected in CFU31-F2 at 9800 ft.

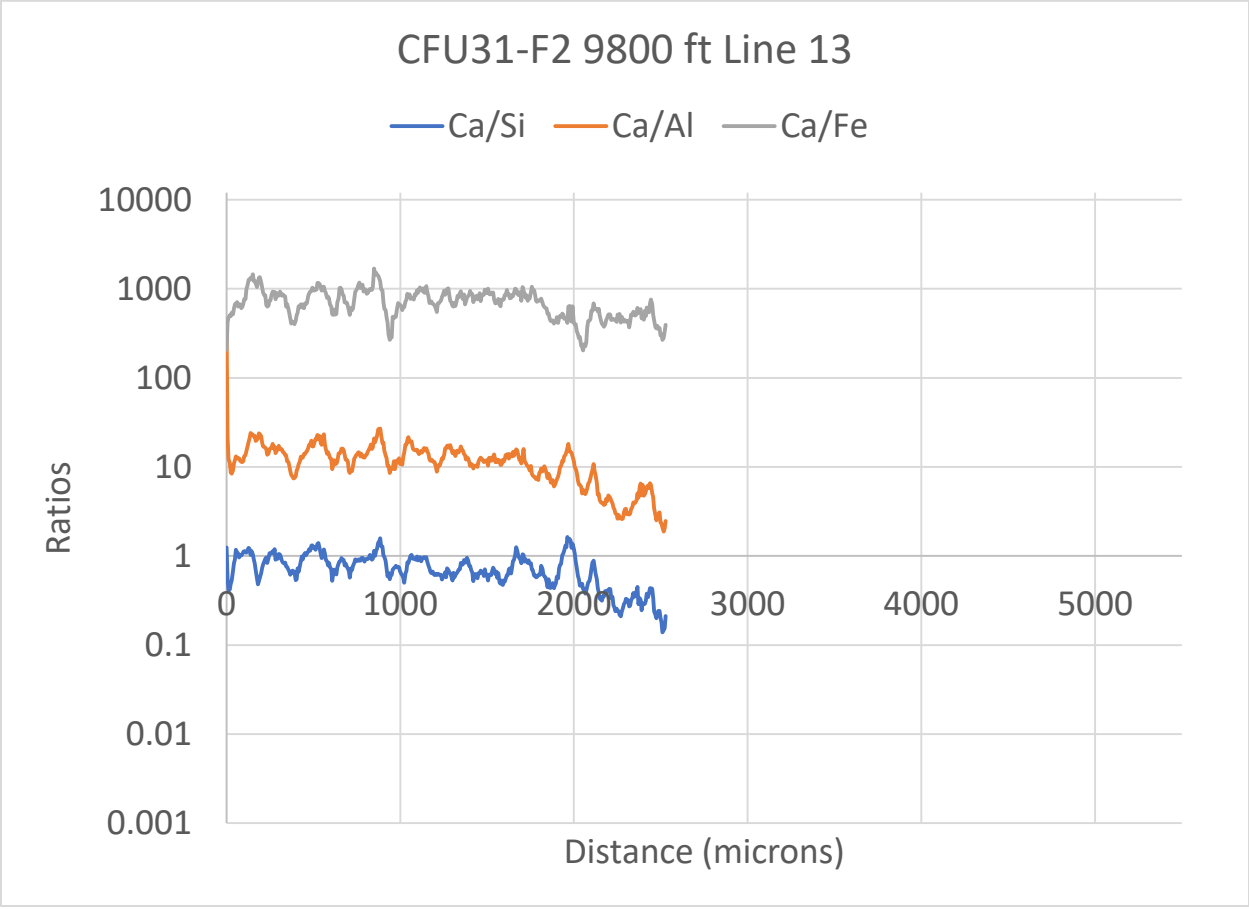

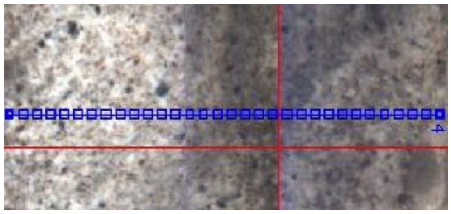

Figure 74 LA-ICP-MS Line 13 results across the sample collected in CFU31-F2 at 9800 ft showing Ca/Si, Ca/Al, and Ca/Fe mole ratios.

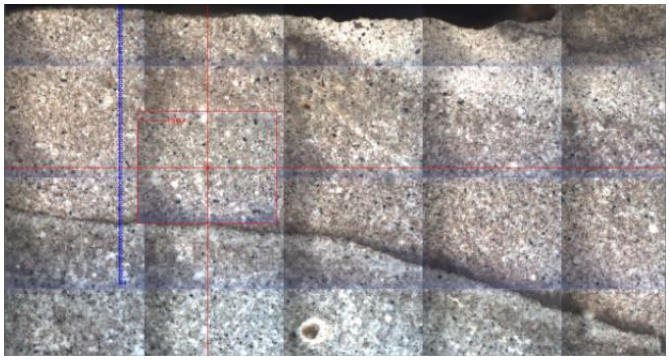

Figure 75 LA-ICP-MS Line 14 across the sample collected in CFU31-F2 at 9800 ft.

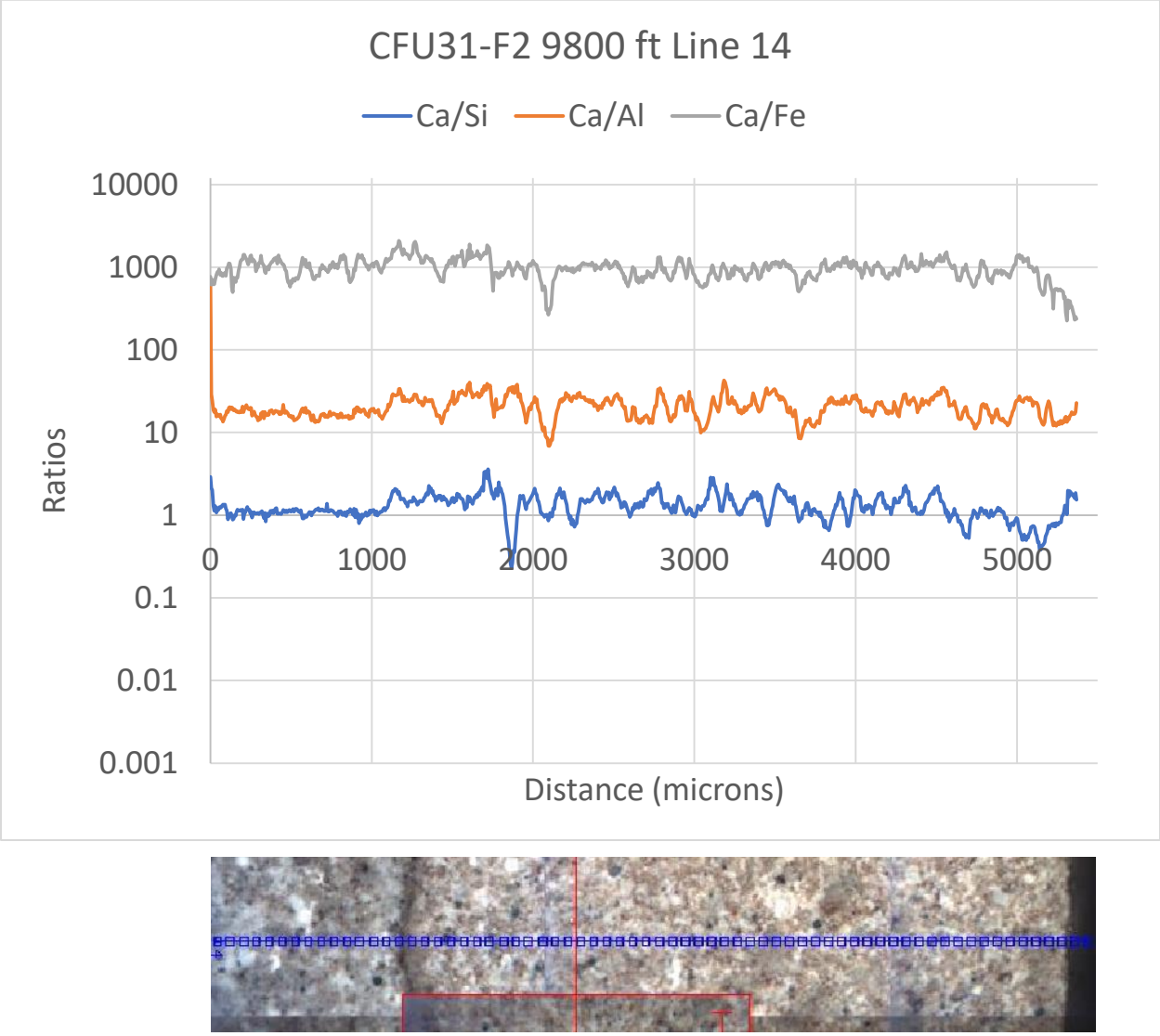

Figure 76 LA-ICP-MS Line 14 results across the sample collected in CFU31-F2 at 9800 ft showing Ca/Si, Ca/Al, and Ca/Fe mole ratios.

Following LA-ICP-MS portions of the sample were crushed and XRD analysis was performed. XRD on the sample collected at 9800 ft was divided into three zones. Zone 1 consisted of the outer fronts in the formation side of the sample between the outermost front and the wide tan front. Zone 2 was the wide tan front. Zone 3 was on the casing side of the sample. The crystalline phase identifications for each zone are shown in Table 19. All zones analyzed showed carbonation. Zone 1 was the most carbonated with 75.4 percent of crystalline phases being calcium carbonate (calcite, vaterite, and aragonite). Zone 2 retained some calcium silicate hydrate.

Table 19 XRD composition data for the cement sample collected at 9800 ft in CFU31-F2.

	Zone 1	**Zone 2**	**Zone 3**
Phase name	**Weight %**	**Weight %**	**Weight %**
Tobermorite	2.3	40	25
Quartz	18.4	25.5	24
Calcite	63	10.3	22
Aragonite	11.7	-	-
Vaterite	0.7	-	2
Zeolite UTD-1	2.2	-	-
Brownmillerite	-	5.6	13
Tilleyite	-	7	14
Srebrodolskite	1.4	2.8	-
Calcium Silicate Hydrate	-	7.3	-
Gehlenite	-	1.4	-

The second pretest was performed at depth of 9795 ft. Figure 77 shows pressure signals recorded by the quartz gauge and the strain gauge, along with the drill-bit penetration and the evolution of the pretest volume during the job. Temperature recorded by the quartz gauge and the strain gauge are also shown. Due to electrical noise, recorded data was processed to remove pressure blips. For illustration, the original uncleaned data is shown for strain gauge pressure and temperature at time interval 1400–1450 s.

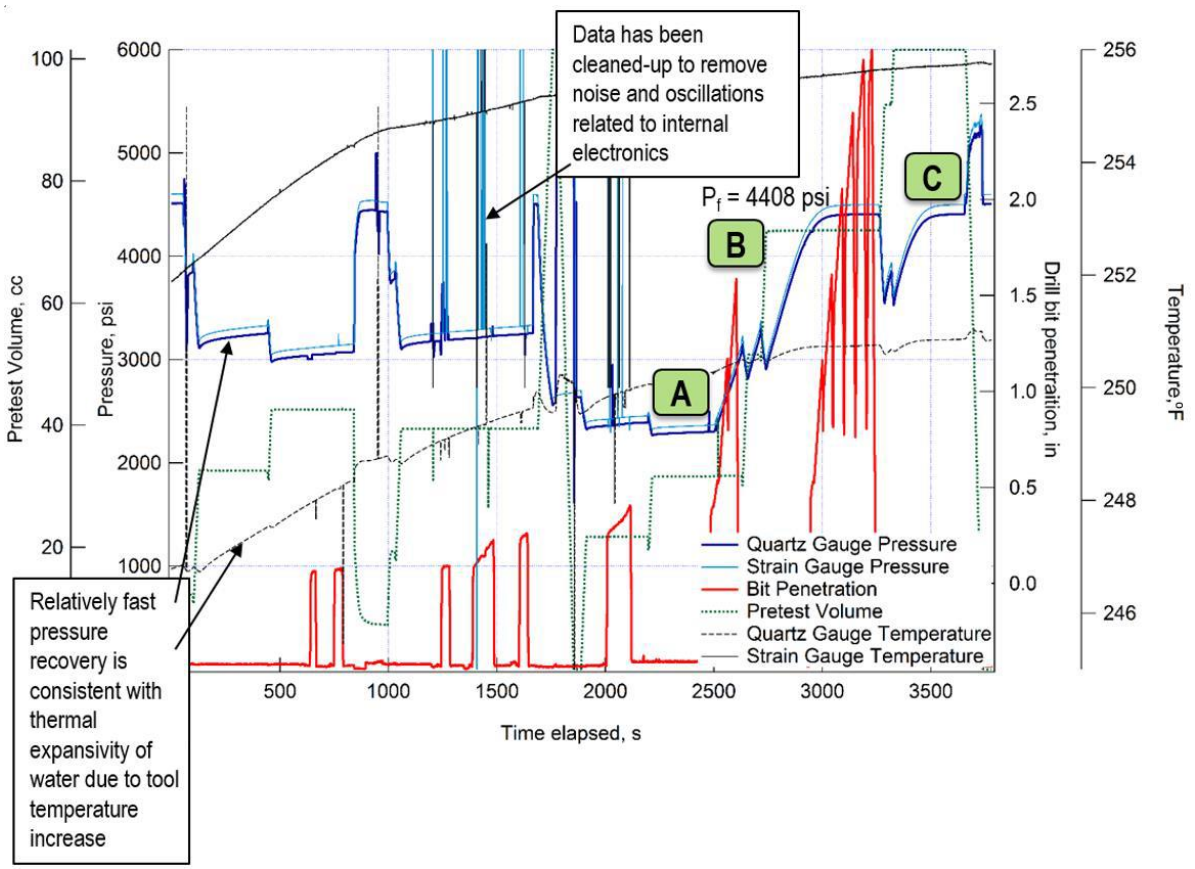

Figure 77 Pressure, drill-bit penetration, temperature, and pretest volume data from CHDT job at 9795 ft.

A packer-seal pretest was performed at 70–480 s. The observed pressure response was consistent with thermal expansion of fluid due to the temperature increase. At T = 250 ^{o}F (approximately 121 ^{o}C) and P = 3000 psi (20.68 MPa), thermal expansivity of water is $\beta = 8\text{x}10\text{-}4\ K^{-1}$, and water compressibility $c = 4.8\text{x}10\text{-}10\ Pa^{-1}$. Therefore, the expected temperature effect on isochoric pressure change is very similar to the one computed for Station 1 and is:

$$\Delta P = \beta / c = 1.6\ \text{MPa/K} \approx 129\ \text{psi/}^{o}\text{F}.$$

The CHDT drill-bit progressed to 0.4” penetration at 2100 s (Figure 78). Assuming that at this point the drill-bit exited the casing (according to the specs, casing thickness is 0.36”), we analyze the pretest that followed (Pretest A in Figure 78) to infer cement permeability according to the methods described above.

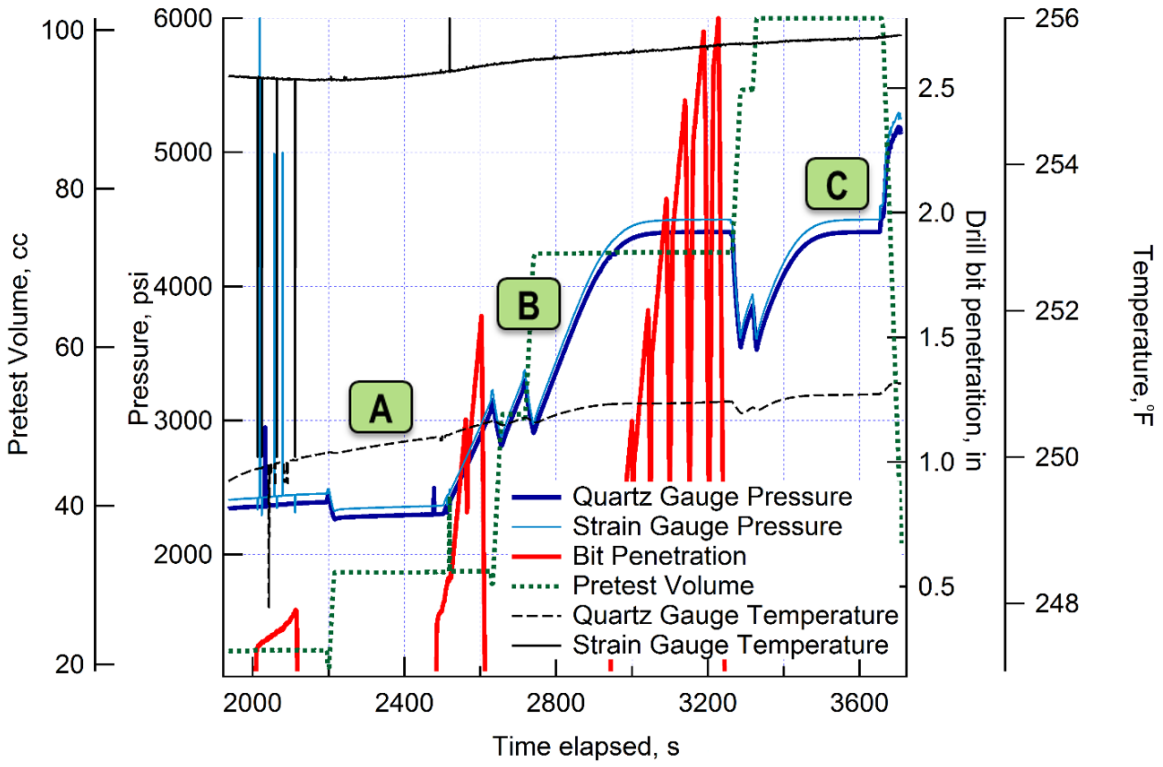

Figure 78 Analysis of data after drill-bit penetration through casing, cement, and into formation (CHDT job at 9795 ft).

Assuming centralized casing, the estimated thickness of the cemented annulus at that depth is 0.75”. However, the sudden change in pressure response around 2500 s with a drill-bit penetration of 0.52” suggests that the formation may be reached at that point or the drill-bit progressed into poor cement. This suggestion is supported by consistent pressure responses observed in Pretest B and Pretest C performed after the drill-bit penetrated into formation. If the bit progressed into formation this would also indicate that the casing is not centralized, and the thickness of cement annulus at Station 2 was only 0.16”. We analyze the pressure build-up during Pretest A after assumed drill-bit penetration into the cemented annulus (Figure 78). Based on the late time pressure analysis (after the drill-bit penetrates into formation), we estimate the formation pressure to be at 4408 psi. This estimate is also consistent with the formation pressure at Station 1 (4292 psi) for a pressure gradient of 0.45 psi/ft. Fixing the formation pressure at 4408 psi during the fit (Eq. 1), we obtain relaxation time constant at 22260 s (Figure 78).

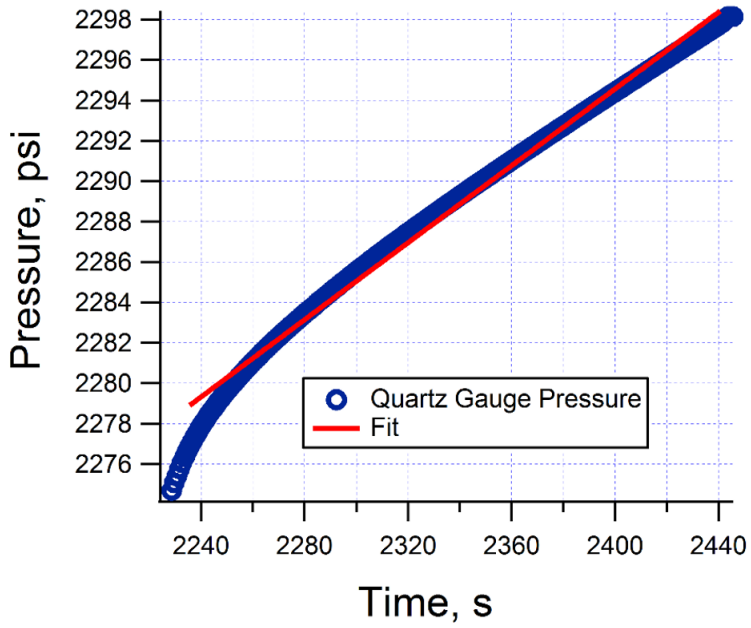

Figure 79 Analysis of pressure fit for Pretest A (Station 2 at depth 9795 ft).

Below, we provide two estimates of cement permeability given Scenario 1 (casing is centralized and cement thickness is 0.75 in) and Scenario 2 (casing is not centralized or contaminated cement is reached, and cement thickness is 0.16 in, as suggested by the pressure response in Figure 77). Viscosity of water at reservoir temperature (250 °F) is 0.00024 Pa s.

Scenario 1: Given that the drill-bit penetration into the cemented annulus is 0.04", for an assumed cement thickness of 0.75 in, we calculate the correction factor $F(rp/lc;lp/lc) = F(0.19;0.05)$ to be 0.2. Substituting these values into Eq. 2, we obtain kc = 0.1 µD, indicating a good quality of cement at this depth.

Scenario 2: Given a cement thickness is 0.16 in, rp/lc = 0.87. The assumption of the underlying model ($rp/lc \ll 1$) is not valid in this case, and the model is not applicable. However, a very slow pressure recovery (comparable with the seal test) indicates that the portion of the annulus tested provides a very good hydraulic isolation. Absence of the pressure response after assumed drill-bit penetration (around 2100 s) might also suggest that the casing at that depth is thicker than 0.4 in, and the drill-bit penetrated through casing only in the subsequent drill-sequence started at 2500 s. Indeed, pressure recovery at 2200–2400 s is consistent with thermal expansion of fluid due to the temperature increase. In this case, no pressure test data is available within cement annulus, and therefore, quantitative cement evaluation is not possible.

4.1.2.4 CFU31-F2 Log Section with little change

Not all sections of the well showed a deterioration of signal in the CBL (Figure 80) and ultrasonic image log (Figure 81). In the region between 9230 and 9304 ft both the DSLT and SCMT CBL amplitudes are around 2 to 3 mV. There is small deterioration in amplitude between 2009 and 2015 between 9282 and 9296 ft. The ultrasonic image logs also show high acoustic impedance (dark color) values in the 2009 and 2015 data over this zone. A cable is visible as a vertical low acoustic impedance (light color) feature in the 2009 and 2015 ultrasonic image logs. At this depth the average of the ratio of overall solid material (the sum of microdebonded and solid cement) to all material behind the casing decreased from 0.99 to 0.93 between 2009 and 2015 (Figure 82).

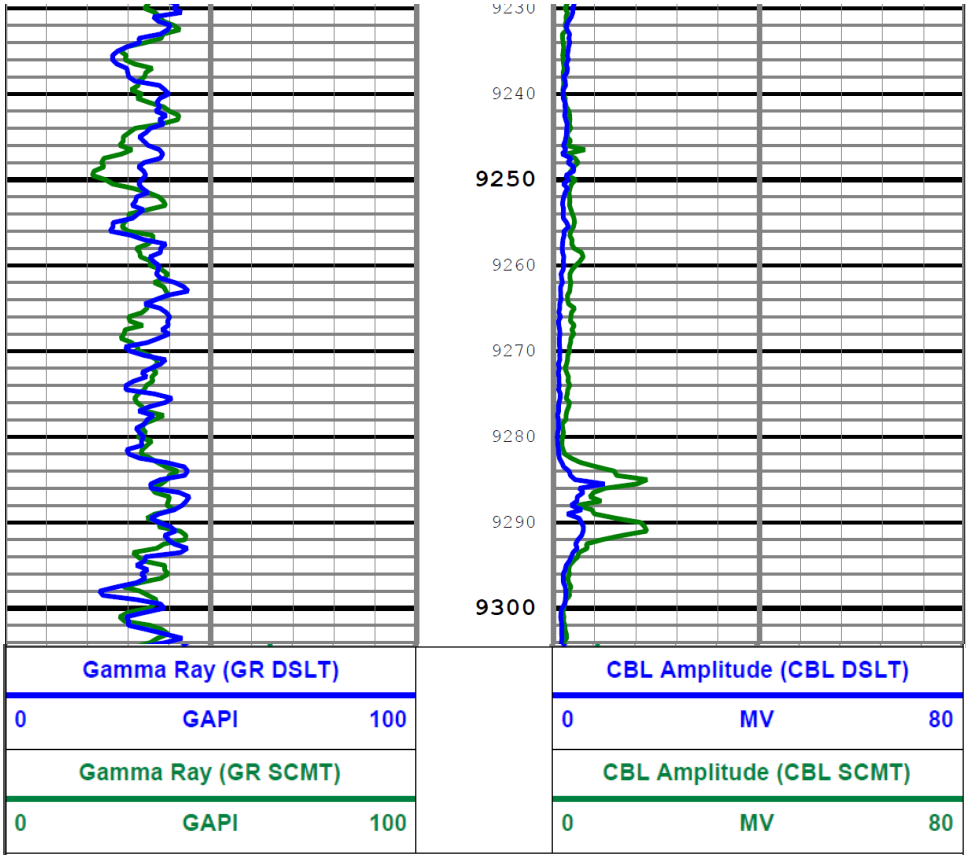

Figure 80 Comparison of CBL data between 9230 and 9304 ft collected in CFU31F-2 showing little change between 2009 and 2015.

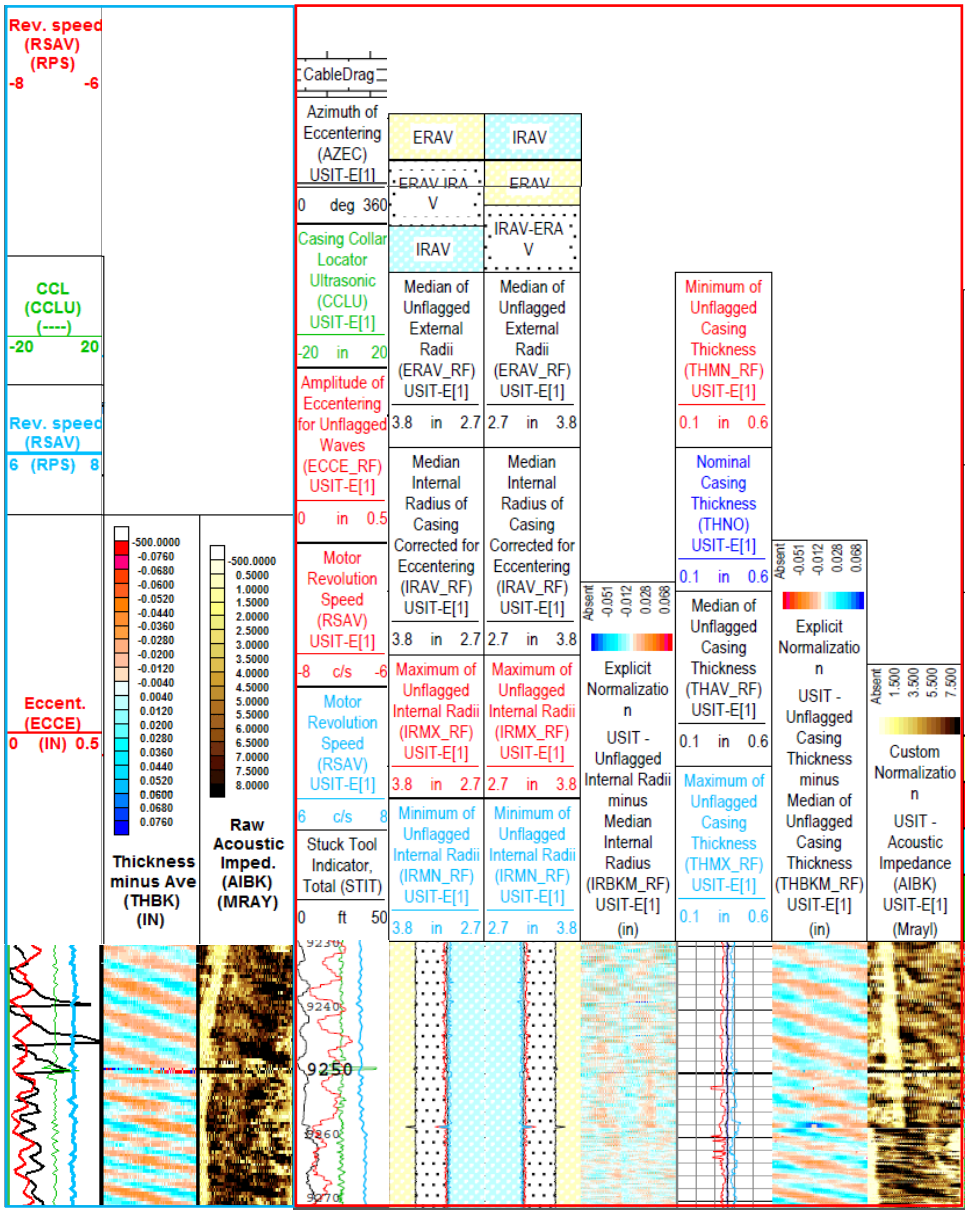

Figure 81 Comparison of ultrasonic image data between 9230 and 9270 ft collected in CFU31F-2 showing little change between 2009 and 2015. A cable is visible in both acoustic impedance tracks (2009 and 2015) as a vertical low acoustic impedance feature. Note the 2009 data are shown on the left and are outlined in blue and the 2015 data are shown on the right and are outlined in red.

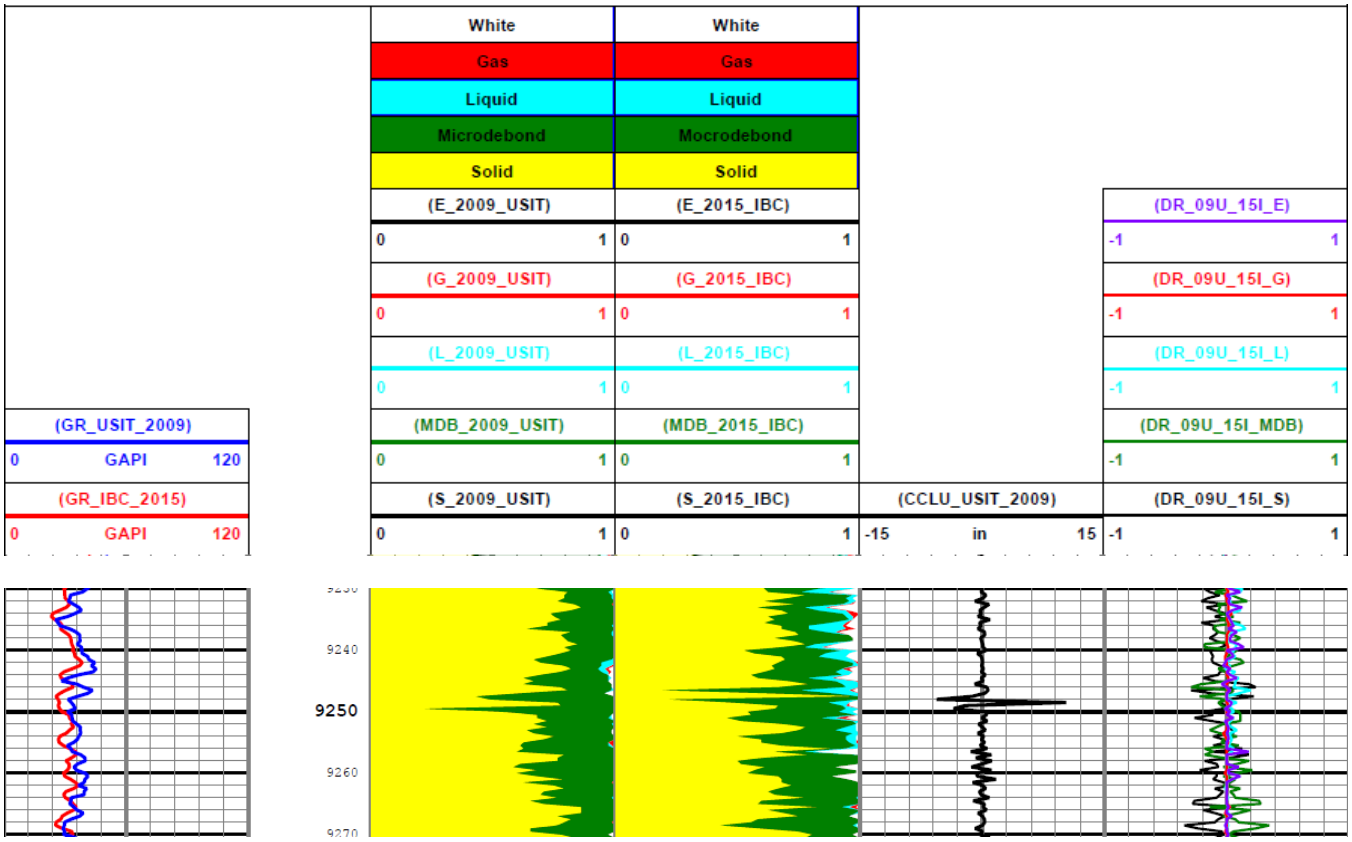

Figure 82 Comparison of ultrasonic data between 9230 and 9270 ft in CFU31F-2. Note the 2009 data are denoted with USIT and the 2015 data are denoted with IBC.

4.2 CFU31-F3

CFU31-F3 was logged using a USIT and a DSLT after construction in 2009. The USIT logs shows cement from around 8,722 ft to the bottom of the log. The CBL shows spotty areas of good bond below 9,630 ft. Table 20 summarizes the interpretation of the 2009 USIT and CBL logs. The monitoring technology attached to the outside of the casing is visible in the raw and processed acoustic impedance tracks in the 2009 ultrasonic image logs. In the Raw Acoustic Impedance track the monitoring hardware is visible as linear vertical and horizontal patterns of low acoustic impedance which translate to linear and horizontal microdebonded or fluid-filled features in the processed track.

Table 20 General log interpretation for the 2009 well integrity logs run in CFU31F-3

Depth (ft)	Well Architecture	USIT	DSLT
7470-8200	7-in 26lb Casing. Control/monitoring lines.	Low acoustic impedance in raw acoustic impedance, generally less than 2 Mrayl (Raw Acoustic Imped. Track). Generally, microdebonded cement and liquid in cement map	CBL and VDL show little bond
8200-8722	7-in 26lb Casing. Control/monitoring lines.	low values of acoustic impedance, generally less than 4 Mrayl, in raw acoustic impedance track. Solid cement, microdebonded cement and liquid in the cement map	CBL between 20 and 50 mV. few formation returns in VDL
8722-9630	7-in 26lb Casing. Control/monitoring lines.	Middle to low values of acoustic impedance, 5 Mrayl or less, in the raw acoustic impedance track. Monitoring control line(s) visible in places in the raw acoustic impedance image. Generally, microdebonded cement with some solid cements and liquids	CBL between 20 and 40 mV. Formation returns in VDL
9630-10220	7-in 26lb Casing. Control/monitoring lines, line splitter, line splice, and pressure gauge.	High to low values of acoustic impedance, 8 Mrayl or less, in the raw acoustic impedance track. Monitoring control line(s), splitter and pressure pad visible. Generally, more solid cement than microdebonded cement in the cement map with some liquid. Lines and splitters and pressure pad visible.	CBL between 4 and 20 mv, generally near 10 mV. VDL shows formation returns
10220-10618	Fiberglass casing with 14 ERT electrodes	Medium acoustic impedance in raw acoustic impedance track. Almost completely solid cement in the cement track. Control lines sometimes visible. Electrodes visible	No CBL in fiberglass. Good formation returns throughout fiberglass section in VDL

The Isolation Scanner and the USIT were used to collect new cement maps between 9600 and 10600 ft in 2015. In general, the logs run in 2015 show a deterioration of cement quality or cement bond over the cemented interval. The fiberglass casing in CFU31-F3 appears to be collapsing based in the logs collected in 2015. The USIT log (Figure 83) shows the average inner radius of the casing (IRAV) being smaller than the original specification (3.1 inches) immediately on entering the fiberglass section having a value of around 2.95 inches. The IRAV proceeds to decrease with depth to the zone where the USIT spinning sub (measurement end) got stuck. The smallest IRAV measured was around 2.8 inches at 10495 ft. Below 10495 the IRAV begins to increase reaching 3.1 inches by 10550 ft. Below 10550 the IRAV is fairly constant. Note, the constriction between 10440 and 10445 is a casing seal receptacle and does have a smaller IRAV than the surrounding casing. In comparison, the USIT log collected in 2009 (Figure 84) shows a constant IRAV throughout the fiberglass section. A comparison of the acoustic impedance values collected in 2009 and 2015 cannot be reliably created given the change in casing properties with depth in the fiberglass section. The “ringing’ of the casing between 2009 and 2015 is very likely different which would affect the values of acoustic impedance and the associated solid-liquid-gas and microdebonding image maps. Only a comparison in the steel casing at 10042 ft is presented.

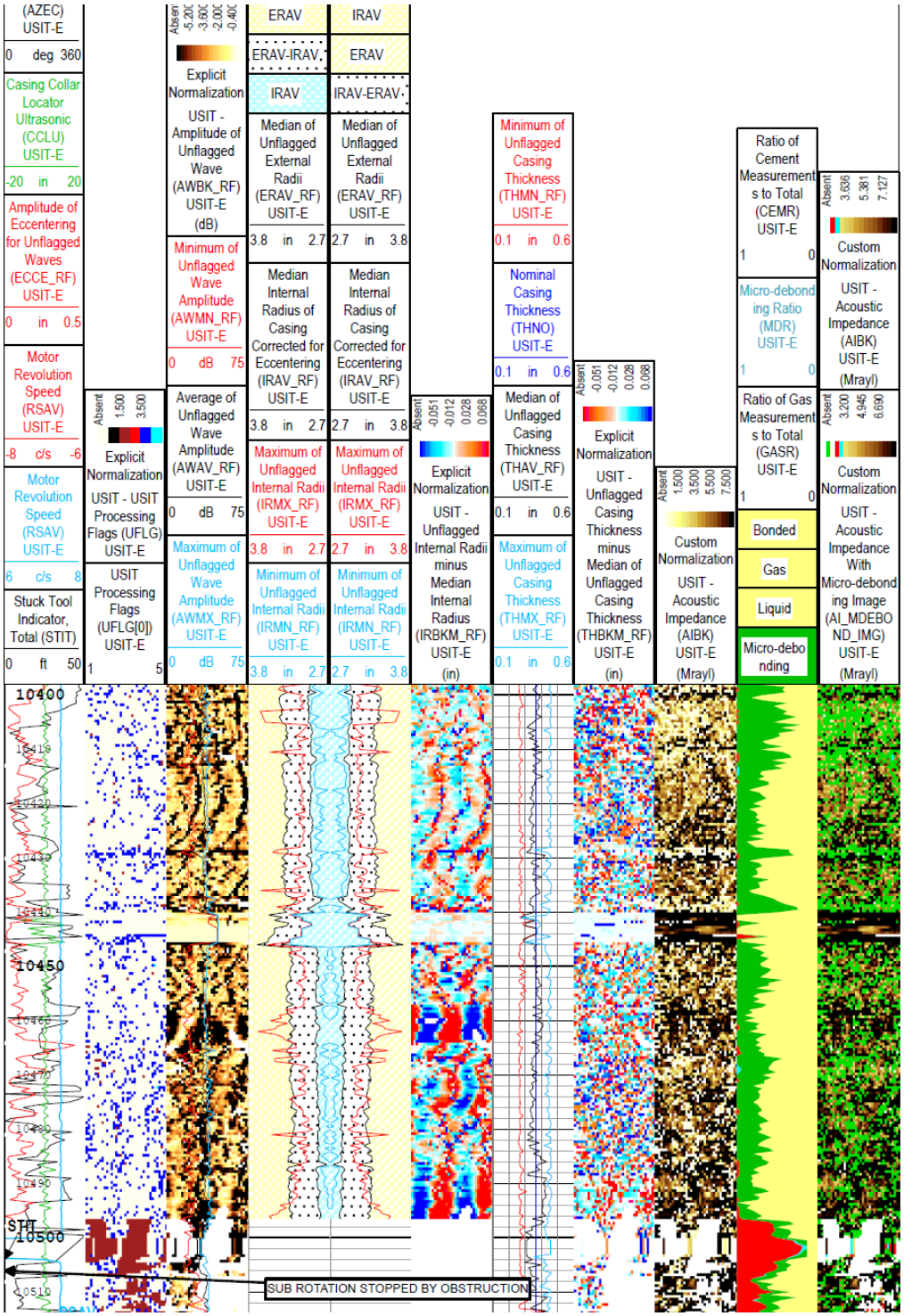

Figure 83 2105 USIT log section collected in CFU31-F3 showing the casing inner-radius (IRAV) shrinking with depth in the fourth and fifth tracks from the left. Note at a depth of 10506 the inner-radius was small enough to stop the rotation of the measurement sub on the tool.

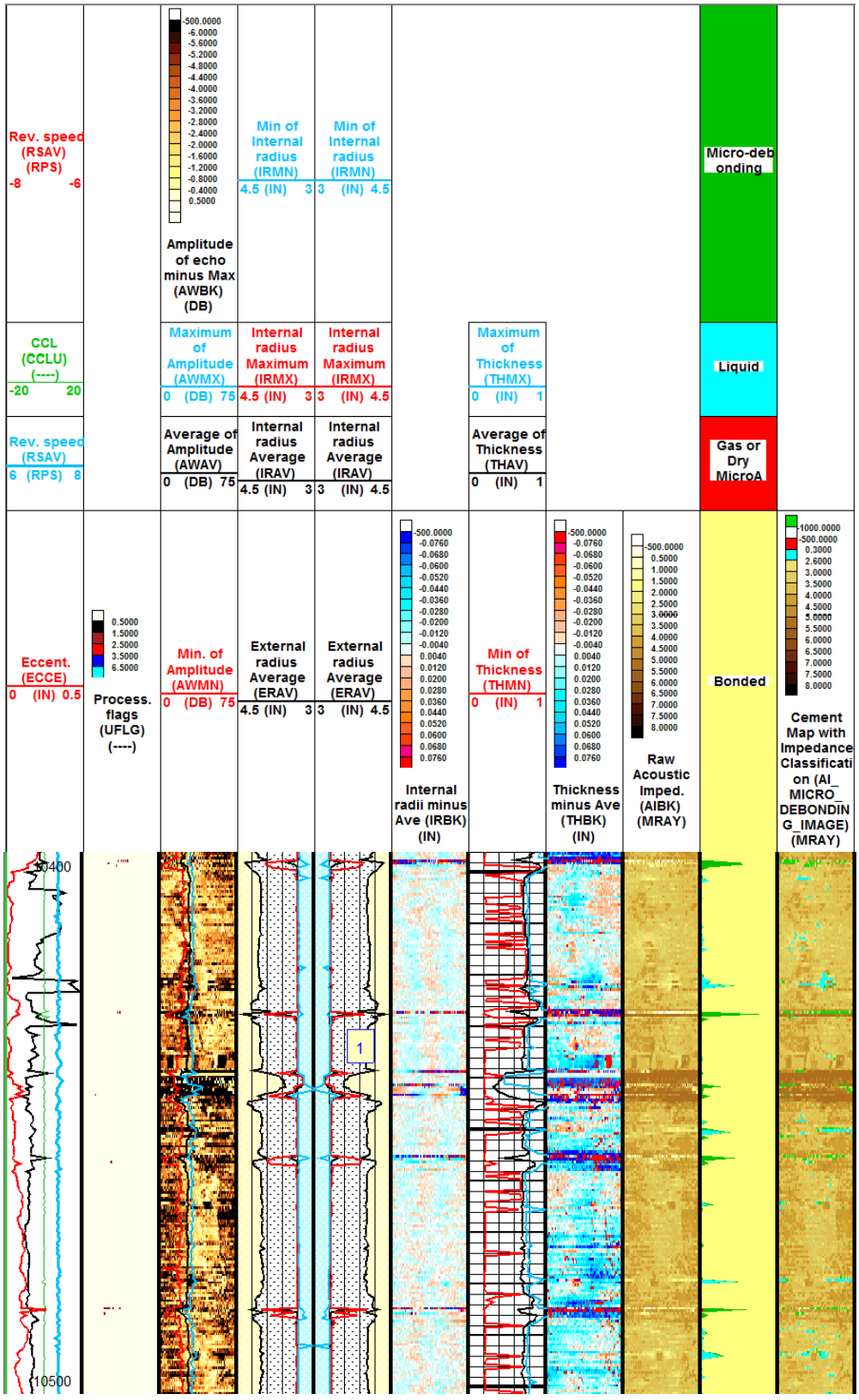

Figure 84 2105 USIT log section collected in CFU31-F3 showing little change in the casing inner-radius (IRAV) with depth.

4.2.1.1 CFU31-F3 10042 ft sidewall core sample

The MSCT tool was employed to collect a sidewall core at 10042 ft. Only casing was collected at this depth. No cement or formation was recovered. Changes in the ultrasonic image logs (USIT and Isolation Scanner) at this depth show a decrease in solid material (green and yellow) and an increase in liquid (blue) from the third track from the left and the fourth and fifth tracks from the left (Figure 85).

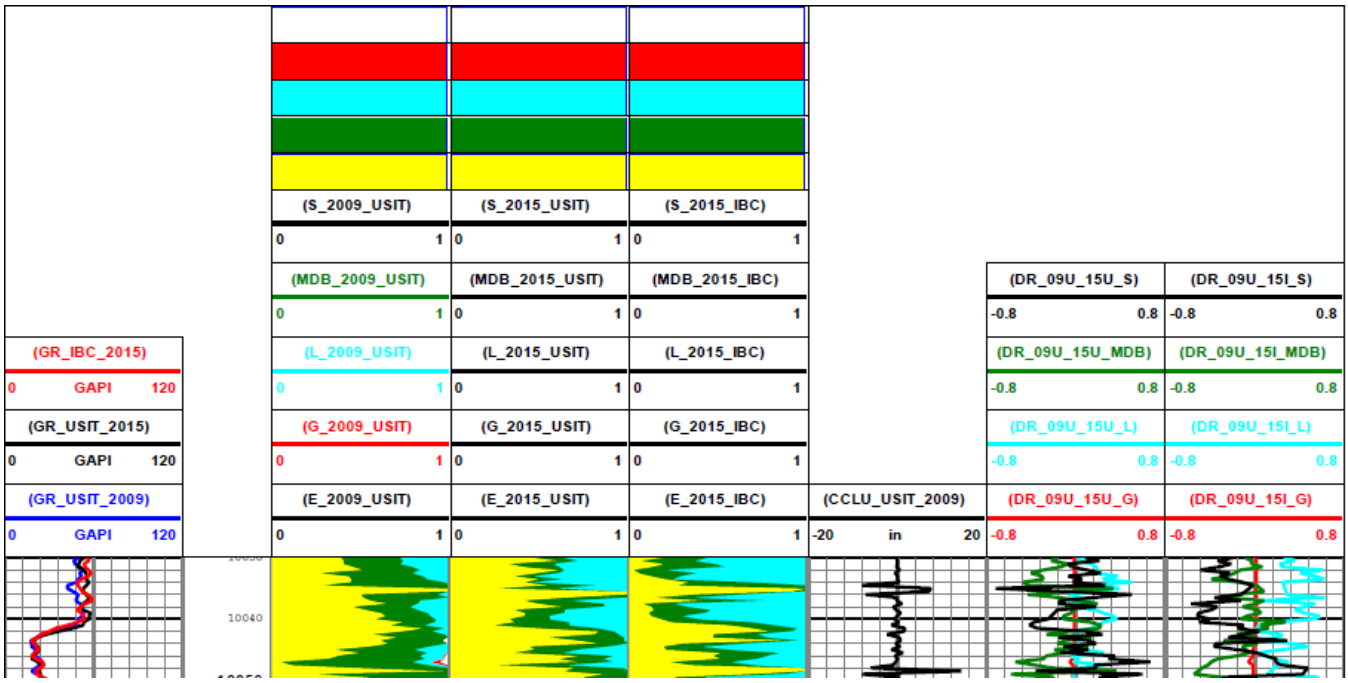

Figure 85 Ultrasonic log comparison in CFU31-F3 at 10.042 ft.

4.2.1.2 CFU31-F3 10268 ft sidewall core sample

The core collected at 10268 ft consisted of solid cement and fiberglass casing (Figure 86). The core shows both light grey and tan discoloration or reacted zones on the formation side.

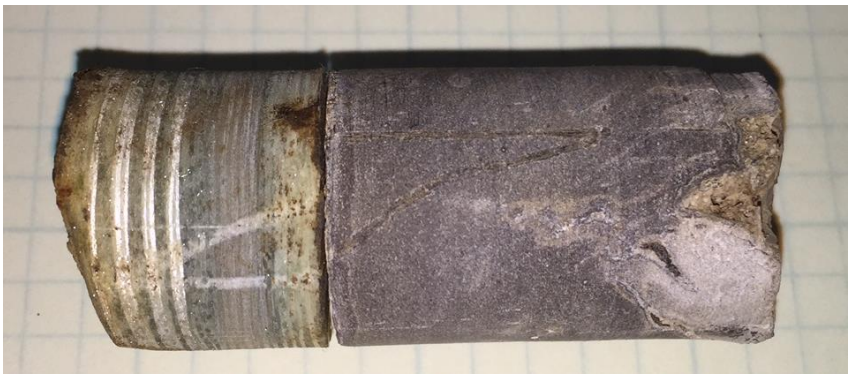

Figure 86 Sidewall core collected in CFU31-F3 at 10268 ft. Note fiberglass casing is shown on the left side of the photo.

Micro-CT images of the cement core (Figure 87) identify multiple zones within the sample that indicate changes in material or reaction fronts. These zones run at a diagonal from the formation end of the sample (bottom of the sample in lower portion of Figure 87). There also appears to one or two reaction fronts (totaling around 1-mm-depth) moving into the cement from the casing side. The CT scan of the casing (Figure 88) shows the casing to be generally uniform with a possible break in the lamination visible in the bottom views in the figure. The micro-CT scan was used to select area to cut the sample for further analyses.

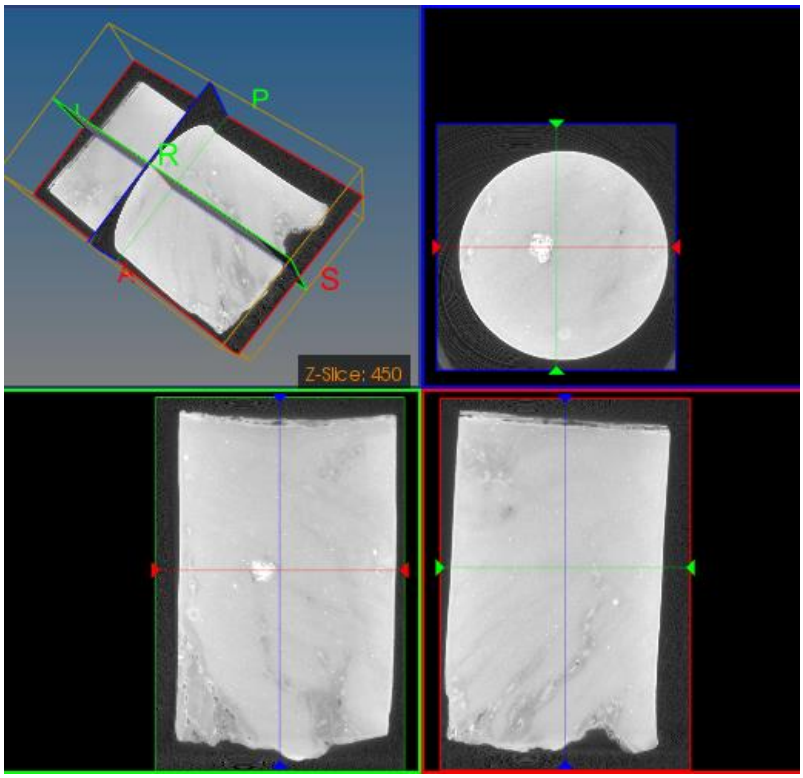

Figure 87 Micro-CT image of the cement sample collected in CFU31-F3 at 10268 ft.

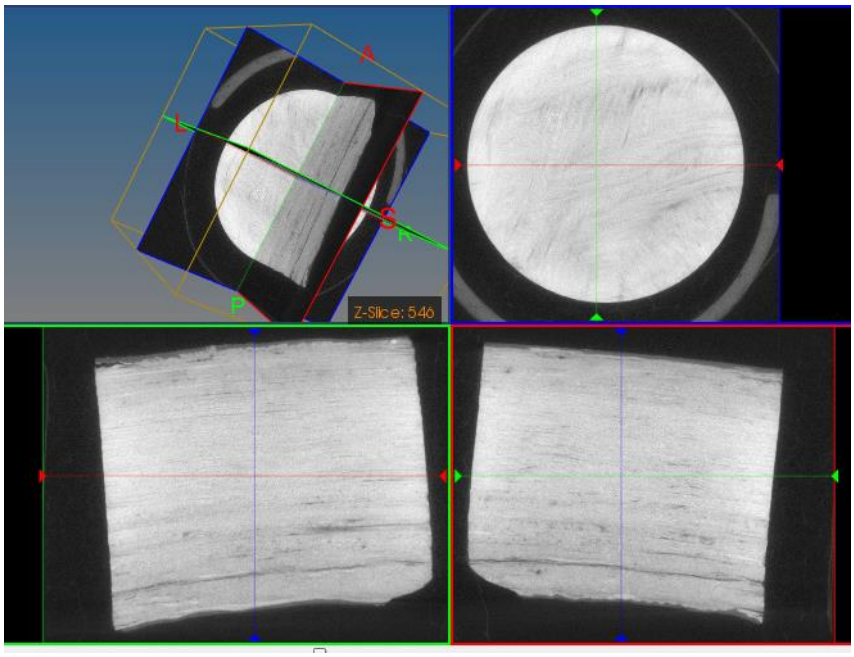

Figure 88 Micro-CT image of the fiberglass casing sample collected in CFU31-F3 at 10268 ft.

Sectioning of the sample (Figure 89) confirmed the existence of multiple diagonal (with respect to the long-axis of the sample) features that appear to be reacted zones and are lighter in color than the surrounding cement. There are also fronts on both ends of the sample. On the casing-side there is an approximately 1-mm-wide light tan front followed a 2- to 3-mm-wide light grey front. On the formation-side there is an approximately 1-mm-wide tan front.

Figure 89 Cement sidewall core collected in CFU31-F3 at 102680 ft.

Portions of the sectioned sample were polished for ESEM imaging and EDS analysis (Figure 90). EDS analyses were conducted on the outer reacted zone of the sample on the formation side (Figure 91). The EDS analyses (Table 21) indicate atomic percentages for calcium are between 15.44 and 24.90 for the points selected and atomic percentages for silica are between 7.10 and 19.49. The Ca/Si ratios ranged between 0.74 and 2.70. Note the points with low Ca/Si ratios (0.74 and 0.79) are high in aluminum indicating areas where tricalcium aluminate was high in the initial cement powder.

Figure 90 Portion of cement collected in CFU31-F3 at 10268 ft used for ESEM and EDS analysis.

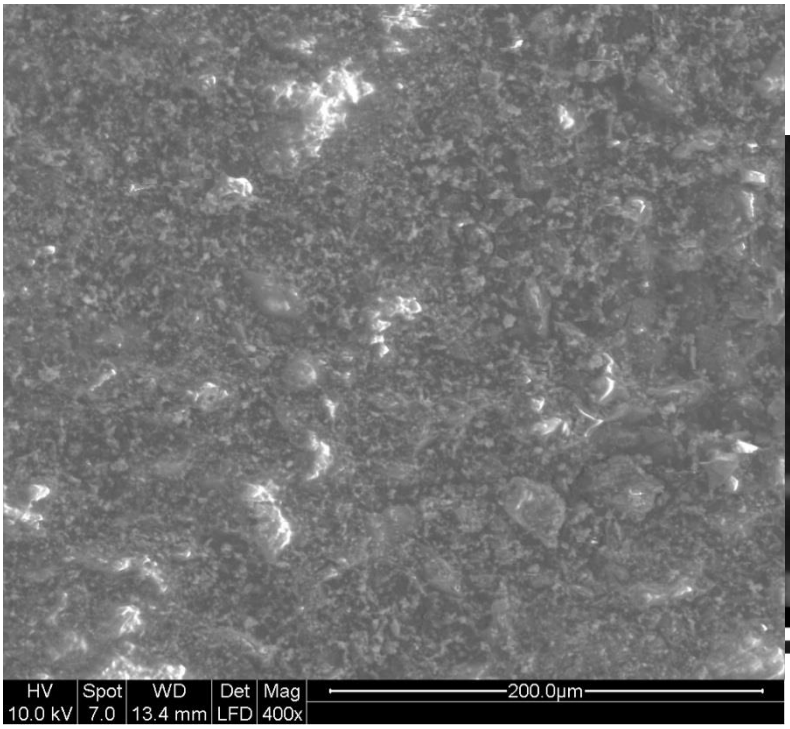

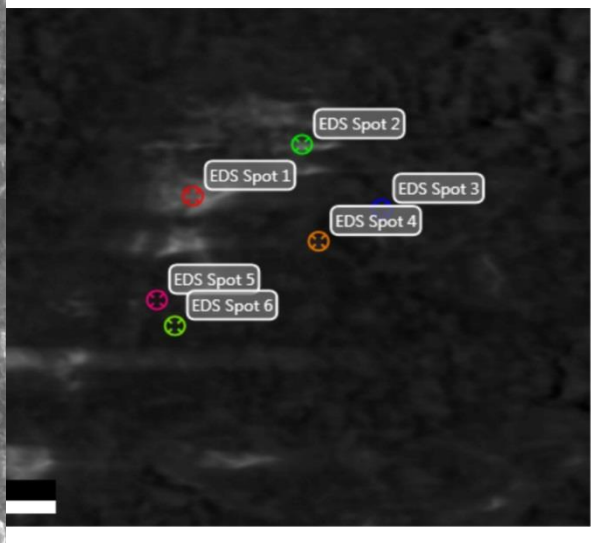

Figure 91 ESEM image collected on the formation side of the sample collected at 10268 ft (Left) and corresponding EDS points (Right).

Table 21 EDS data corresponding to the points shown in Figure 91.

	EDS1	EDS2	EDS3	EDS4	EDS5	EDS6
Element	Atom %	Atom %	Atom %	Atom %	Atom %	Atom %
O K	68.45	62.26	52.98	58.86	59.94	62.81
SiK	7.10	11.67	16.05	19.49	11.35	17.20
NaK	1.67	2.58	0.52	-	1.40	1.07
ClK	0.92	1.89	1.66	2.27	1.18	2.03
MgK	1.03	-	1.89	2.91	0.50	3.02
AlK	1.67	3.20	1.99	1.04	1.63	1.20
CaK	19.17	18.41	24.90	15.44	23.47	12.66
Mo L	-	-	-	-	0.53	-

	Ratio	Ratio	Ratio	Ratio	Ratio	Ratio
Ca/Si	2.70	1.58	1.55	0.79	2.07	0.74

EDS analysis was conducted in the light grey zone (Figure 92) adjacent to the tan zone on the formation side of the sample. The atomic percentages ranged from 14.45 to 19.19 for calcium and 11.15 to 17.26 for silicon. The Ca/Si ranged between 1.07 to 1.32.

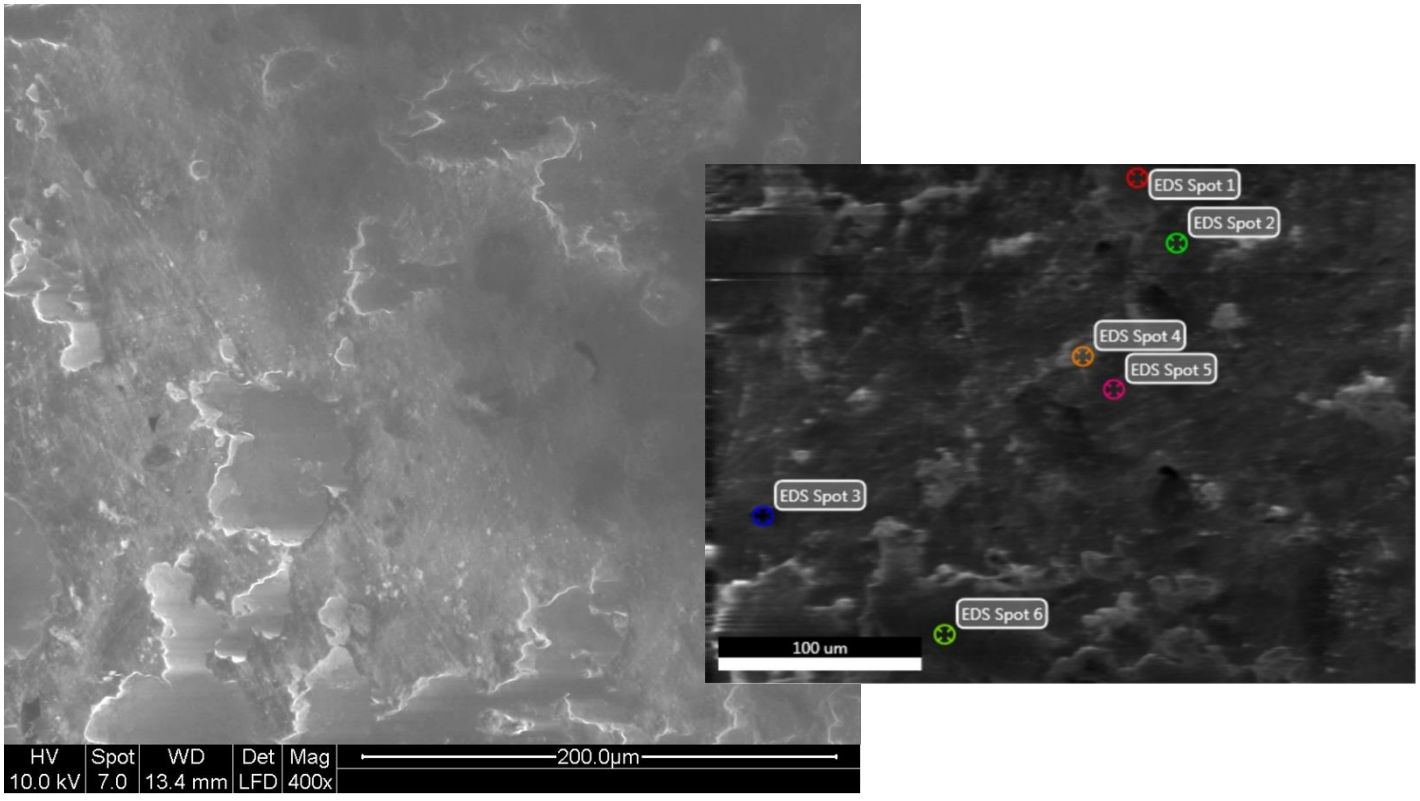

Figure 92 ESEM image collected in the light grey zone near the tan front on the formation-side of the sample collected at 10268 ft (Left) and corresponding EDS points (Right).

Table 22 EDS data corresponding to the points shown in Figure 92.

	EDS1	EDS2	EDS3	EDS4	EDS5	EDS6
Element	Atom %	Atom %	Atom %	Atom %	Atom %	Atom %
O K	60.88	66.37	64.32	64.79	66.82	62.40
SiK	16.42	11.15	17.26	14.30	11.39	16.09
NaK	-	1.51	-	1.51	1.77	-
ClK	0.92	1.21	-	1.21	1.08	-
MgK	1.56	1.18	-	-	-	-
AlK	1.41	3.81	-	2.15	4.50	2.32
CaK	18.81	14.76	18.43	16.05	14.45	19.19

	Ratio	Ratio	Ratio	Ratio	Ratio	Ratio
Ca/Si	1.15	1.32	1.07	1.12	1.27	1.19

EDS conducted on the center of the sample (Figure 93 and Table 23). The calcium atomic percentages range between 10.47 and 20.40. The silica atomic percentages range between 4.64 and 15.53 percent. The Ca/Si ratios ranged between 0.98 and 3.68. The data collected can be divided into two groups based on Ca/Si. One group (EDS 1-5 and 11) have Ca/Si between 0.98 and 1.41 and the other group (EDS 6-10) have Ca/Si between 2.05 and 3.68.

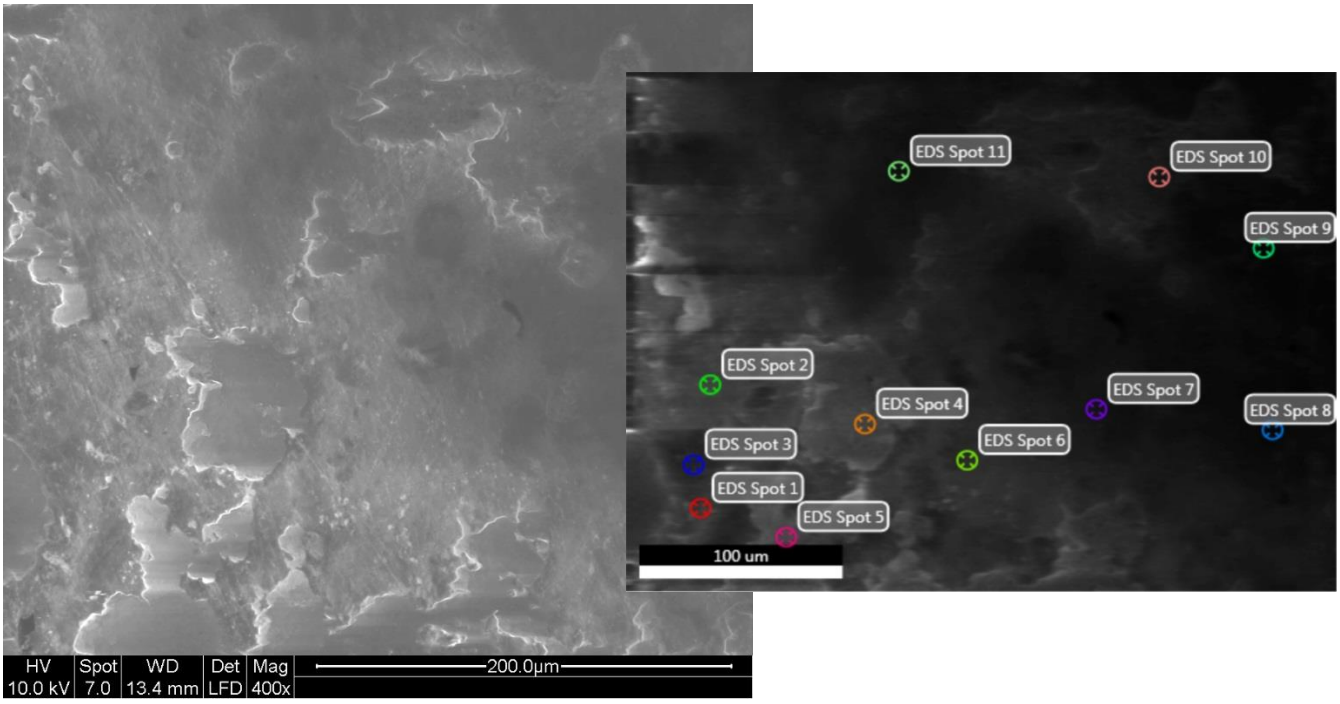

Figure 93 ESEM image collected in the center of the sample collected at 10268 ft (Left) and corresponding EDS points (Right).

Table 23 EDS data corresponding to the points shown in Figure 92.

	EDS1	EDS2	EDS3	EDS4	EDS5	EDS6	EDS7	EDS8	EDS9	EDS10	EDS11
Element	Atom %	Atom %	Atom %	Atom %	Atom %	Atom %	Atom %	Atom %	Atom %	Atom %	Atom %
O	60.38	65.60	66.59	58.55	60.33	69.08	59.63	67.69	61.05	70.18	64.00
Si	14.54	15.53	10.66	14.22	11.66	7.15	8.99	6.82	6.91	4.64	14.14
Na	2.56	1.73	-	2.67	1.77	1.60	-	-	-	-	-
Cl	2.34	1.75	1.66	2.57	1.80	1.11	5.22	1.52	4.31	1.59	2.10
Mg	0.92	-	9.00	-	-	-	-	-	1.34	-	-
Al	1.45	-	1.61	1.94	8.01	1.59	-	-	-	4.97	0.79
Ca	17.81	15.39	10.47	20.06	16.43	18.75	18.40	20.40	17.57	17.08	15.87
S	-	-	-	-	-	0.72	-	-	-	-	-

	Ratio	Ratio	Ratio	Ratio	Ratio	Ratio	Ratio	Ratio	Ratio	Ratio	Ratio
Ca/Si	1.22	0.99	0.98	1.41	1.41	2.62	2.05	2.99	2.54	3.68	1.12

EDS conducted on front at the casing-side of the sample (Figure 94 and Table 24). The calcium atomic percentages range between 4.15 and 22.07. The silica atomic percentages range between 2.29 and 16.17. The Ca/Si ratios ranged between 0.51 and 2.85. Three EDS points exhibited carbon with atomic percentage between 8.53 and 21.63.

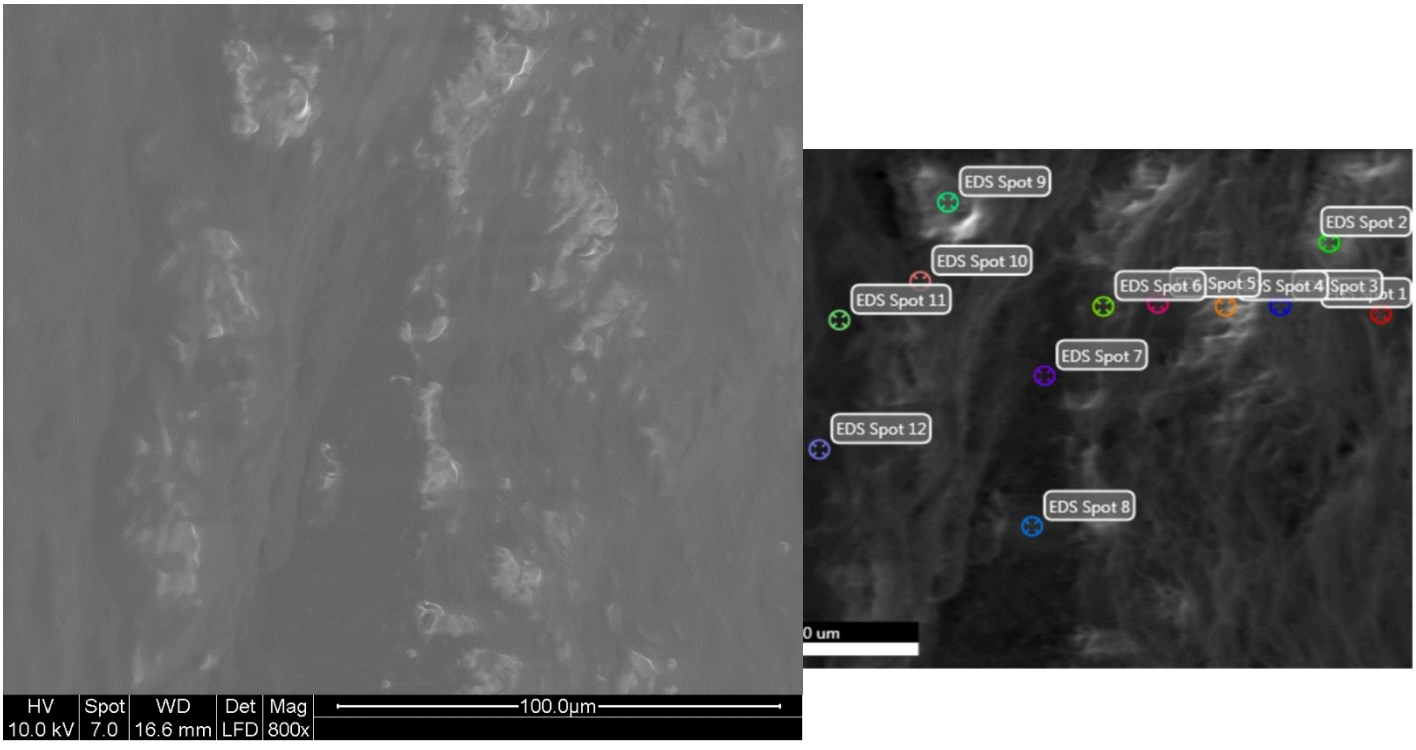

Figure 94 ESEM image collected at the casing-side edge of the sample collected at 10268 ft (Left) and corresponding EDS points (Right).

Table 24 EDS data corresponding to the points shown in Figure 94.

	EDS1	EDS2	EDS3	EDS4	EDS5	EDS6	EDS7	EDS8	EDS9	EDS10	EDS11	EDS12
Element	Atom %	Atom %	Atom %	Atom %	Atom %	Atom %	Atom %	Atom %	Atom %	Atom %	Atom %	Atom %
C	21.63	-	-	9.60	-	8.53	-	-	-	10.71	-	-
O	57.77	70.39	70.95	49.92	60.54	67.89	66.78	69.47	69.47	67.01	69.62	62.16
Si	5.27	12.91	12.09	16.17	8.19	2.29	6.55	10.63	10.63	4.34	6.32	2.64
Na	1.11	-	-	-	-	-	-	-	-	1.35	1.19	-
Cl	-	-	-	-	-	-	-	-	-	-	0.91	-
Mg	0.79	-	-	-	-	-	-	-	-	-	-	-
Al	3.94	1.00	2.11	2.24	27.13	4.49	19.27	6.95	6.95	4.24	12.13	28.97
Ca	9.48	15.70	14.85	22.07	4.15	16.81	7.40	12.95	12.95	12.35	9.82	6.23
	Ratio	Ratio	Ratio	Ratio	Ratio	Ratio	Ratio	Ratio	Ratio	Ratio	Ratio	Ratio
Ca/Si	1.80	1.22	1.23	1.36	0.51	7.34	1.13	1.22	1.22	2.85	1.55	2.36

LA-ICP-MS was conducted on the sectioned sidewall core starting on the formation side and moving toward the casing side of the sample. The LA-ICP-MS scan line images and corresponding data are presented in Figure 95 through Figure 116. The first line (Figure 95 and Figure 96) shows the ratios can be divided into four sections: The outer tan reacted layer, the white reacted layer, a dark grey zone, and a white zone that is part of the diagonal white zones throughout the sample. The tan zone runs between the edge of the sample and extends to around 600 microns into the sample. The Ca/Si for this zone shows peaks with values between, approximately, 0.8 and 1.75. The white layer extends from the end of the tan layer to around 2,700 microns into the sample. The Ca/Si in this zone is generally flat with a value around 0.98. The third, dark grey, cement zone runs between the end of the white front and around 4,300 microns. The Ca/Si in this zone rises from near 1 to around 7.7 before dropping to around 1.8. The last zone on the line, a diagonal white zone, runs from the end of the grey zone to the end of the line. The Ca/Si in this zone drops from around to 1.8 to around 0.75. Lines 2 through 6 (Figure 97 through Figure 104) are generally flat as they move toward the casing side of the sample with Ca/Si values around 0.9 in the white zones and Ca/Si around 1.6 in the grey zones. Line 7 (Figure 105 and Figure 106) show the lines that lead to the casing-side edge of the sample and corresponding plots. The plots show the Ca/Si lowers from around 1.5 to around 1 at around 1250 microns when it encounters a light grey zone. In the light grey zone the Ca/Si rises back up to 1.5 and the slowly drops to around 1.2 around 2,700 microns where it reaches a light grey front. In the light grey front the Ca/Si is generally between 1 and 1.2 until around 3,700 microns. At 3,700 microns there is a light tan front on the edge of the sample that has a Ca/Si peak that rises to around 7.24 at 3,955 microns and drops off to 1.04 at 4,039 microns. The Ca/Si starts to rise again at the end of the line. Line 8 (Figure 107 and Figure 108) is a similar scan but it does not include the first light grey zone encountered in Line 7. Lines 9 through 11 (Figure 109 through Figure 114) show similar behavior to data described above but were collected perpendicular to the long axis of the sample near the formation side.

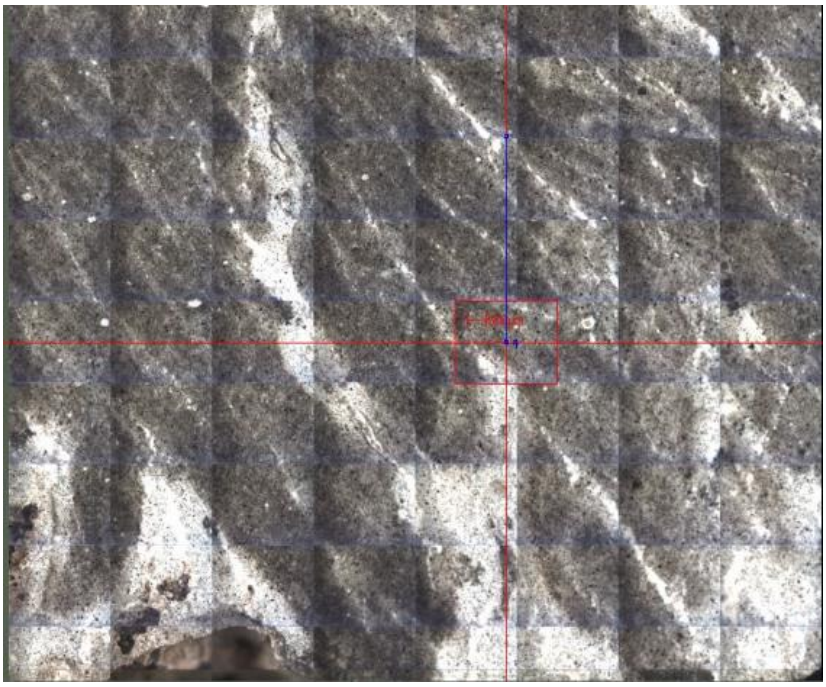

Figure 95 LA-ICP-MS Line 1, 2, and 3 across sample collected in CFU31-F3 at 10268 ft.

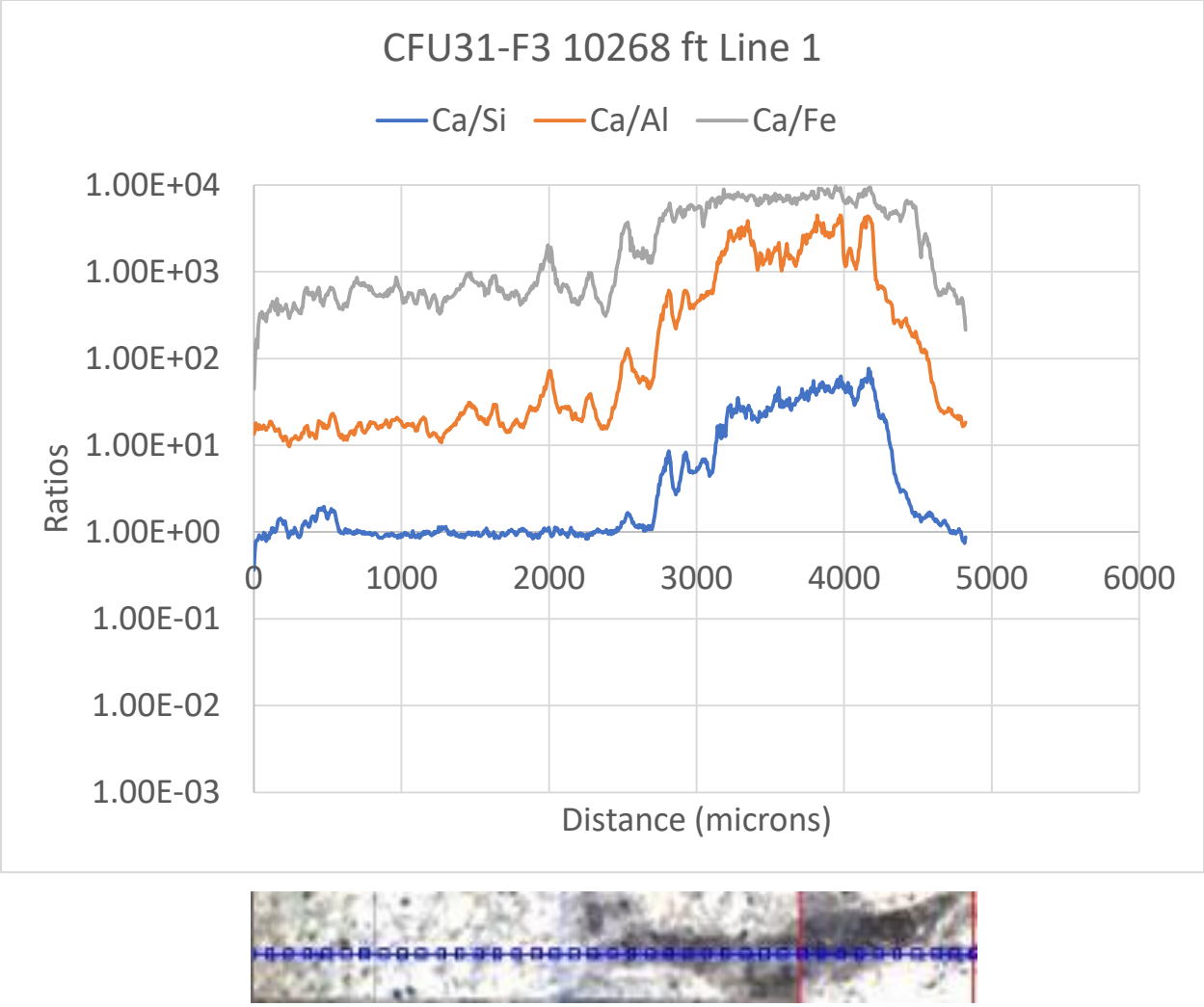

Figure 96 LA-ICP-MS Line 1 results across the sample collected in CFU31-F3 at 10268 ft showing Ca/Si, Ca/Al, and Ca/Fe mole ratios.

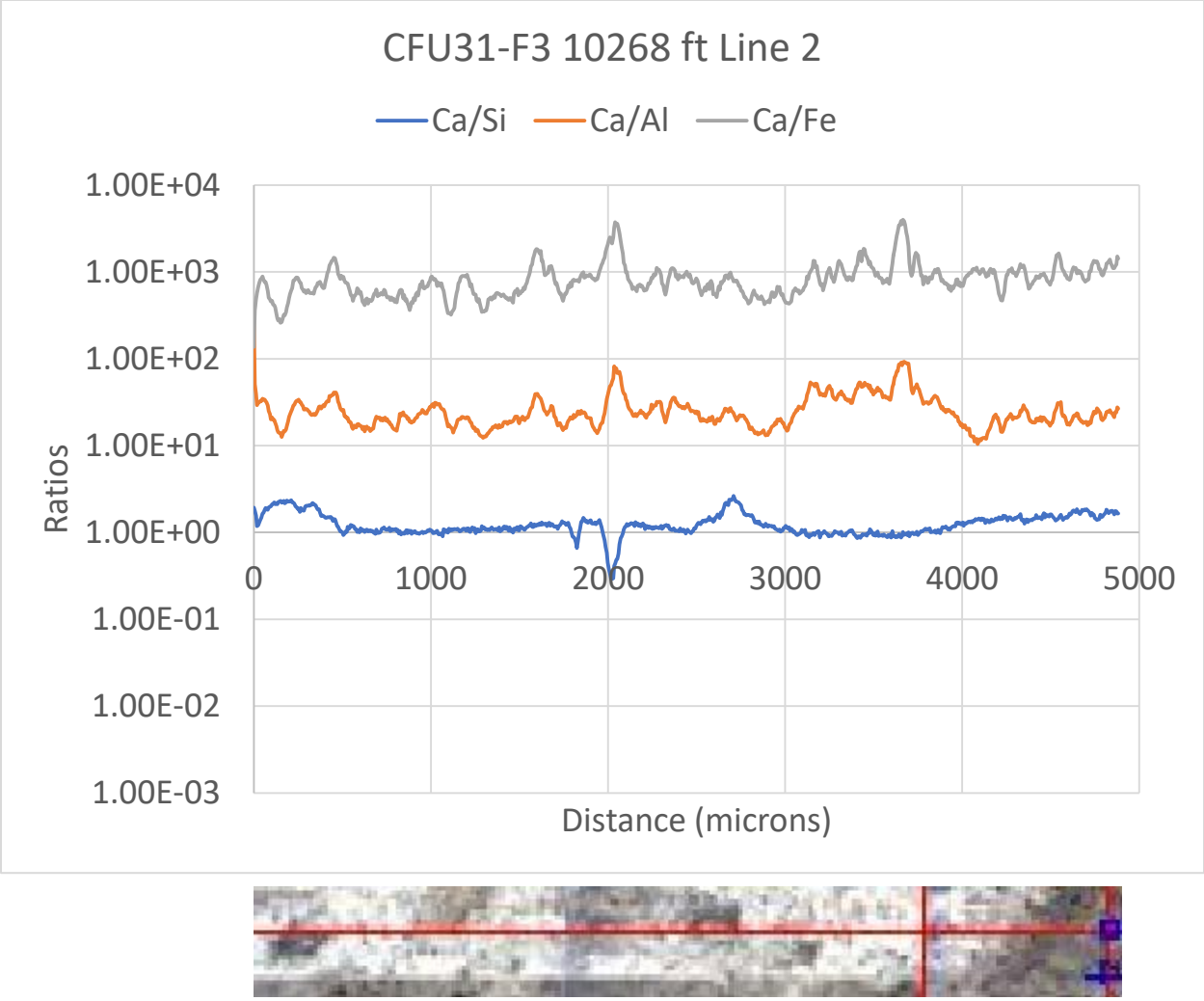

Figure 97 LA-ICP-MS Line 2 results across the sample collected in CFU31-F3 at 10268 ft showing Ca/Si, Ca/Al, and Ca/Fe mole ratios.

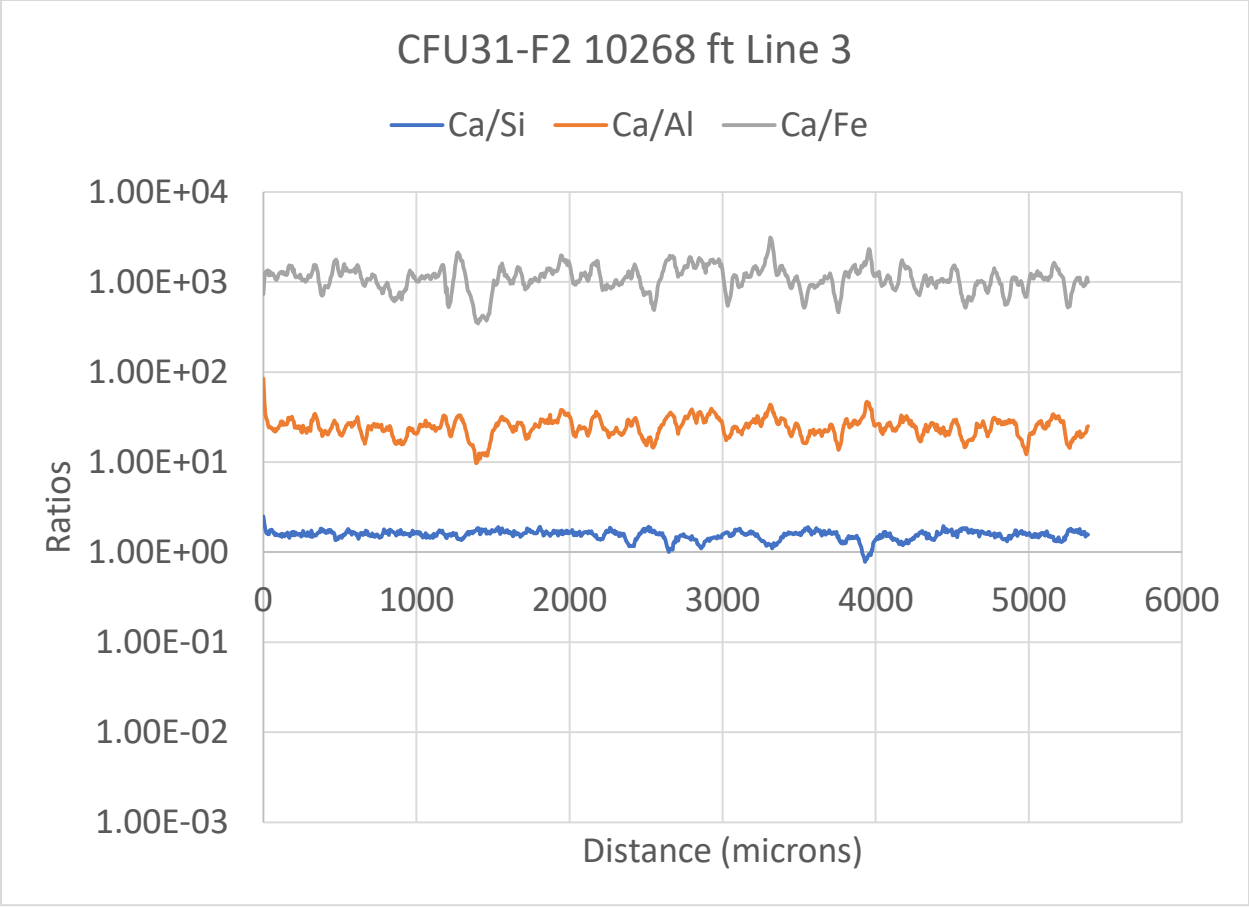

Figure 98 LA-ICP-MS Line 3 results across the sample collected in CFU31-F3 at 10268 ft showing Ca/Si, Ca/Al, and Ca/Fe mole ratios.

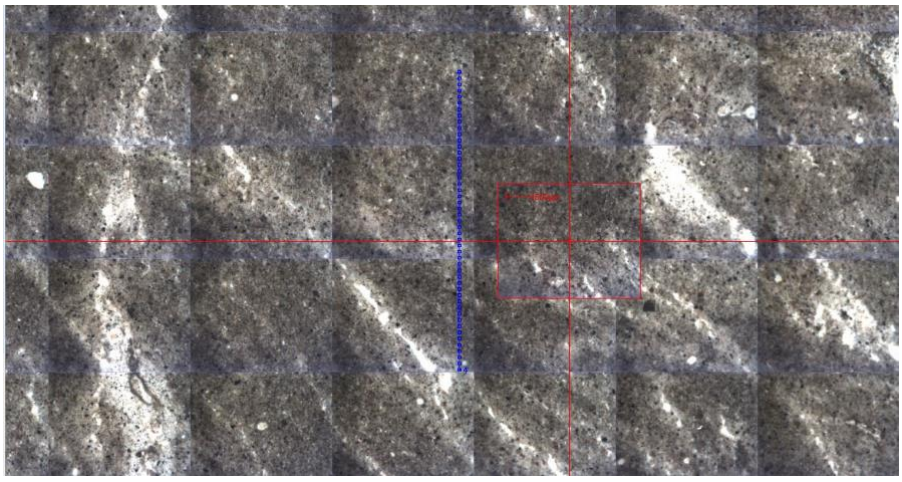

Figure 99 LA-ICP-MS Line 4 across the sample collected in CFU31-F3 at 10268 ft.

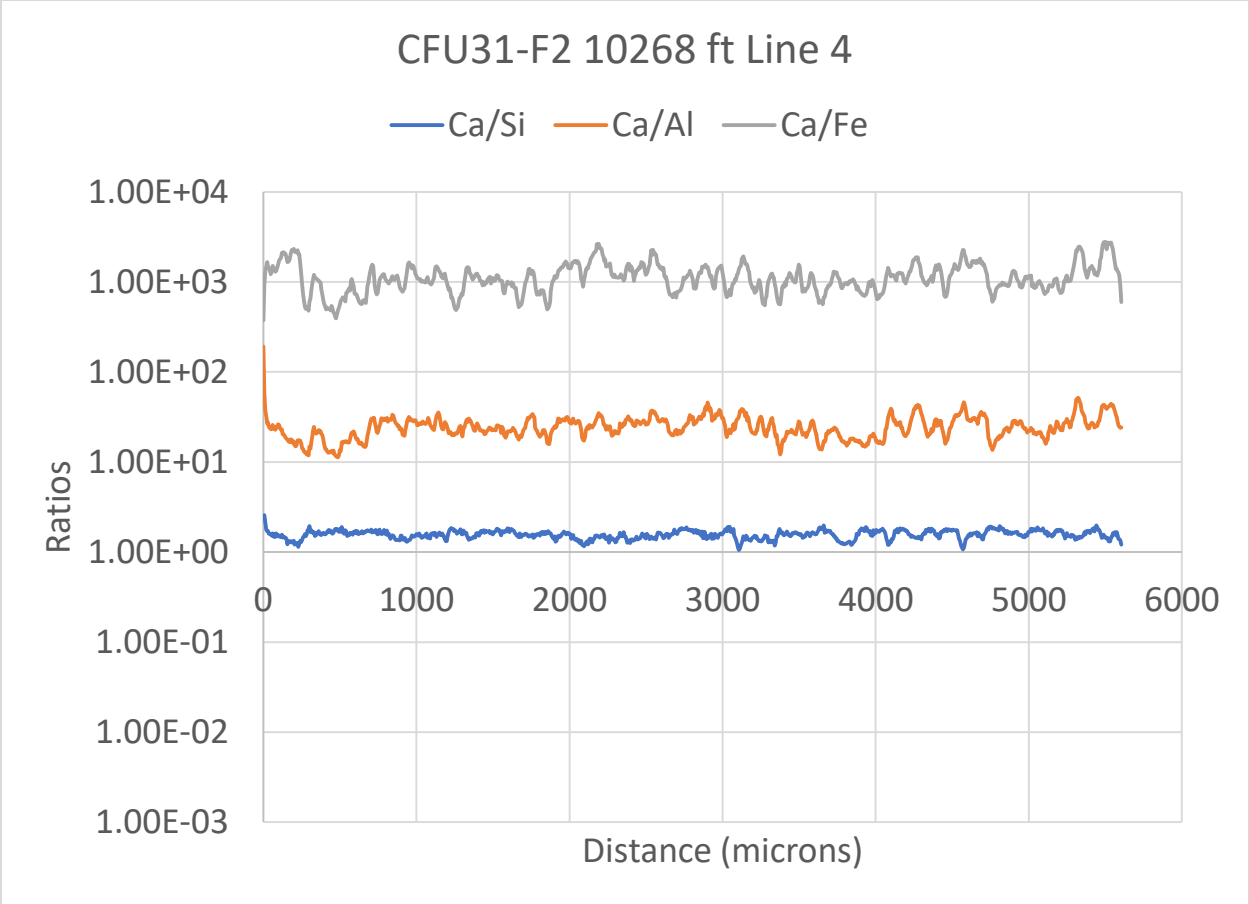

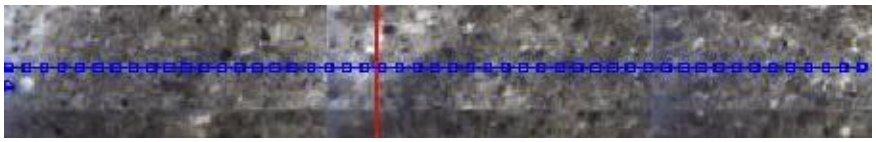

Figure 100 LA-ICP-MS Line 4 results across the sample collected in CFU31-F3 at 10268 ft showing Ca/Si, Ca/Al, and Ca/Fe mole ratios.

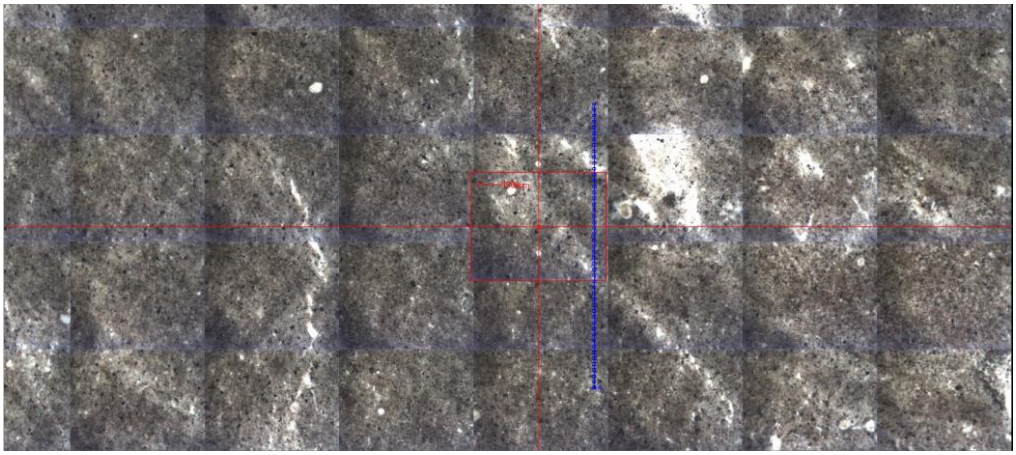

Figure 101 LA-ICP-MS Line 5 across the sample collected in CFU31-F3 at 10268 ft.

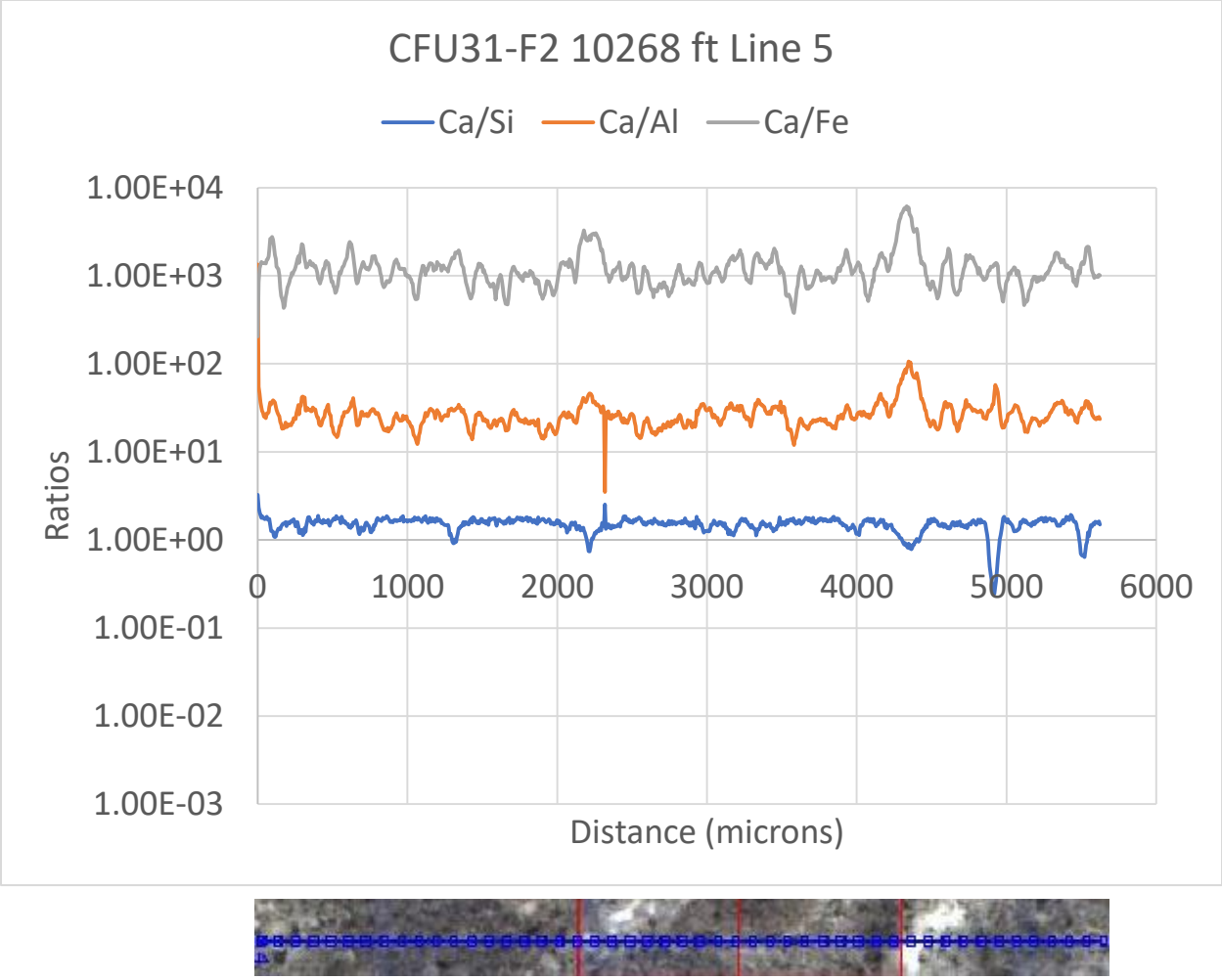

Figure 102 LA-ICP-MS Line 5 results across the sample collected in CFU31-F3 at 10268 ft showing Ca/Si, Ca/Al, and Ca/Fe mole ratios.

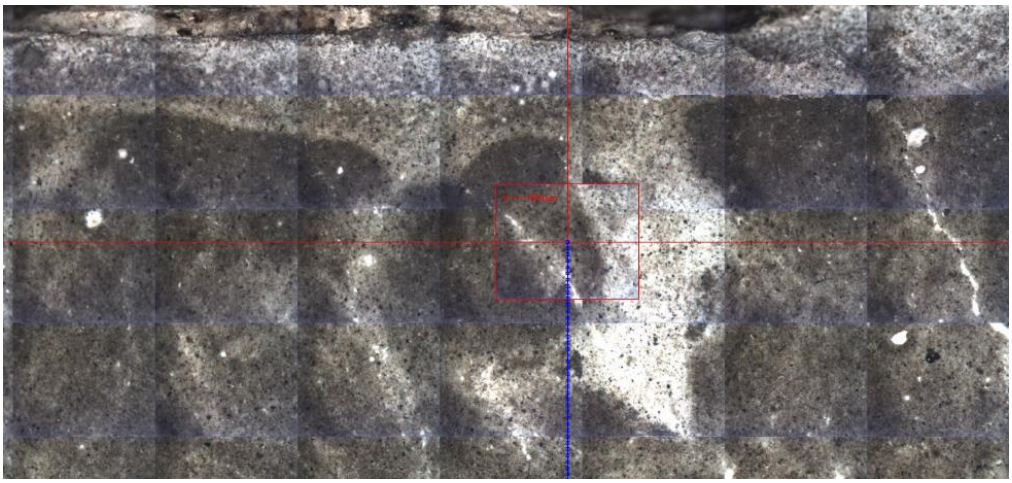

Figure 103 LA-ICP-MS Line 6 across the sample collected in CFU31-F3 at 10268 ft.

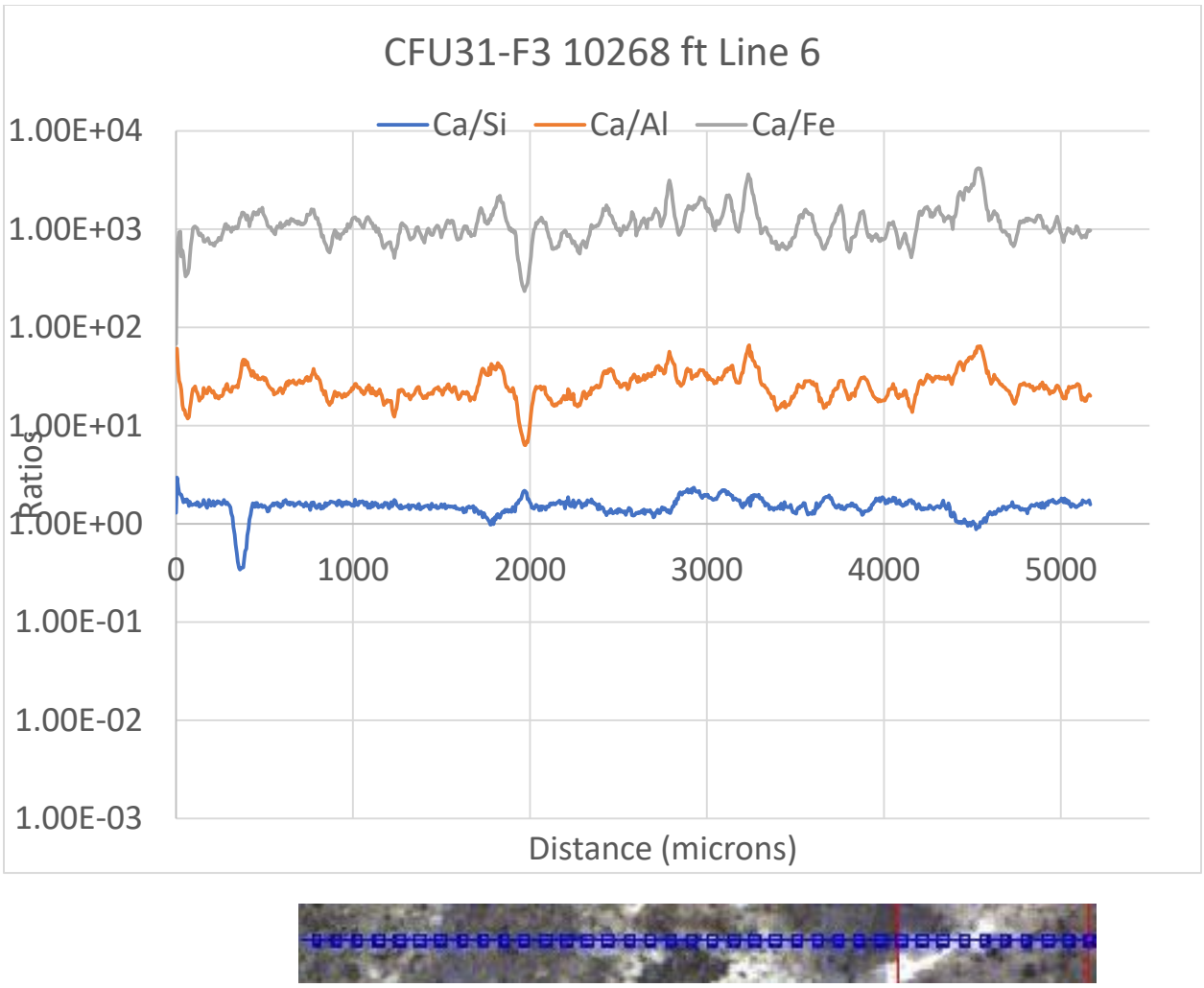

Figure 104 LA-ICP-MS Line 6 results across the sample collected in CFU31-F3 at 10268 ft showing Ca/Si, Ca/Al, and Ca/Fe mole ratios.

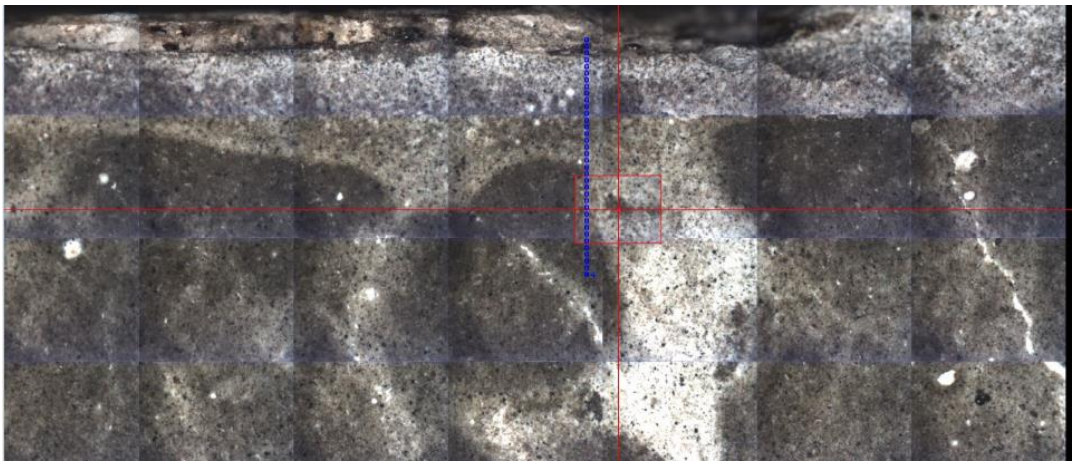

Figure 105 LA-ICP-MS Line 7 across the sample collected in CFU31-F3 at 10268 ft.

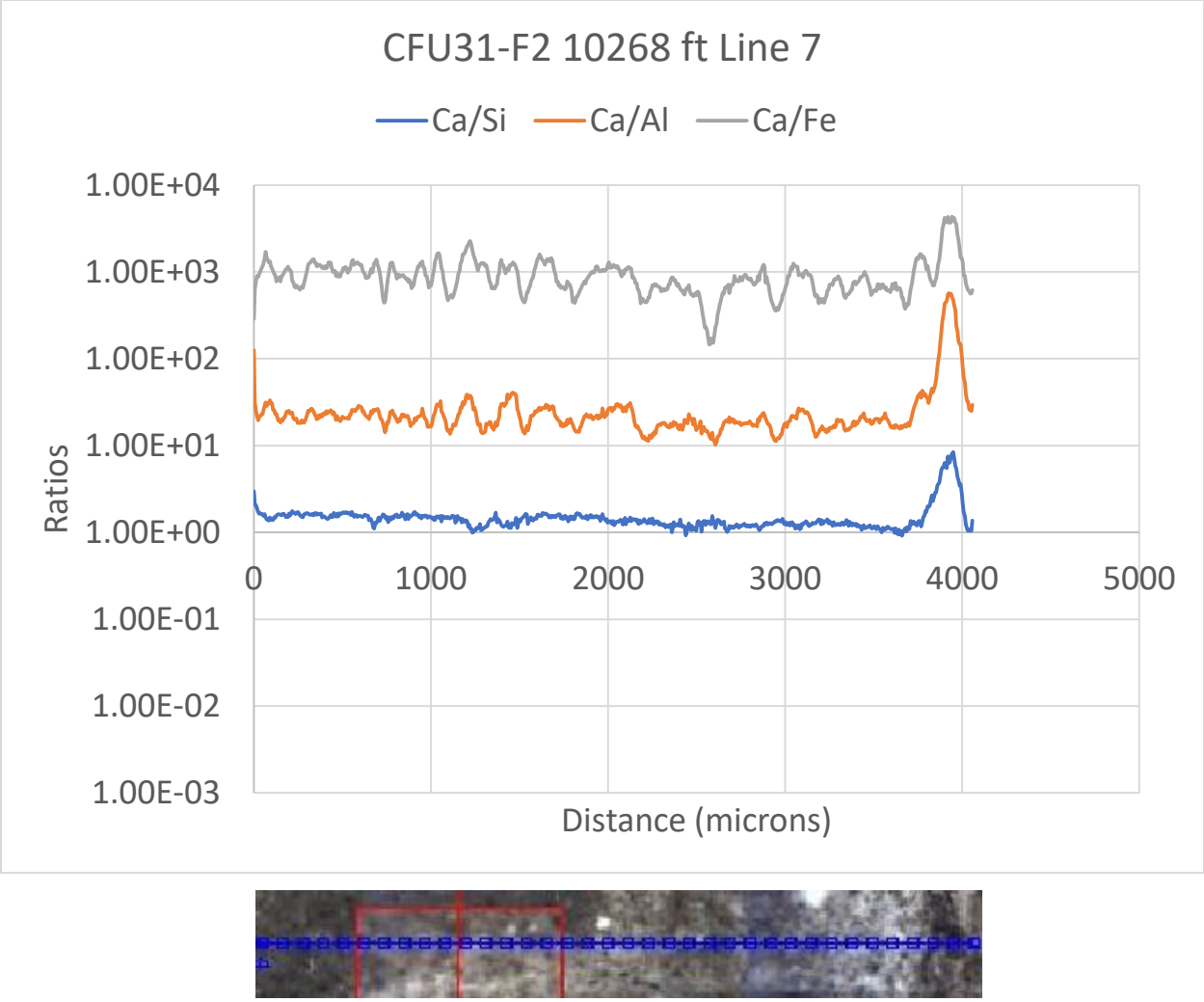

Figure 106 LA-ICP-MS Line 7 results across the sample collected in CFU31-F3 at 10268 ft showing Ca/Si, Ca/Al, and Ca/Fe mole ratios.

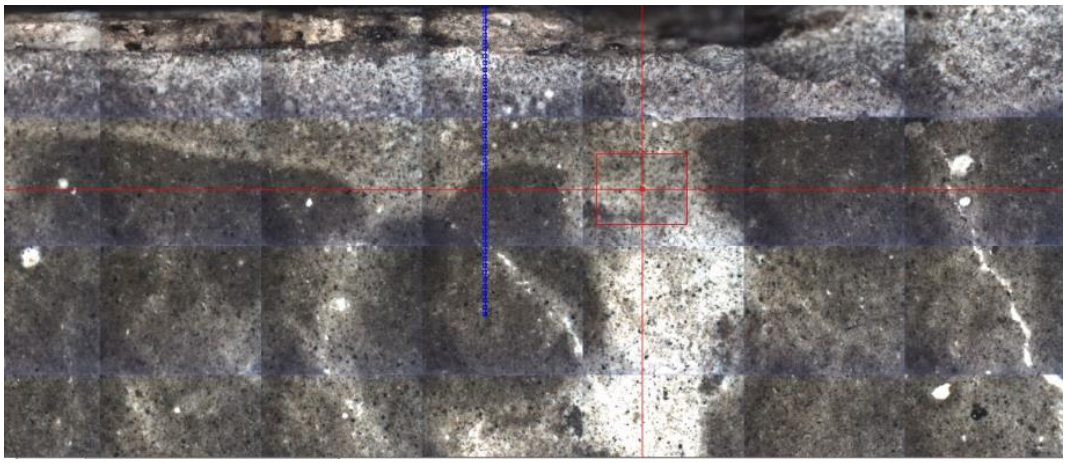

Figure 107 LA-ICP-MS Line 8 across the sample collected in CFU31-F3 at 10268 ft.

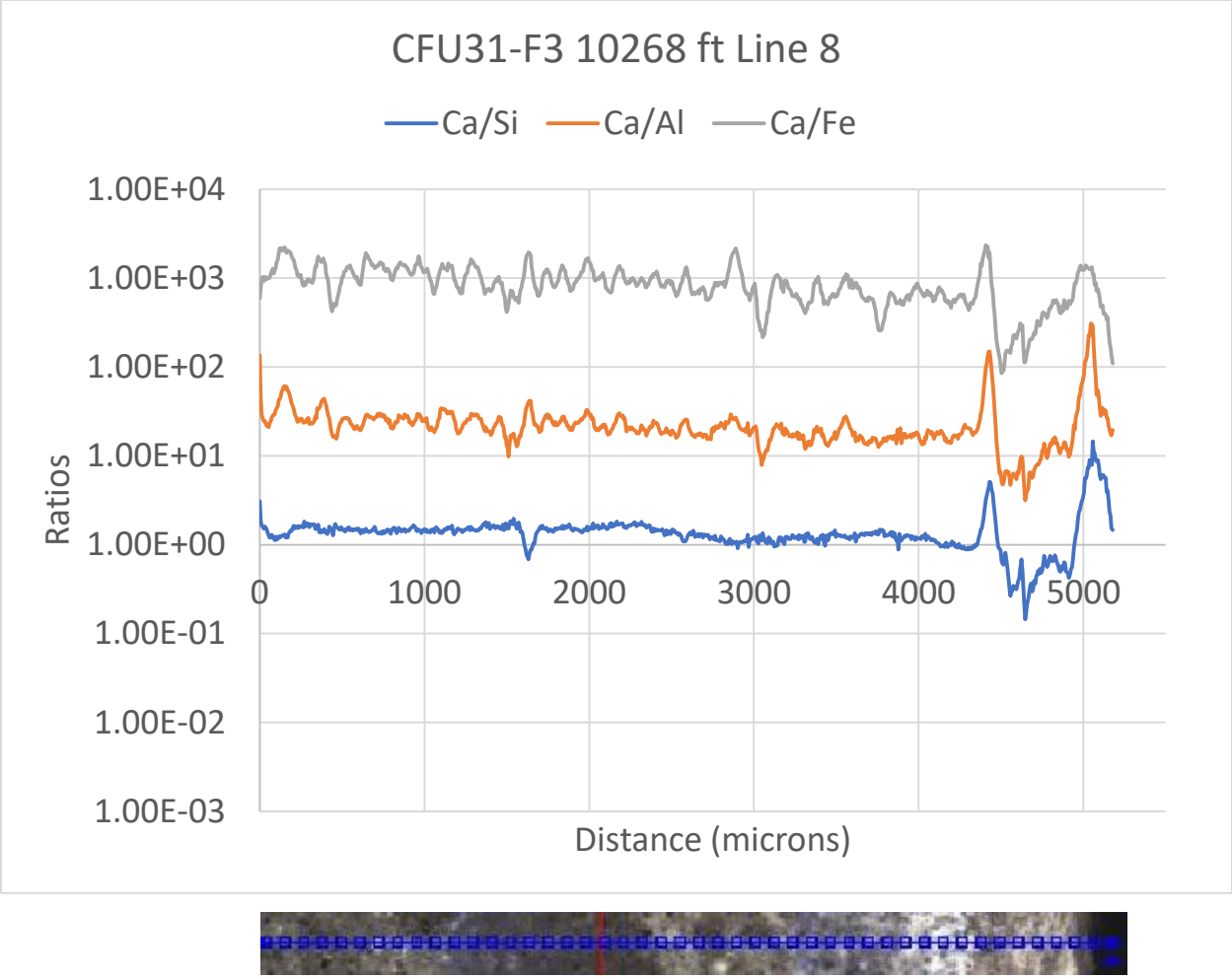

Figure 108 LA-ICP-MS Line 8 results across the sample collected in CFU31-F3 at 10268 ft showing Ca/Si, Ca/Al, and Ca/Fe mole ratios.

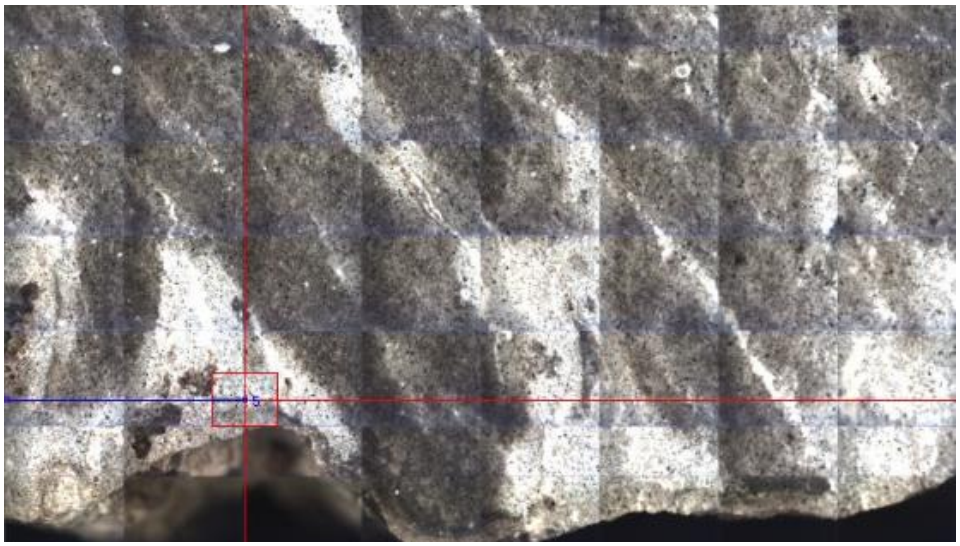

Figure 109 LA-ICP-MS Line 9 across the sample collected in CFU31-F3 at 10268 ft.

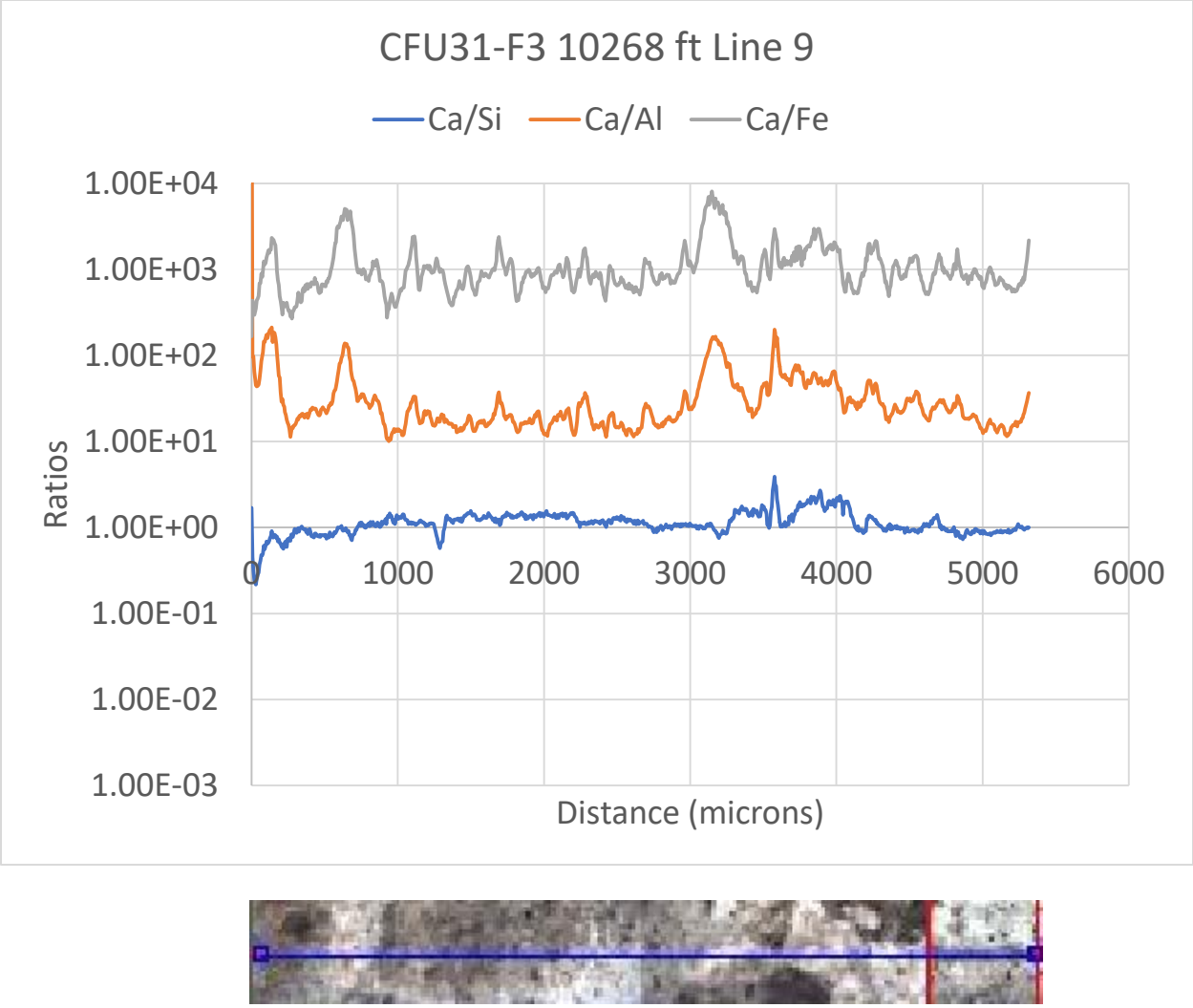

Figure 110 LA-ICP-MS Line 9 results across the sample collected in CFU31-F3 at 10268 ft showing Ca/Si, Ca/Al, and Ca/Fe mole ratios.

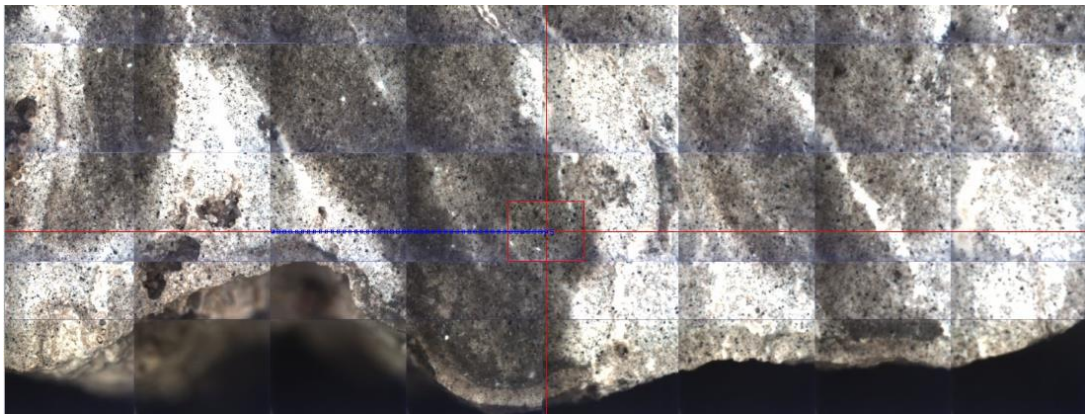

Figure 111 LA-ICP-MS Line 10 across the sample collected in CFU31-F3 at 10268 ft.

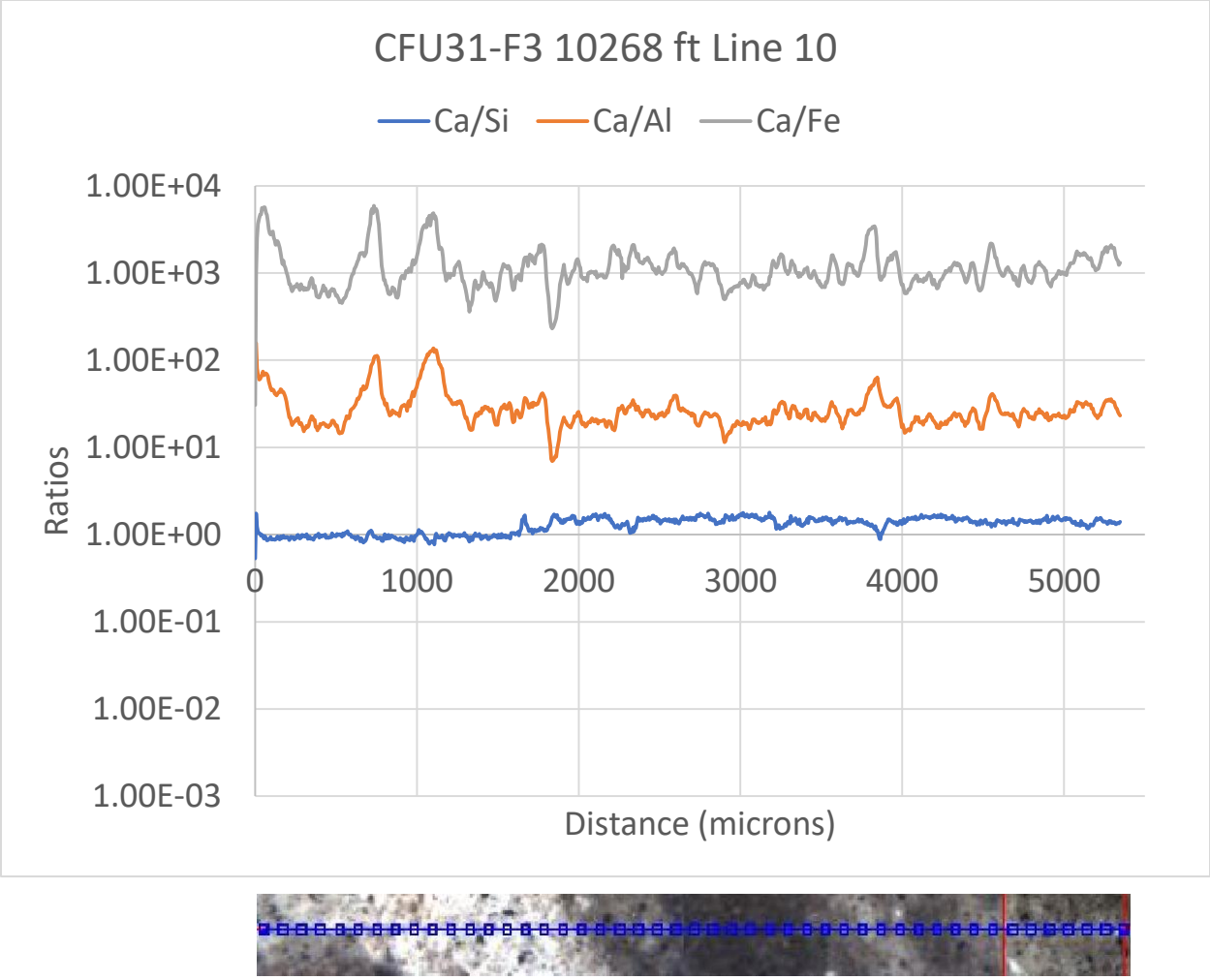

Figure 112 LA-ICP-MS Line 10 results across the sample collected in CFU31-F3 at 10268 ft showing Ca/Si, Ca/Al, and Ca/Fe mole ratios.

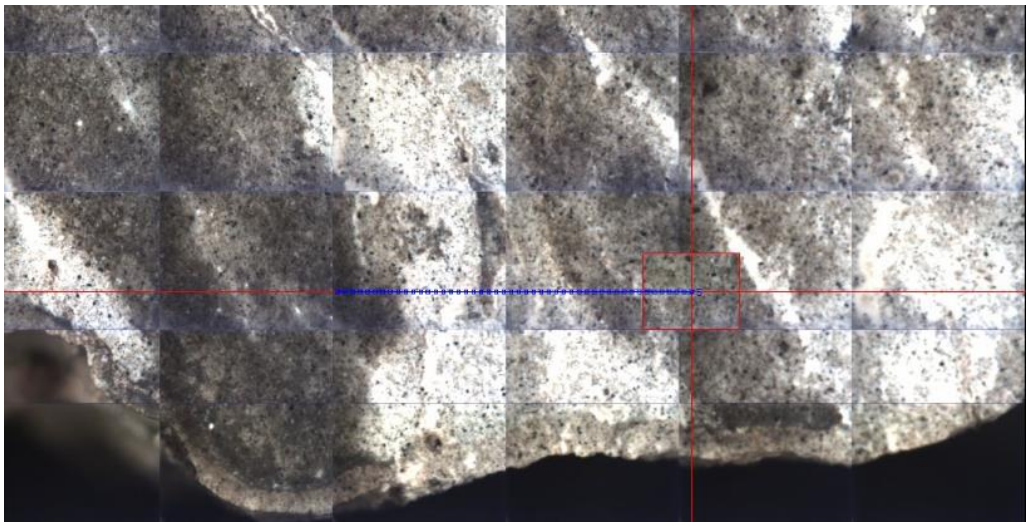

Figure 113 LA-ICP-MS Line 11 across the sample collected in CFU31-F3 at 10268 ft.

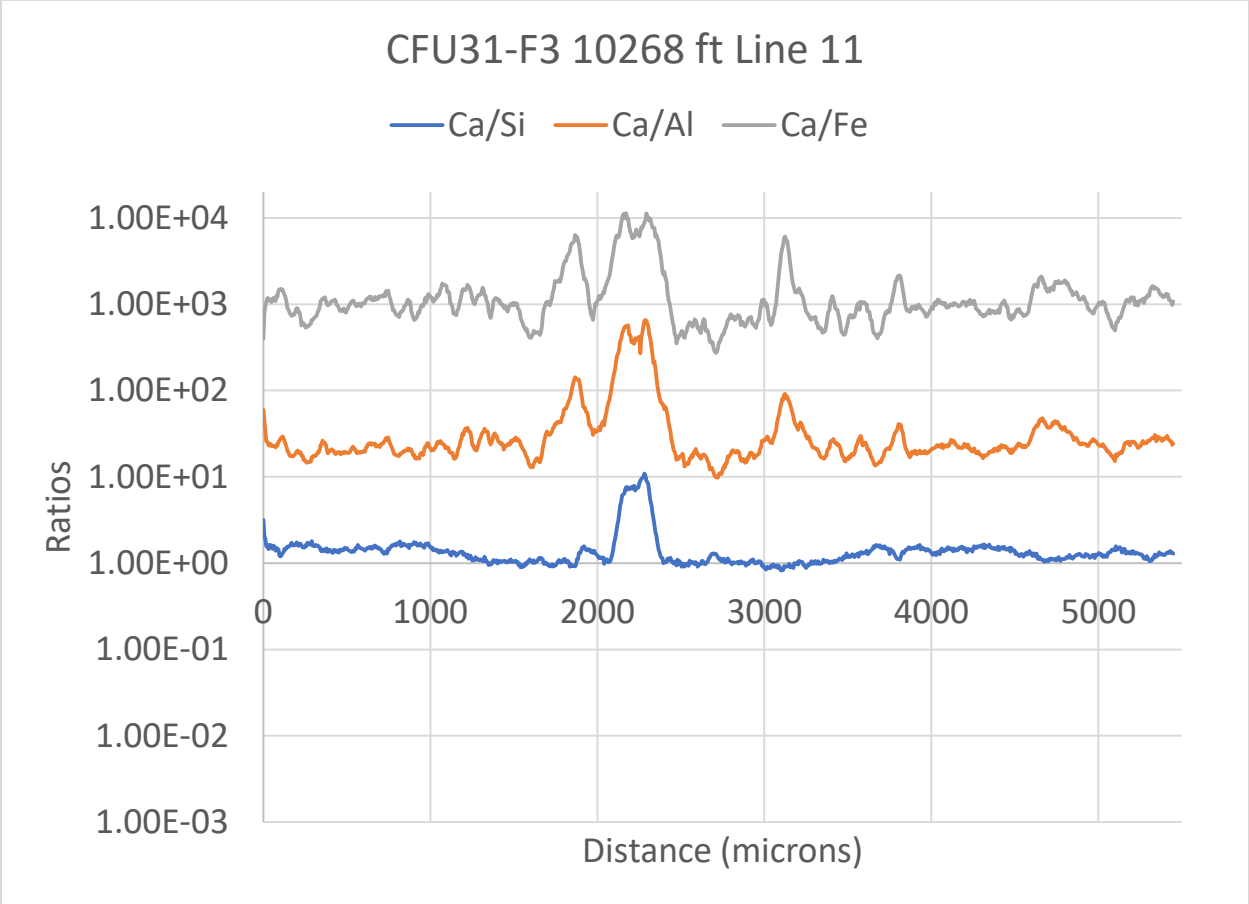

Figure 114 LA-ICP-MS Line 11 results across the sample collected in CFU31-F3 at 10268 ft showing Ca/Si, Ca/Al, and Ca/Fe mole ratios.

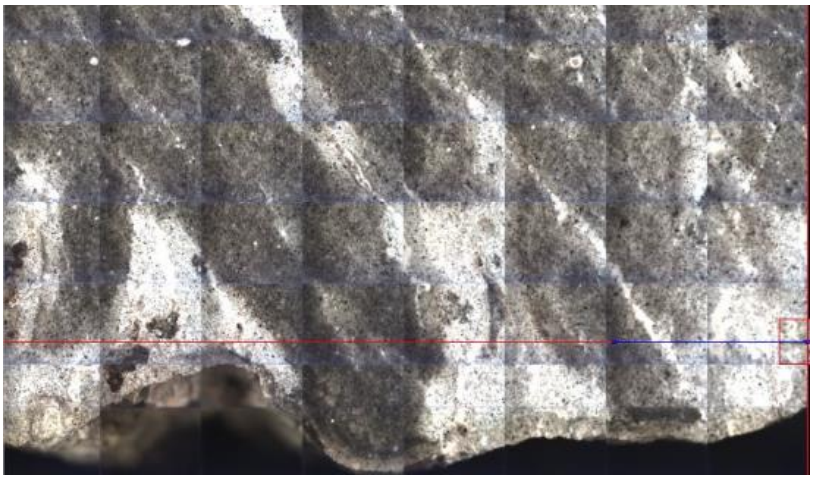

Figure 115 LA-ICP-MS Line 12 across the sample collected in CFU31-F3 at 10268 ft.

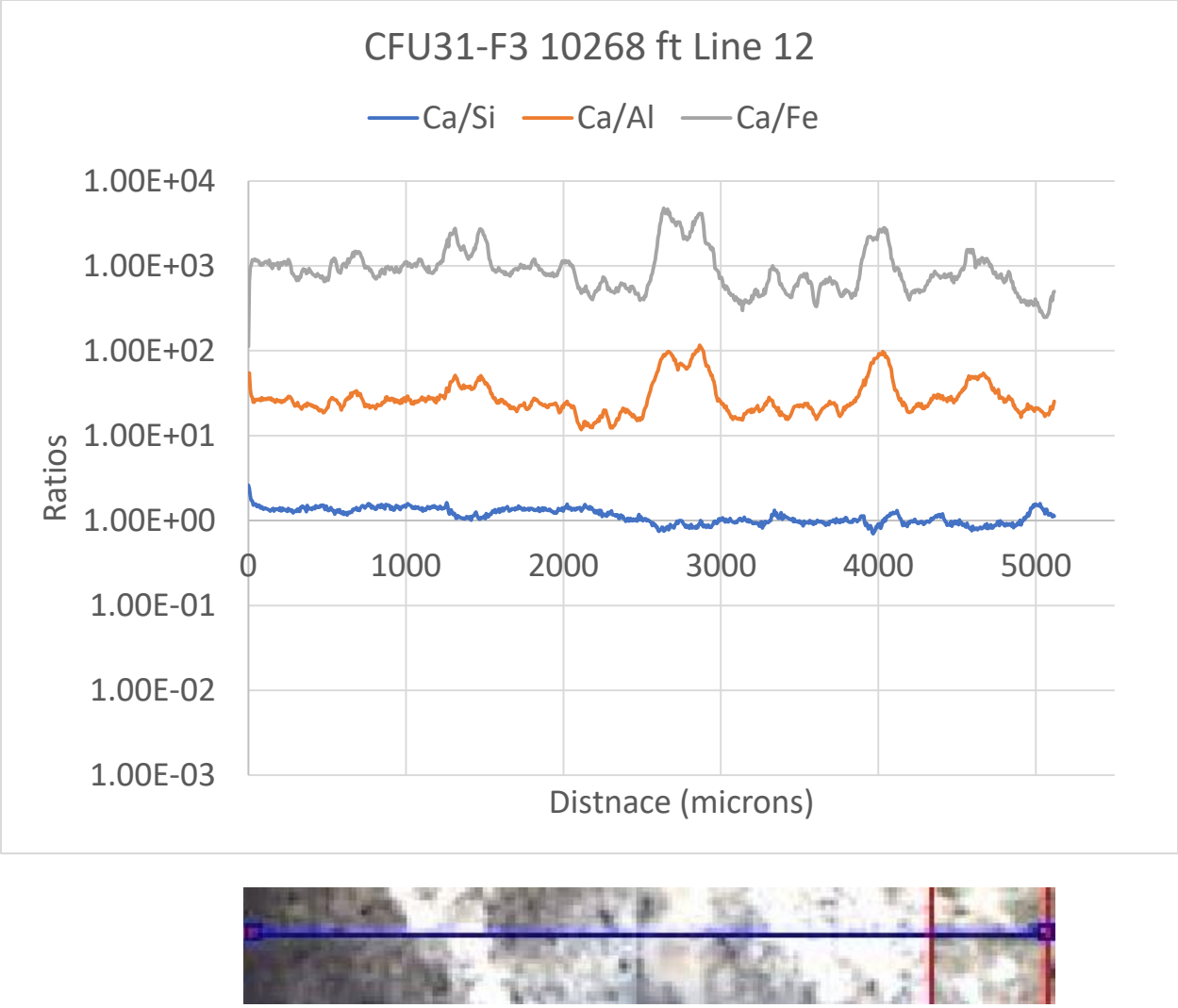

Figure 116 LA-ICP-MS Line 12 results across the sample collected in CFU31-F3 at 10268 ft showing Ca/Si, Ca/Al, and Ca/Fe mole ratios.

Following LA-ICP-MS, portions of the sample were crushed and XRD analysis was performed. XRD on the sample collected at 10268 ft was divided into three zones. Zone 1 consisted of the light colored reacted material on the formation side of the sample. Zone 2 was from the center of the sample and contained some of the diagonal reacted zones. Zone 3 included the light-colored front in the casing side of the sample. The crystalline phase identifications for each zone are shown in Table 19. All zones analyzed showed carbonation. Zone 3 was the most carbonated with 70 percent of crystalline phases being calcium carbonate (calcite and vaterite). Zone 2 was the least carbonated with calcium carbonate making up 10.1 percent of the crystalline phases.

Table 25 XRD results collected on portions of the sample collected in CFU31-F3 at 10268 ft.

	Zone 1	Zone 2	Zone 3
Phase name	**Weight %**	**Weight %**	**Weight %**
Sodium Chloride	12	10	4
Quartz	13	24	3.1
Tobermorite M	22	18	6.5
Tobermorite 9A	-	34	14
Calcite	28	8	63
Vaterite,	13	2.1	7
Brownmillerite	5.9	-	-
Srebrodolskite	-	1.7	-
Tilleyite	7	-	-
Faujasite-Ca, dehydrated	-	3.3	2

4.2.1.3 CFU31-F3 10380 ft sidewall core sample

The core collected at 10380 ft consisted of solid cement, cable, lines, and sampling line, and fiberglass casing (Figure 117). The cement core shows both light grey and tan discoloration or reacted zones on the casing /cable side.

Figure 117 Sidewall core collected in CFU31-F3 showing the fiberglass casing on the left, control lines in the center, and cement on the right.

Micro-CT images of the cement core (Figure 118) identify multiple zones within the sample that appear to be changes in material or reaction fronts running from the casing/cable side of the cement. The CT scan of the casing (Figure 119) shows the casing to be generally uniform with a possible partial break in the lamination visible in the

bottom views in the figure. The micro-CT scan of the cement was used to select area to cut the sample for further analyses.

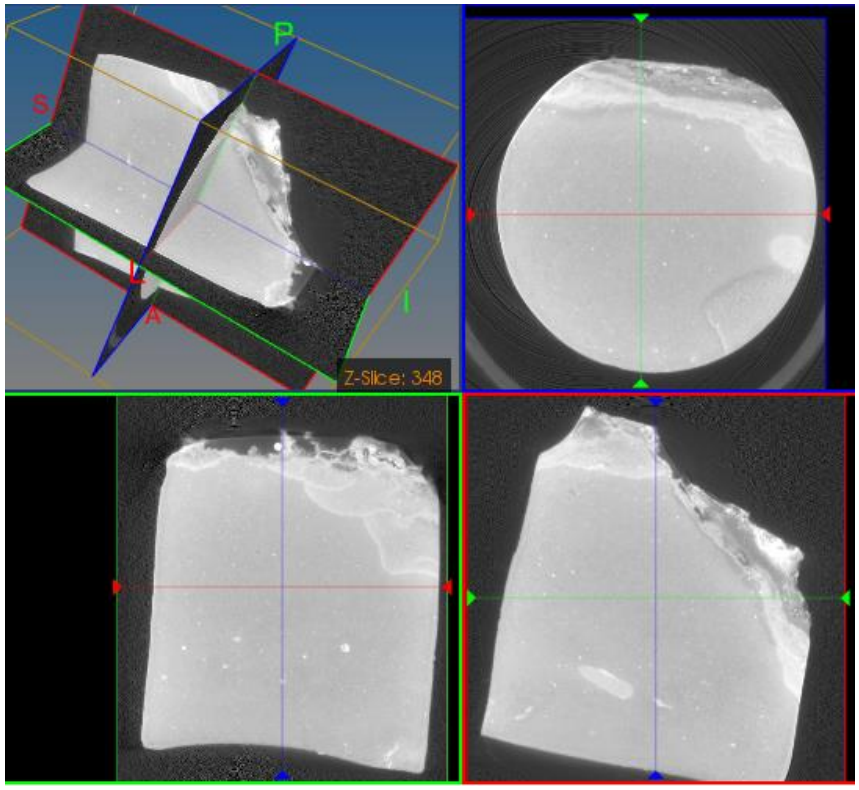

Figure 118 Micro-CT image of the cement sample collected in CFU31-F3 at 10380 ft.

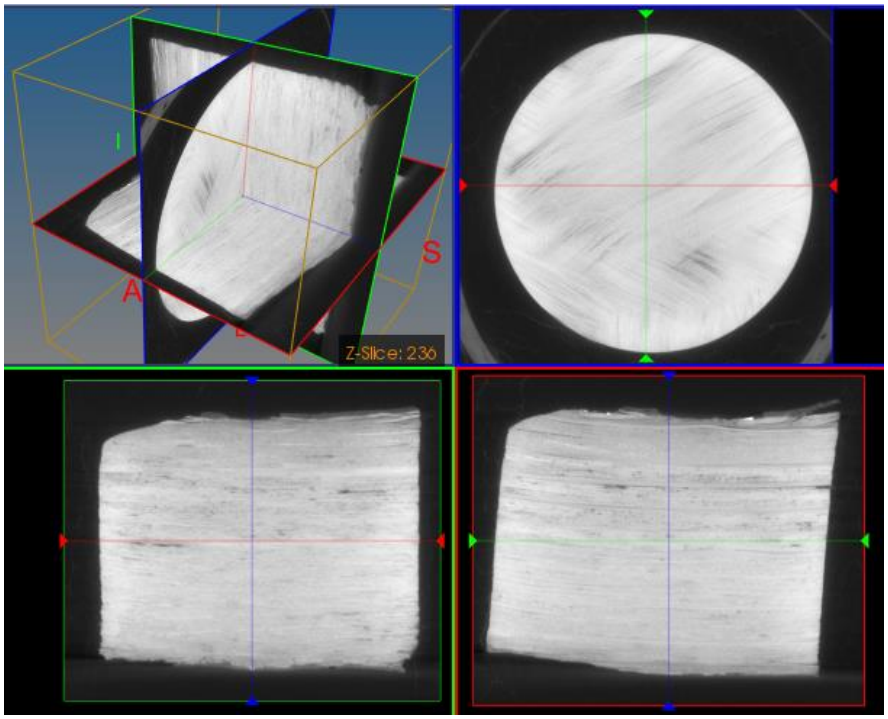

Figure 119 Micro-CT image of the fiberglass casing sample collected in CFU31-F3 at 10380 ft.

Sectioning of the sample (Figure 120) confirmed multiple fronts on the casing/cable side and a tan front on the formation side. Note the front on the formation side of the core continues on the outer side of the core sample, parallel to the long axis of the sample.

Figure 120 Sectioned cement sidewall core collected in CFU31-F3 at 10380 ft.

ESEM imaging and EDS mapping were performed on the control line / casing side of the sample. The mapping delineates fronts near the edge of the sample. Figure 121 shows EDS map images of Si, Ca, O, C, Al, and Fe. The maps show a calcium carbonate front from the lower right to the upper left of the images. The front can be identified as the darkest part of the Si map and the lightest part of the Ca and C maps. Immediately in front of the calcium carbonate front is a Ca-depleted that can be identified as the darkest part in the Ca map. Figure 122 shows the same calcium carbonate front visible in Figure 121 in the lower left corner. The figure also shows isolated calcium carbonate rich zones in the center of the maps and another calcium carbonate front in the upper right of the maps.

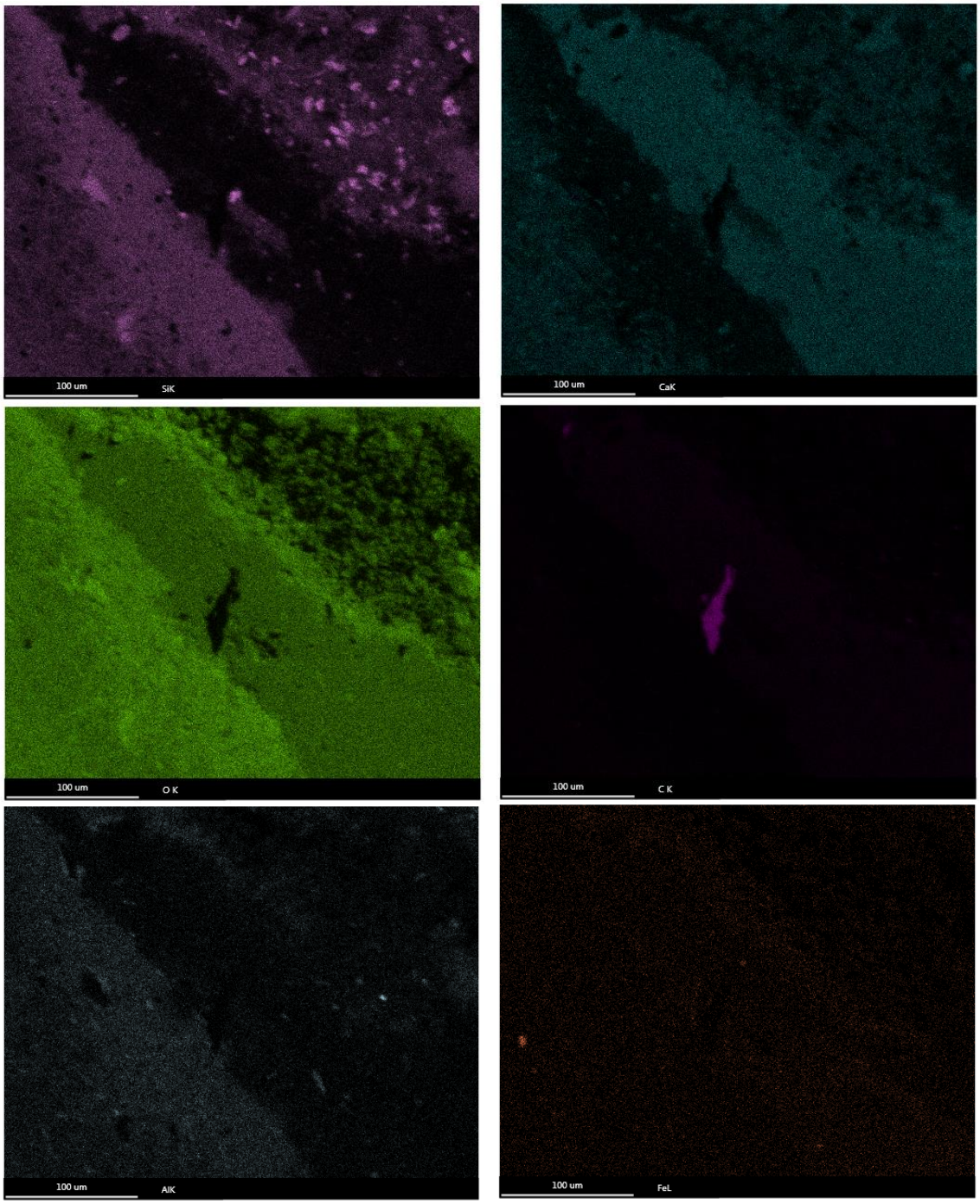

Figure 121 EDS image of the control line / casing side of the sample.

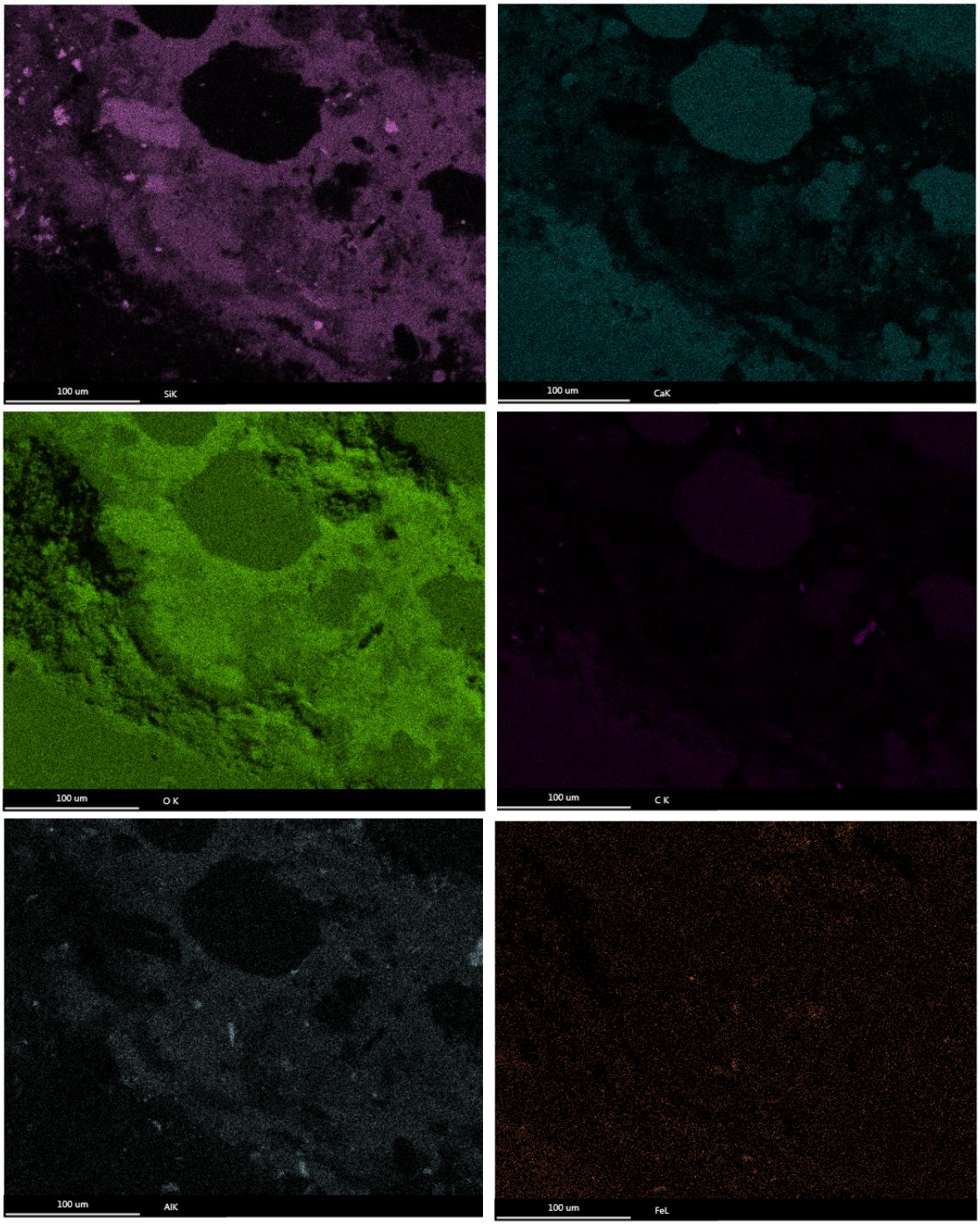

Figure 122 EDS image of the control line / casing side of the sample adjacent to the image shown in Figure 121.

The sectioned sidewall core was analyzed with LA-ICP-MS starting on the formation side and moving toward the casing side of the sample. The LA-ICP-MS scan line images and corresponding data are presented in Figure 123 through Figure 140. The first line (Figure 123 and Figure 124) shows large variation over the first 2700 microns, across several tan and dark brown zones. Over this distance, the Ca/Si varies between 15.2 and 0.05. After 2,700 microns there are two light grey reacted zones with dark grey edges, in these zones the Ca/Si varies between around 0.6 and 2.1. Around 4,800 microns the line encounters a darker grey cement with a Ca/Si between 0.4 and 0.9. Lines 2, 3 and 4 (Figure 125 to Figure 130) are generally smooth in comparison to Line 1 with Ca/Si rising from around 0.6 to between 0.8 and 1.1 over a combined distance of 15,790 microns. Line 5 (Figure 131 and Figure 132) is similar to Line 4 until around 4100 where it jumps to closer to 2 and then down to 1.26 around 4,292 microns. Note there is a dark grey zone between 530 and 4,292 microns Between 4,292 microns and the end the sample at 4496 microns the Ca/Si rises to 2.75 before dropping to 0.9 at the edge of the sample. Lines 6 and 7 are across the highly reacted, casing/cable side the sample to provide additional data on the Ca/Si and other ratios as the LA-ICP-MS measured into the sample. Lines 1 through 7 were conducted on the left-most portion of the section sample in Figure 120. Lines 8 and 9 (Figure 137 to Figure 140) were collected on the right-most portion of the sample in Figure 120 and show additional examples of ratio variations across the highly reacted zone.

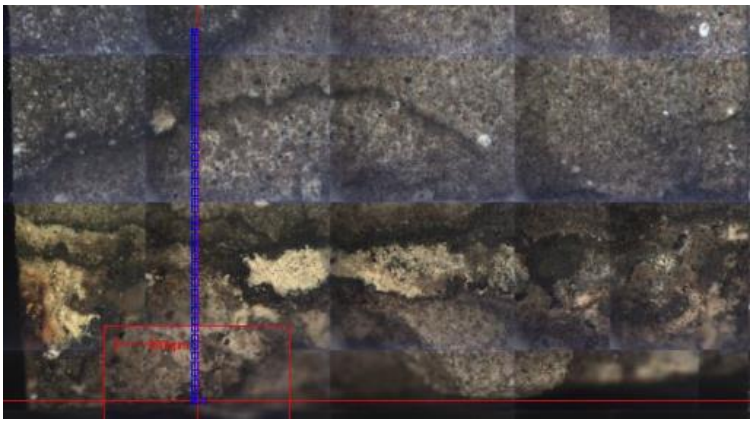

Figure 123 LA-ICP-MS Line 1 across the sample collected in CFU31-F3 at 10380 ft.

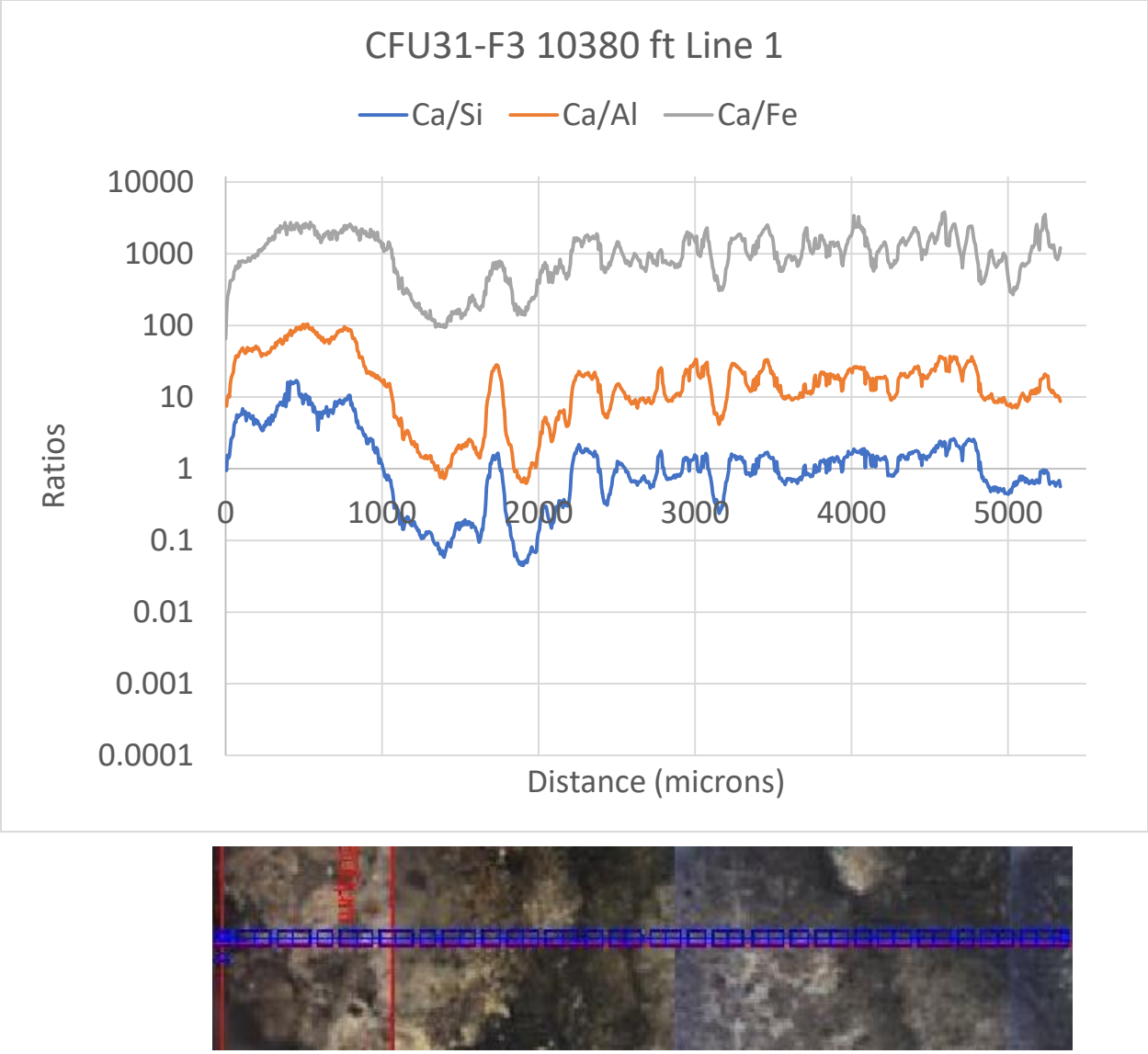

Figure 124 LA-ICP-MS Line 1 results across the sample collected in CFU31-F3 at 10380 ft showing Ca/Si, Ca/Al, and Ca/Fe mole ratios.

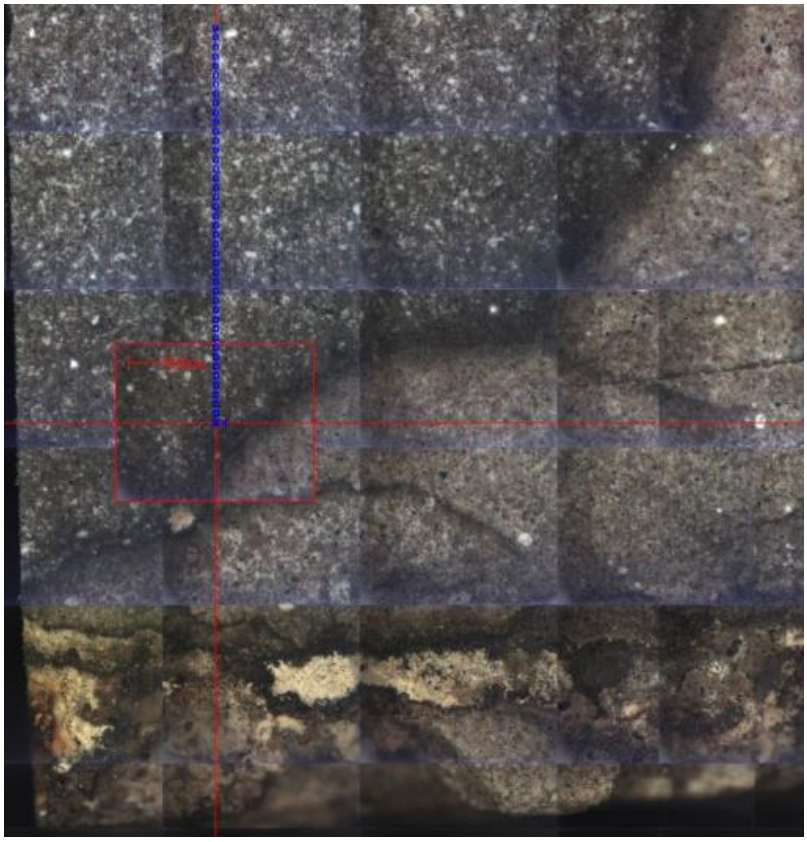

Figure 125 LA-ICP-MS Line 2 across the sample collected in CFU31-F3 at 10380 ft.

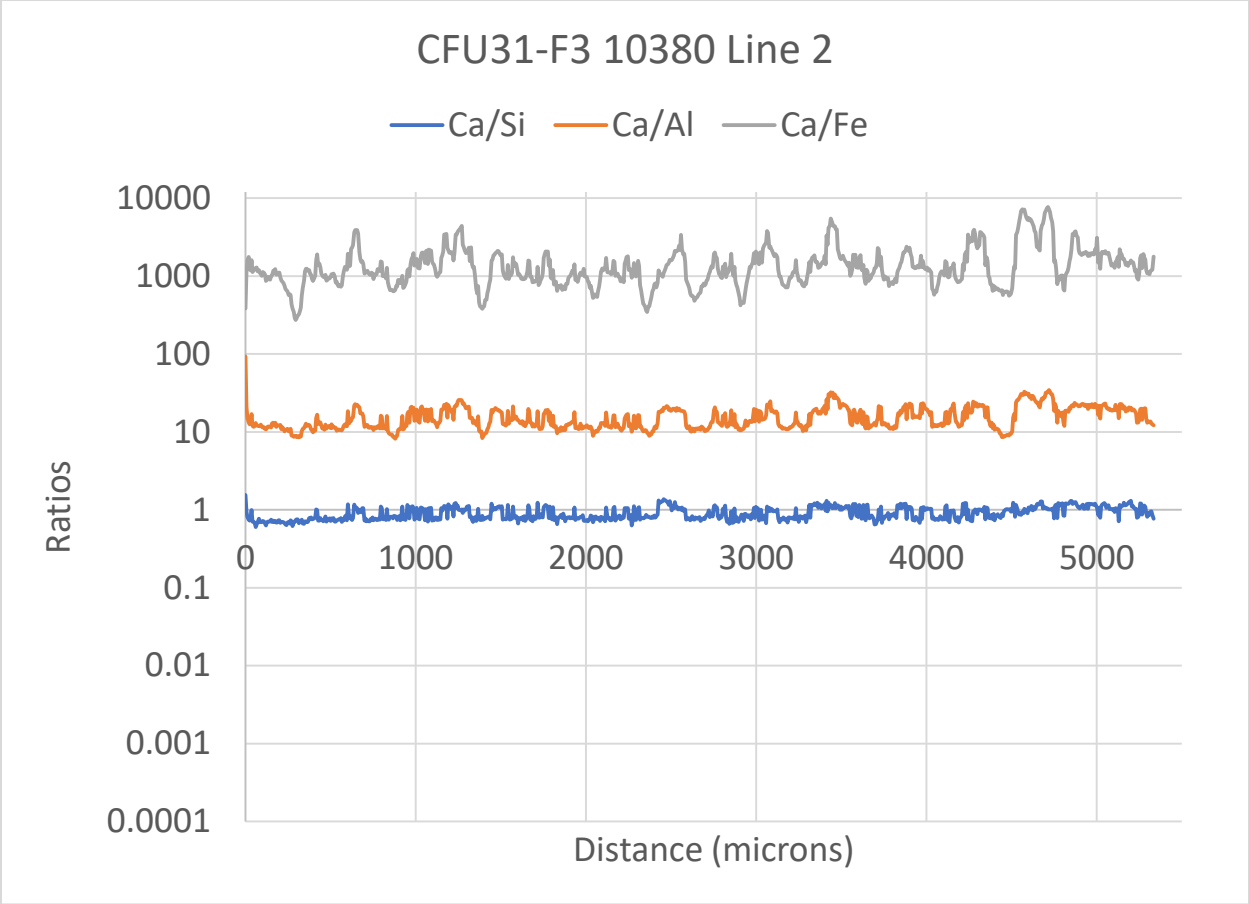

Figure 126 LA-ICP-MS Line 2 results across the sample collected in CFU31-F3 at 10380 ft showing Ca/Si, Ca/Al, and Ca/Fe mole ratios.

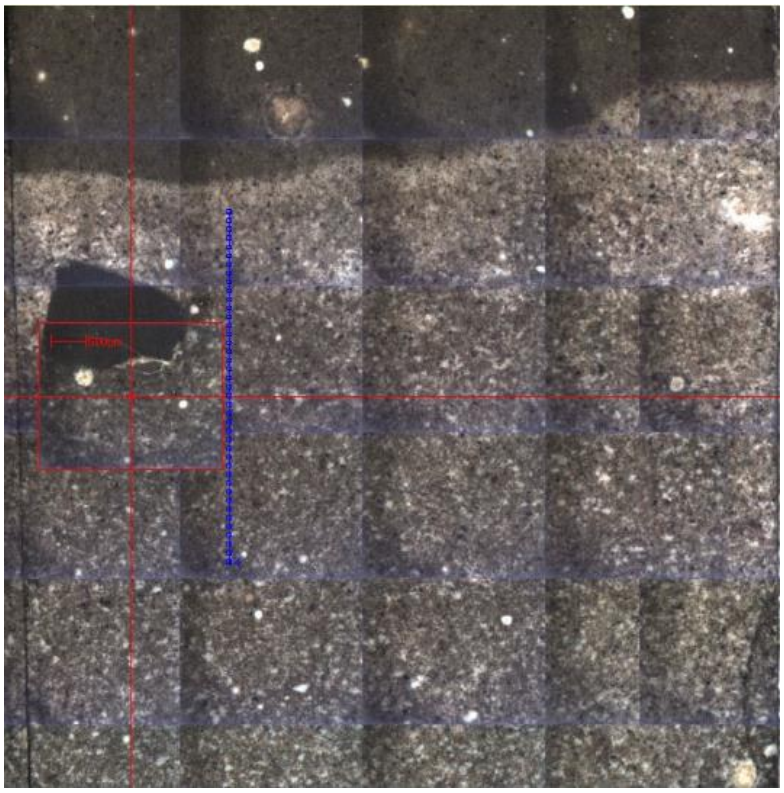

Figure 127 LA-ICP-MS Line 3 across the sample collected in CFU31-F3 at 10380 ft.

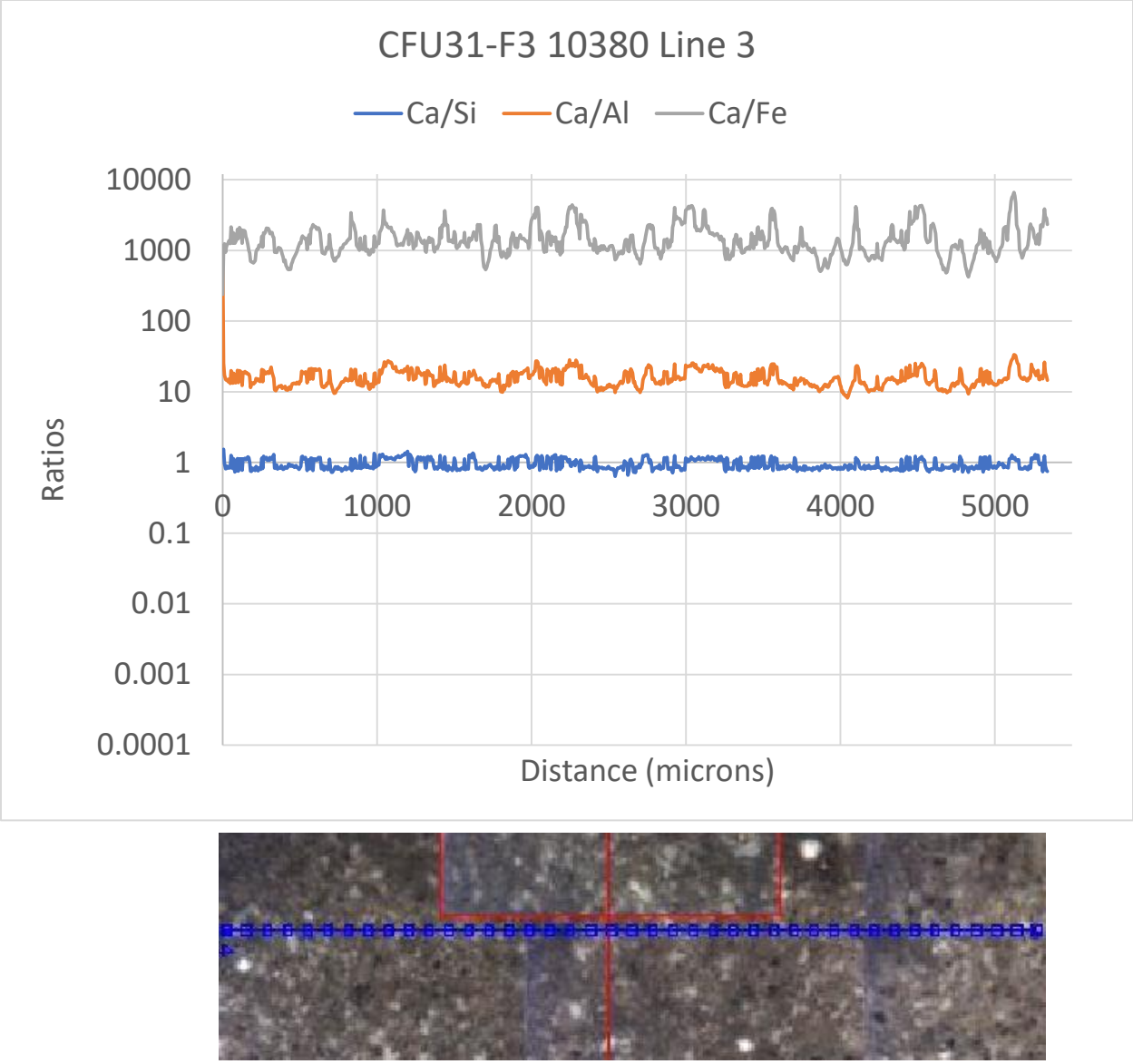

Figure 128 LA-ICP-MS Line 3 results across the sample collected in CFU31-F3 at 10380 ft showing Ca/Si, Ca/Al, and Ca/Fe mole ratios.

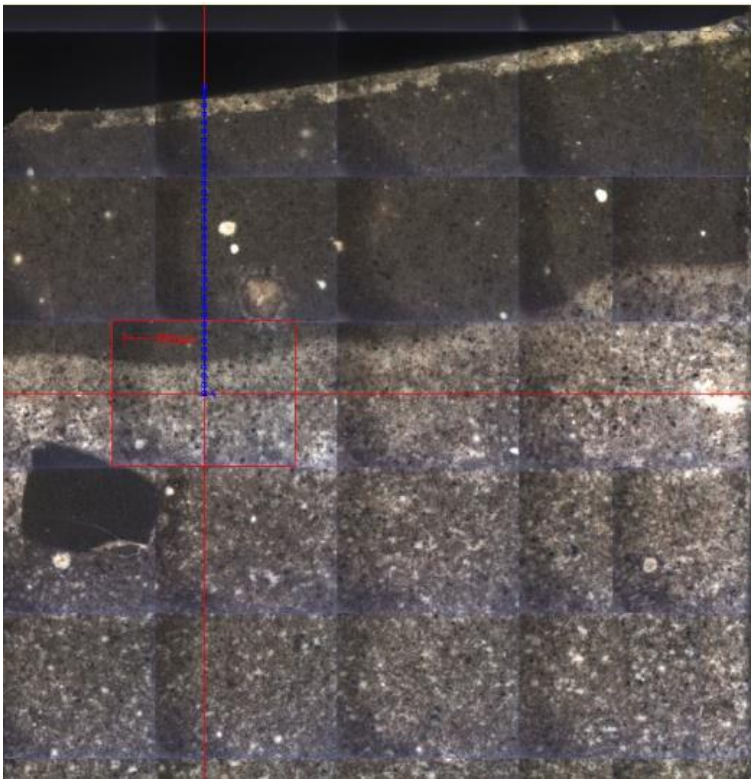

Figure 129 LA-ICP-MS Line 4 across the sample collected in CFU31-F3 at 10380 ft.

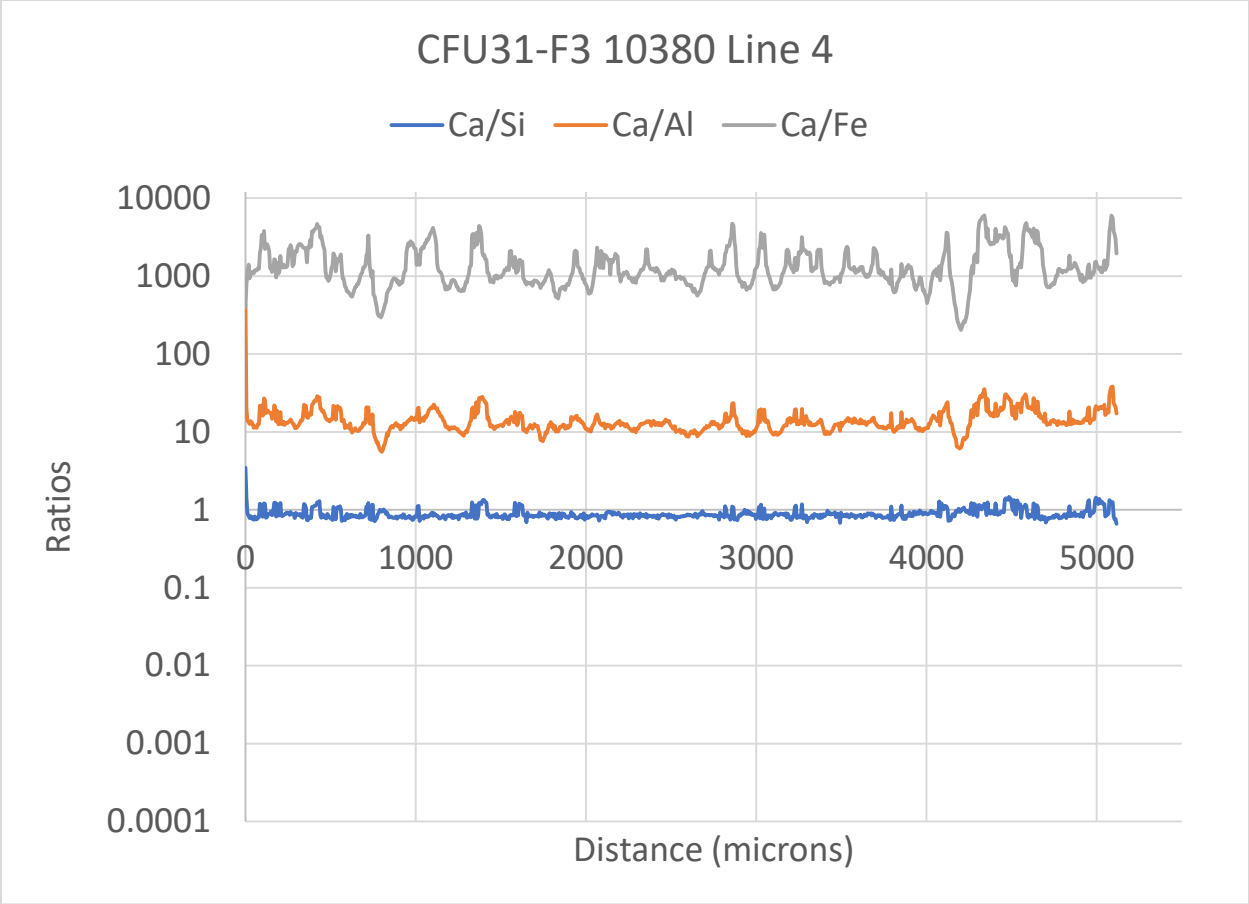

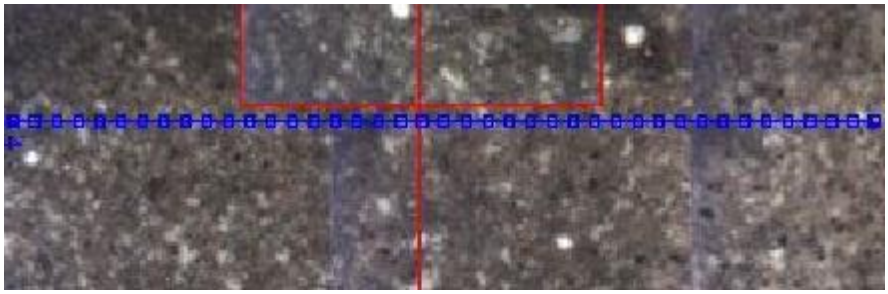

Figure 130 LA-ICP-MS Line 4 results across the sample collected in CFU31-F3 at 10380 ft showing Ca/Si, Ca/Al, and Ca/Fe mole ratios.

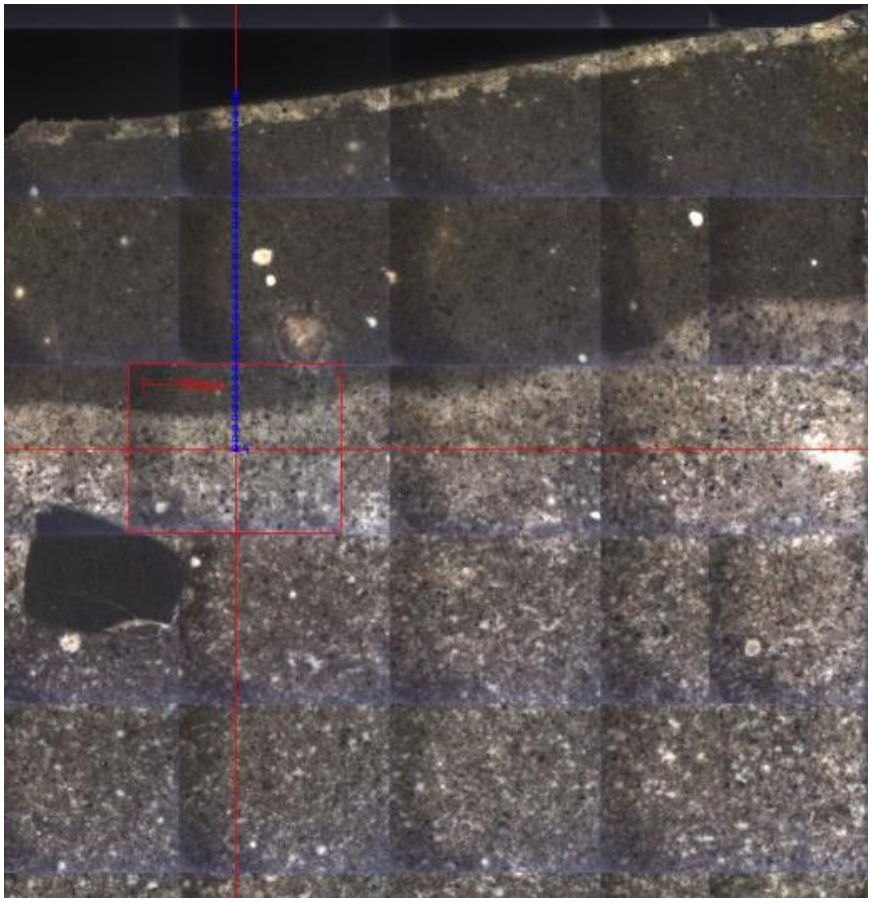

Figure 131 LA-ICP-MS Line 5 across the sample collected in CFU31-F3 at 10380 ft.

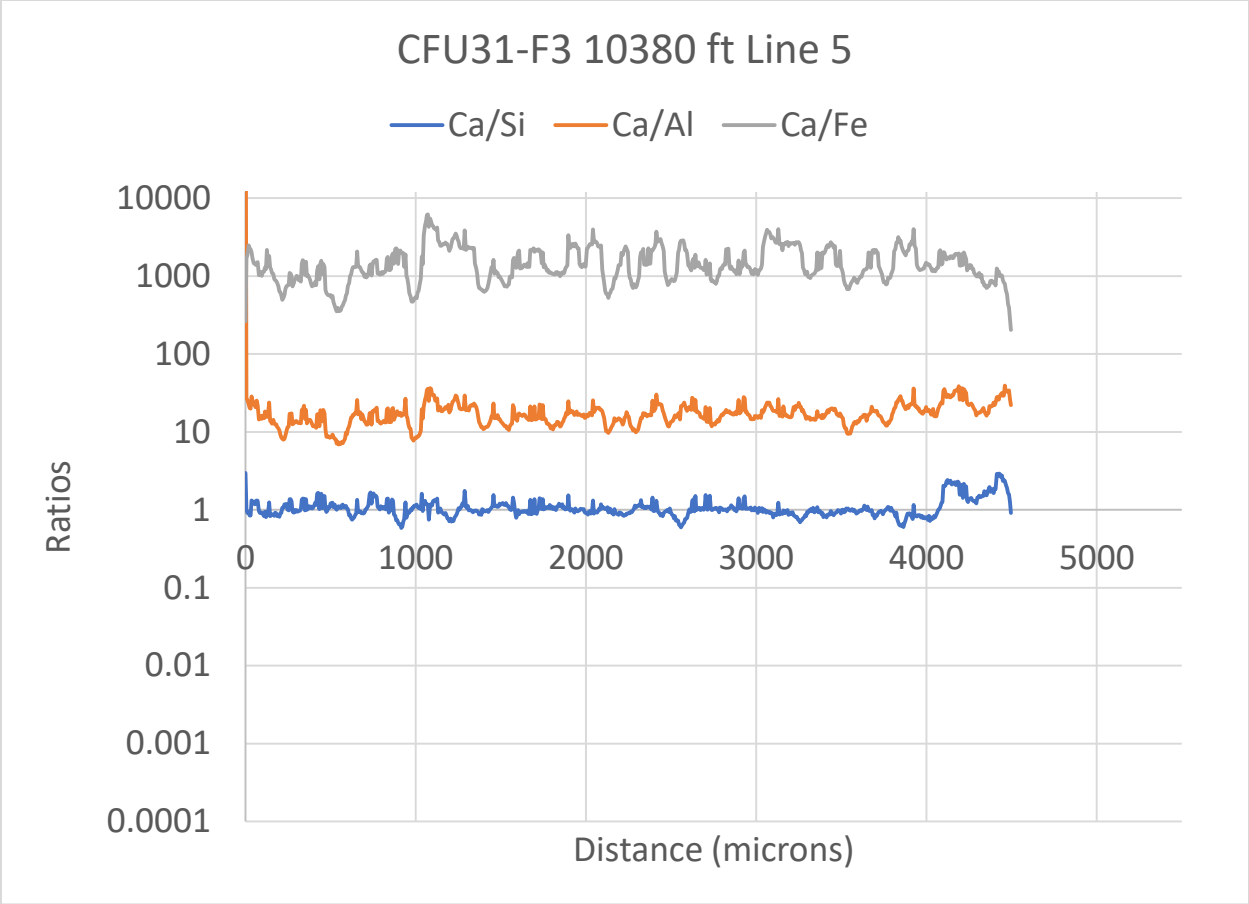

Figure 132 LA-ICP-MS Line 5 results across the sample collected in CFU31-F3 at 10380 ft showing Ca/Si, Ca/Al, and Ca/Fe mole ratios.

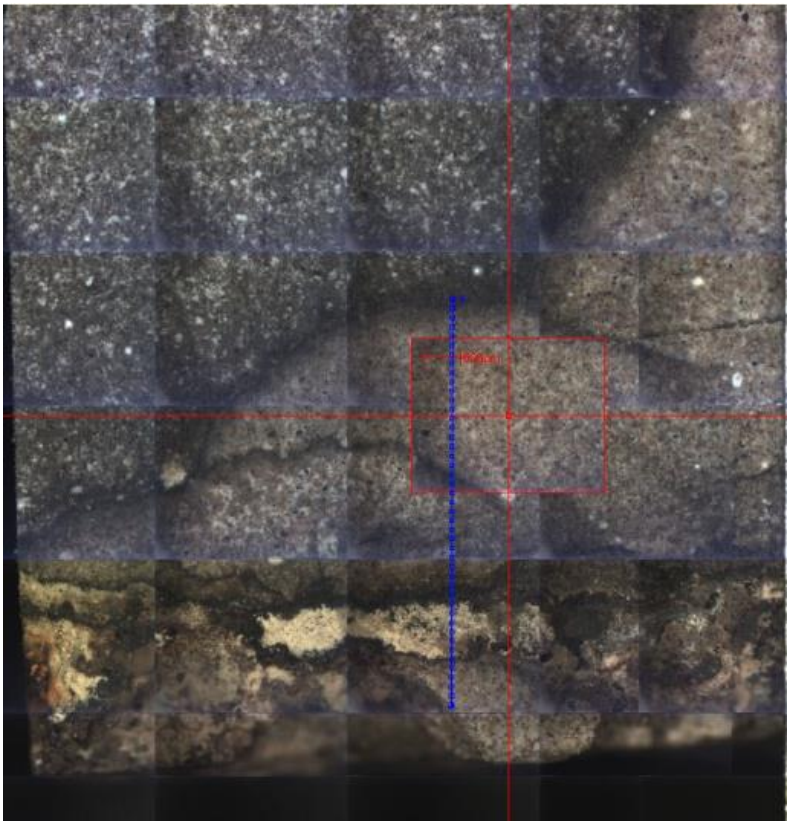

Figure 133 LA-ICP-MS Line 6 across the sample collected in CFU31-F3 at 10380 ft.

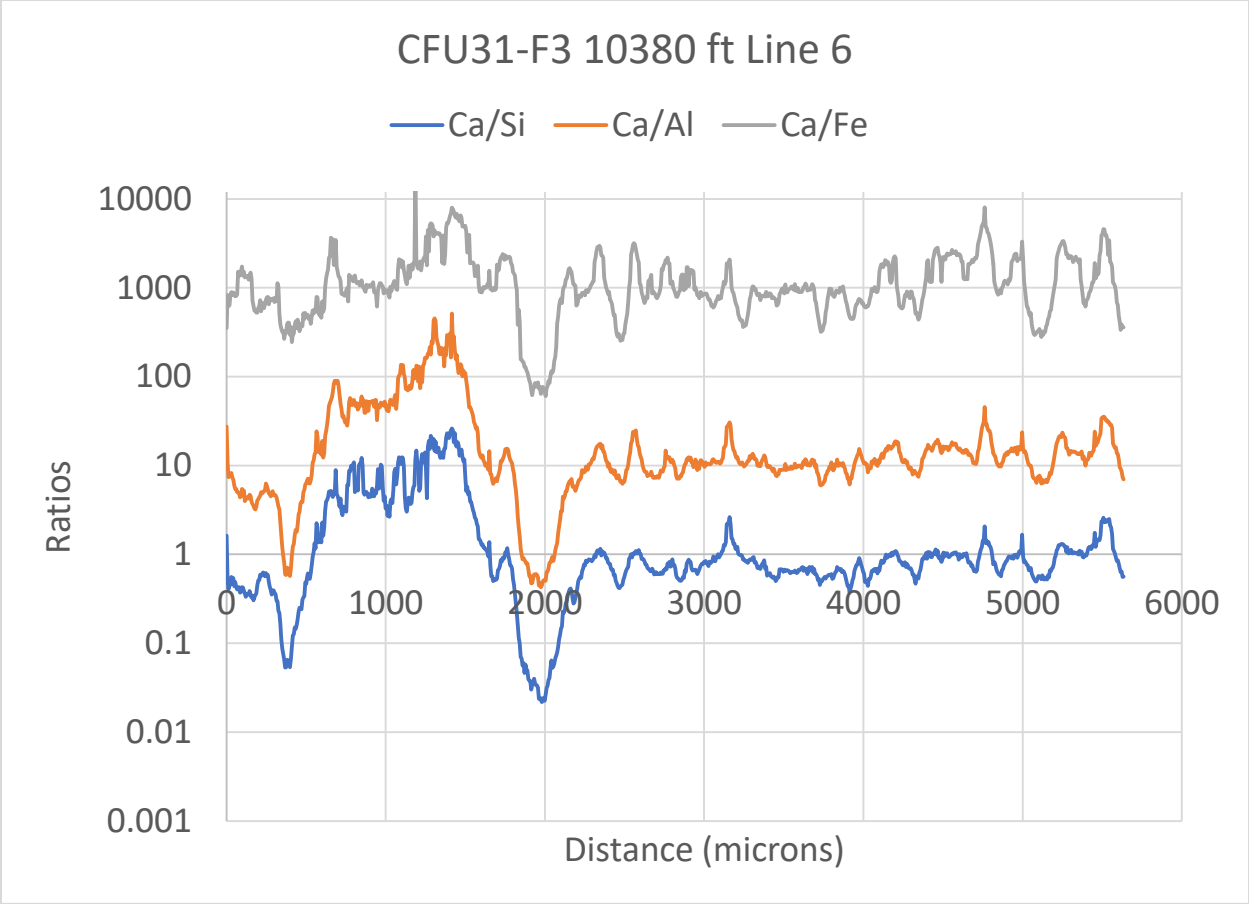

Figure 134 LA-ICP-MS Line 6 results across the sample collected in CFU31-F3 at 10380 ft showing Ca/Si, Ca/Al, and Ca/Fe mole ratios.

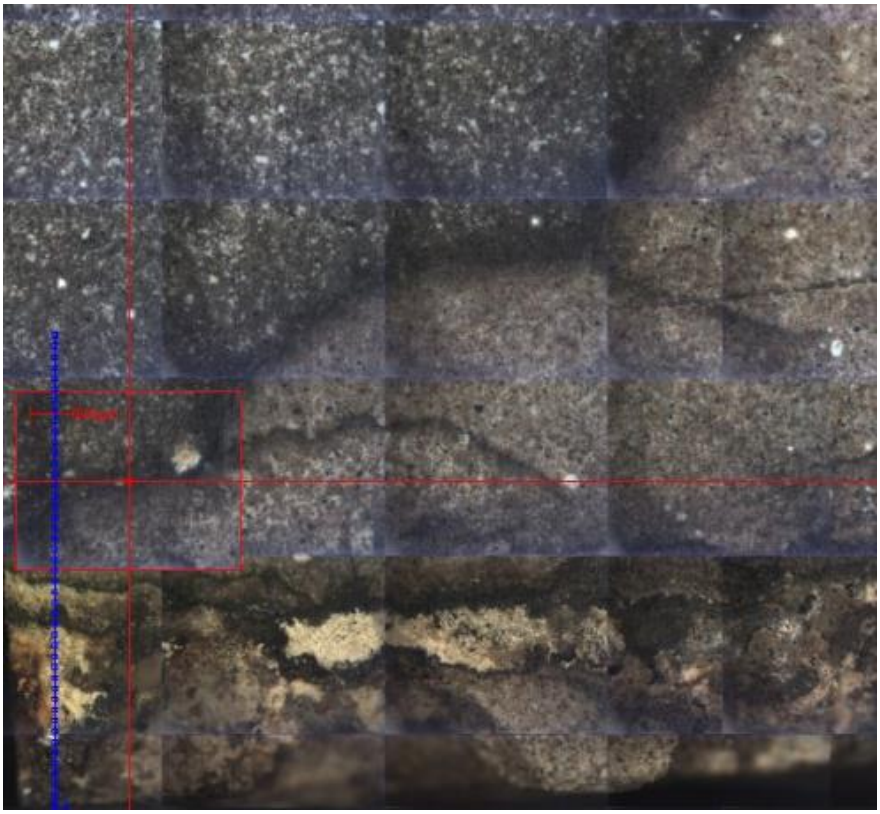

Figure 135 LA-ICP-MS Line 7 across the sample collected in CFU31-F3 at 10380 ft.

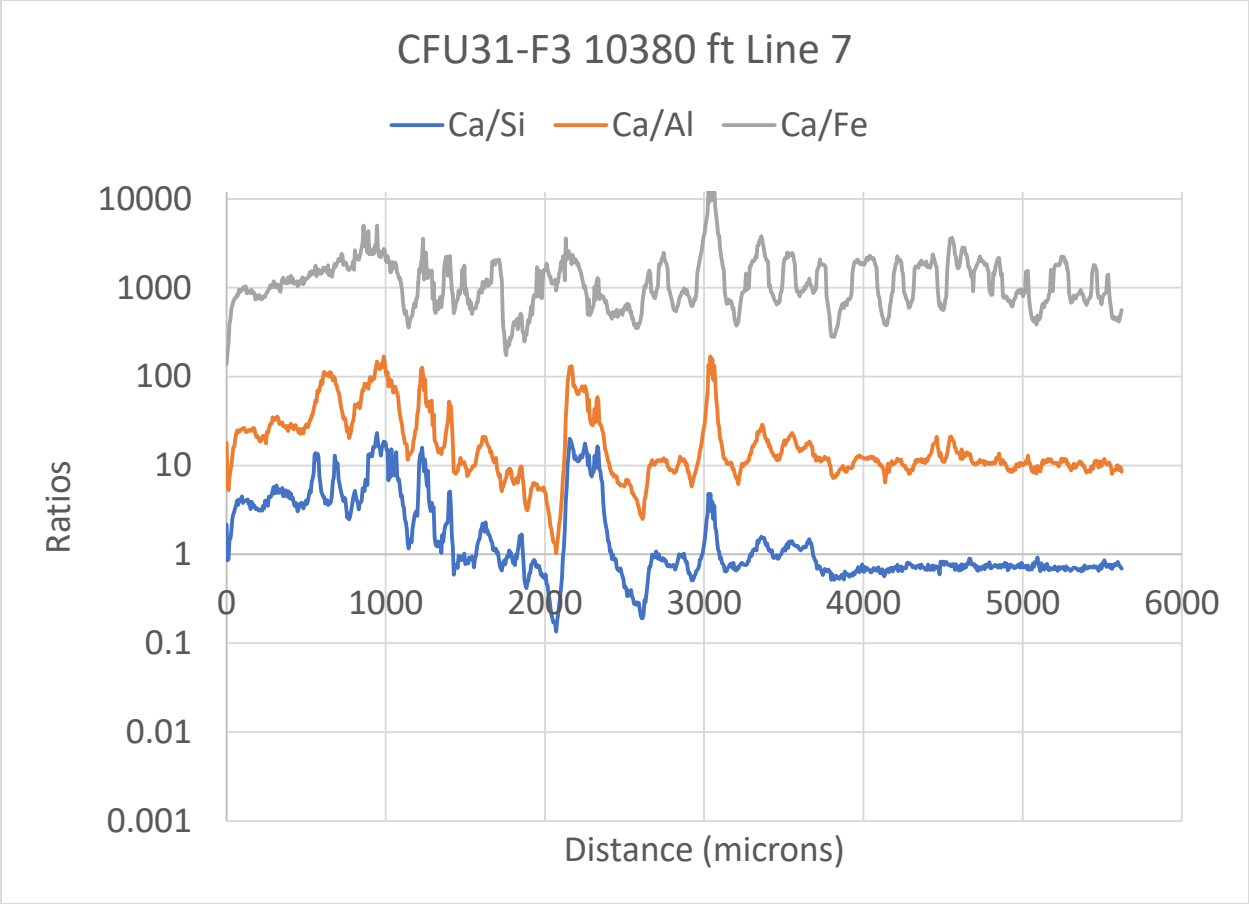

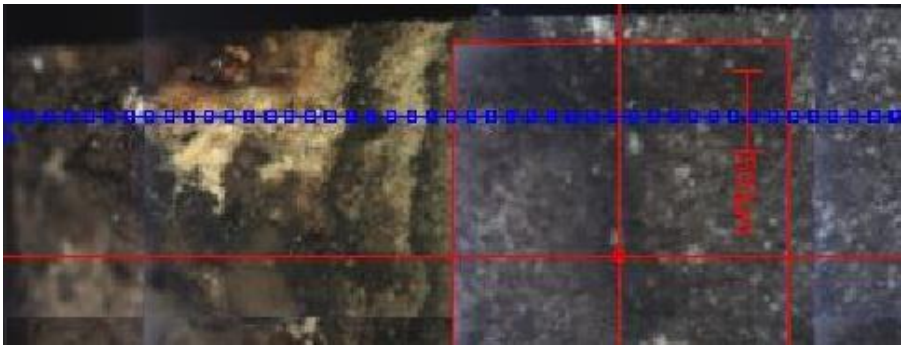

Figure 136 LA-ICP-MS Line 7 results across the sample collected in CFU31-F3 at 10380 ft showing Ca/Si, Ca/Al, and Ca/Fe mole ratios.

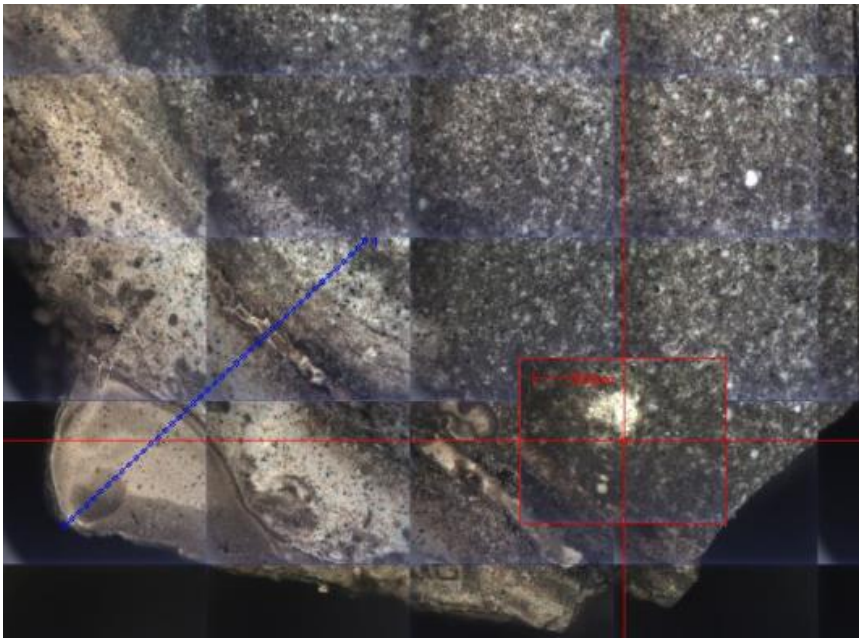

Figure 137 LA-ICP-MS Line 8 across the sample collected in CFU31-F3 at 10380 ft.

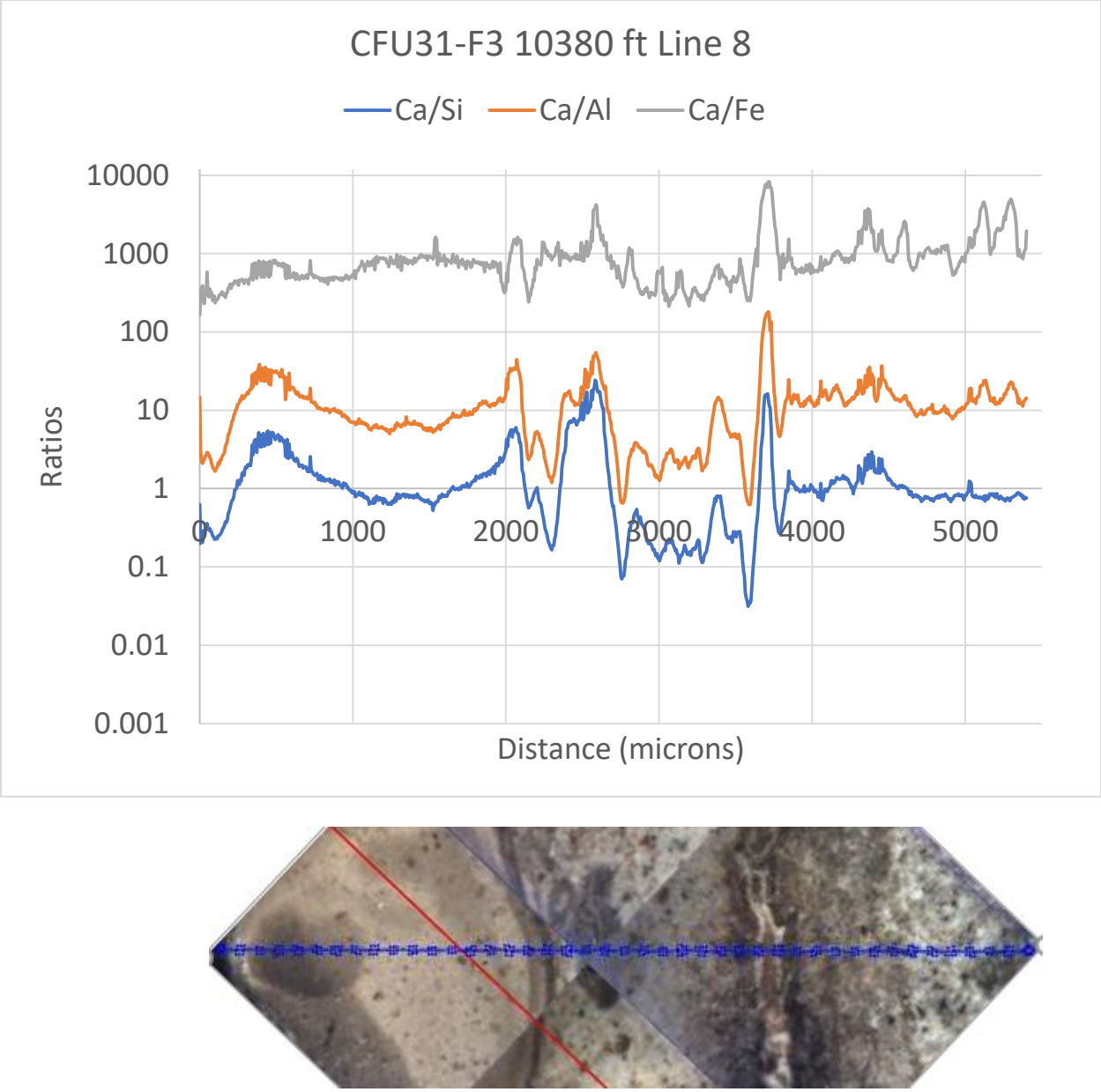

Figure 138 LA-ICP-MS Line 8 results across the sample collected in CFU31-F3 at 10380 ft showing Ca/Si, Ca/Al, and Ca/Fe mole ratios.

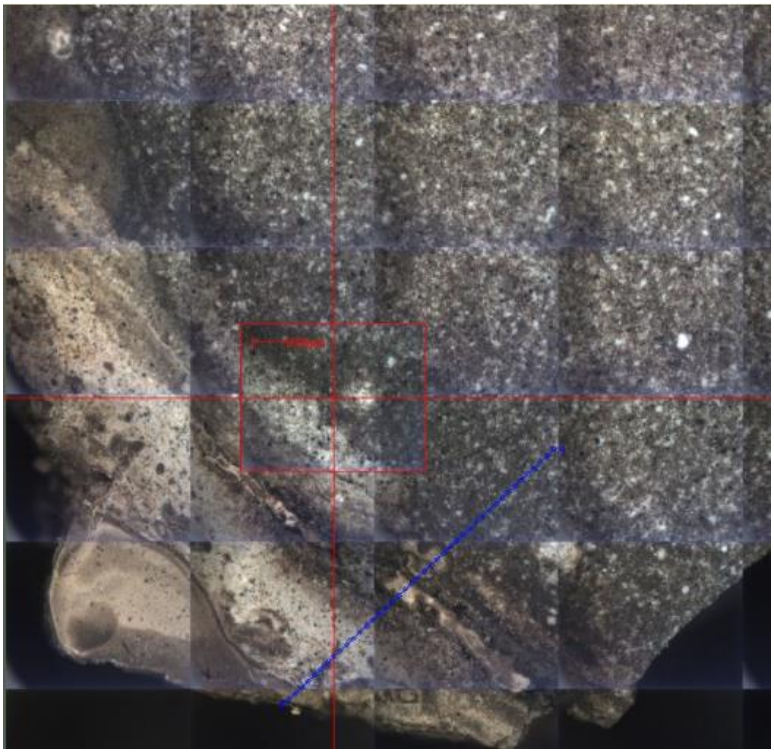

Figure 139 LA-ICP-MS Line 9 across the sample collected in CFU31-F3 at 10380 ft.

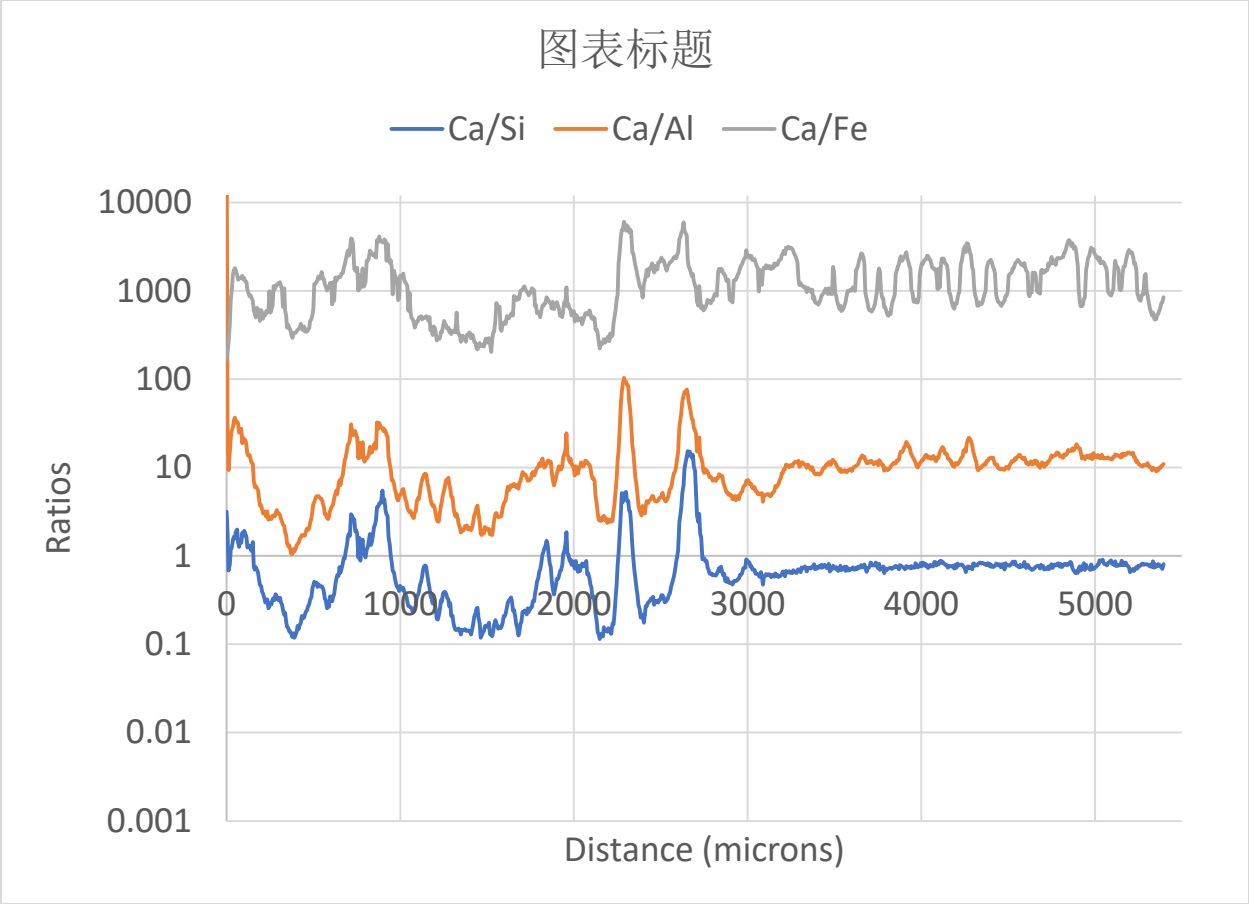

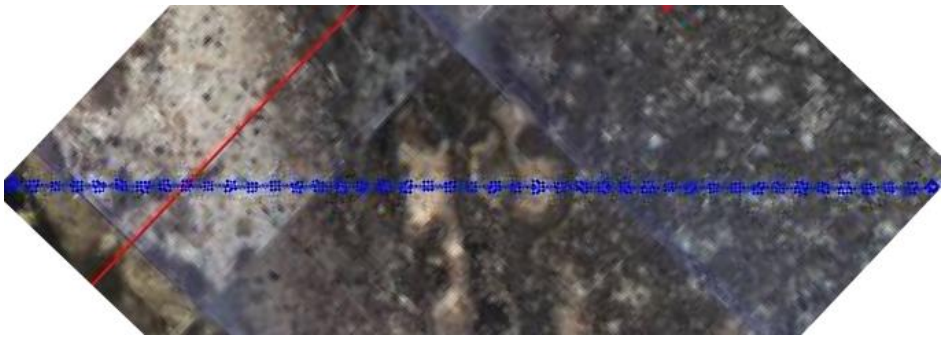

Figure 140 LA-ICP-MS Line 9 results across the sample collected in CFU31-F3 at 10380 ft showing Ca/Si, Ca/Al, and Ca/Fe mole ratios.

Following LA-ICP-MS portions of the sample were crushed and XRD analysis was performed. XRD on the sample collected at 10380 ft was divided into three zones. Zone 1 consisted of the reacted, tan, zone at the control line / casing side of the sample. Zone 2 was in the center of the sample and Zone 3 was at the formation end of the sample. The crystalline phase identifications for each zone are shown in Table 26. All zones analyzed showed carbonation. Zone 1 was the most carbonated with 84 percent of crystalline phases consisting of calcite. Zone 2 was the least carbonated with calcium carbonate making up 12 percent of the crystalline phases. Zone 3 contained 10.7 percent calcite and 19 percent vaterite.

Table 26 XRD data collected on the cement sidewall core sample collected in CFU31-F3 at 10380 ft.

	Zone 1	Zone 2	Zone 3
Phase name	**Weight %**	**Weight %**	**Weight %**
Halite	2.3	15	15.2
Quartz	8.4	10.7	19
Calcite	84	15	12
Vaterite	-	19	-
Faujasite-Ca, dehydrated	-	3	-
Tobermorite M	4.2	-	16.2
Tobermorite 9A	-	38	-
Tilleyite	0.4	-	19
Brownmillerite, Fe-rich	0.1	-	7.1
Wollastonite, ferroan 1A	0.6	-	11

4.2.1.4 CFU31-F3 10450 ft sidewall core sample

The core collected at 10450 ft consisted of solid cement and fiberglass casing (Figure 117). The cement core is uniform in color with no obvious fronts.

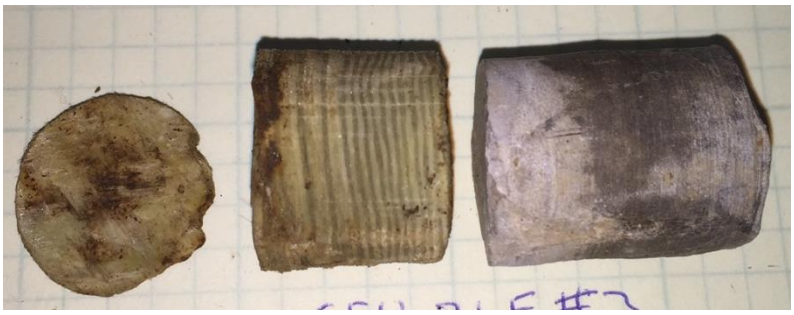

Figure 141 Sidewall core collected in CFU31-F3 at 10450 ft showing fiberglass casing on the left and cement on the right.

Micro-CT images of the cement core (Figure 142) identify a reaction front or a change in material properties from the casing side of the sample to approximately 4-mm into the sample. The CT scan of the casing (Figure 143) shows the casing is internally damaged with multiple partial delaminations. The micro-CT scan was used to select area to cut the sample for further analyses.

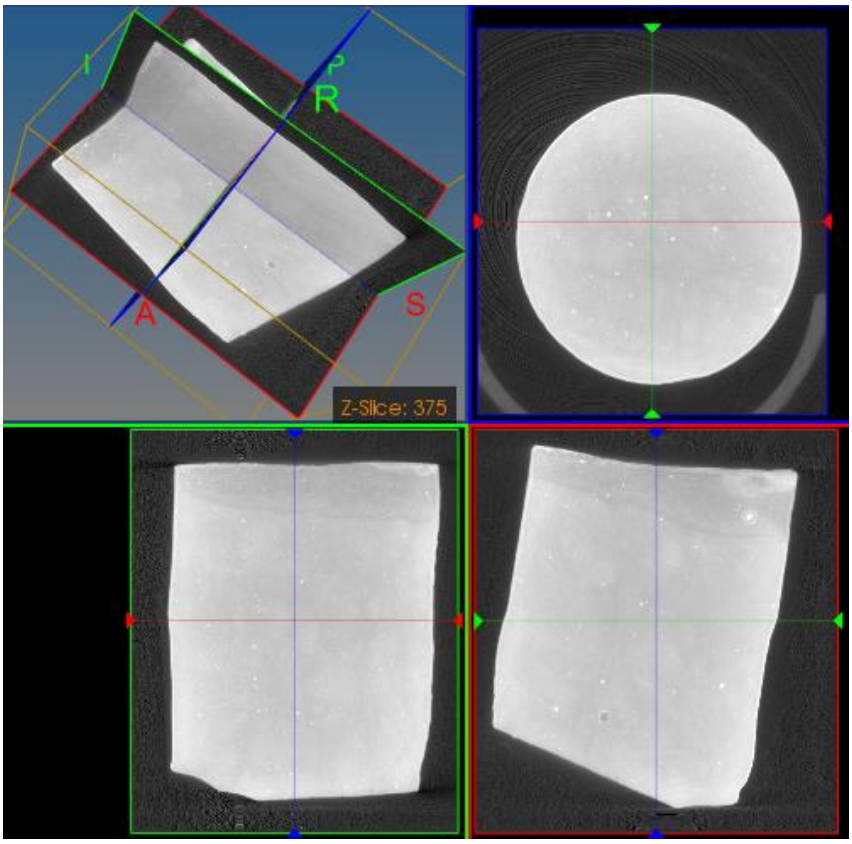

Figure 142 Micro-CT image of the cement sample collected in CFU31-F3 at 10450 ft.

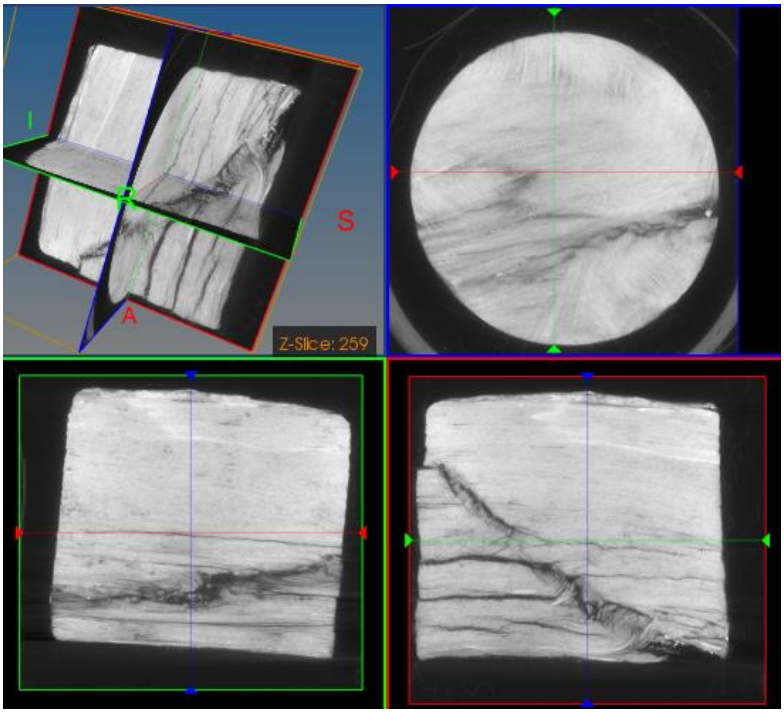

Figure 143 Micro-CT image of the fiberglass sample collected in CFU31-F3 at 10450 ft.

Sectioning of the sample (Figure 144) confirmed the fronts apparent in the micro-CT images. The fronts visible in the sectioned sample are a 4-mm-wide tan front followed by an 1/2-mm-wide light grey front.

Figure 144 Cement sidewall core collected in CFU31-F3 at 10450 ft.

The sectioned sidewall core was analyzed using LA-ICP-MS starting on the formation side and moving toward the casing side of the sample. The LA-ICP-MS scan line images and corresponding data are presented in Figure 144 through Figure 159. The first line (Figure 145 and Figure 146) starts out measuring the tan zone (0 to 1300 microns) at the end of the casing side of the sample and then measures the light grey zone (1,300 to 5,200 microns). In the tan zone the Ca/Si has several peaks and ranges between 0.5 and 7. In the light grey zone the Ca/Si begins with a value around 1 and slowly rises to around 1.25. Line 2 (Figure 147 and Figure 148) shows Ca/Si slowly rises from around 1.3 to 1.5 over the length of the line. Lines 3 through 5 (Figure 149 to Figure 153) are generally flat with Ca/Si around 1.5. Line 6 (Figure 154 and Figure 155) is similar to Lines 3 through 5 from the beginning of the line to 3,480 microns where the Line meets the light tan front and Ca/Si jumps to around 3 and then drops off to 1.25 at the end of the sample. The last two lines in the sample are along a crack (Line 7; Figure 156 and Figure 157) and parallel to the crack (Line 8; Figure 158 and Figure 159). The Ca/Si over both scans is similar with values of Ca/Si around 1.6.

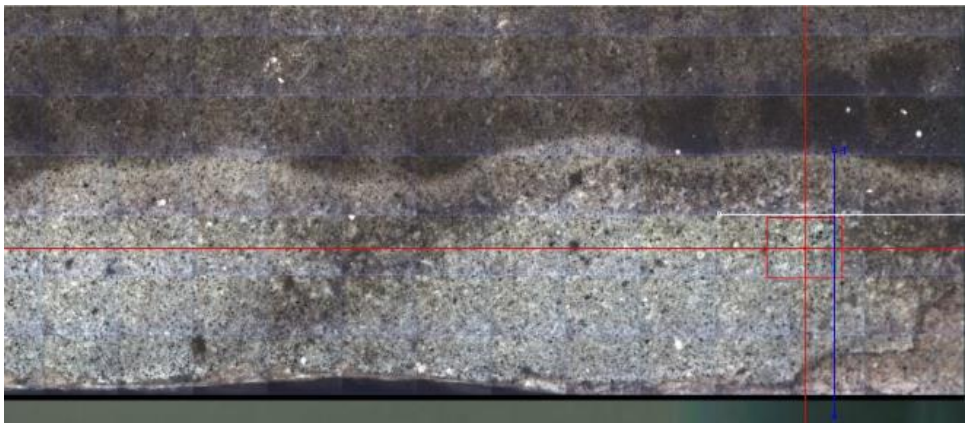

Figure 145 LA-ICP-MS Line 1 across the sample collected in CFU31-F3 at 10450 ft.

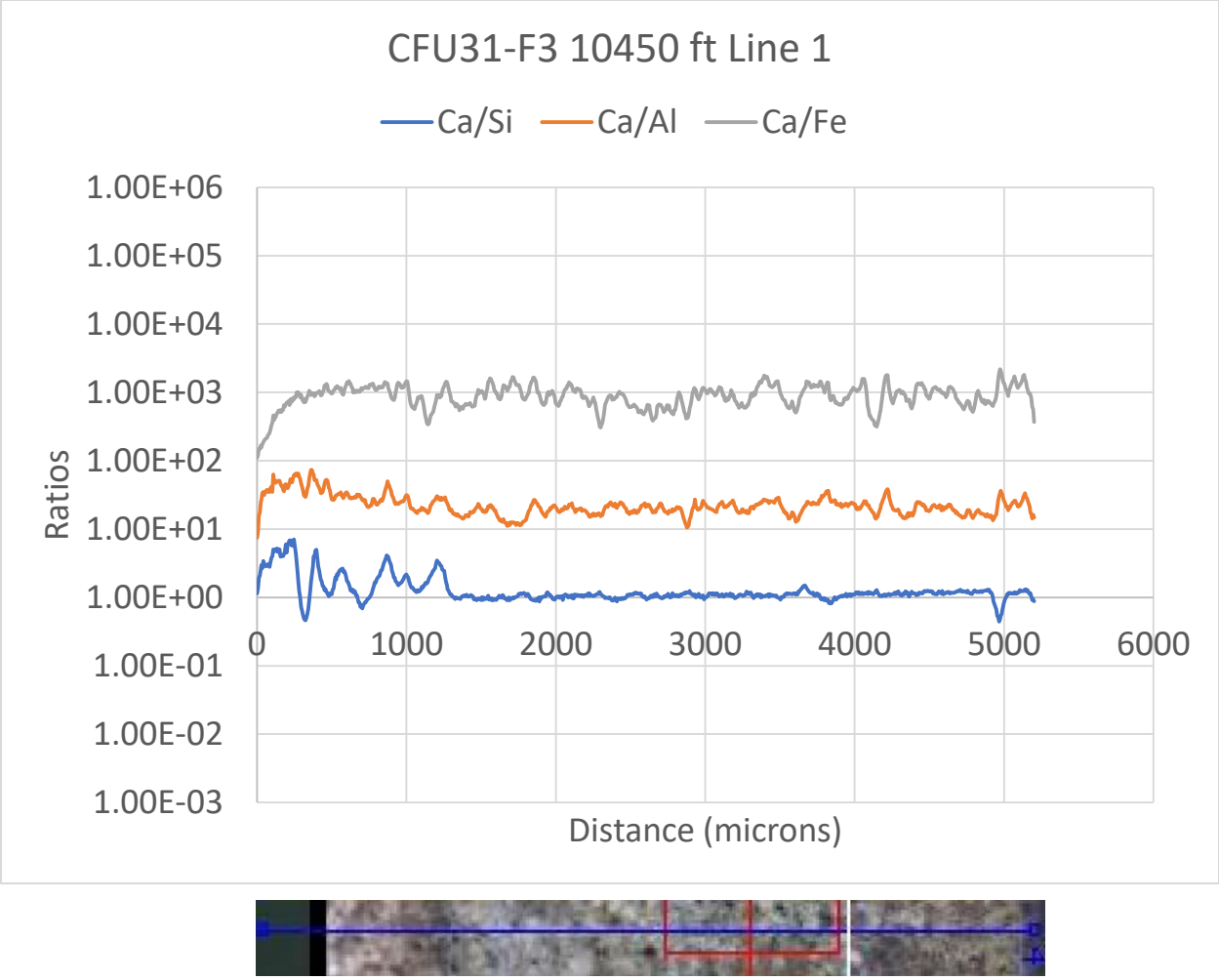

Figure 146 LA-ICP-MS Line 1 results across the sample collected in CFU31-F3 at 10450 ft showing Ca/Si, Ca/Al, and Ca/Fe mole ratios.

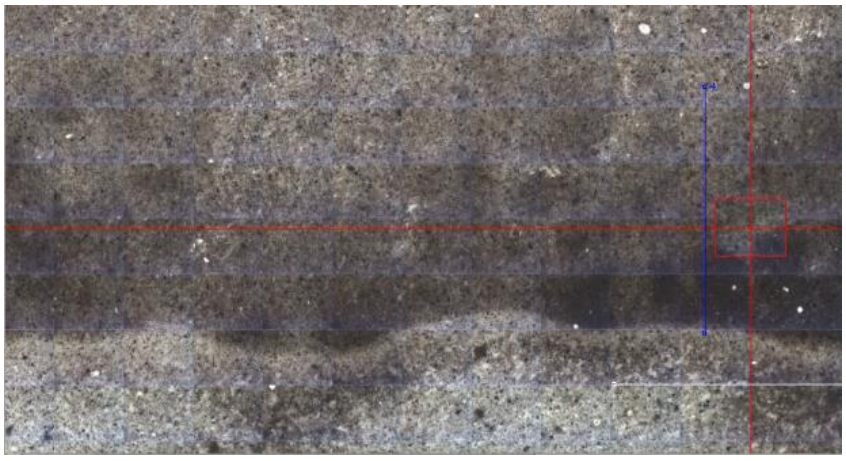

Figure 147 LA-ICP-MS Line 2 across the sample collected in CFU31-F3 at 10450 ft.

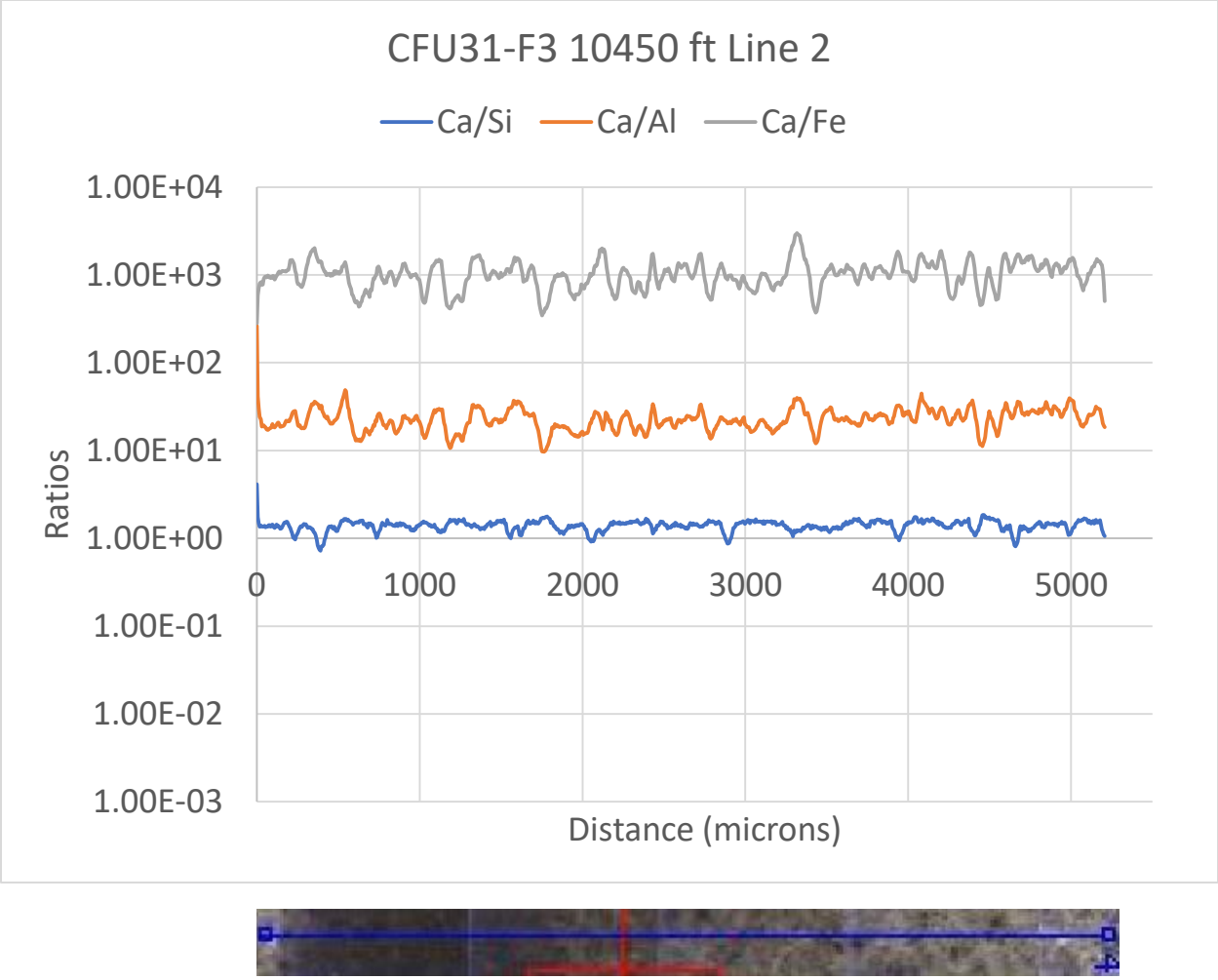

Figure 148 LA-ICP-MS Line 2 results across the sample collected in CFU31-F3 at 10450 ft showing Ca/Si, Ca/Al, and Ca/Fe mole ratios.

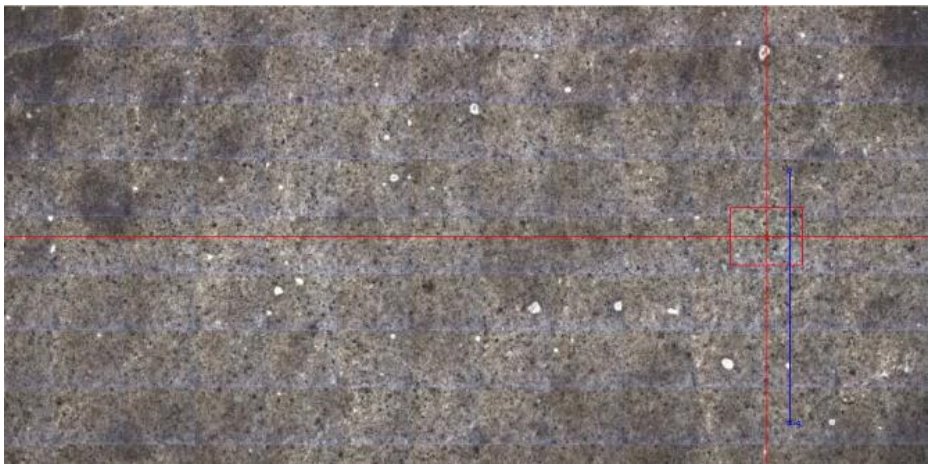

Figure 149 LA-ICP-MS Line 3 across the sample collected in CFU31-F3 at 10450 ft.

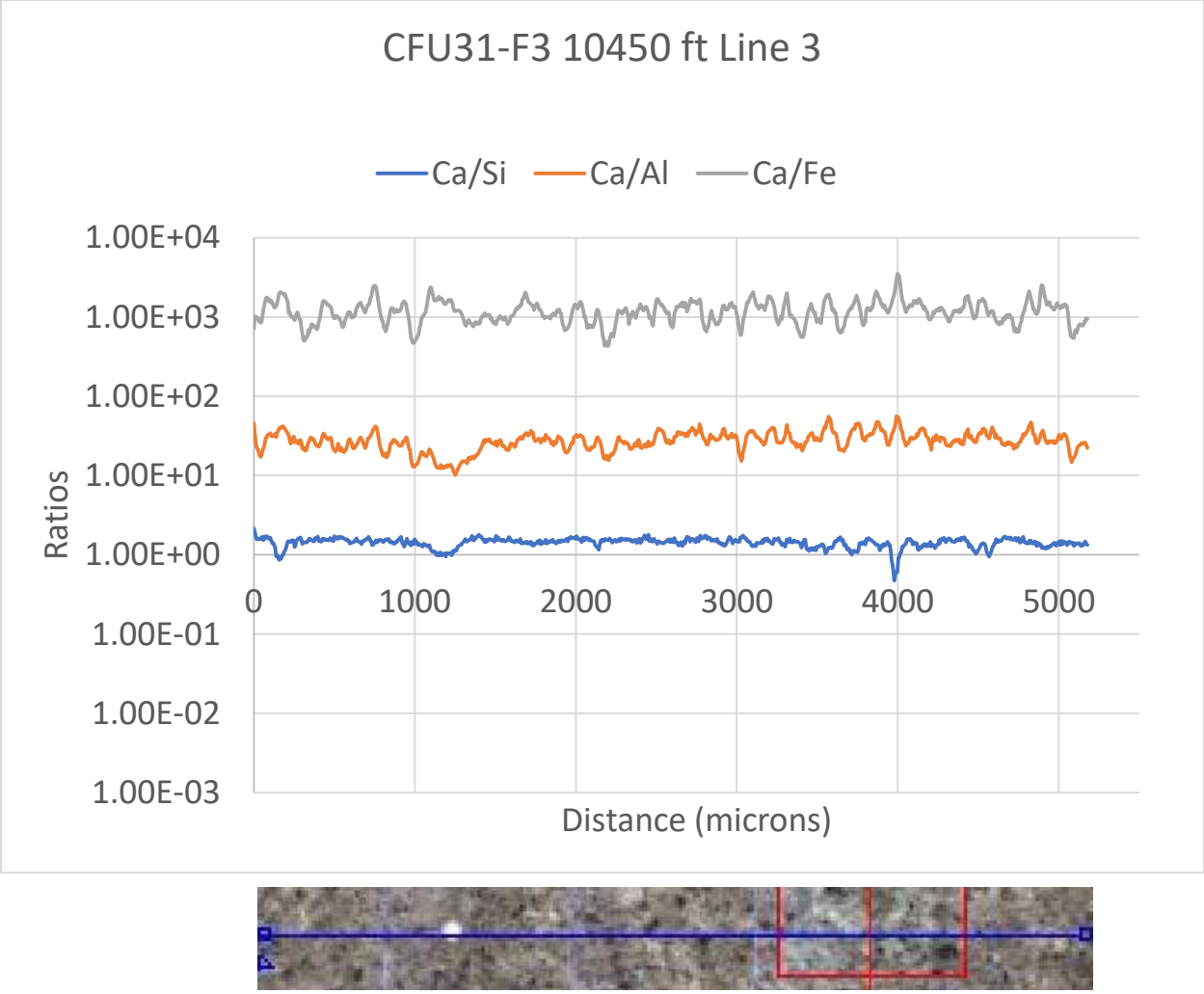

Figure 150 LA-ICP-MS Line 3 results across the sample collected in CFU31-F3 at 10450 ft showing Ca/Si, Ca/Al, and Ca/Fe mole ratios.

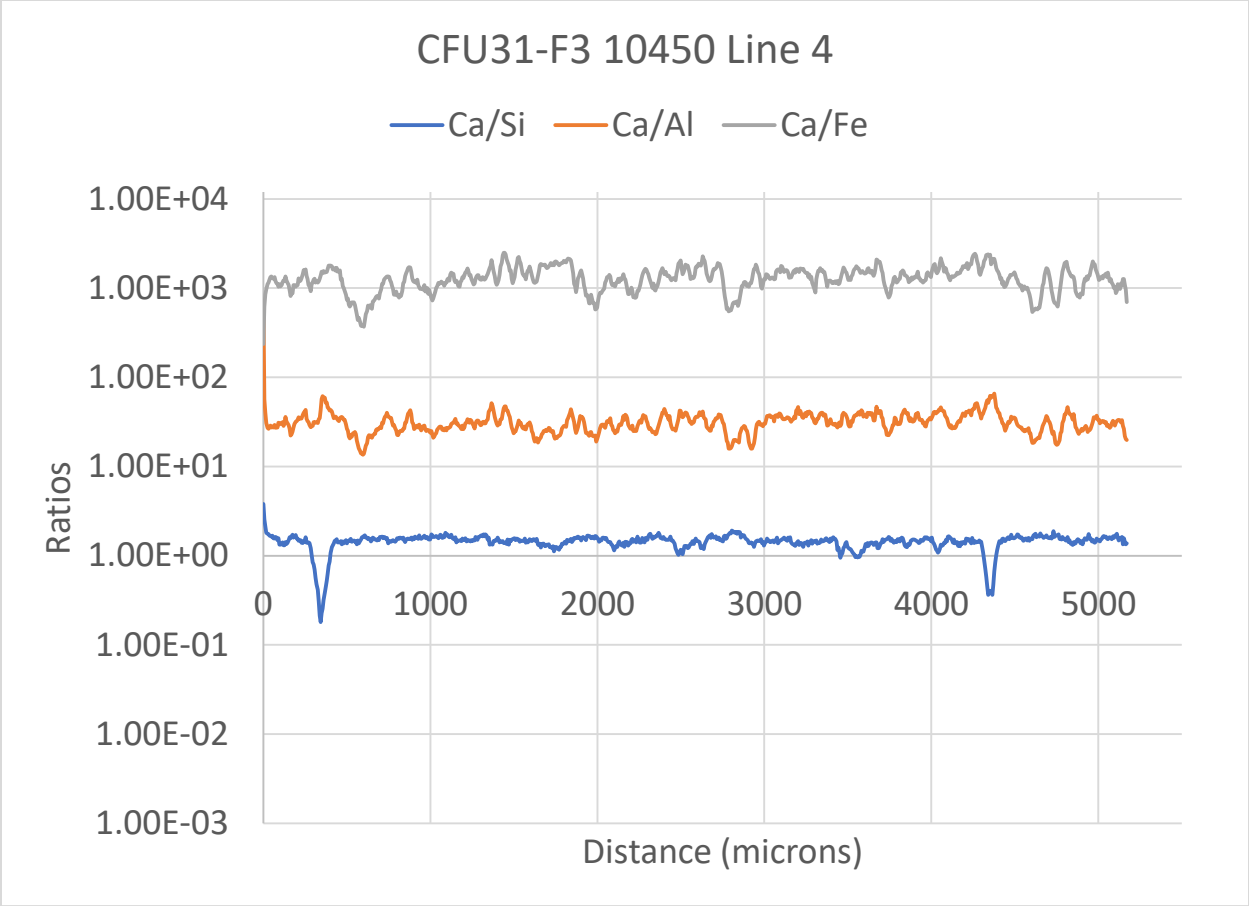

Figure 151 LA-ICP-MS Line 4 results across the sample collected in CFU31-F3 at 10450 ft showing Ca/Si, Ca/Al, and Ca/Fe mole ratios.

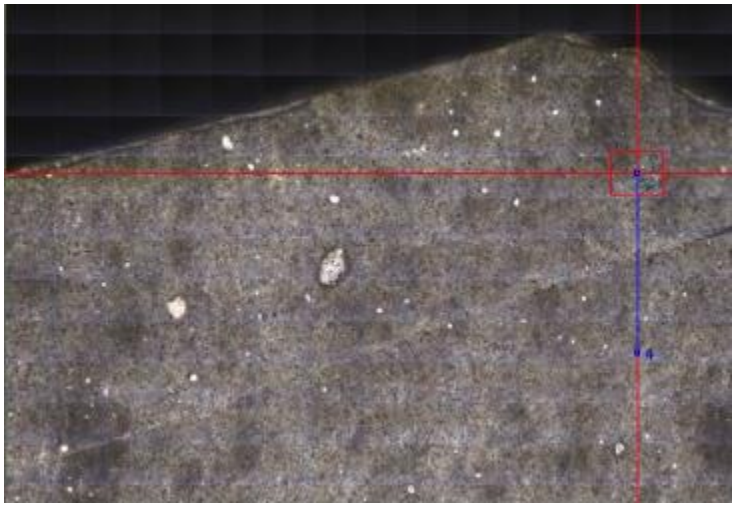

Figure 152 LA-ICP-MS Line 5 across the sample collected in CFU31-F3 at 10450 ft.

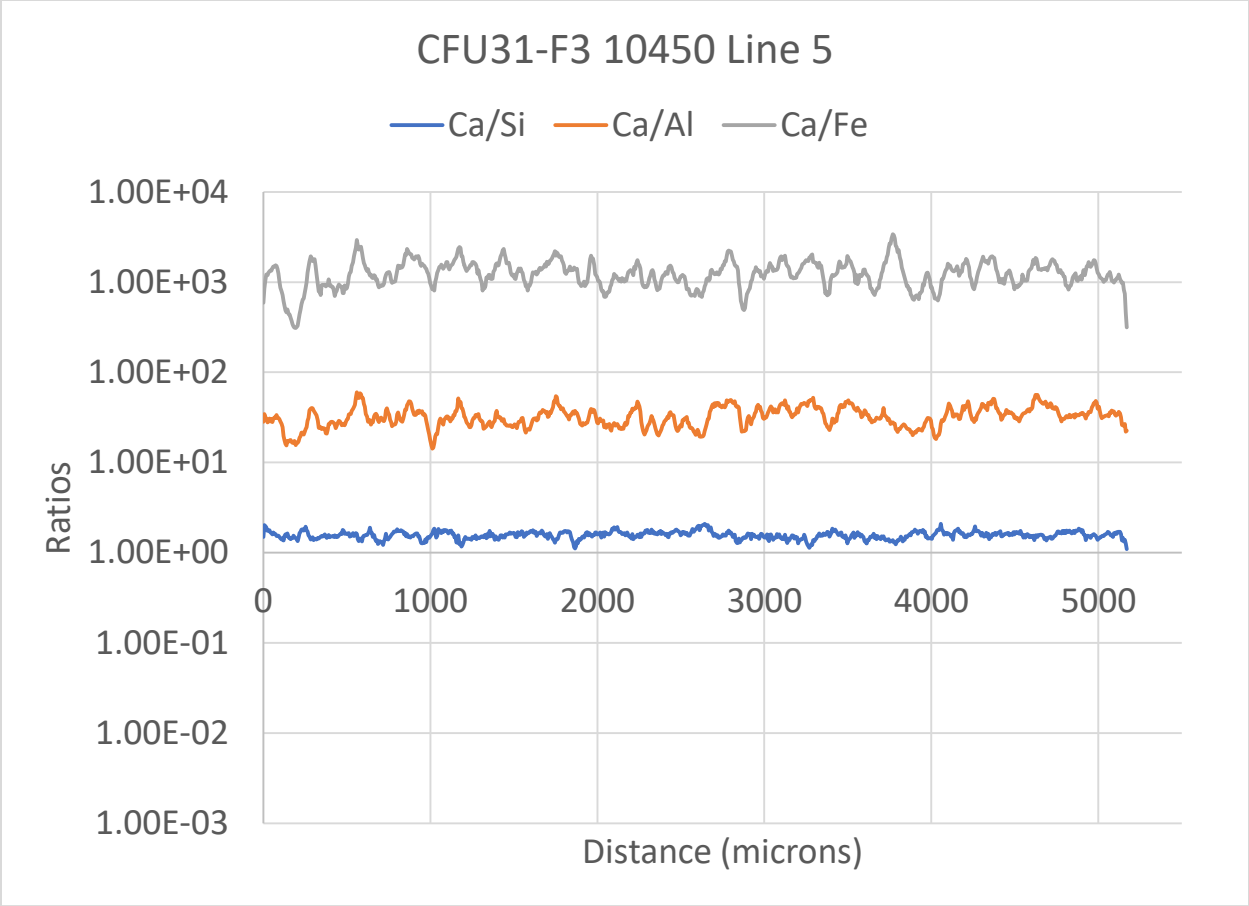

Figure 153 LA-ICP-MS Line 5 results across the sample collected in CFU31-F3 at 10450 ft showing Ca/Si, Ca/Al, and Ca/Fe mole ratios.

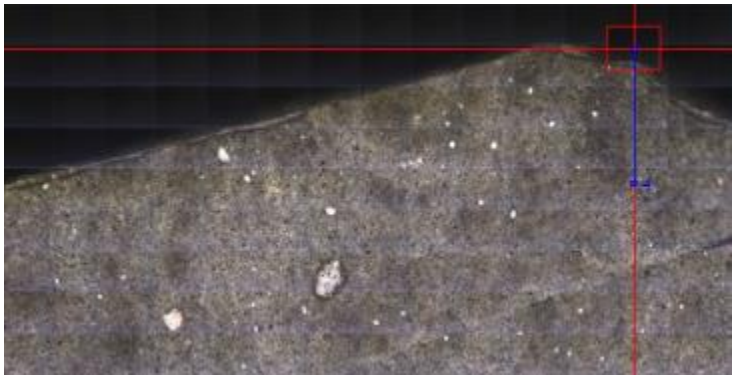

Figure 154 LA-ICP-MS Line 6 across the sample collected in CFU31-F3 at 10450 ft.

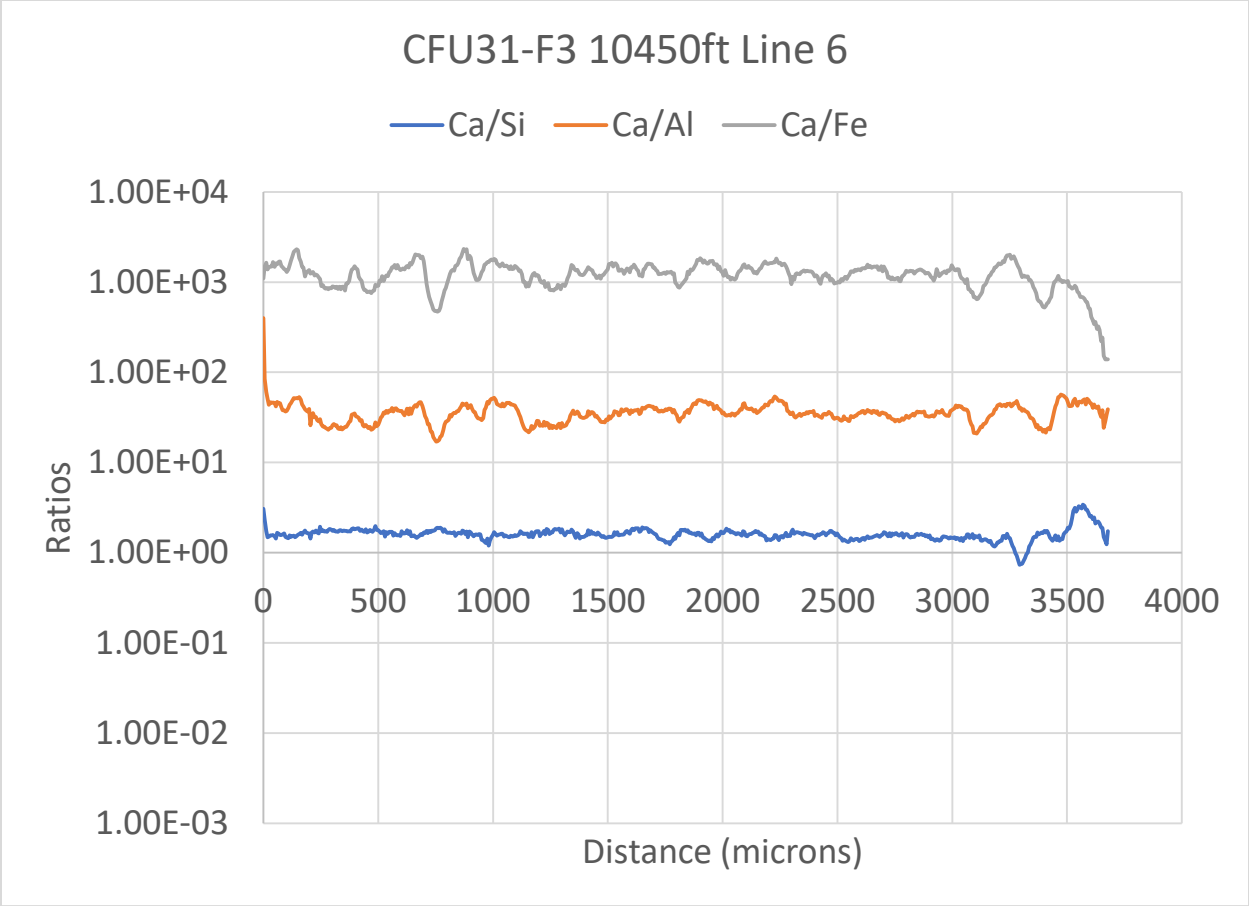

Figure 155 LA-ICP-MS Line 6 results across the sample collected in CFU31-F3 at 10450 ft showing Ca/Si, Ca/Al, and Ca/Fe mole ratios.

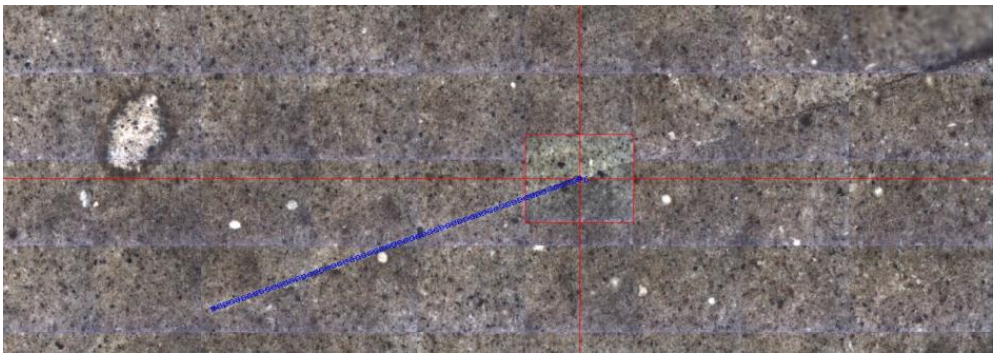

Figure 156 LA-ICP-MS Line 7 across the sample collected in CFU31-F3 at 10450 ft.

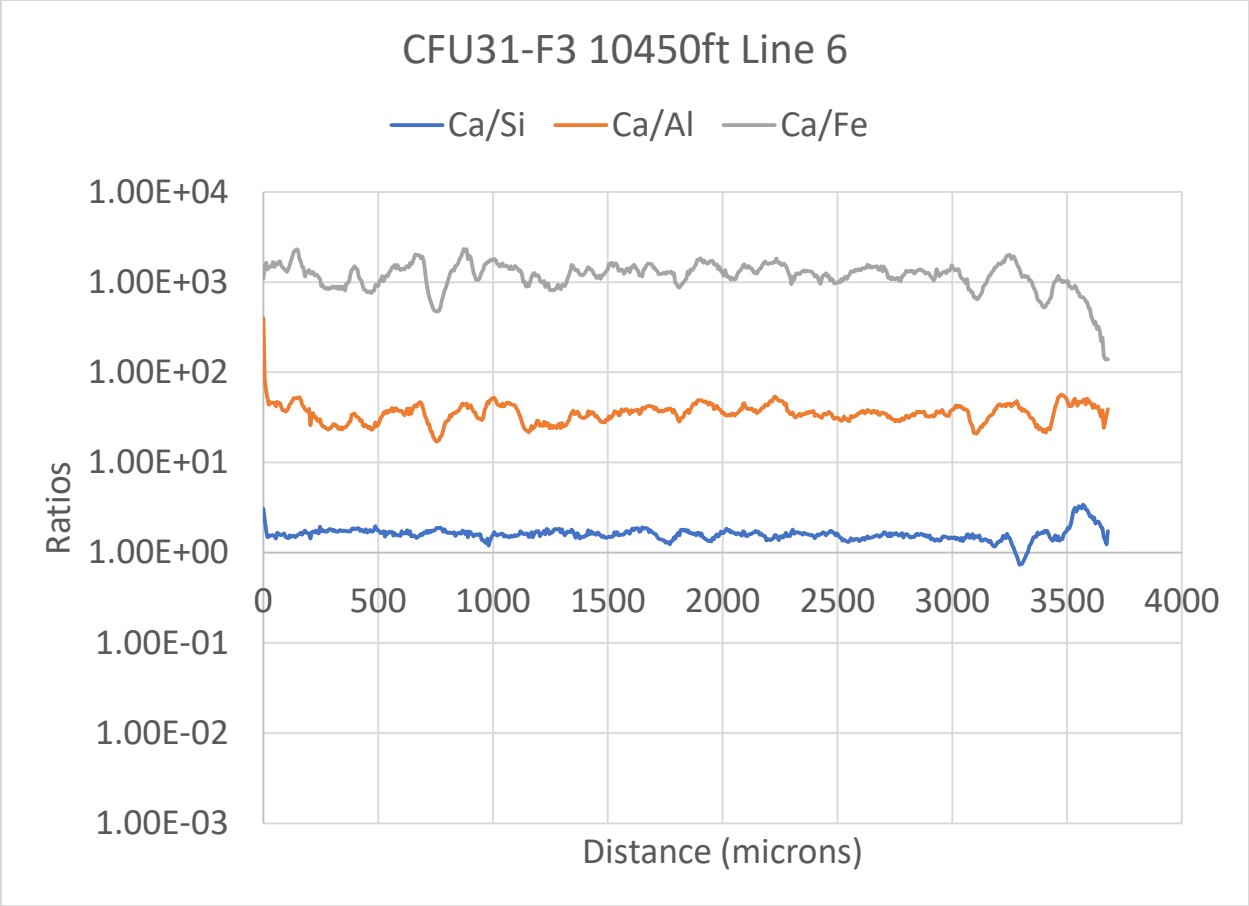

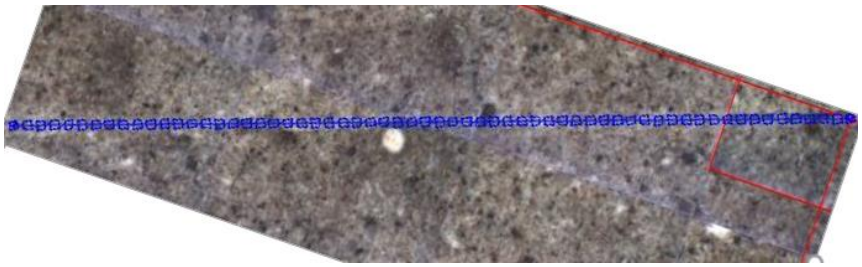

Figure 157 LA-ICP-MS Line 7 results across the sample collected in CFU31-F3 at 10450 ft showing Ca/Si, Ca/Al, and Ca/Fe mole ratios.

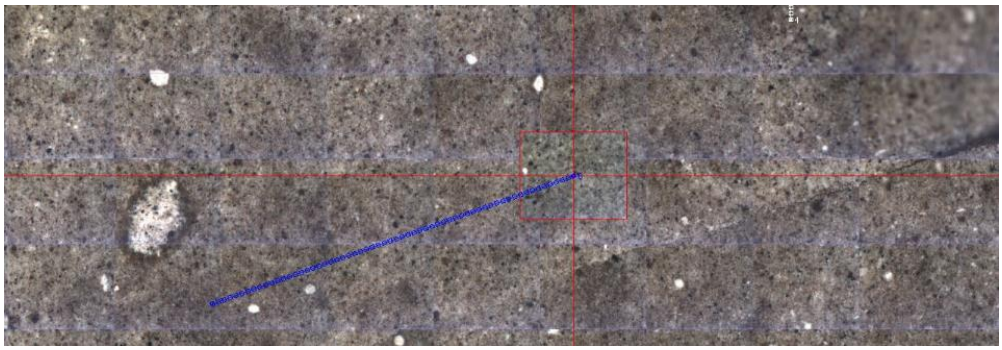

Figure 158 LA-ICP-MS Line 8 across the sample collected in CFU31-F3 at 10450 ft.

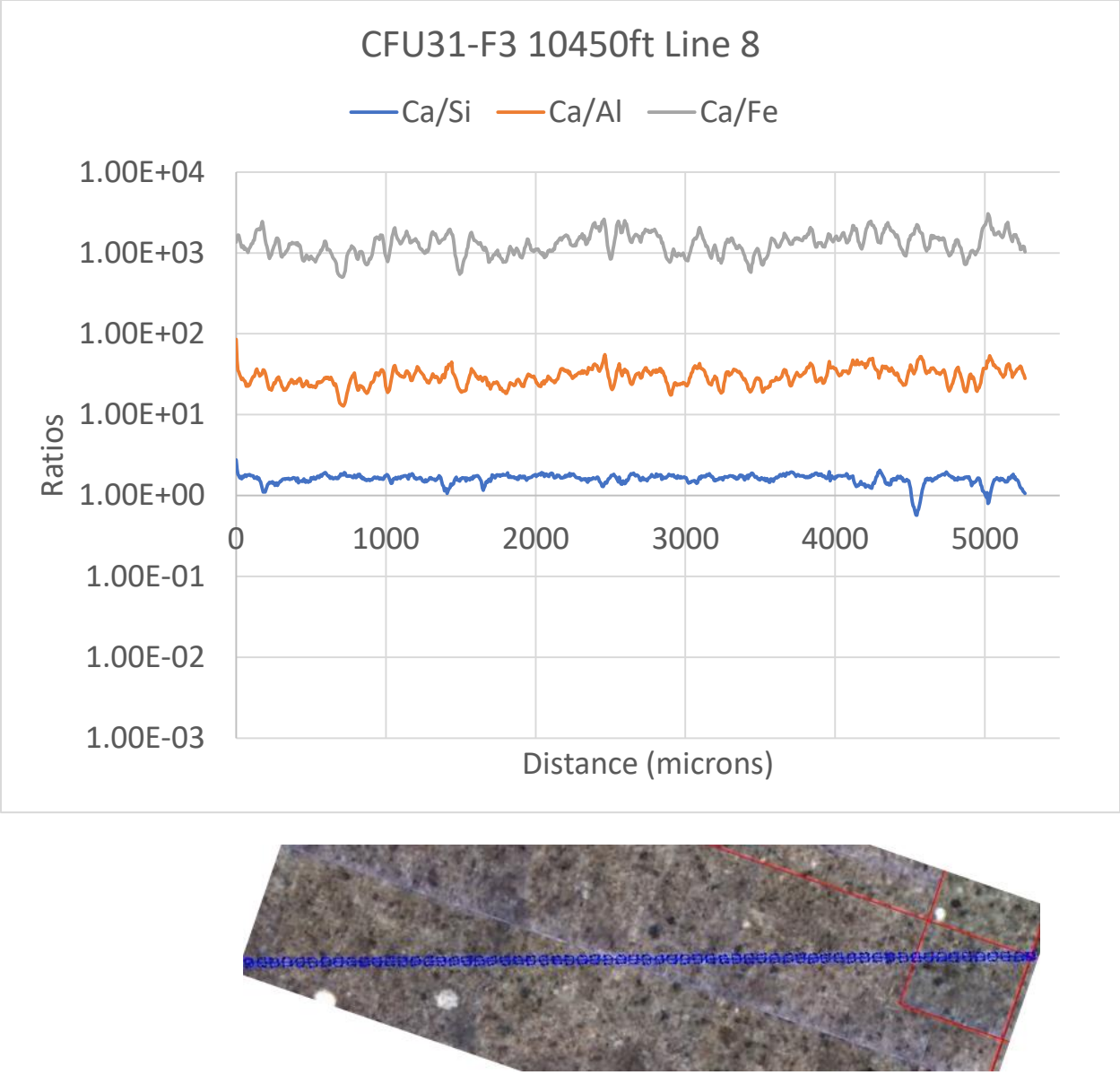

Figure 159 LA-ICP-MS Line 8 results across the sample collected in CFU31-F3 at 10450 ft showing Ca/Si, Ca/Al, and Ca/Fe mole ratios.

Following LA-ICP-MS portions of the sample were crushed and XRD analysis was performed. XRD on the sample collected at 10450 ft was divided into two zones. Zone 1 consisted of the reacted zones on the casing side of the sample and Zone 2 was a portion of the visually unreacted center of the sample. Table 27 shows the XRD data collected. The data from both zones if somewhat similar with both zones being carbonated. Zone 1 has 28 percent calcite and 19 percent vaterite and Zone 2 has 29 percent calcite and 13 percent vaterite.

Table 27 XRD data for the cement sidewall core collected in CFU31-F3 at 10450 ft.

	Zone 1	Zone 2
Phase name	**Weight %**	**Weight %**
Calcite	28	29
Tobermorite M	20	20
Halite	6	9
Vaterite	19	13
Brownmillerite	2	10
Faujasite (dehydrated, Ca-exchanged)	4.2	2.9
Quartz	21	16

4.2.1.5 CFU31-F3 10470 ft sidewall core sample

The core collected at 10470 ft consisted of solid cement and fiberglass casing (Figure 160). The cement core is uniform in color with no obvious fronts. The casing exhibited some delamination.

Figure 160 Sidewall core collected in CFU31-F3 at 10470 ft showing fiberglass casing on the left and cement on the left.

Micro-CT images of the cement core (Figure 161) identify multiple reactions fronts or changes in material moving roughly perpendicular to the long axis of the sample. The CT scan of the casing (Figure 162) shows the casing has a partial delamination. The micro-CT scan of the cement was used to select area to cut the sample for further analyses.

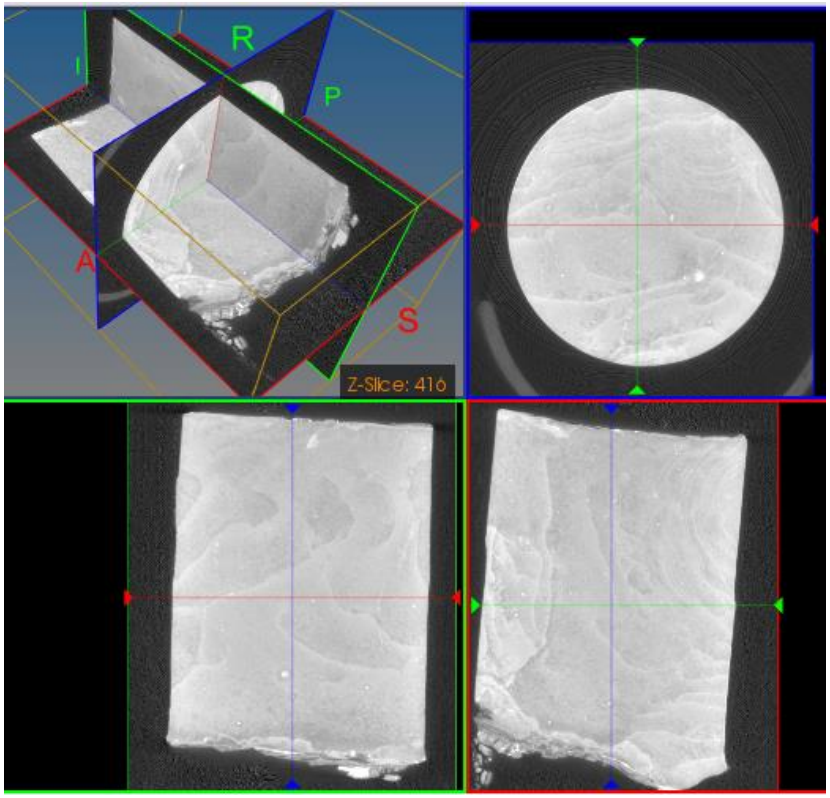

Figure 161 Micro-CT image of the cement sample collected in CFU31-F3 at 10470 ft.

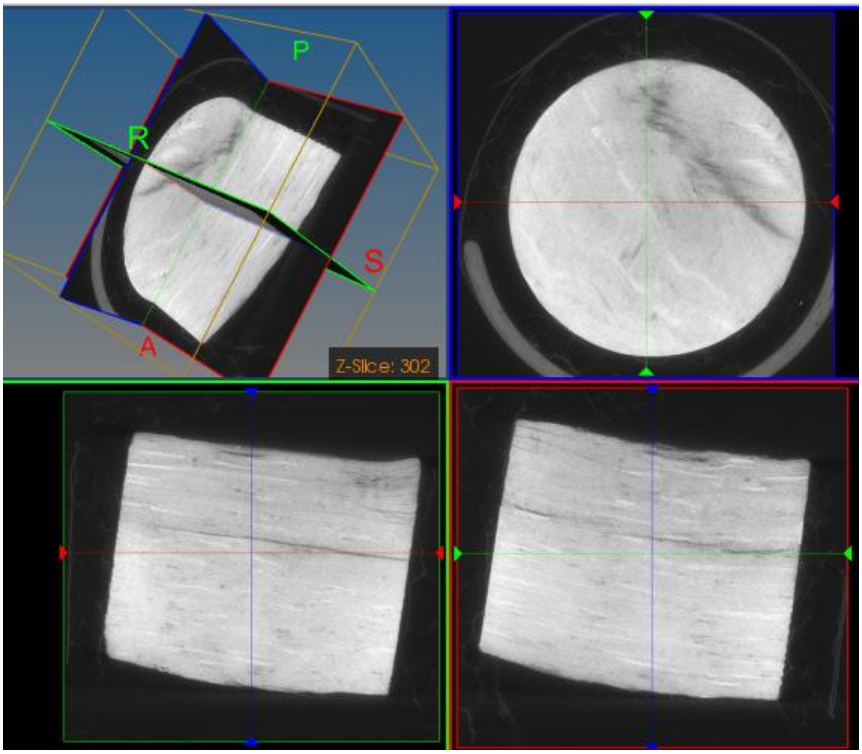

Figure 162 Micro-CT image of the fiberglass sample collected in CFU31-F3 at 10470 ft.

Sectioning of the sample (Figure 163) confirmed multiple fronts moving into or across the sample from ends moving along the long axis of the sample and in the center of the sample moving perpendicular to the long axis of the sample.

Figure 163 Cement sidewall core collected in CFU31-F3 at 10470 ft.

The sectioned sidewall core was analyzed with LA-ICP-MS starting on the formation side and moving toward the casing side of the sample. The LA-ICP-MS scan line images and corresponding data are presented in Figure 164 through Figure 177. Lines 1 through 6 (Figure 164 through Figure 175) are parallel to the long-axis of the sample. These lines show variation in the elemental ratios throughout the sample with definite changes at transitions between fronts. Line 7 (Figure 176 and Figure 177) is a scan running perpendicular to the long-axis of the sample from the edge towards the center.

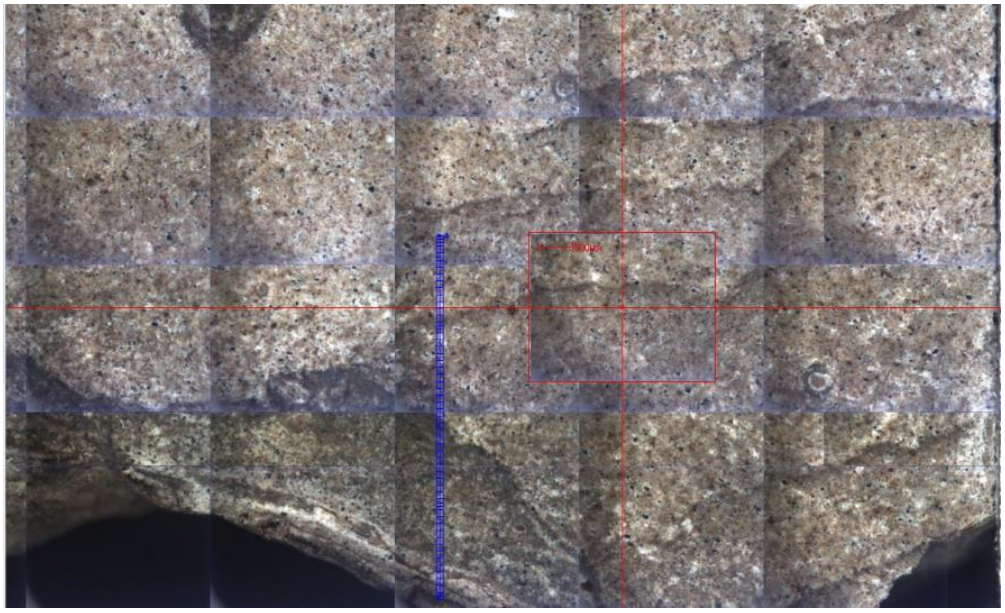

Figure 164 LA-ICP-MS Line 1 across the sample collected in CFU31-F3 at 10470 ft.

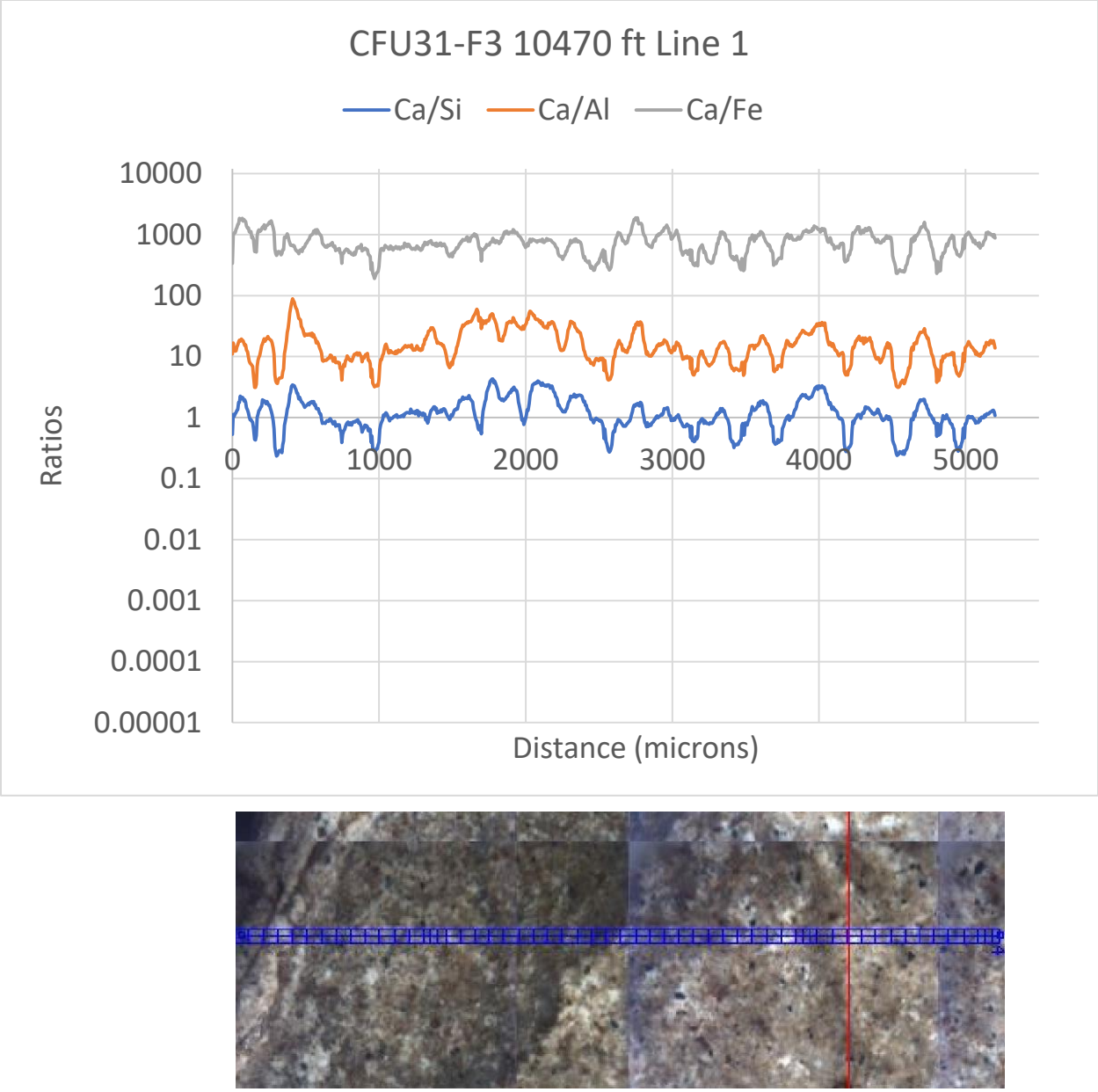

Figure 165 LA-ICP-MS Line 1 results across the sample collected in CFU31-F3 at 10470 ft showing Ca/Si, Ca/Al, and Ca/Fe mole ratios.

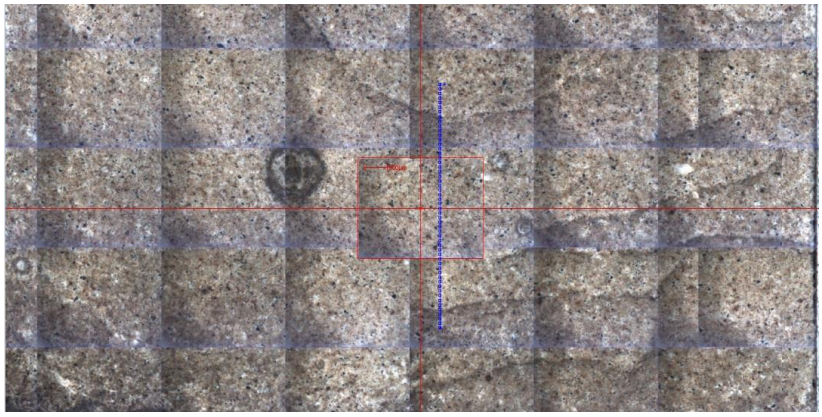

Figure 166 LA-ICP-MS Line 2 across the sample collected in CFU31-F3 at 10470 ft.

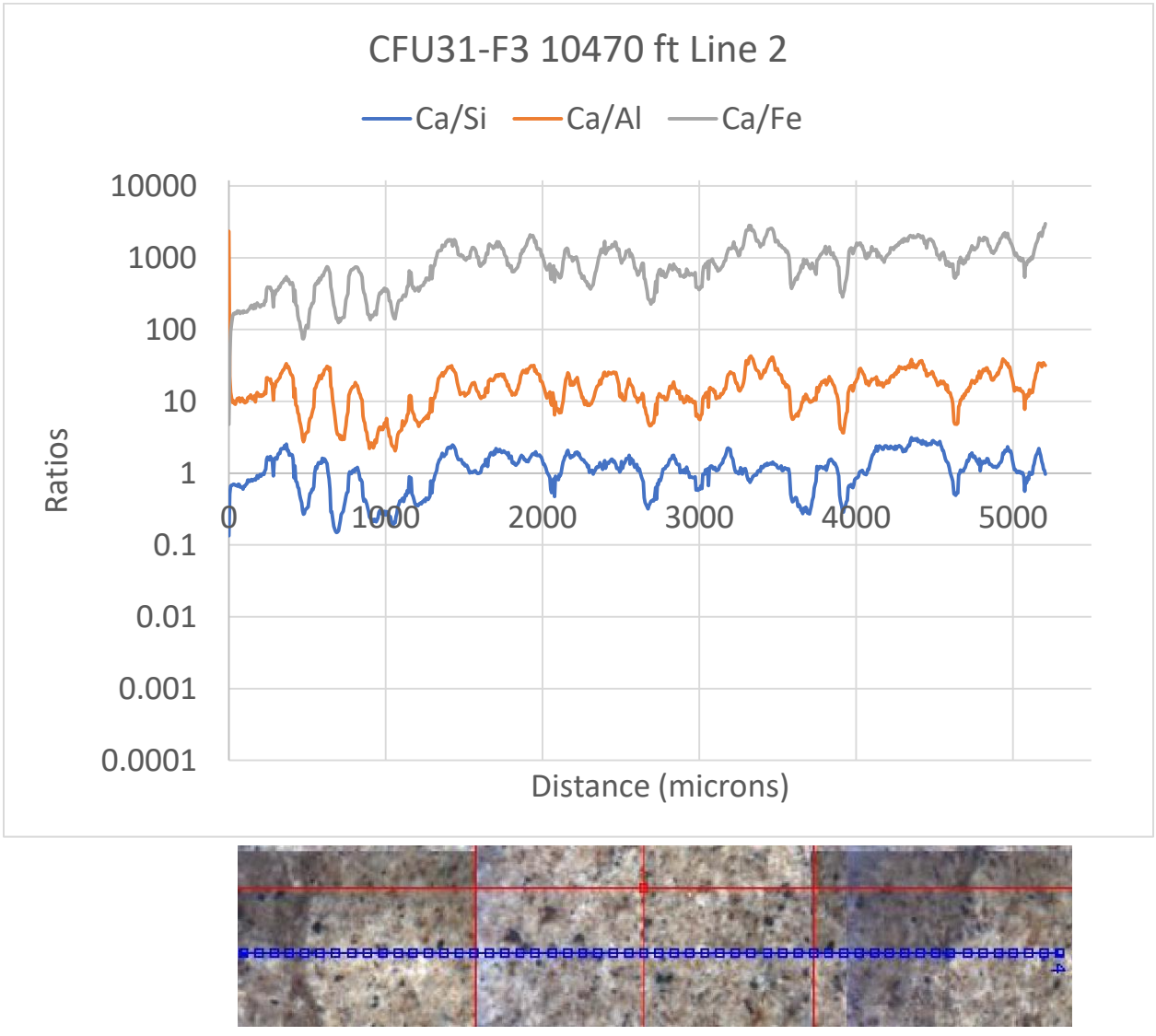

Figure 167 LA-ICP-MS Line 2 results across the sample collected in CFU31-F3 at 10470 ft showing Ca/Si, Ca/Al, and Ca/Fe mole ratios.

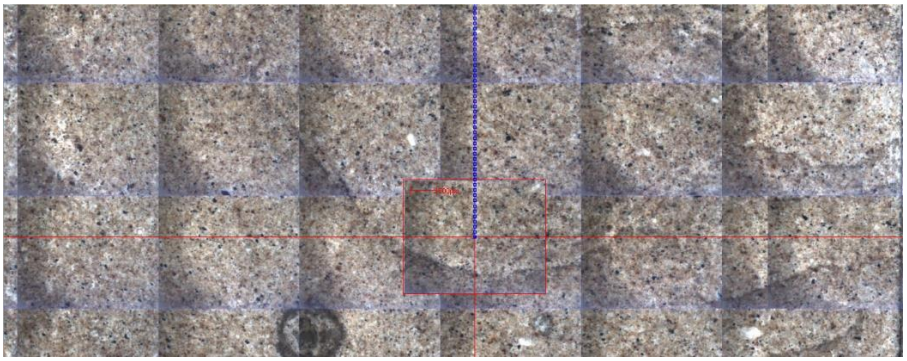

Figure 168 LA-ICP-MS Line 3 across the sample collected in CFU31-F3 at 10470 ft.

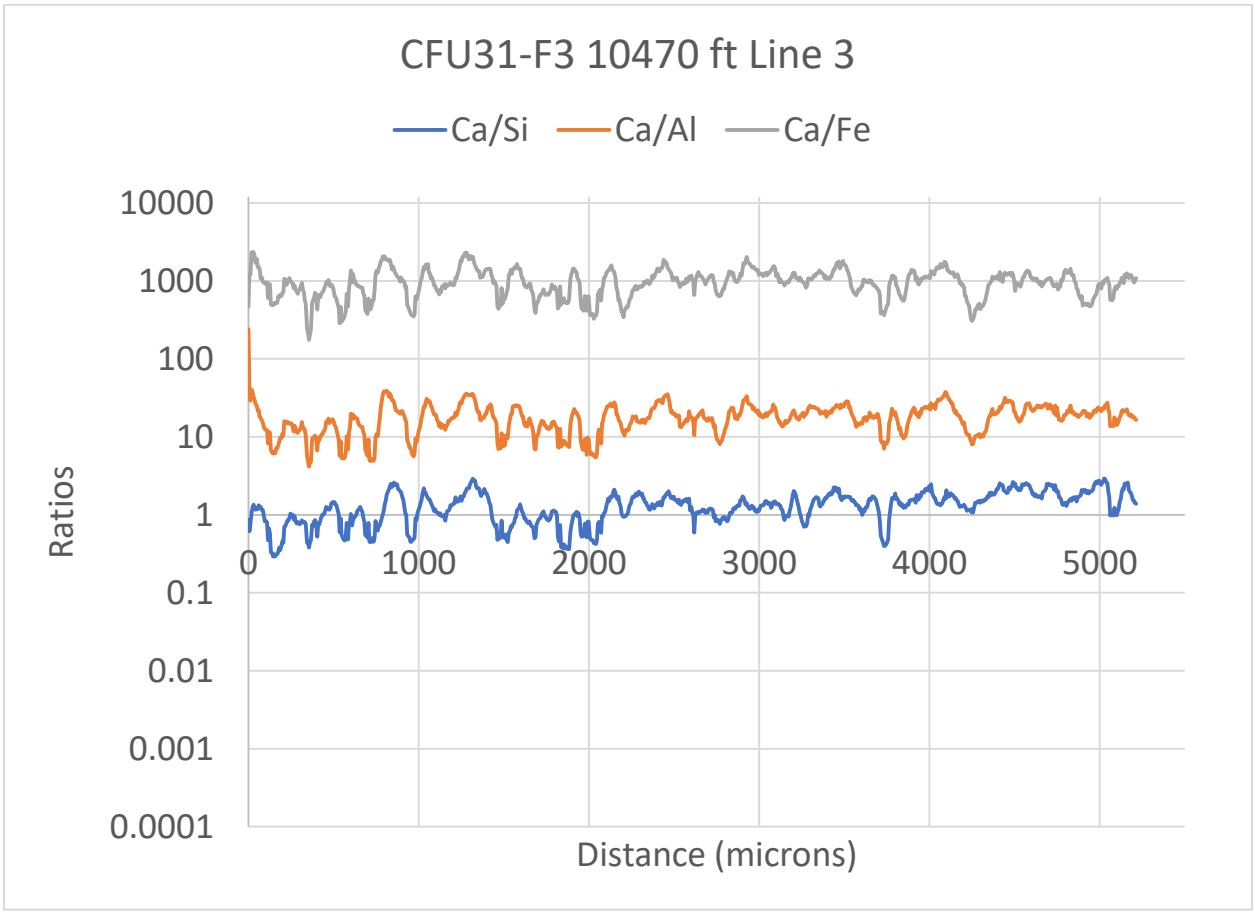

Figure 169 LA-ICP-MS Line 3 results across the sample collected in CFU31-F3 at 10470 ft showing Ca/Si, Ca/Al, and Ca/Fe mole ratios.

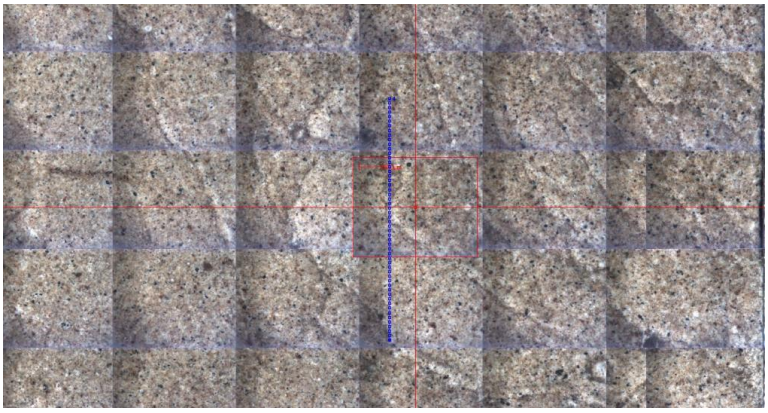

Figure 170 LA-ICP-MS Line 4 across the sample collected in CFU31-F3 at 10470 ft.

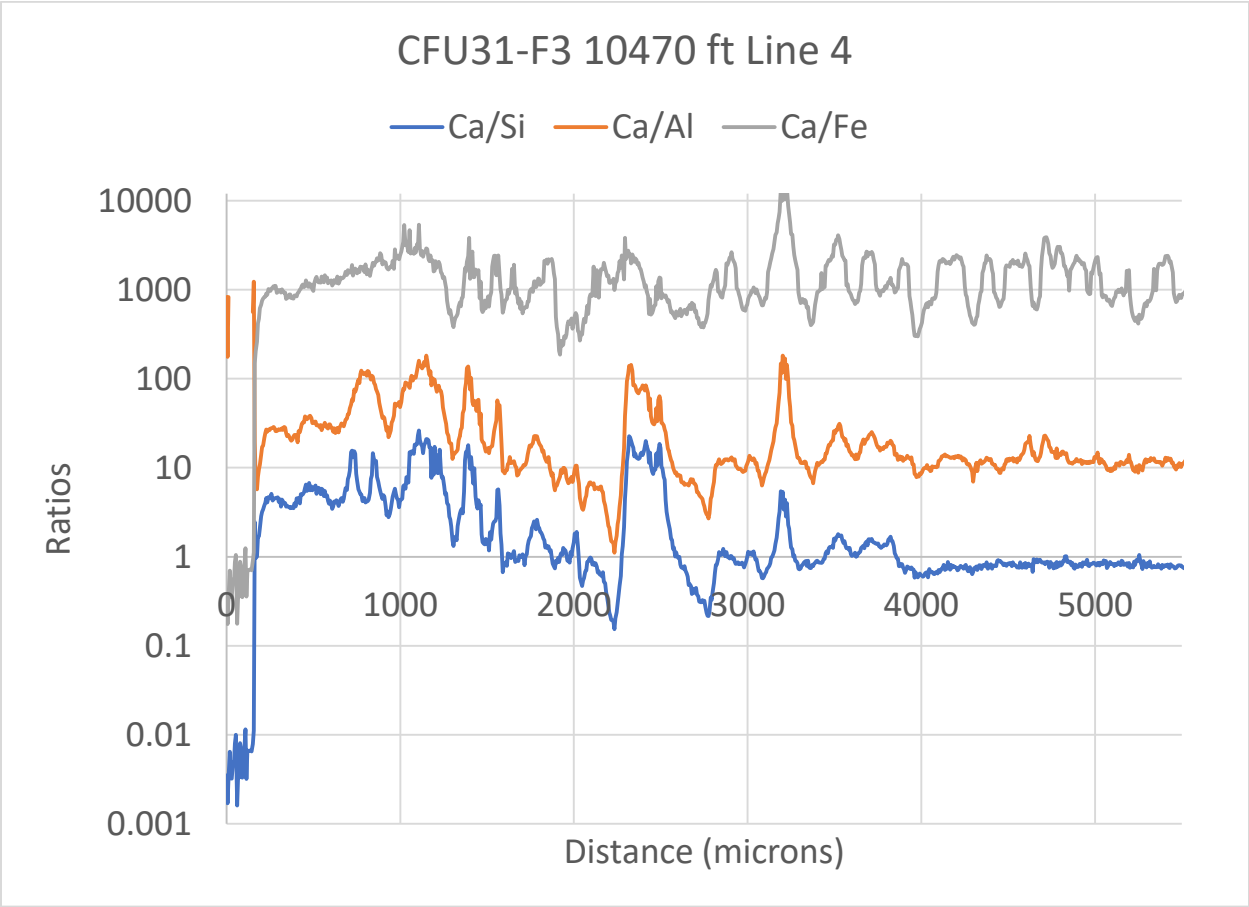

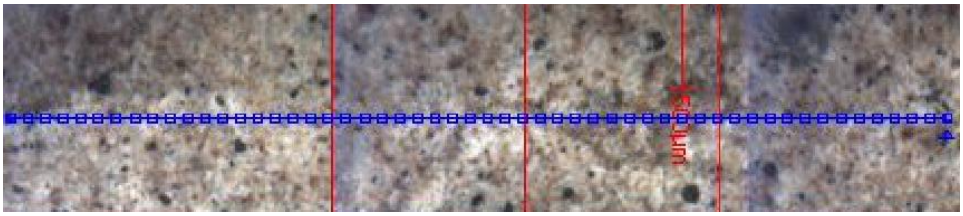

Figure 171 LA-ICP-MS Line 4 results across the sample collected in CFU31-F3 at 10470 ft showing Ca/Si, Ca/Al, and Ca/Fe mole ratios.

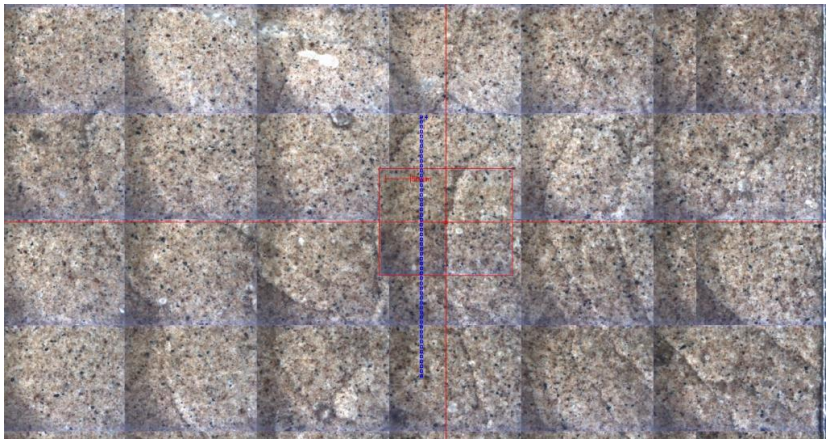

Figure 172 LA-ICP-MS Line 5 across the sample collected in CFU31-F3 at 10470 ft.

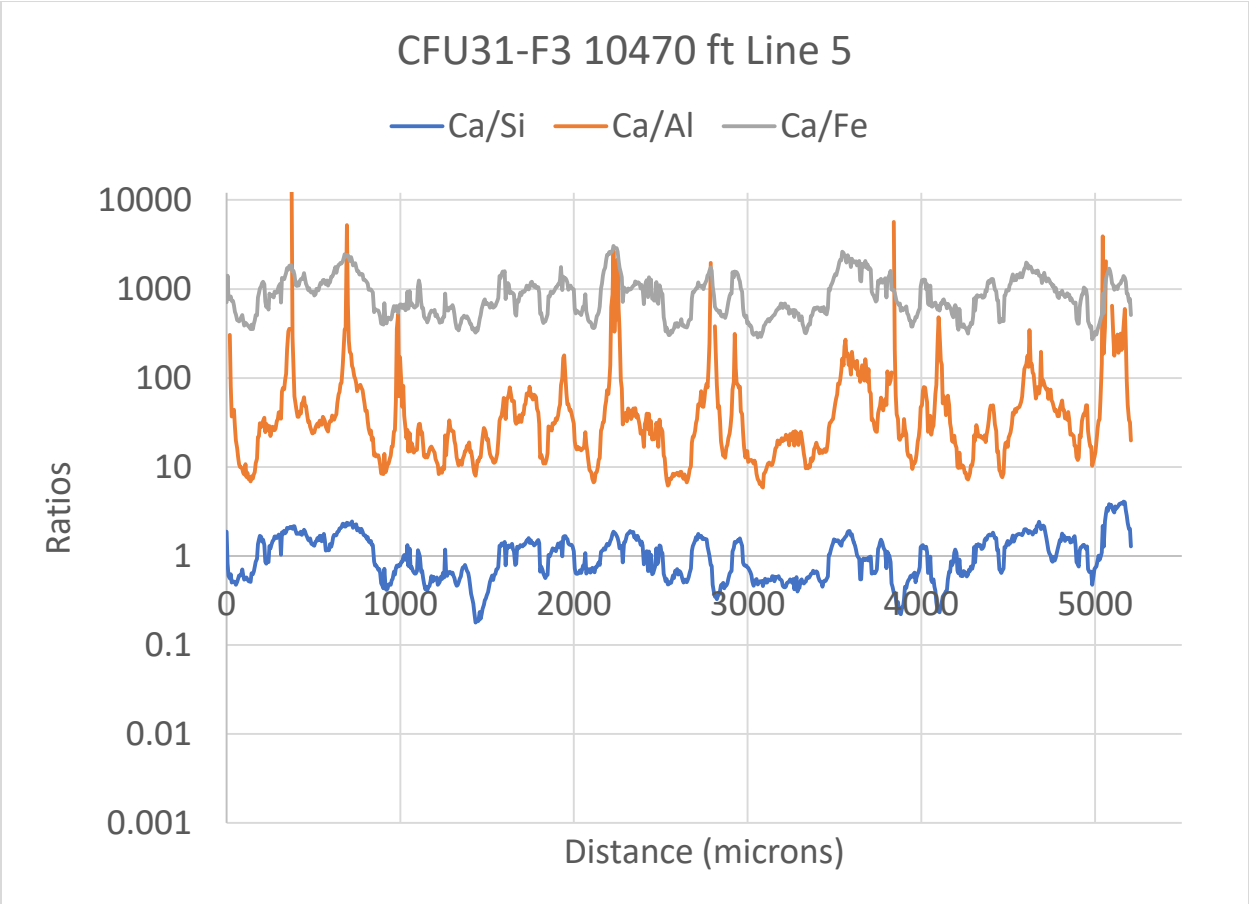

Figure 173 LA-ICP-MS Line 5 results across the sample collected in CFU31-F3 at 10470 ft showing Ca/Si, Ca/Al, and Ca/Fe mole ratios.

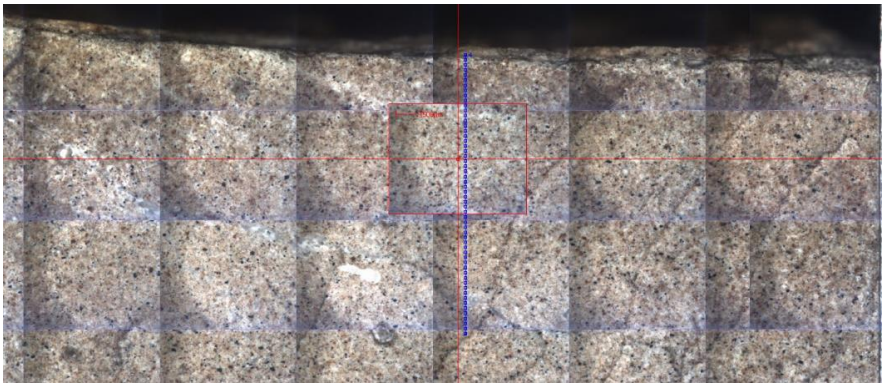

Figure 174 LA-ICP-MS Line 6 across the sample collected in CFU31-F3 at 10470 ft.

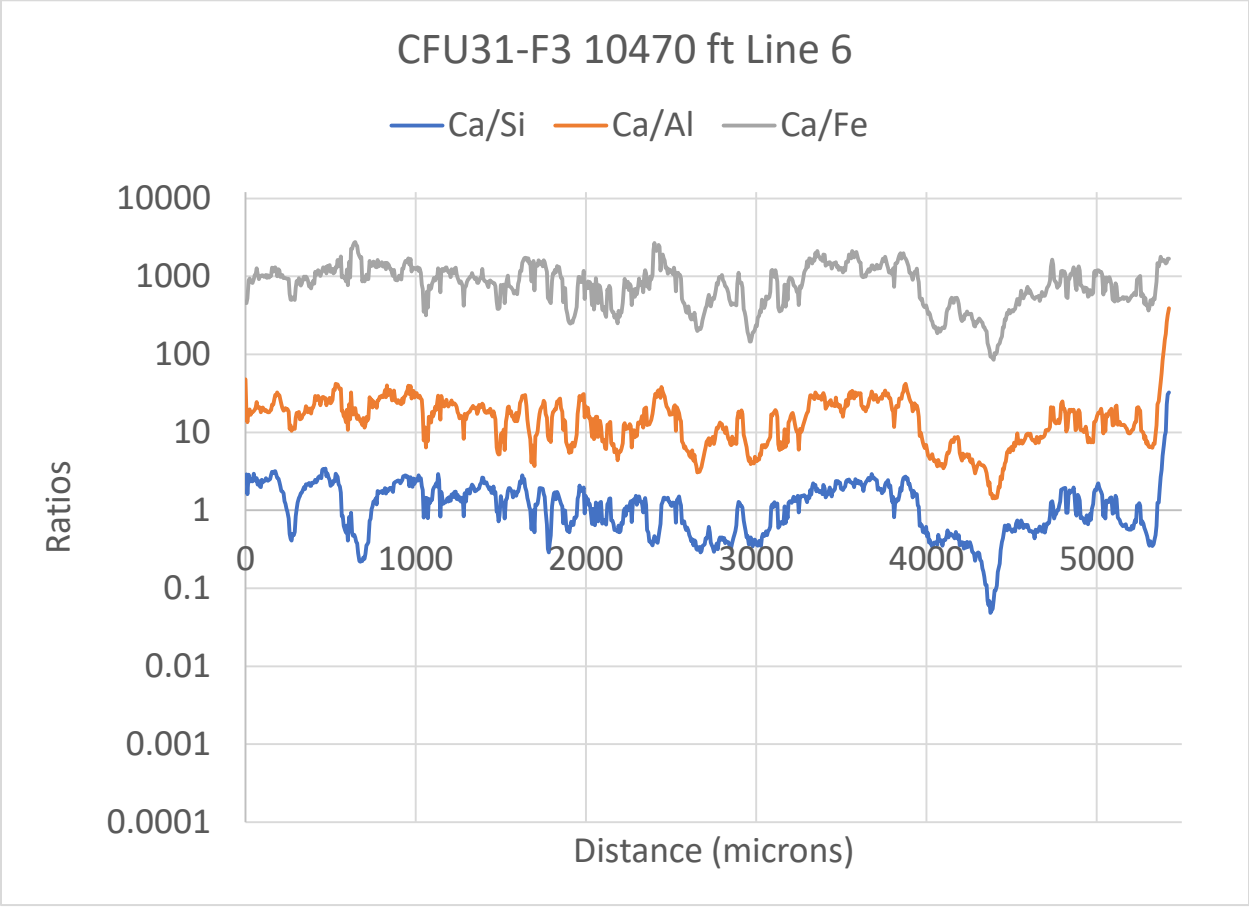

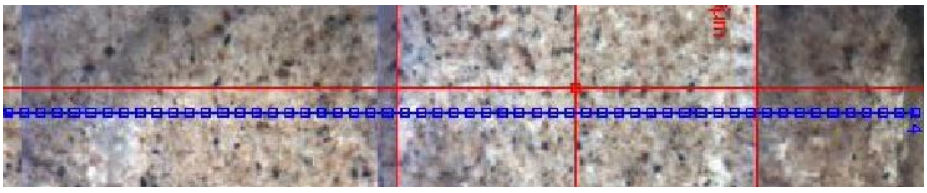

Figure 175 LA-ICP-MS Line 6 results across the sample collected in CFU31-F3 at 10470 ft showing Ca/Si, Ca/Al, and Ca/Fe mole ratios.

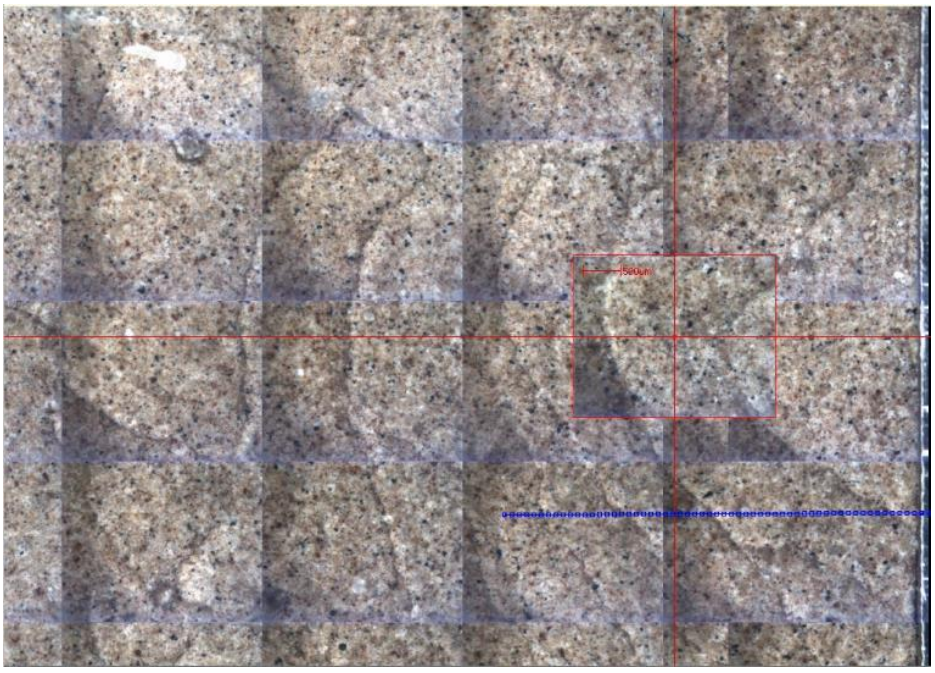

Figure 176 LA-ICP-MS Line 7 across the sample collected in CFU31-F3 at 10470 ft.

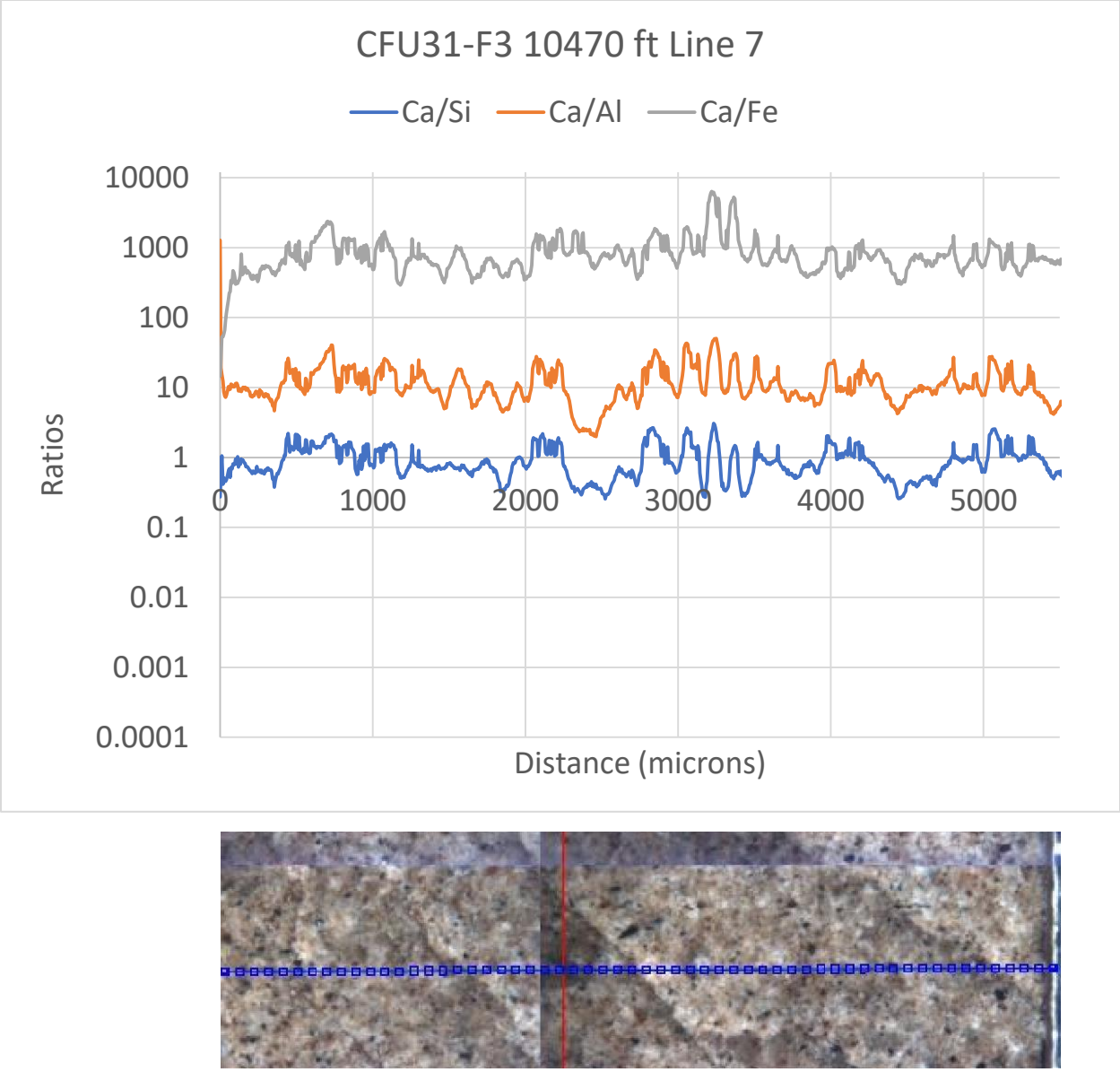

Figure 177 LA-ICP-MS Line 7 results across the sample collected in CFU31-F3 at 10470 ft showing Ca/Si, Ca/Al, and Ca/Fe mole ratios.

Following LA-ICP-MS portions of the sample were crushed and XRD analysis was performed. XRD on the sample collected at 10470 ft was divided into three zones. Zone 1 was at the formation side of the sample, Zone 2 was in the center of the sample, and Zone 3 was at the casing side of the sample. Table 28 shows the XRD data collected. Each zone was heavily carbonated Zone 1 contained 83.5 percent calcite and 10.2 percent aragonite (93.7 percent calcium carbonate). Zone 2 contained 44 percent calcite and 49 percent aragonite (93 percent calcium carbonate). Zone 3 contained 33 percent calcite and 62 percent aragonite (95 percent calcium carbonate).

Table 28 XRD results for cement sidewall core collected in CFU31-F3 at 10470 ft

	Zone 1	Zone 2	Zone 3
Phase name	**Weight %**	**Weight %**	**Weight %**
Calcite	83.5	44	33
Aragonite	10.2	49	62
Quartz alpha	5.07	3.4	1.2
Halite	1.22	2.85	2.55
Faujasite (dehydrated, Ca-exchanged)	-	0.97	0.63

4.2.1.6 CFU31-F3 10477 ft sidewall core sample

The core collected at 10477 ft consisted of solid cement and fiberglass casing (Figure 178). The cement core is uniform in color with no obvious fronts. The casing exhibited severe delamination.

Figure 178 Sidewall core collected in CFU31-F3 at 10477 ft showing fiberglass casing on the left and cement on the left.

Micro-CT images of the cement core (Figure 179) identifies multiple reactions fronts or changes in material moving roughly perpendicular to the long axis of the sample. There is also a feature that may be a fracture that runs parallel to the long axis of the sample. The micro-CT scan was used to select area to cut the sample for further analyses.

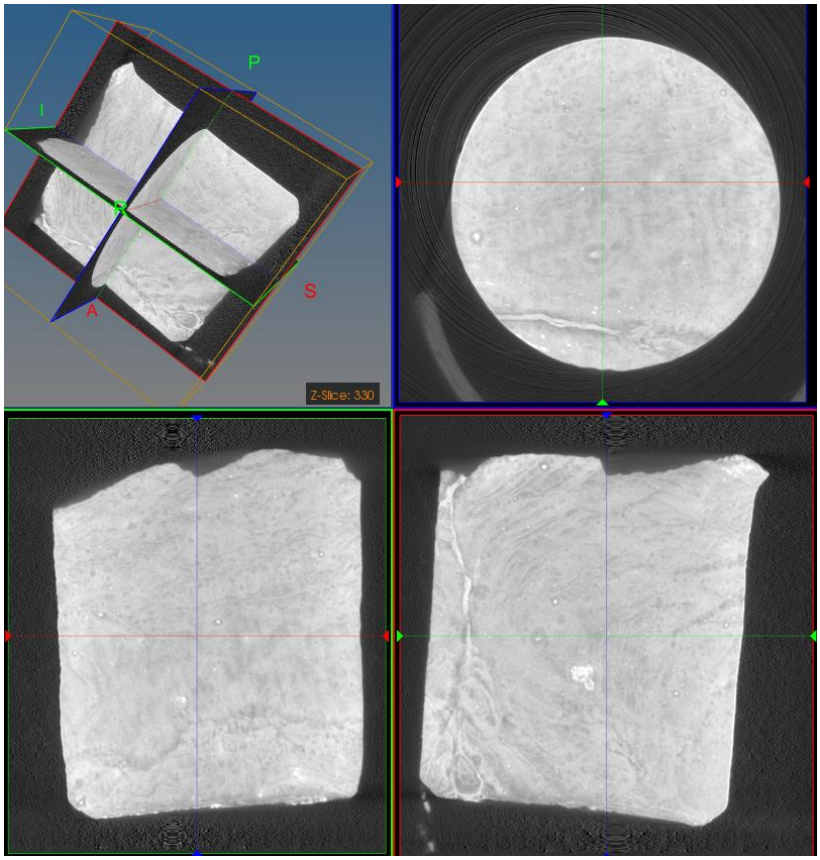

Figure 179 Micro-CT image of the cement sample collected in CFU31-F3 at 10477 ft.

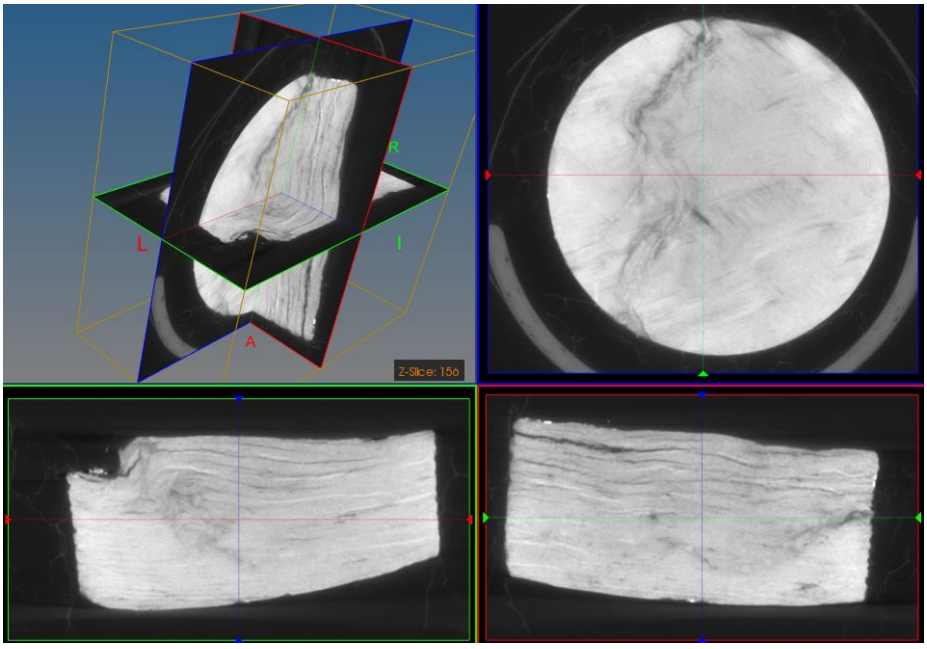

Figure 180 Micro-CT image of the fiberglass sample collected in CFU31-F3 at 10477 ft.

Sectioning of the sample (Figure 181) shows uniform material with cracks that have been filled on and multiple circular features ranging in size from around 10 to 1,000 microns.

Figure 181 Cement sidewall core collected in CFU31-F3 and 10477 ft.

ESEM imaging and EDS mapping were performed on the sample. The mapping delineates a front near the edge of the sample (Figure 182), the transition from one zone or front to another (Figure 183) and a zone that is fairly homogenous (Figure 184). Each of the figures shows EDS map images of Si, Ca, O, C, Al, and Fe. Each of the maps also carbonation. Carbonation can be identified where Si appears depleted (dark) and Ca, O, and C appear enriched (bright).

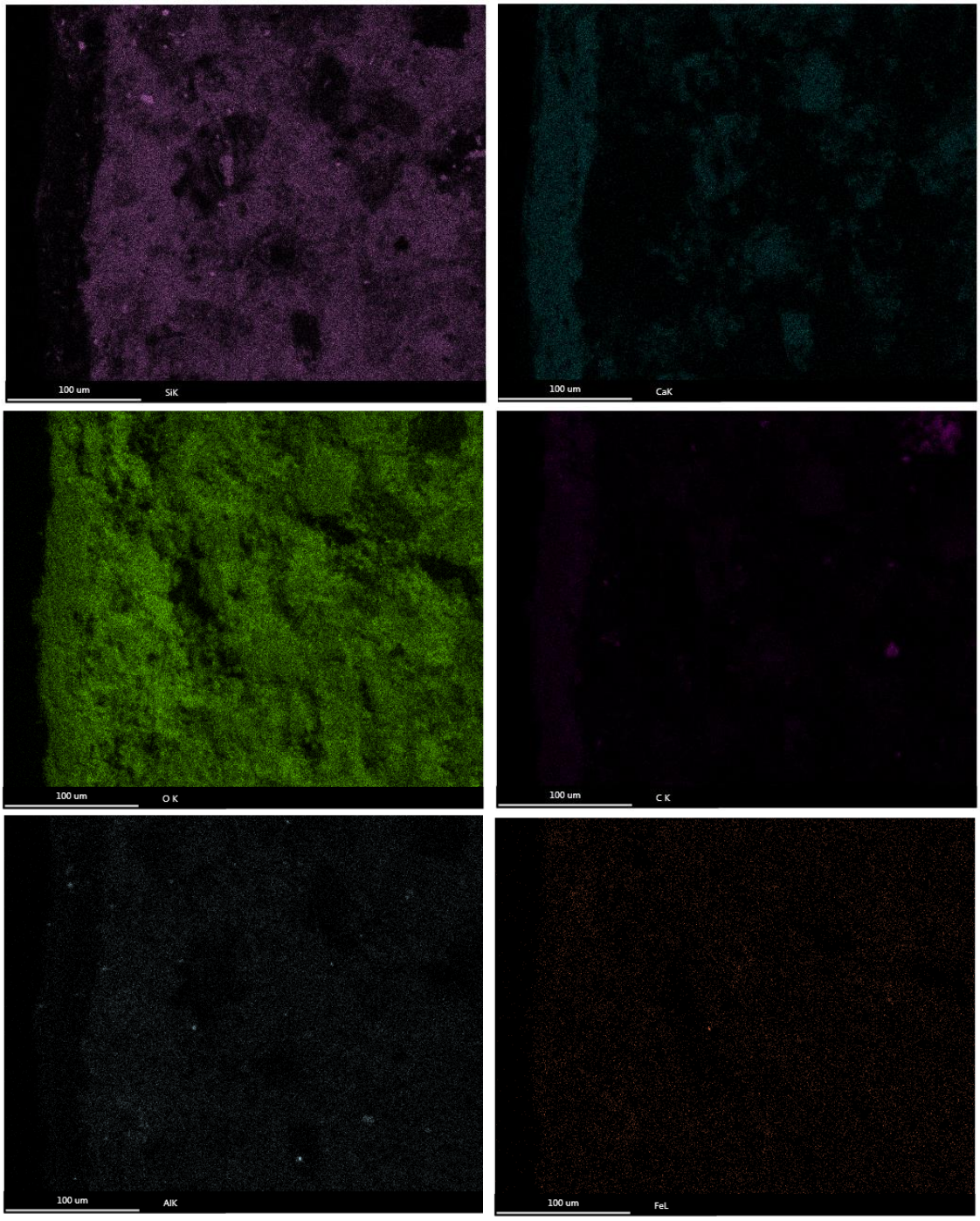

Figure 182 EDS Maps of the casing edge of the cement collected at 10477 ft.

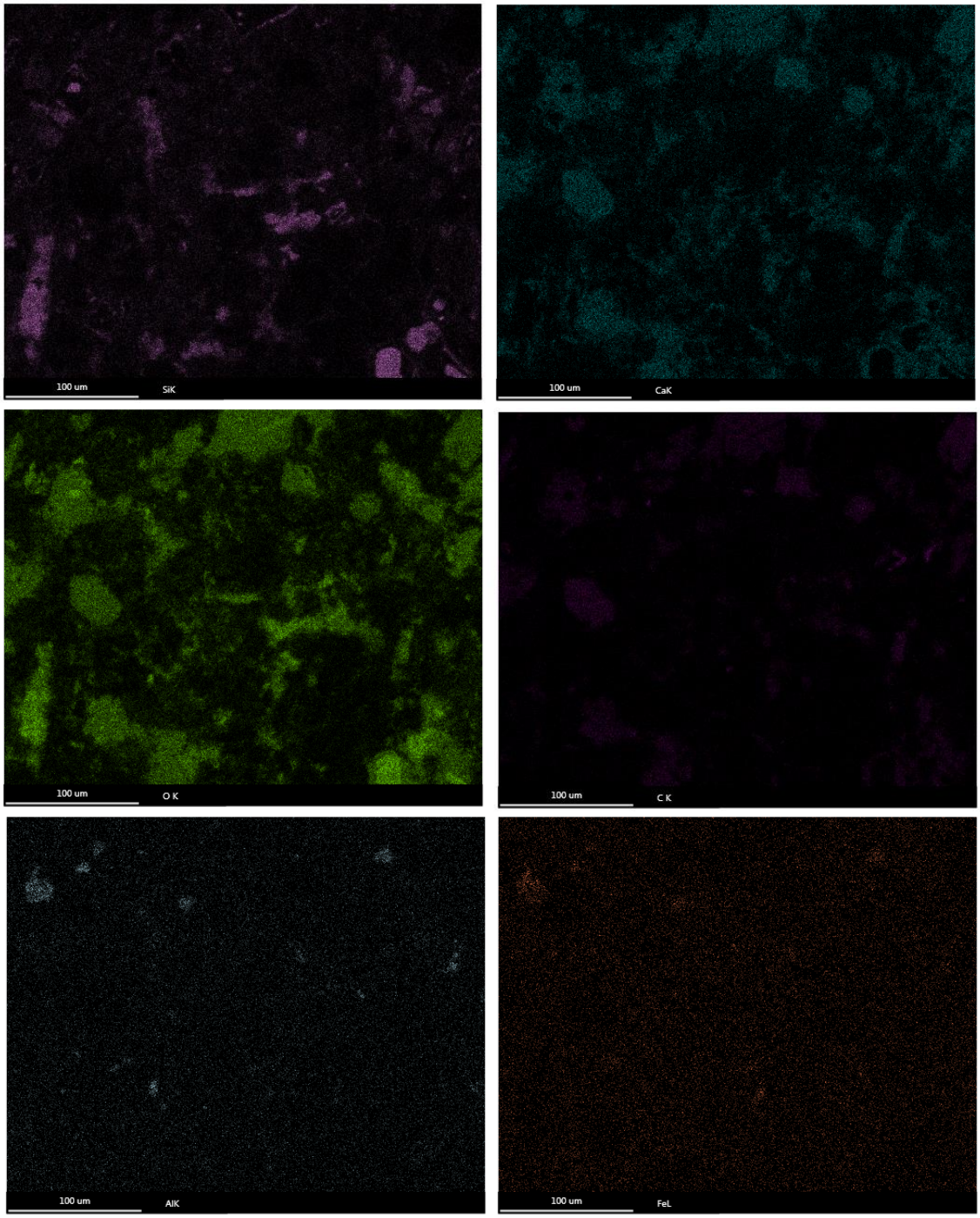

Figure 183 EDS Maps collected approximately 2.7 mm from the casing side in the sample collected at 10477 ft.

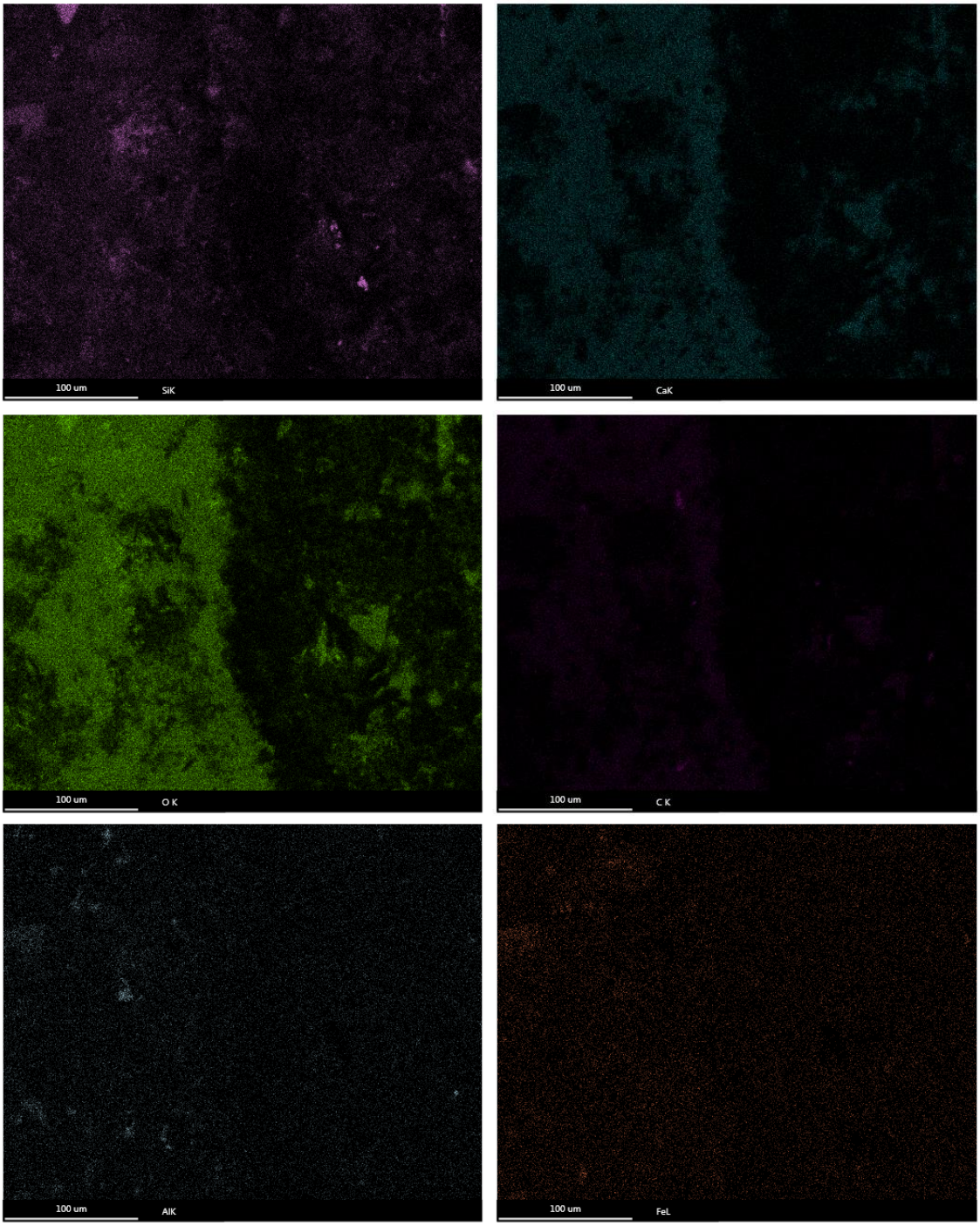

Figure 184 EDS Maps collected approximately 7.1 mm from the casing side in the sample collected at 10477 ft.

The sectioned sidewall core was analyzed using LA-ICP-MS starting on the casing side and moving toward the formation side of the sample. The LA-ICP-MS scan line images and corresponding data are presented in Figure 185 through Figure 208. The lines collected in this sample are similar to the lines collected in the 10470 ft cement core, with variation across the sample. Both the round features and filled-in cracks exhibit very large variation ratios, increases and decreases by an order of magnitude.

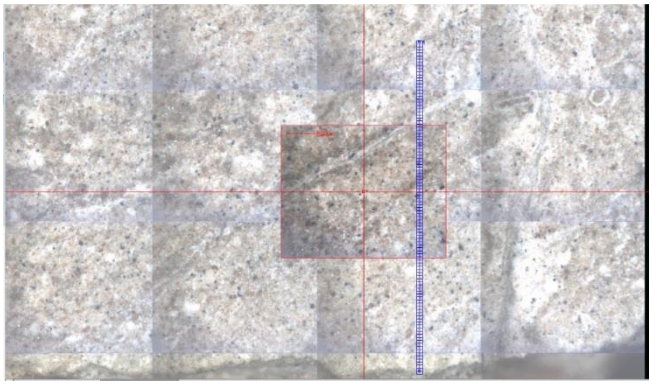

Figure 185 LA-ICP-MS Line 1 across the sample collected in CFU31-F3 at 10477 ft.

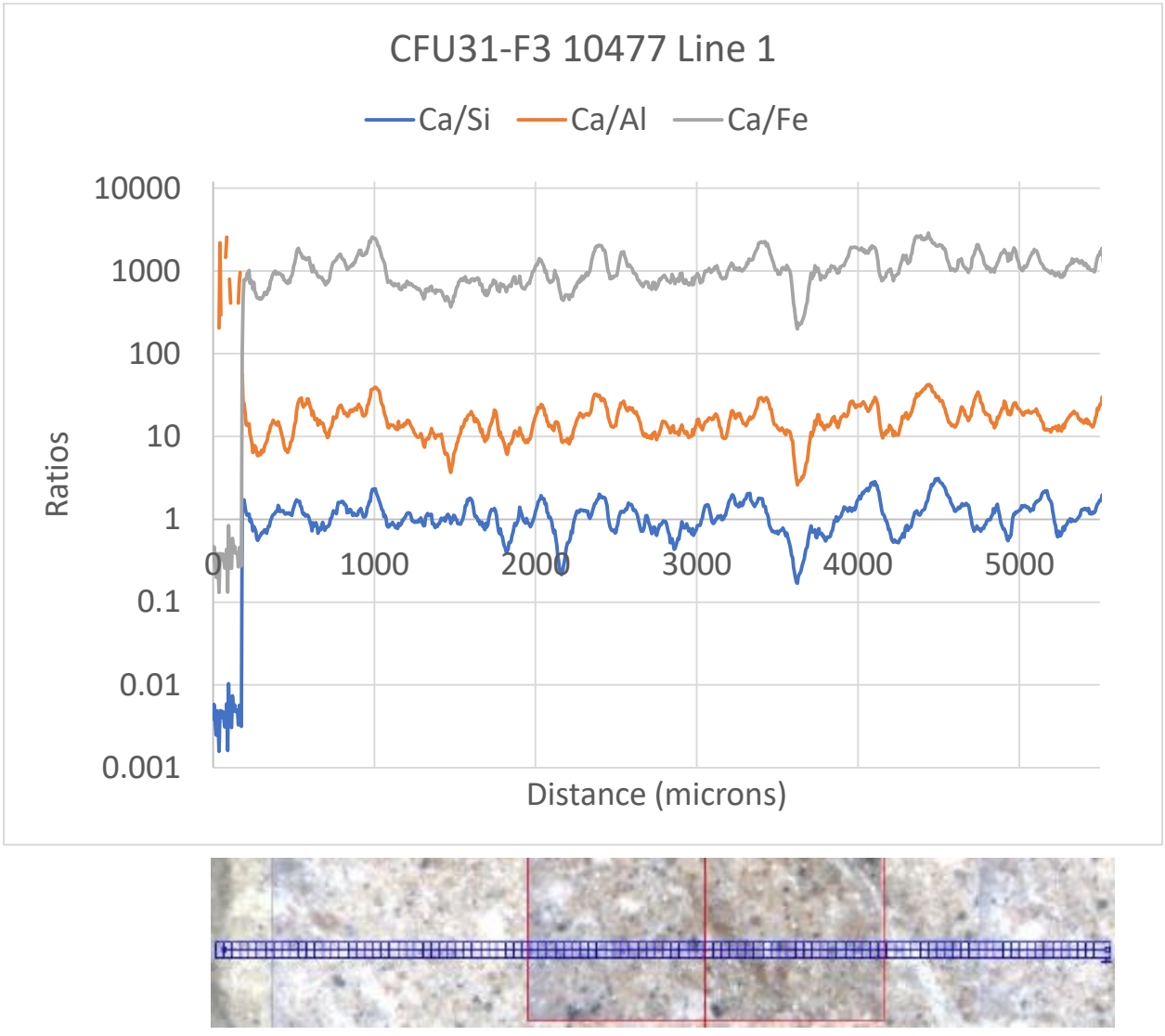

Figure 186 LA-ICP-MS Line 1 results across the sample collected in CFU31-F3 at 10477 ft showing Ca/Si, Ca/Al, and Ca/Fe mole ratios.

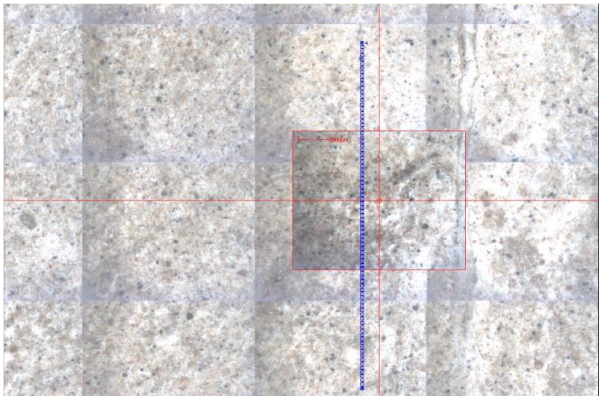

Figure 187 LA-ICP-MS Line 2 across the sample collected in CFU31-F3 at 10477 ft.

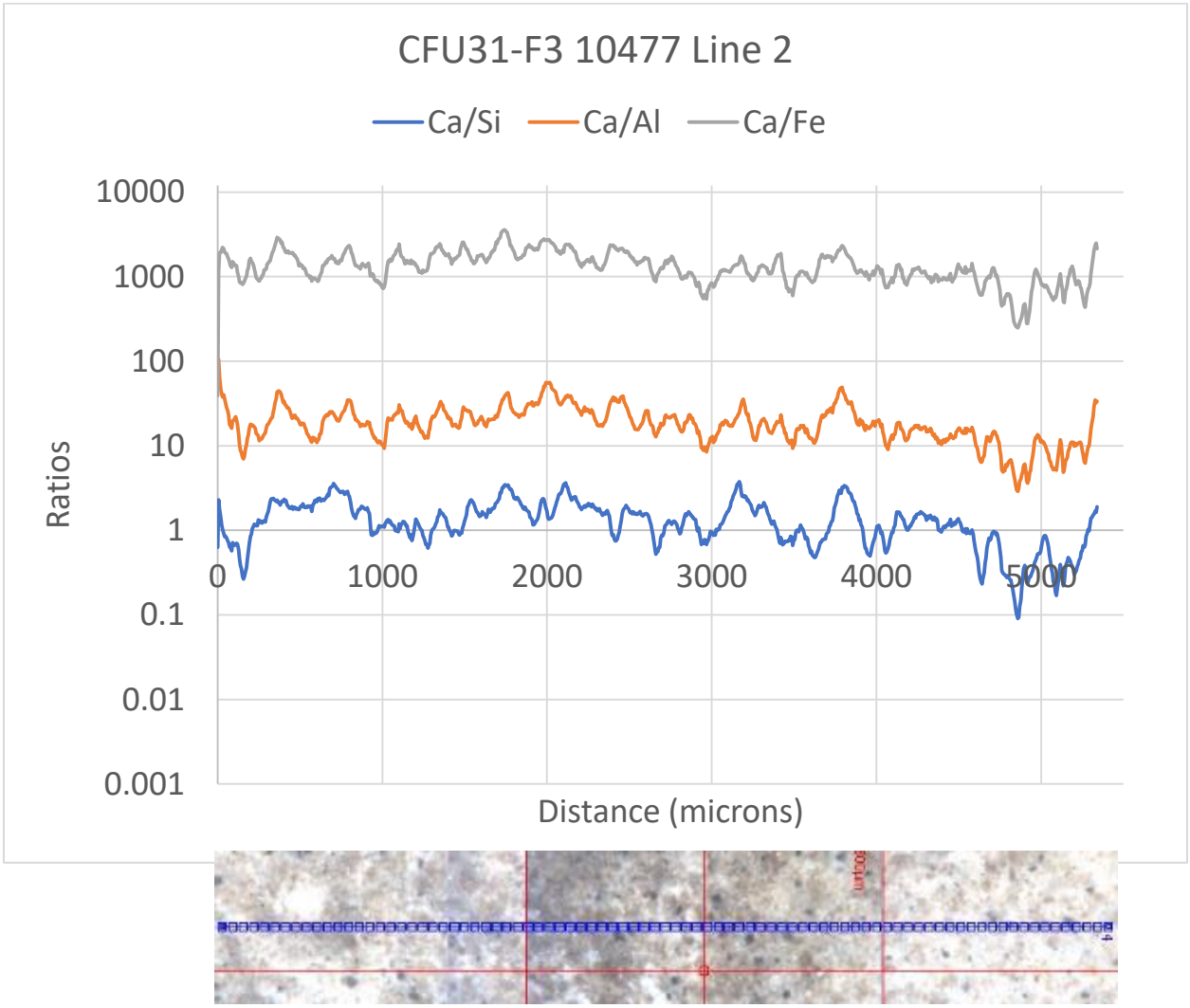

Figure 188 LA-ICP-MS Line 2 results across the sample collected in CFU31-F3 at 10477 ft showing Ca/Si, Ca/Al, and Ca/Fe mole ratios.

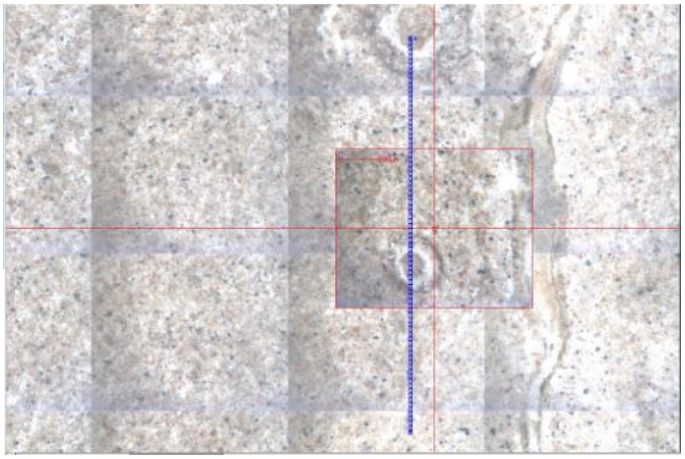

Figure 189 LA-ICP-MS Line 3 across the sample collected in CFU31-F3 at 10477 ft.

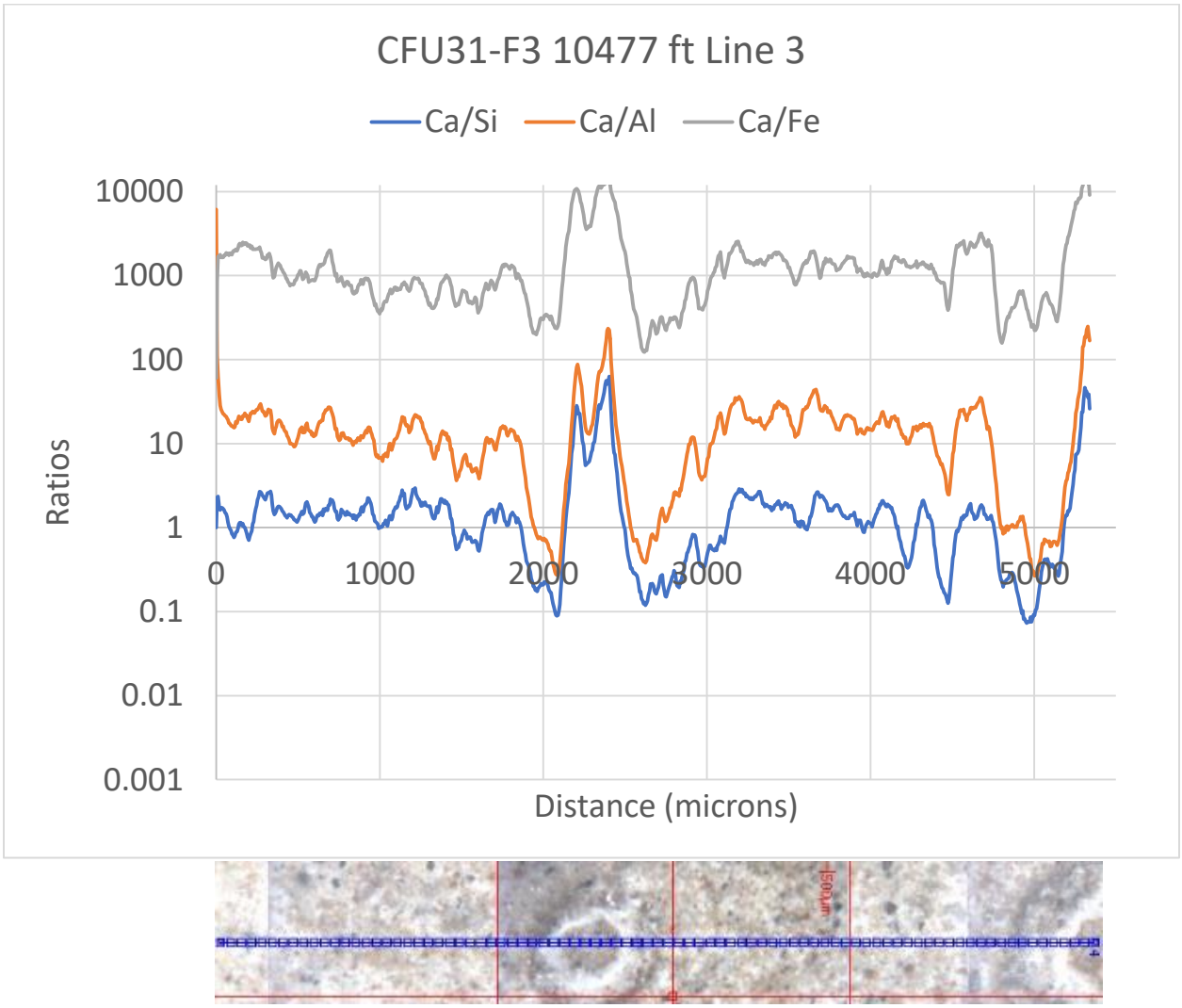

Figure 190 LA-ICP-MS Line 3 results across the sample collected in CFU31-F3 at 10477 ft showing Ca/Si, Ca/Al, and Ca/Fe mole ratios.

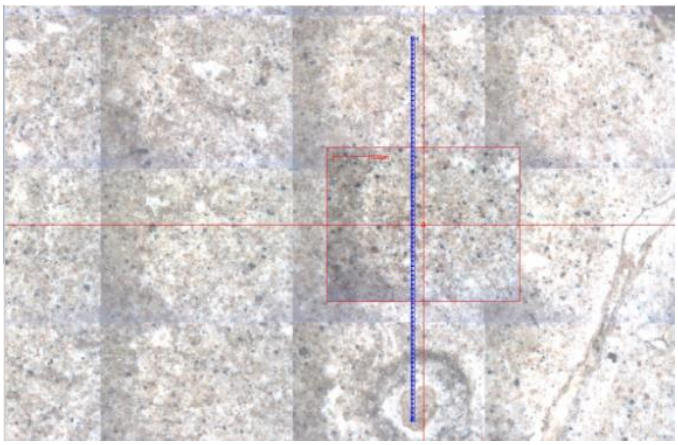

Figure 191 LA-ICP-MS Line 4 across the sample collected in CFU31-F3 at 10477 ft.

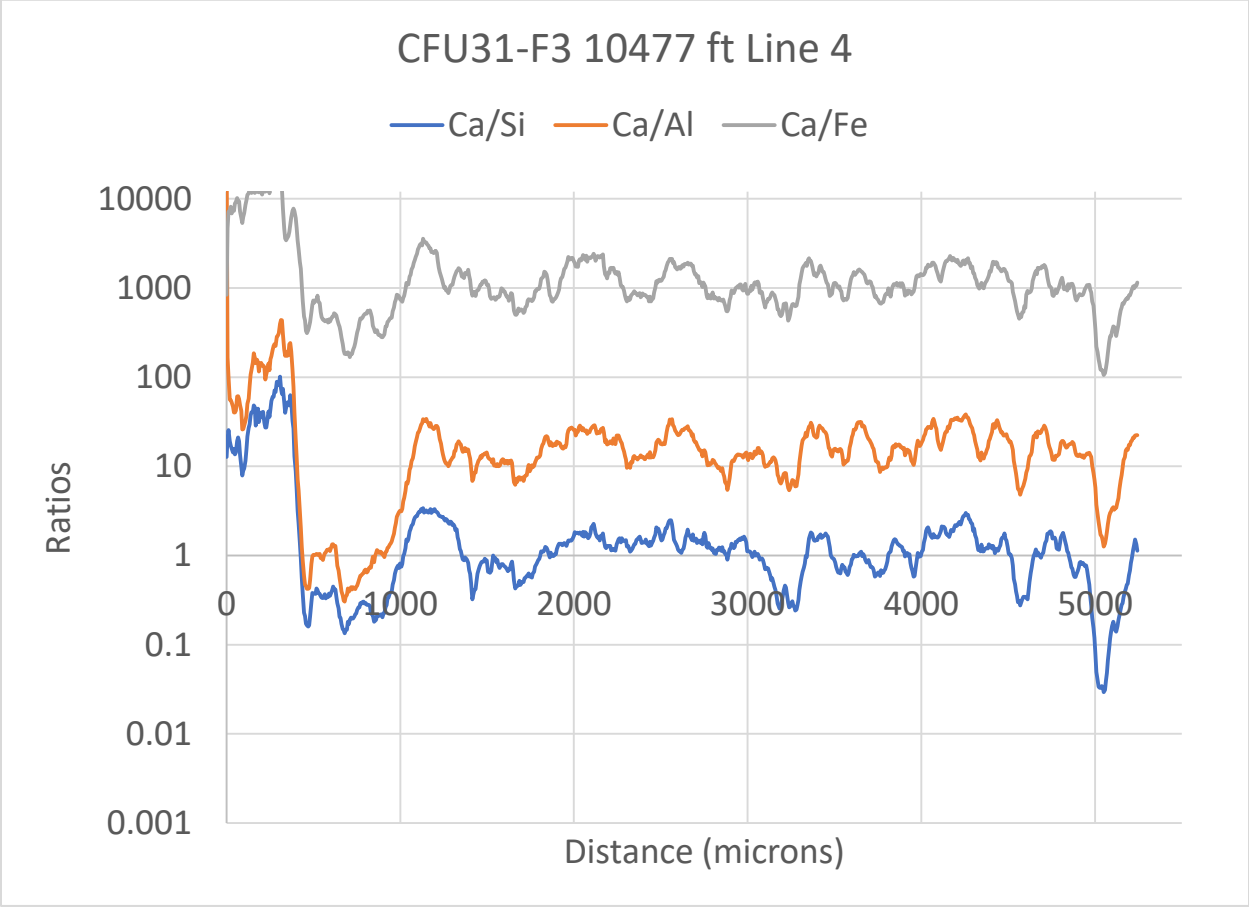

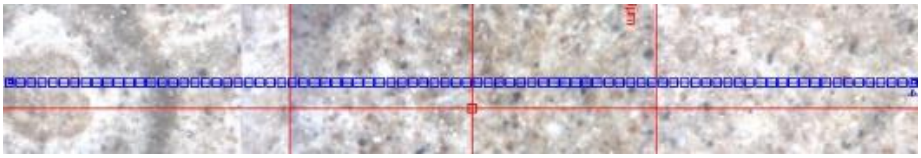

Figure 192 LA-ICP-MS Line 4 results across the sample collected in CFU31-F3 at 10477 ft showing Ca/Si, Ca/Al, and Ca/Fe mole ratios.

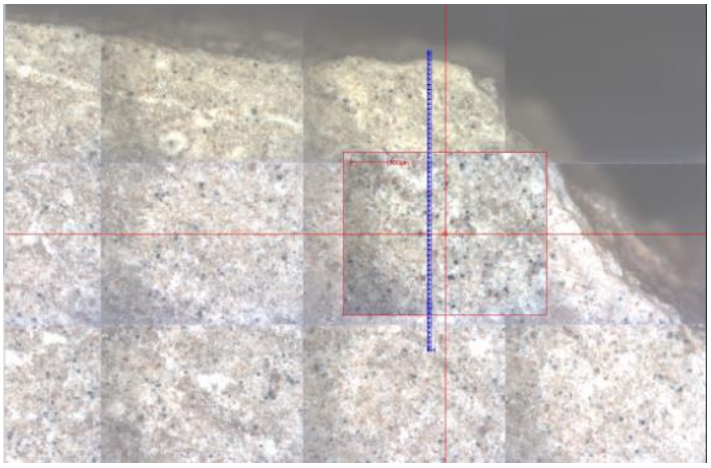

Figure 193 LA-ICP-MS Line 5 across the sample collected in CFU31-F3 at 10477 ft.

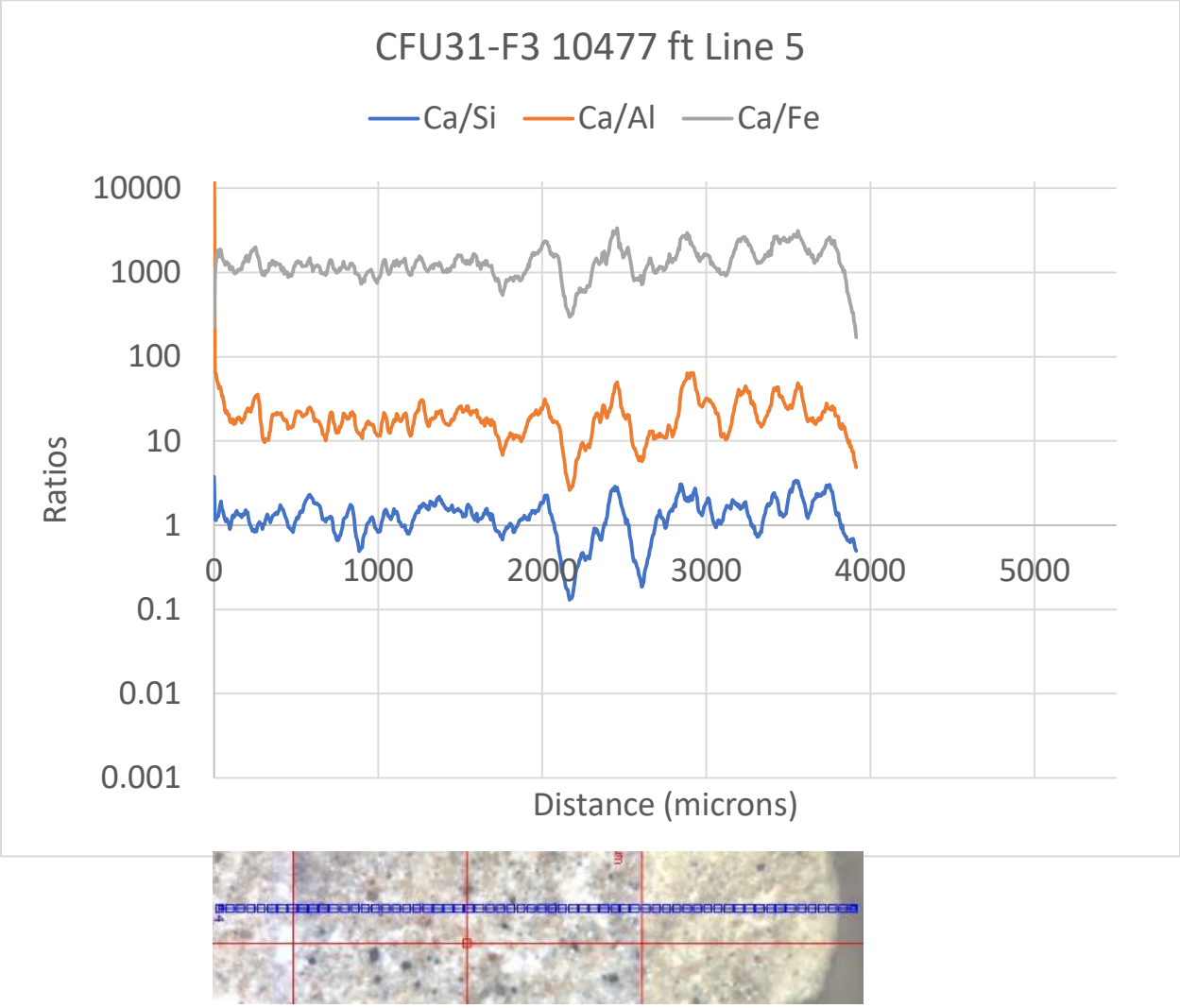

Figure 194 LA-ICP-MS Line 5 results across the sample collected in CFU31-F3 at 10477 ft showing Ca/Si, Ca/Al, and Ca/Fe mole ratios.

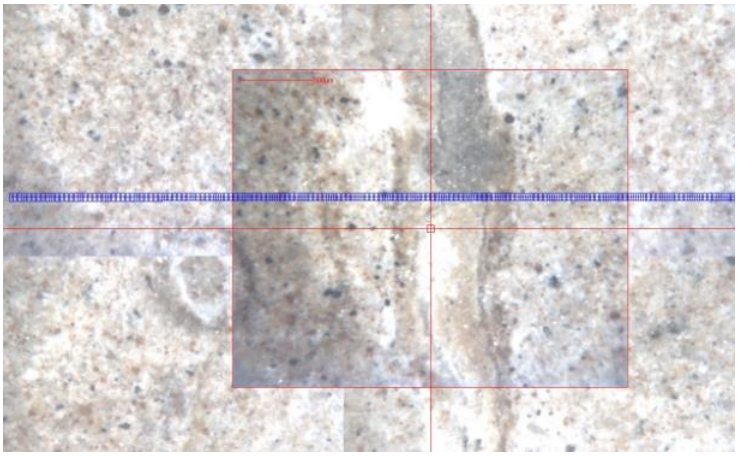

Figure 195 LA-ICP-MS Line 6 across the sample collected in CFU31-F3 at 10477 ft.

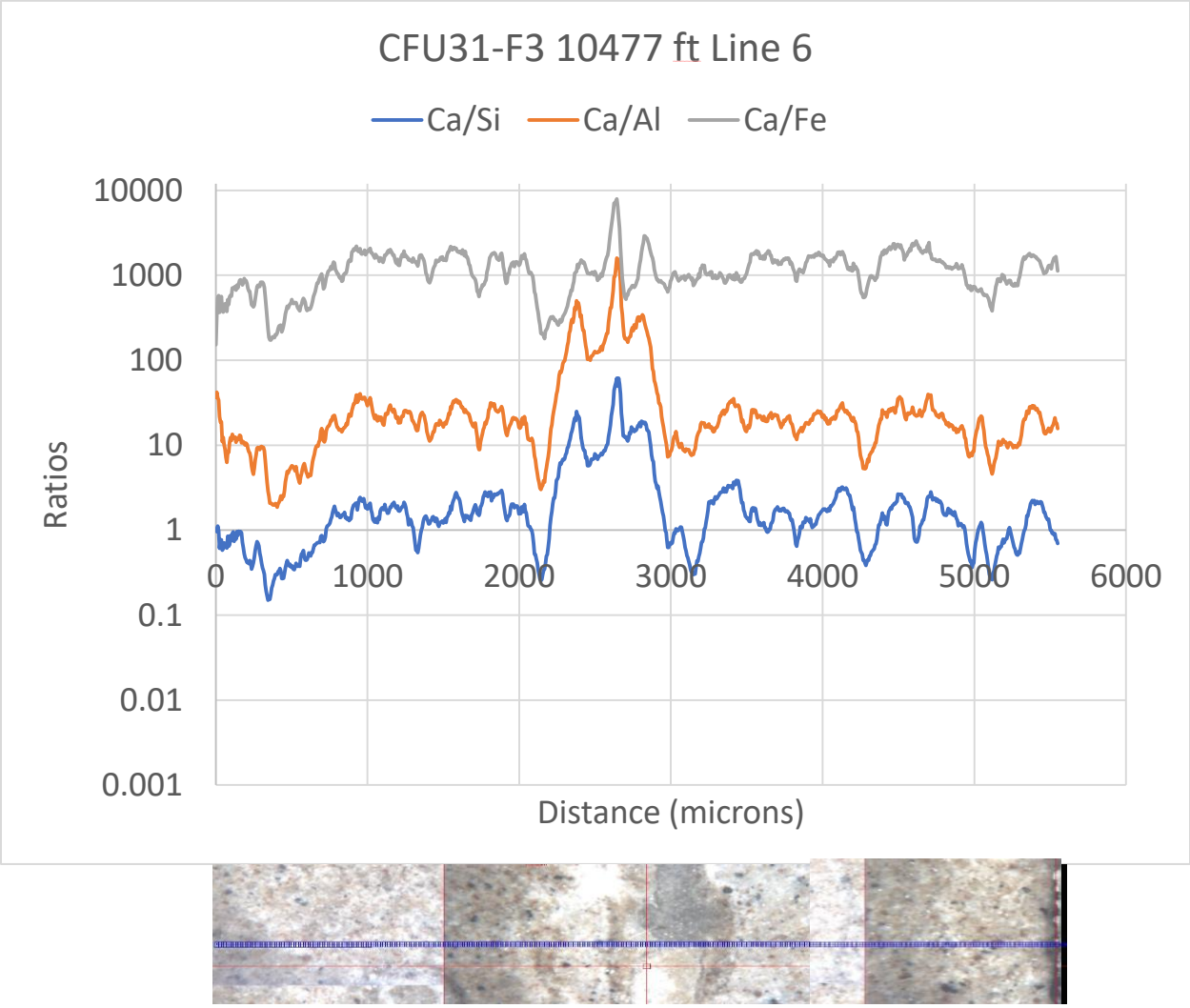

Figure 196 LA-ICP-MS Line 6 results across the sample collected in CFU31-F3 at 10477 ft showing Ca/Si, Ca/Al, and Ca/Fe mole ratios.

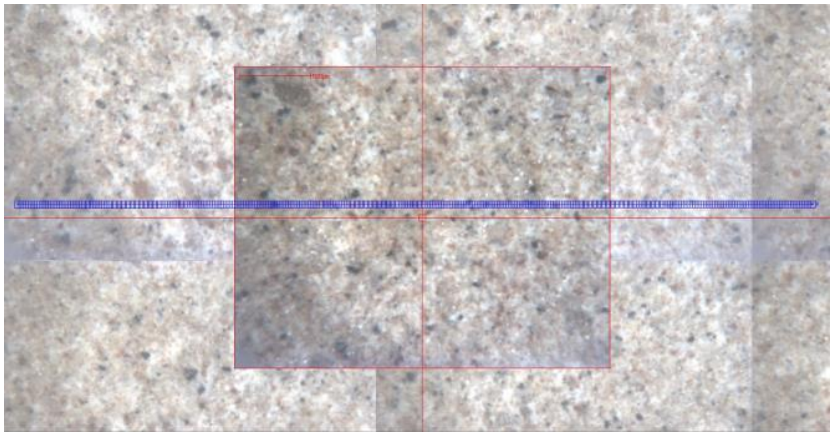

Figure 197 LA-ICP-MS Line 7 across the sample collected in CFU31-F3 at 10477 ft.

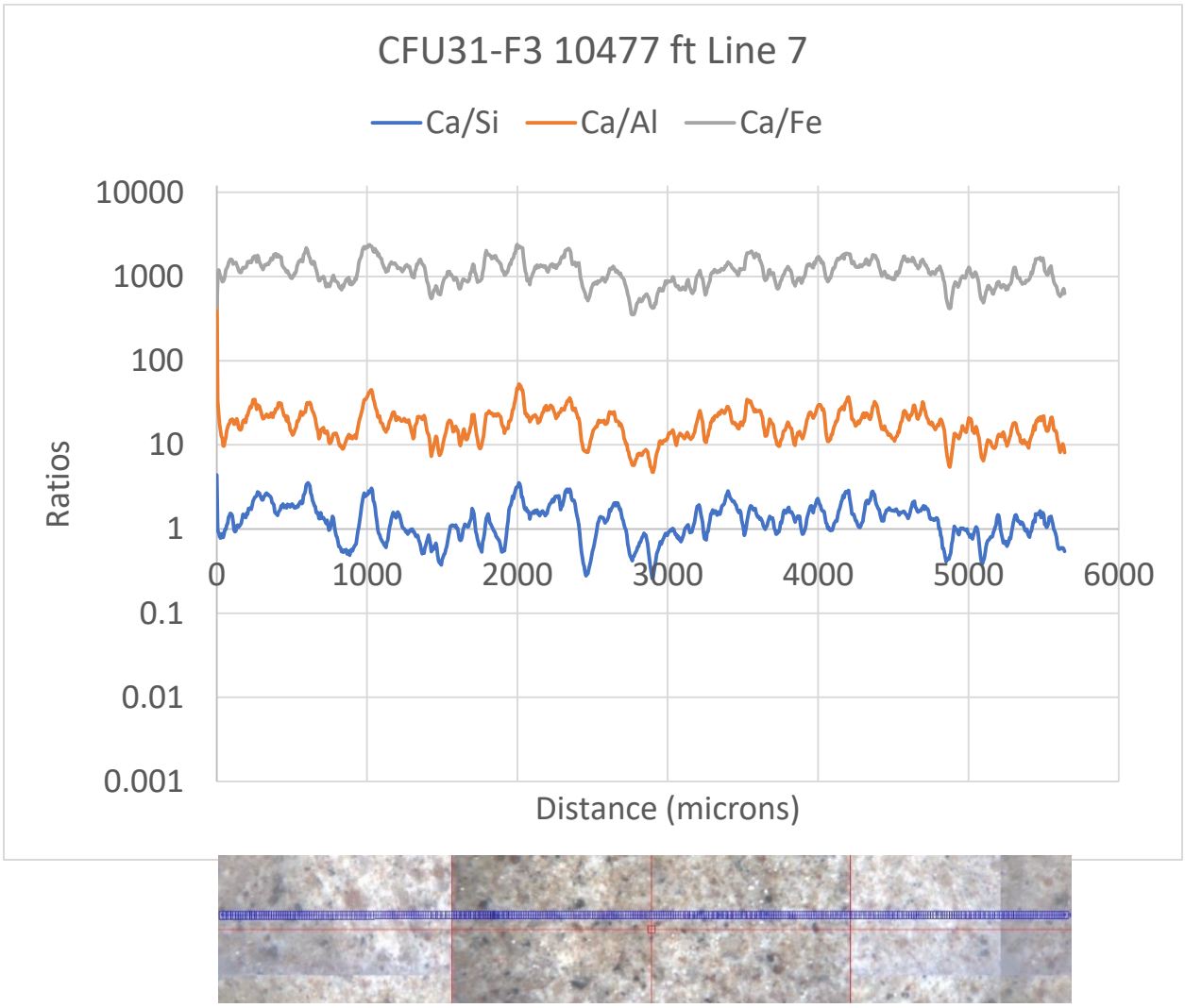

Figure 198 LA-ICP-MS Line 7 results across the sample collected in CFU31-F3 at 10477 ft showing Ca/Si, Ca/Al, and Ca/Fe mole ratios.

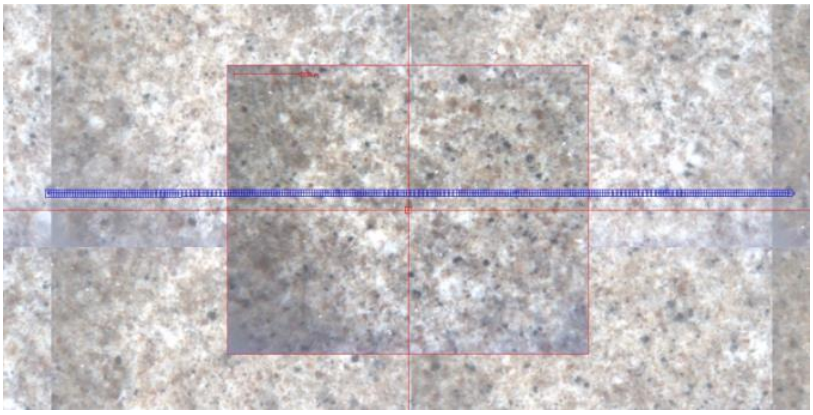

Figure 199 LA-ICP-MS Line 8 across the sample collected in CFU31-F3 at 10477 ft.

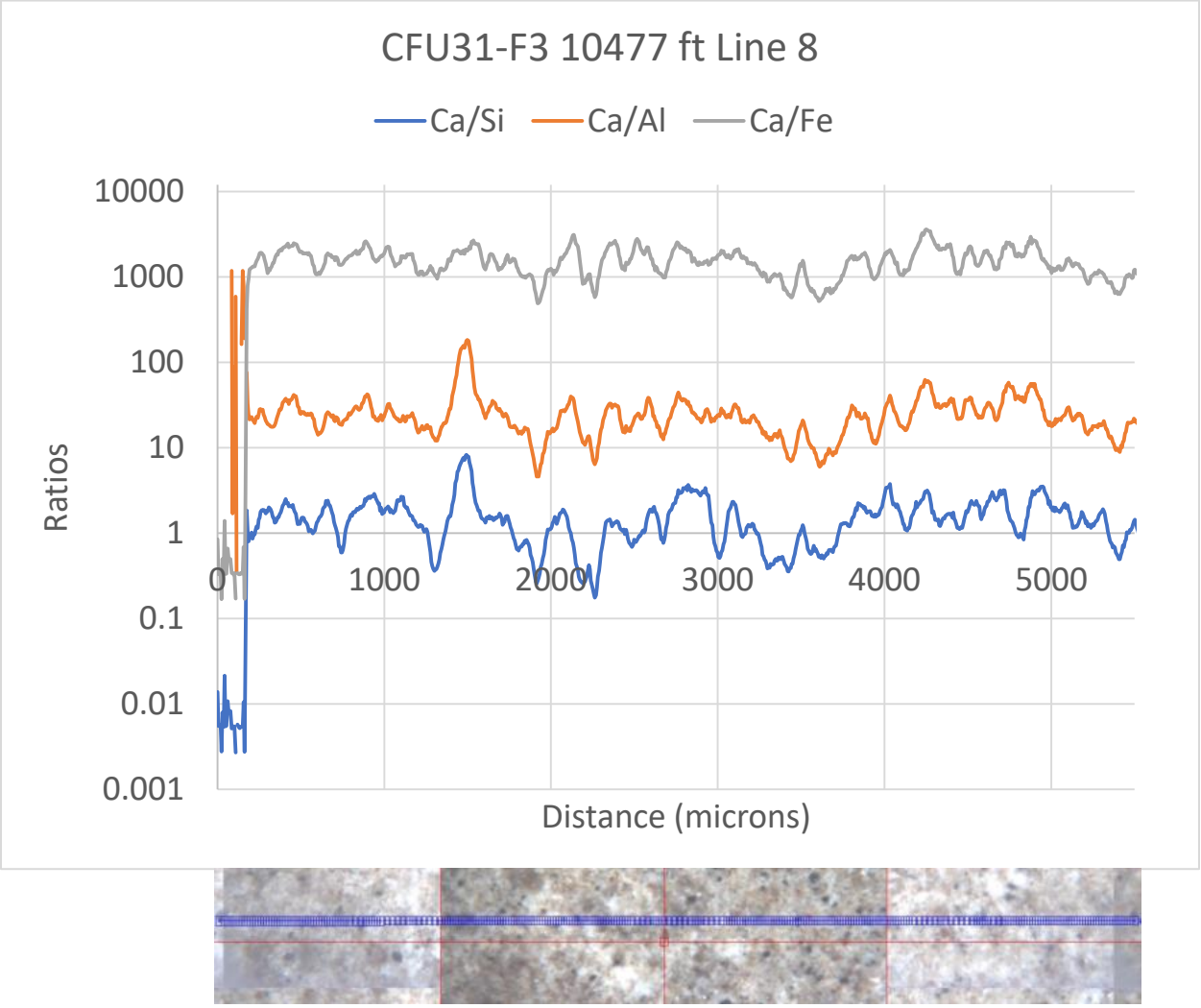

Figure 200 LA-ICP-MS Line 8 results across the sample collected in CFU31-F3 at 10477 ft showing Ca/Si, Ca/Al, and Ca/Fe mole ratios.

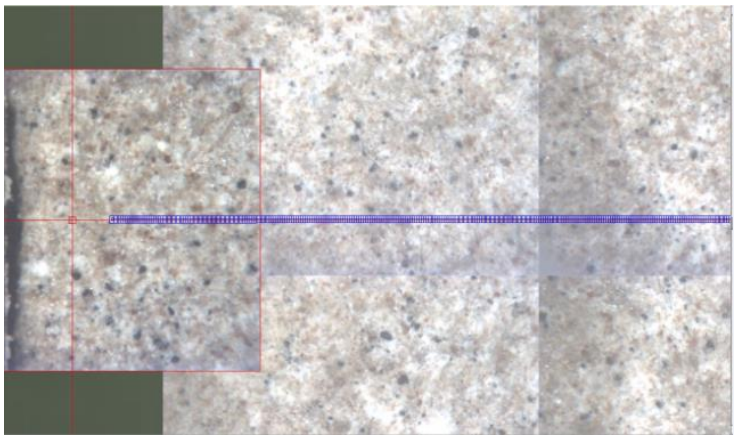

Figure 201 LA-ICP-MS Line 9 across the sample collected in CFU31-F3 at 10477 ft.

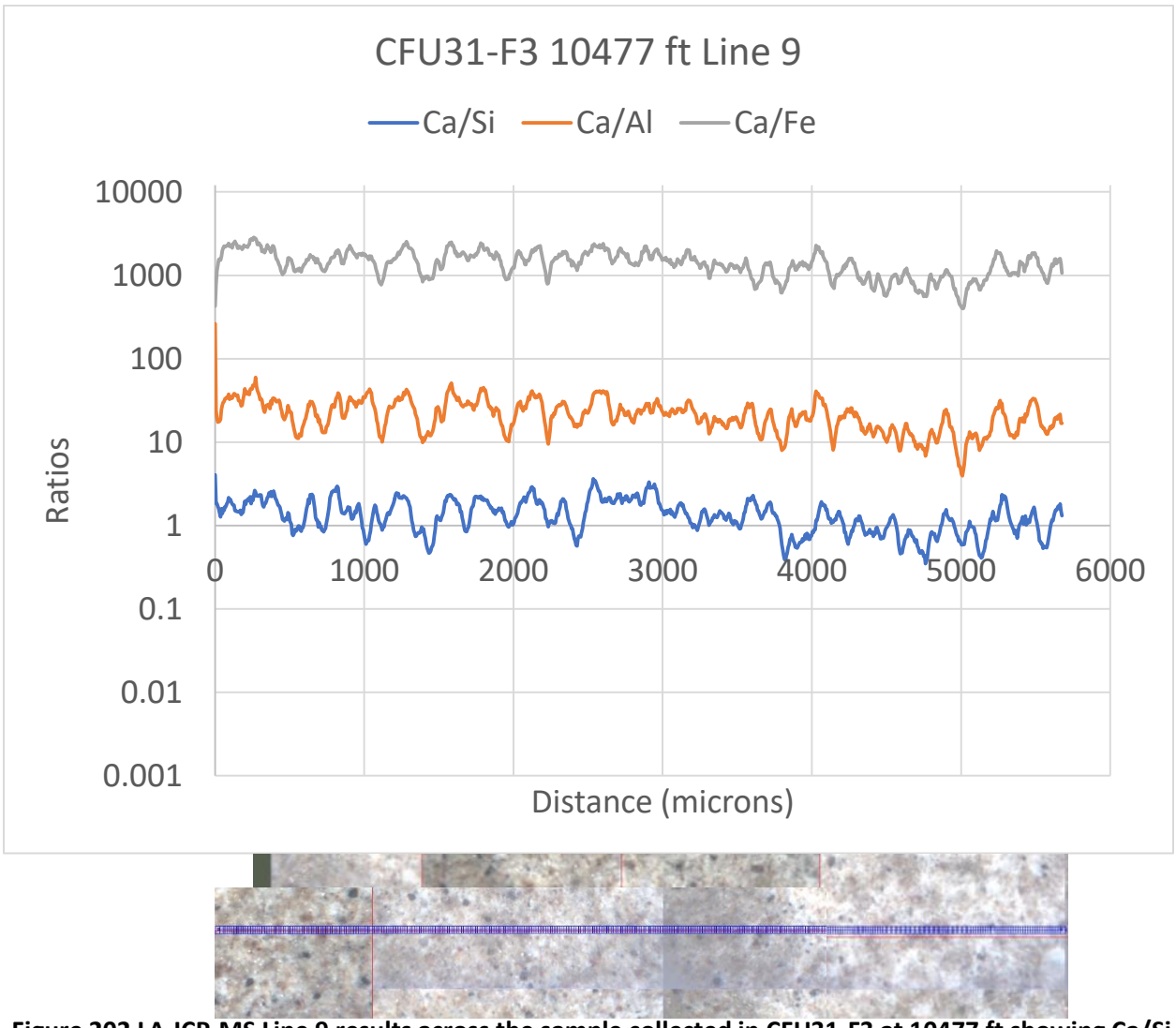

Figure 202 LA-ICP-MS Line 9 results across the sample collected in CFU31-F3 at 10477 ft showing Ca/Si, Ca/Al, and Ca/Fe mole ratios.

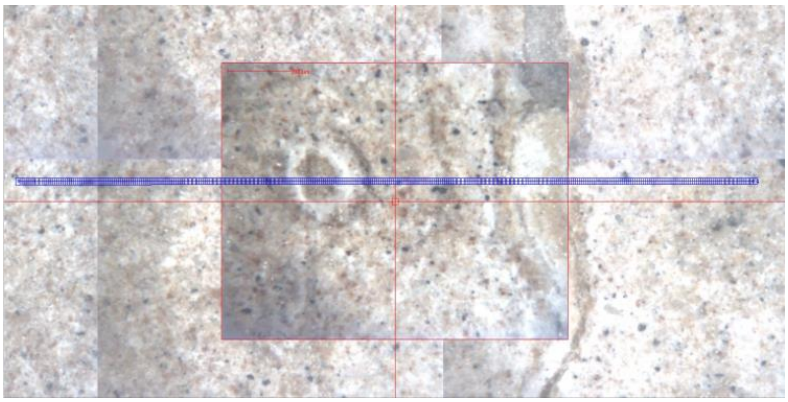

Figure 203 LA-ICP-MS Line 10 across the sample collected in CFU31-F3 at 10477 ft.

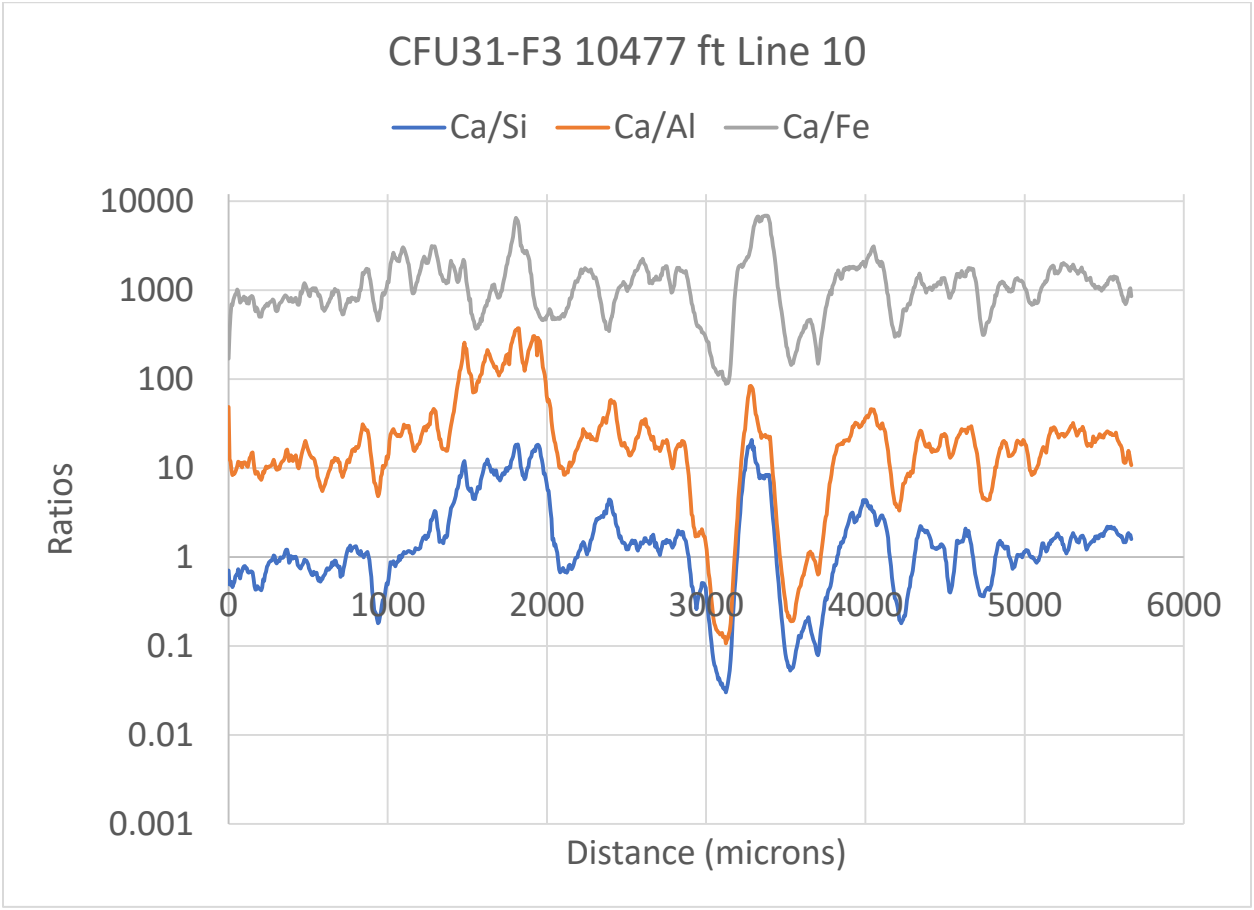

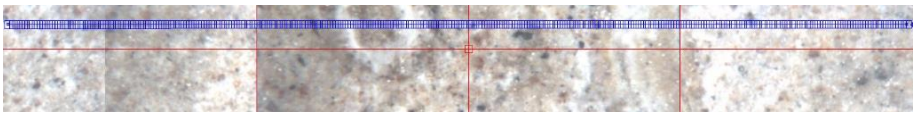

Figure 204 LA-ICP-MS Line 10 results across the sample collected in CFU31-F3 at 10477 ft showing Ca/Si, Ca/Al, and Ca/Fe mole ratios.

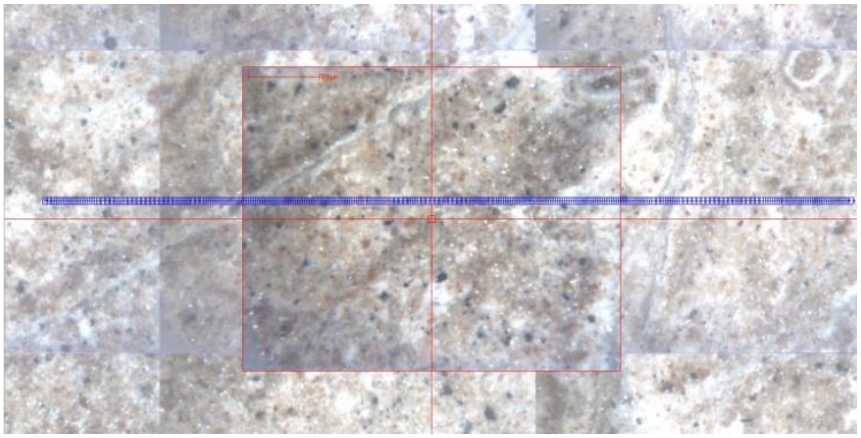

Figure 205 LA-ICP-MS Line 11 across the sample collected in CFU31-F3 at 10477 ft.

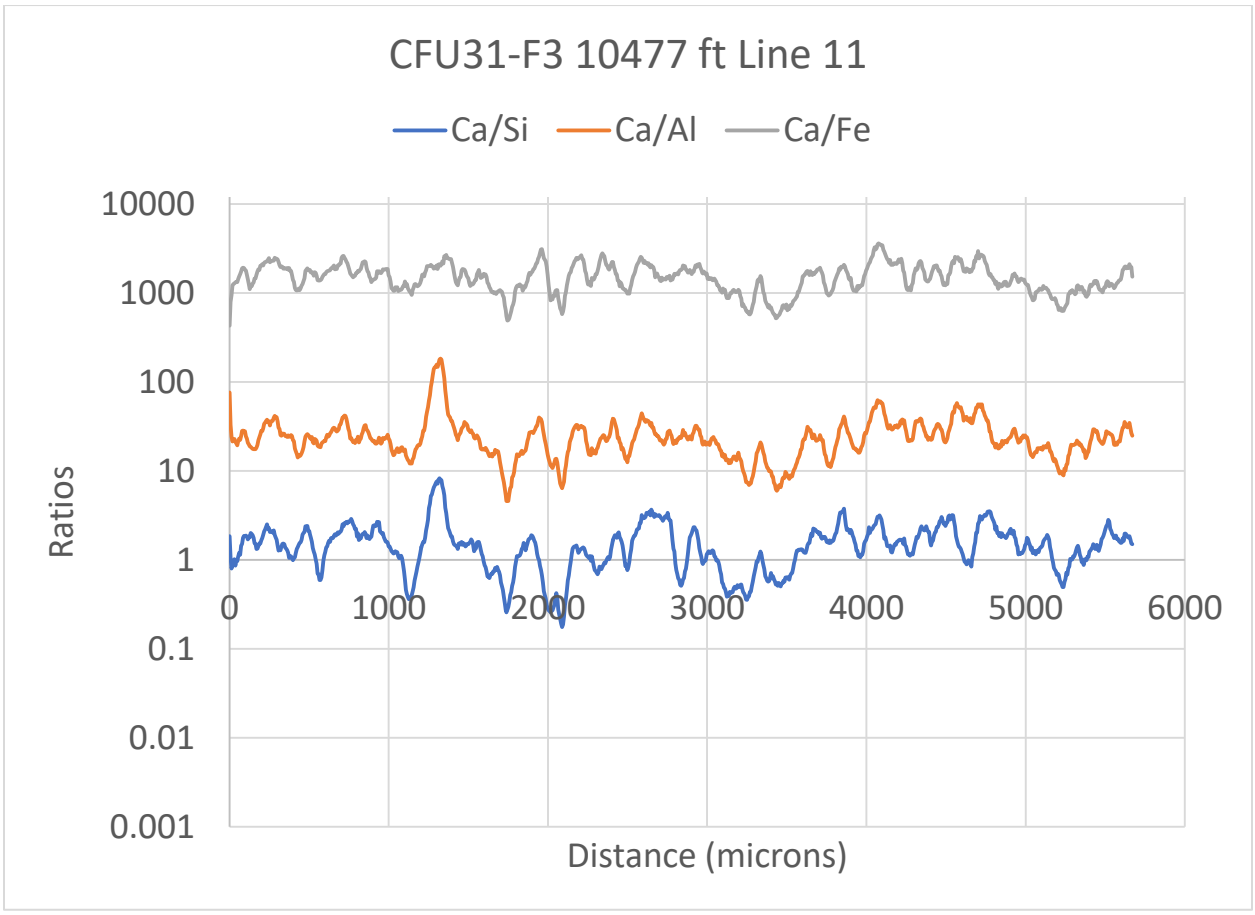

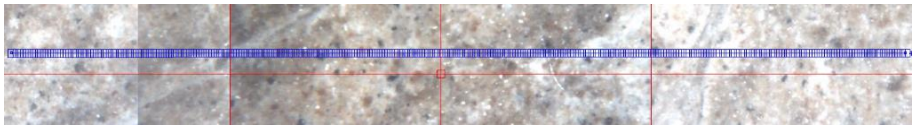

Figure 206 LA-ICP-MS Line 11 results across the sample collected in CFU31-F3 at 10477 ft showing Ca/Si, Ca/Al, and Ca/Fe mole ratios.

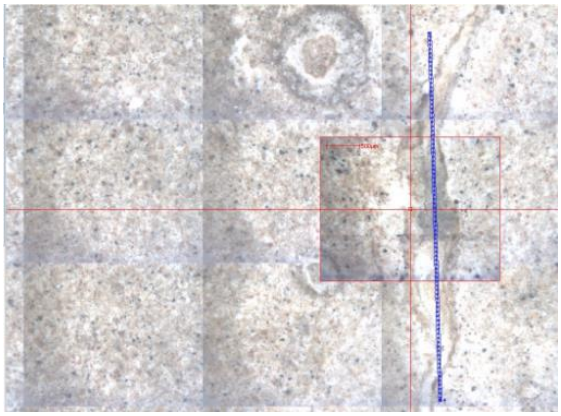

Figure 207 LA-ICP-MS Line 12 across the sample collected in CFU31-F3 at 10477 ft.

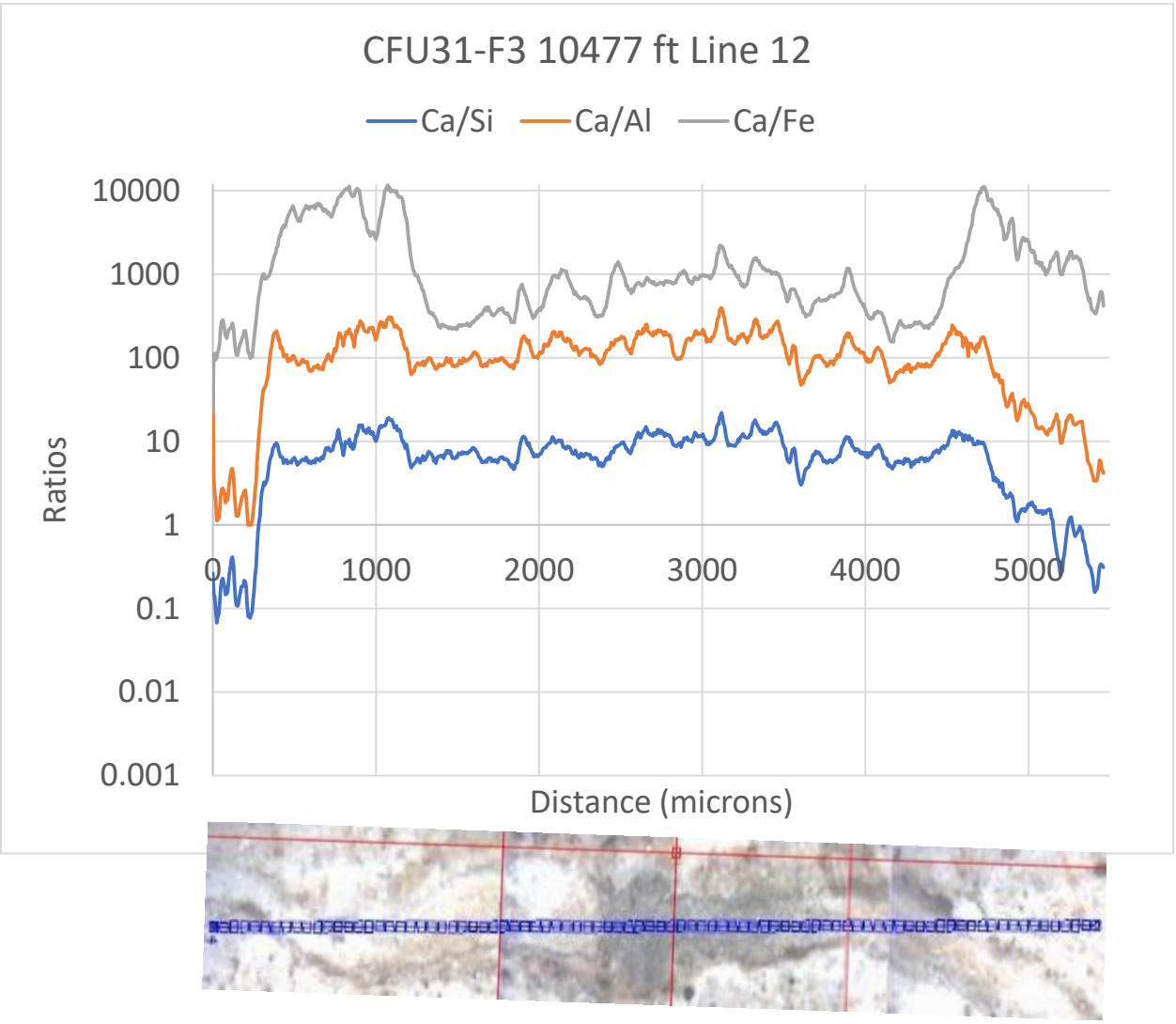

Figure 208 LA-ICP-MS Line 12 results across the sample collected in CFU31-F3 at 10477 ft showing Ca/Si, Ca/Al, and Ca/Fe mole ratios.

Portions of the sample were crushed and XRD analysis was performed. XRD on the sample collected at 10477 ft was divided into three zones. Zone 1 was at the casing side of the sample, Zone 2 was in the center of the sample, and Zone 3 was at the formation side of the sample. Table 28 shows the XRD data collected. Each zone was heavily carbonated Zone 1 contained 39.3 percent calcite and 52 percent aragonite (91.3 percent calcium carbonate). Zone 2 contained 49 percent calcite and 44 percent aragonite (93 percent calcium carbonate). Zone 3 contained 40 percent calcite and 48 percent aragonite (88 percent calcium carbonate).

Table 29 XRD results from cement sidewall core collected in CFU31-F3 at 10477 ft

	Zone 1	Zone 2	Zone 3
Phase name	**Weight %**	**Weight %**	**Weight %**
Aragonite	52	44	48
Calcite	39.3	49	40
Halite	2.07	1.63	3.01
Quartz	5.24	5.6	7.7
Faujasite-Ca, dehydrated	1.26	0.383	0.98

5 Discussion

The 2009 image log collected in CFU31-F2 shows generally high (8 Mrayl) to middle (5 Mrayl) acoustic impedance cements from 9100 ft to the bottom of the log at 10642 ft. These values indicate solid cement in the annulus between the casing and formation. Above 9100 ft the acoustic impedance is generally lower indicating debonded solid or liquid behind the casing. The collection of a solid cement core sample at 7900 ft shows that competent cement reached well above the where the logs show good cement/good bond. Cables or control lines are visible as low acoustic impedance features between the CO_2 reservoir at 10438 ft and 8020 ft where low acoustic impedance values in the log generally transition from being interpreted as debonded solid to fluid. The low acoustic impedance values in the area of the cable and hardware in the well indicate that the cable and hardware is not bonded to the casing and could represent a pathway along the casing.

Deterioration of the acoustic impedance and CBL signals in the logs is evident over much of the section that was relogged in 2015. The zone showing little change, between 9230 and 9304 ft, probably rules out differences in the tools as the cause for the deterioration in other portions of the well. The 2015 ultrasonic image maps also show the cables and monitoring hardware running between about 9000 ft and the bottom of the log. Above 9000 ft the overall low acoustic impedance in the Raw Acoustic Impedance track makes identifying the cable impossible. The image logs collected in CFU31-F3 exhibit similar behavior to those collected in CFU31-F2. The core point at 10042 ft, in the steel casing shows a decrease in solid material behind the casing between 2009 and 2015.

The identification of the monitoring equipment on the outside of the casing is a concern for CCUS monitoring at this and other projects. Control lines and cables for downhole sensors and gauges must run from the surface to the zone being monitored. The low acoustic impedance values that make these features visible in the log indicate that there is weak or no cement or cement bond. The combination of low acoustic impedance and the necessity of vertical control lines could allow a direct path for CO_2 out of the reservoir if there is monitoring technology located below the reservoir seal.

Each of the cored depths showed changes in acoustic impedance and CBL amplitude. Each of the cores collected in each well showed evidence of carbonation. The XRD data for each core show calcium carbonate phases. The core at 7900 ft contained a crack surrounded by a visible reaction front. The LA-ICP-MS analysis shows an increase in Ca/Si moving away from the crack and a spike in Ca/Si on the left visible edge of the front (Figure 17 and Figure 19) which may indicate a calcium carbonate front. XRD analysis on the crack zone indicated a higher calcium carbonate percentage that in the non-crack zone indicating that the crack is acting as a pathway for CO_2.

Visual analysis of the core collected at 9530 shows reaction fronts moving into the sample from the casing side. LA-ICP-MS shows a Ca/SI spike near the casing-side of the sample (Figure 31) and then a slow increase in Ca/SI moving away from the casing side, indicating that Ca is likely depleted from leaching or carbonation between the spike and center of the sample. XRD analyses further strengthens the case that the sample is carbonating. The XRD identified carbonation in each of the three zones analyzed (Table 15). The zone closest to the casing had the highest carbonation and the zone nearest the formation had the second highest amount of carbonation. High values of calcium carbonate at both ends of the sample implies that CO_2 or carbonic acid is moving along the interface between the casing and formation and moving along the interface between the cement and formation. The CHDT pretest conducted at 9530 ft also determined that the cement behind the casing at the test depth, five feet below the sidewall core, was not providing hydraulic isolation.

The core collected at 9800 ft is similar to the core collected at 9530 ft, it has visible reaction fronts moving into it. However, the more extensive reaction fronts are moved into the sample from the formation side instead of the casing side of the sample. LA-ICP-MS of the sample identifies multiple zones with high Ca/Si in the fronts moving into the sample from the formation side that may be the result of leaching and carbonation. Calcium carbonate was identified in all of the zones assessed. The zone closest to the formation, Zone 1, was highly carbonated with three polymorphs of calcium carbonate identified and calcium carbonate making up 75.4 percent of the crystalline phases. Like the sample collected at 9530 ft, the sample at 9800 ft showed higher carbonation near the ends than in the center, with Zone 3 consisting of 24 percent calcium carbonate. Tobormorite, a C-S-H mineral, is highest in the center zone, Zone 2 (40 percent) and lowest near the formation side of the sample, Zone 1, (2.3 percent). High values of calcium carbonate on both ends of the sidewall core and higher values of cement minerals in the center of the core indicate that CO_2 or carbonated brine is moving along both the casing-cement and cement-formation interfaces. The CHDT pretest conducted at 9795 ft determined that the cement behind the casing at the test depth, five feet above the sidewall core capable of providing isolation, with an estimated permeability of 0.1 μD, however, the cement maybe be thin. The ultrasonic logs over the test interval show some solid cement, however, they largely the material behind the casing is microdebonded. This may imply that the CHDT tested the solid and not the microdebonded material or the cement does not fill the entire annulus.

All of the cores collected in CFU31-F3 also showed carbonation. The core collected at 10268 showed visible reaction fronts moving into the sample at both sides as well as reacted zones throughout the rest of the sample. LA-ICP-MS within the sample show increases in Ca/SI at both ends and in the center of the sample (Figure 96, Figure 97, and Figure 106). XRD was conducted near each end and in the center of the sample. Each of the zones measured showed calcium carbonate. Both of the ends of the sample showed more carbonation that the zone in the center of the sample. The formation end of the sample was the most carbonated with 70 percent of the crystalline phases consisting of calcite or vaterite.

The core collected at 10380 ft consisted of casing, control line, and cement. The cement portion of the core showed visible reaction fronts moving into the sample from the control line / casing side. LA-ICP-MS on the sample shows large increases in Ca/Si on near the edge on the control line / casing side (Figure 124, Figure 134, Figure 136, Figure 138, and Figure 140) and a smaller increase on the formation side (Figure 132). XRD conducted on the sample show carbonation in each of the zones analyzed (Table 26). The carbonation is highest adjacent to the control line / casing interface, with 84 percent calcite, and smallest near the formation with 12 percent calcite. The casing at this depth looks generally competent in the sample collected. However, there is some delamination is visible toward the inside of the casing. The logs at this depth cannot provide information on the control line as a leakage pathway in the fiberglass casing. With processing for steel casing the fiberglass sections appears to be mostly microdebonded material and no control line is visible. With processing for fiberglass casing the material behind the casing is solid but the image of the cable are not visible in the steel section implying that the fiberglass

processing is not sensitive to the control line (Figure 209). However, the logs further up the well imply that control line is not bonded to the casing. This in combination with the large amount of carbonation along the control line is a strong indication that it is acting as a leakage pathway along the well.

The sample collected at 10450 ft also shows indications of interaction with CO_2. The sample was collected at the top of the reservoir zone. Visual analysis of the cement portion of the core shows fronts moving into the sample from the casing side. LA-ICP-MS shows a large increase in Ca/Si on the casing end and a smaller increase near the formation end of the sample. XRD conducted on the sample confirms carbonation. XRD was conducted on the casing side of the sample and in the center of the sample. XRD was not conducted on the formation end of the sample because it appears that the core is broken and the cement-to-formation interface was not collected. Both zones showed carbonation, with the formation side of the sample showing 28 percent of the crystalline phases being composed of calcite and the center of sample being composed of 29 percent calcite (Table 27).

The cores collected at 10470 and 10477 are very similar. They were both collected from the middle of the reservoir zone. Each of the samples were highly carbonated. Visual analysis of the sample collected at 10470 ft shows a series of fronts entering the sample from the casing-cement and cement-formation interfaces as well as moving through the cement along the cemented annulus. The sample collected at 10477 ft shows visual indications of a crack that has been filled in with calcium carbonate. LA-ICP-MS on both sidewall cores shows variation in Ca/Si with the fronts and an increase in Ca/Si in the crack in the 10477-ft sample. XRD conducted on both samples shows that samples are highly carbonated. Calcium carbonate percentages ranged from 93 to 95 in the 10470-ft sample and from 88 to 92 in the 10477-ft sample.

The high calcium carbonate weight percentages in the samples do not represent the entire sample however they are an indication that the cements (C-S-H) in the sample have nearly completely reacted (Equations 3 and 5); replacing the C-S-H with a with calcium carbonate and amorphous silicate hydrate that may not show up in XRD analysis.

The carbonation of the cores collected at 10470 and 10477 ft in the CO_2 zone is not surprising. Those cements provide insight into the endpoint for cement carbonation if the reaction stops are the creation of calcium carbonate and there is not further dissolution (Equations 3 and 5). All of the sidewall cores collected between 10470 and 7900 ft show carbonation at one or both of the interfaces indicating that the casing-cement and cement-formation interfaces act as migration pathways for CO_2. The results of the LA-ICP-MS show a depletion of calcium, low Ca/Si, near the ends of the samples with an enrichment in calcium, high Ca/Si, further in. This implies that the reactions taking place in the samples collected between 10470 and 7900 are progressing past Equations 3 and 5 and proceeding with calcium carbonate dissolution at the interfaces, Equations 6 and 7. This is in general agreement with Duguid et al. [5] and Carey et al. [1] who have found that the interfaces in the well are more conductive than the porous network of the cement.

The estimated Ca/Si and other ratios presented in the background section (2) are lower than those in the “steady” portions of the LA-ICP-MS results. This is likely due to not being able to scale the LA-ICP-MS results against a reference cement sample of cement and not an indication that the cement in the well is different than what was recorded.

The degradation of the fiberglass casing in the reservoir CO_2 zone can be seen in both the logs and the casing samples collected. The logs show the worst damage in the CO_2 zone with less damage above the CO_2 zone and the least damage below the CO_2 zone (Based in IRAV, Figure 83). This is also indicates that CO_2 is migrating along the casing, buoyant CO_2 will migrate up from the reservoir causing more damage above the CO_2 zone than below the CO_2 zone. The quick degradation of the casing, over 6 years, indicates a need to carefully choose materials that are compatible with the ambient environment when designing the well.

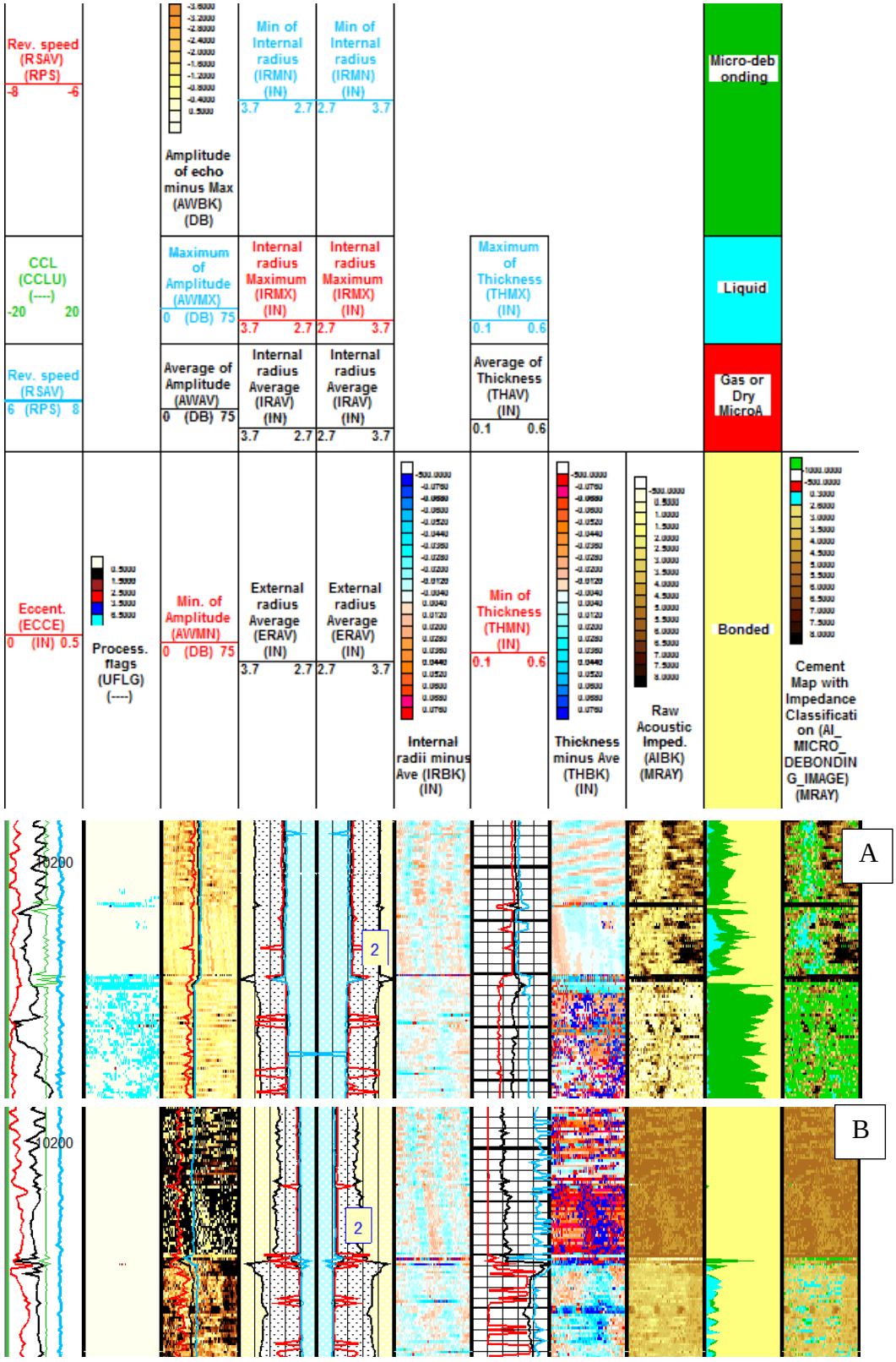

Figure 209 Log sections showing the steel to fiberglass transition in CFU31-F3 with steel processing (A) and fiberglass processing (B).

6 Conclusions

The CFU31F-2 and CFU31F-3 monitoring wells were constructed to test monitoring technologies in and above a commercial CO_2-EOR project. The materials selected and the design of the well were optimized for monitoring. Carbonation in CFU31-F2 was seen as high as 7900 ft, above what was considered top of cement based on the logs. Time-lapse comparison of cement bond amplitude data and acoustic impedance maps show a deterioration of signal that implies a deterioration of cement bond or cement along much of the cemented annulus in the long-string section. Analysis of sidewall cores using XRD and LA-ICP-MS validated the log interpretation by confirming the degradation of cement (carbonation) along the casing-cement interface.

The ultrasonic image maps also clearly identify the control lines and monitoring technology attached to the outside of the of the long-string casing on each well studied. The control lines appear as microdebonded or fluid filled vertical features implying that they could act as leakage pathways. The sidewall core through the control line at 10380 ft confirms that CO_2 is migrating along the control line with heavily carbonated cement at the control line interface. LA-ICP-MS and XRD on formation interface of the sidewall cores collected in both wells indicates that CO_2 is also moving of the cement-formation interface.

LA-ICP-MS and XRD indicate that the amount carbonation in the center of the cores was less than the carbonation at the interfaces. Indicating that CO2 is reaching the center of the cores by diffusing in from the interfaces and not migrating up from the reservoir though the porous matrix of the cement. This agrees with Duguid et al. [5] and Carey et al. [1] who have found that the interfaces in the well are more conductive than the porous network of the cement.

Both the materials used to construct the well and the decision to attach monitoring technology to the outside of the well may have contributed to the migration of CO_2 along the interfaces. Careful consideration should be given to material selection to ensure that it does not degrade when in contact with the fluids in the reservoir and overlying strata. The addition of the control line on the outside of the casing complicated the cement placement and likely caused no cement to bond to the casing adjacent to the control line leading out of the reservoir. Further study of other wells with external lines should be conducted to see of the results of the construction of CFU31-F2 and -F3 is normal or an exception.

References

[1] Carey JW, Wigand M, Chipera SJ, WoldeGabriel G, Pawar R, Lichtner PC, Wehner SC, Raines MA, Guthrie GD Analysis and performance of oil well cement with 30 years Of CO_2 exposure from the SACROC Unit, West Texas, USA. International J of Greenhouse Gas Control 2007:1:75–85.

[2] Hawkes C, and Gardner C., Pressure transient testing for assessment of wellbore integrity in the IEAGHG Weyburn–Midale CO2
Monitoring and Storage Project, International J of Greenhouse Gas Control, 2012:16:S50–S61.

[3] Duguid A, Carey JW, and Butsch R, Well Integrity Assessment of a 68 Year Old Well at a CO_2 Injection Project, Proceedings of the 12th International Conference on Greenhouse Gas Technologies, Austin, TX, October 2014, Energy Procedia, 2014:63:5691 – 5706.

[4] Crow W, Carey JW, Gasda SE, Williams DB, Celia MA. Wellbore integrity of a CO_2 producer. International Journal of Greenhouse Gas Control 2010:4(2):186–197.

[5] Duguid A, Butsch R, Carey JW, Celia M, Chugunov N, Gasda S, Ramakrishnan TS, Stamp V, and Wang J, Pre-injection Baseline Data Collection to Establish Existing Wellbore Leakage Properties, 11th International

Conference on Greenhouse Gas Technologies, Kyoto, Japan, September 2012, Energy Procedia, 2013:37:5661 – 5672.

[6] Hovorka SD, Meckel TA, Trevino RH, Monitoring a large-volume injection at Cranfield, Mississippi-Project design and recommendations, Int J of Greenhouse Gas Control, 2013:18:345-360.

[7] Butsch R, Brown AL, Bryans B, Kolb C, Hovorka S, Integration of well-based subsurface monitoring technologies: lessons learned at SECARB study, Cranfield, MS, Int J of Greenhouse Gas Control, 2013:18:409-420.

[8] Yang X, Chen X, Carrigan CR, Ramirez AL, Uncertainty quantification of CO_2 saturation estimated from electrical resistance tomography data at the Cranfield site, Int J of Greenhouse Gas Control, 2014:27:59-68.

[9] Carrigan CR, Yang X, LaBrecque DJ, Larsen D, Freeman D, Ramirez AL, Daily W, Aines R, Newmark R, Friedmann J, and Hovorka S, Electrical resistance tomographic monitoring of CO_2 movement in deep geologic reservoirs, Int J of Greenhouse Gas Control, 2013:18:401-408.

[10] Kutchko, B., Strazisar, B. R., Dzombak, D.A., Lowry, G. V., and Thaulow, N.: "Degradation of cell cement by CO_2 under geologic sequestration conditions," *Environmental Science and Technology,* (2007), Vol. 41, No. 13, pp. 4787-4792.

[11] Duguid, A., Radonjic, M., Scherer, G. W.: "The effect of carbonated brine on well cement used in geologic formations," *12th International Congress on the Chemistry of Cement*, Montreal, Canada, July 8-13, 2007.

[12] Duguid, A., Radonjic, M., Scherer, G. W.: "The effect of carbonated brine on the interface between well cement and geologic formations under diffusion-controlled conditions," *8th International Conference on Greenhouse Gas Control Technologies*, Trondheim, Norway, June 19-22, 2006.

[13] Duguid, A., Radonjic, M., Bruant, R., Scherer, G. W.: "Degradation of well cements exposed to carbonated brine," *Proceedings of the 4th Annual Conference on Carbon Capture and Sequestration*, Washington D.C., May 2-5, 2005.

[14] Barlet-Gouédard, V., Rimmelé, G., Goffé, B, and Porcherie, O.: "Mitigation strategies for the risk of CO_2 migration through wellbores," paper SPE 98924 presented at the 2006 IADC/SPE drilling conference, Miami, Florida, 21-23 February 2006.

[15] Andac, M., and Glasser, F. P.: "Long-term leaching mechanisms of portland cement-stabilized municipal solid waste flyash in carbonated water," *Cement and Concrete Research* (1999), 29, 179–186.

[16] Revertegat, E., Richet, C., and Gégout, P.: "Effect of pH on the durability of cement pastes," *Cement and Concrete Research*, (1992), Vol. 22, pp. 259–272.

[17] Onan, D. D.: "Effects of supercritical carbon dioxide on well cements," paper SPE 12593 presented at the 1984 Permian Basin Oil and Gas Recovery Conference, Midland, TX, March 8-9, 1984.

[18] Bruckdorfer, R. A.: "Carbon dioxide corrosion in oilwell cements," paper SPE 15176 presented at the 1986 Rocky Mountain Regional Meeting of SPE, Billings MT, May 19-21, 1986.

[19] Mississippi Oil and Gas Board, Well Database, accessed September, 2016, http://www.ogb.state.ms.us/welldatamenu.php

[20] Mississippi Oil and Gas Board, Form 3-1 for well CFU31F-2, accessed September, 2016, http://www.ogb.state.ms.us/welldatamenu.php

[21] Mississippi Oil and Gas Board, Form 3-1 for well CFU31F-3, accessed September, 2016, http://www.ogb.state.ms.us/welldatamenu.php

[22] Mississippi Oil and Gas Board, Production Data for well CFU31F-1, accessed September, 2016, http://www.ogb.state.ms.us/welldatamenu.php

[23] Nelson EB, and Guillot D, Well Cementing. Schlumberger, Sugar Land, Texas, 2006.

[24] Federal Highway Administration, accessed April, 2017, https://www.fhwa.dot.gov/pavement/recycling/fach01.cfm

[25] Souza, P.P., Soares, R.A., Anjos, M.A., Freitas, J.O., Martinelli, A.E., and Melo, D.F., "Cement slurries of oil wells under high temperature and pressure: the effects of the use of ceramic waste and silica flour," Brazilian Journal of Petroleum and Gas, 2012: v. 6, no. 3, pp 105-113.

[26] Ramakrishnan TS. Chugunov N. Duguid A. Tombari J. Method and tool for evaluating fluid dynamic properties of a cement annulus surrounding a casing. US Patent 7753118 (2010).

[27] Ramakrishnan TS. Chugunov N. Duguid A. Tombari J. Tool and method for evaluating fluid dynamic properties of a cement annulus surrounding a casing. US Patent 7753117 (2010).

[28] Lemmon EW. Huber ML. McLinden MO. REFPROP – Reference Fluid Thermodynamic and Transport Properties. NIST Standard Reference Database 23, Version 8.0. (2007).